The Dissertation Committee for Nasim Mohammadi Estakhri certifies that this is the approved version of the following Dissertation:

Manipulating Light-Matter Interactions with Plasmonic Metamolecules and Metasurfaces: A Route to Control Absorption and Scattering at the Nanoscale

Committee:

Andrea Alù, Supervisor

Ananth Dodabalapur

Xiaoqin Li

Hao Ling

Zheng Wang

Manipulating Light-Matter Interactions with Plasmonic Metamolecules and Metasurfaces: A Route to Control Absorption and Scattering at the Nanoscale

by

Nasim Mohammadi Estakhri, B.Sc.; M.Sc.

Dissertation

Presented to the Faculty of the Graduate School of

The University of Texas at Austin

in Partial Fulfillment

of the Requirements

for the Degree of

DOCTOR OF PHILOSOPHY

The University of Texas at Austin

August 2016

Dedication

To my wonderful parents and my lovely sisters.

Acknowledgements

This work wouldn't have been possible without the help and support of many people and I want to take this opportunity to express my gratitude for their valuable support. First, I am deeply grateful to my Ph.D. advisor, Prof. Andrea Alù. Since I first met Andrea in 2011, I have learned a lot from him, inspired by his passion for research, and benefited from his guidance and support. I would also like to thank my other committee members: Prof. Ananth Dodabalapur, Prof. Elaine Li, Prof. Hao Ling, and Prof. Zheng Wang for their attendance to my proposal and defense, their support, and their precious guidance during my Ph.D. I want to thank Prof. Bank, Prof. Wang, and Prof. Yilmaz for their valuable courses that educated me. I am also very grateful to Prof. Dodabalapur, Prof. Elaine Li, Prof. Polman, Prof. Beruete, and Prof. Shih, for our exciting collaborative projects. I also want to thank Prof. Engheta for his support and encouragement during my Ph.D.

I want to thank all my colleagues: Christos Argyropoulos, Yang Zhao, Xing-Xiang Liu, Dimitrios Sounas, Jason Soric, Pai-Yen Chen, Sebastian Gomez, Amir Askarpoor, Romain Fleury, Yakir Hadad, Shannon Miller, Caleb Sieck, Mykhailo Tymchenko, Ali Miri, Sarah Elias, Ian Williamson, Khai Le, Nicholas Estep, Francesco Monticone, Ahmet Kord, Costas Valagiannopoulos, and Bakhtyar Orazbayev. I appreciate all the amazing time we spent together and our lively discussions. I also want to sincerely thank Melody Singleton, Melanie Gulick, Barry Levitch, and Karen Little from ECE department.

And finally, I want to thank my dearest family. My mom and dad who have always been my greatest supporters and my sisters, Nazanin and Nooshin, for their unconditional love and friendship for me.

Manipulating Light-Matter Interactions with Plasmonic Metamolecules and Metasurfaces: A Route to Control Absorption and Scattering at the Nanoscale

Nasim Mohammadi Estakhri, Ph.D.
The University of Texas at Austin, 2016

Supervisor: Andrea Alù

The interaction of electromagnetic waves with materials is at the basis of several phenomena influencing our everyday lives. Throughout the past few decades we are witnessing a rapid progress in the development of new platforms to engineer and design different aspects of wave-matter interaction for applications ranging from green energy harvesting, to high speed data communication, and medicine. In line with these developments, the advent of metamaterials, or artificially structured materials, introduces an alternative path to mold and control electromagnetic waves with degrees of freedom that are not accessible in natural materials. There is, however, a strong need to broaden the range of applicability of metamaterials thorough strong nanoscale light management, real-time tunability, ease of fabrication, and lowering the losses. In this study we discuss that to what extent it is possible to engineer the scattering, absorption, and local wave-matter interaction of metamolecules, as the basic building-blocks of metamaterials, as well as assembles of them forming complex systems.

In this work, first, we propose and investigate new nanoparticle geometries with tailored complex absorption and scattering signatures. We demonstrate that plasmonic-based nanostructures can be tailored to provide unprecedented control of their scattering and absorption/emission response over broad bandwidths, specifically in the optical frequency range. We show that judicious combination of plasmonic-dielectric singular nanoparticles provides very efficient broadband and controllable light absorption and amplification. Based on these composite elements, we propose a nanoscale optical switch with strong sensitivity and tunability. These engineered nanoparticles are also particularly interesting for applications in nonlinear optics, spasing, and energy-harvesting devices.

Next, we answer the fundamental question of "to what extent the unwanted scattering from a general absorbing body may be reduced?". We demonstrate the theoretical limitations of a furtive sensor and provide a proof of the concept implementation of minimum-scattering superabsorbers at optical and microwave frequencies. Based on our theoretical analysis, we also explore experimental realization of microwave low-scattering antennas. This study is of particular importance for the near-field subdiffractive probing and closely-packed antenna designs.

Last, we propose a new degree of freedom in controlling the propagation and scattering of light through proper arrangements of dissimilar metamolecules over a surface, i.e. gradient metasurfaces. We theoretically investigate and design metasurfaces that are capable of performing complex wave shaping functionalities such as cloaking, yet, over a single ultrathin volume. Our full analytical approach enables us to underline the inherent limitations and wide range of capabilities of metasurfaces, and we propose novel techniques to significantly improve the efficiency of wave manipulation by metasurfaces. We also investigate the proposed concept of local wave manipulation in several practical applications in beam steering, improved energy harvesting, and cloaking arbitrary obstacles, accompanied by experimental realization of negative reflection from optical metasurfaces. Such unprecedented control of optical wave propagation along with compatibility of metasurfaces with standard lithographic techniques and on-chip technology will significantly impact the future application of metasurfaces, paving the way toward flat, compact optical devices.

Table of Contents

List of Tables

List of Figures

Figure 8.4: (a) A time snapshot of the electric field distribution when the object (without cloak) is illuminated by a 45° Gaussian beam. The ground plane and the scatterer are made of PEC material, and the length and height of the object are $L = 1500$ nm and $H = 200$ nm. (b) Electric field distribution when the object is covered with the designed metasurface (cloaked). The metasurface thickness is $h = 50$ nm, placed on top of the original object and conformally following its shape with $d = 100$ nm spacing. (c) 3D sketch of the deigned cloaking set-up. (d) Phase of the total electric field on a hypothetical boundary placed at 20 nm distance above the metasurface, as indicated by the white arrow in panel (c). The corresponding amplitude is also shown in the inset. (e) Angular dependence of the carpet cloak metasurface: the total field intensity along a half circle enclosing the system (dashed-line in panel a) is shown for three different incident angles. Blue and red curves refer to cloaked and uncloaked cases, and the gray curve indicates the reference response in the absence of any surface bump. All fields are calculated through full-wave simulations of the entire setup [19]. (Reprinted with permission from Philosophical Transactions A, Vol. 373, Issue 2049, pp. 20140351 (2015). Copyright 2015 The Royal Society Publishing).177

Chapter 1: Introduction

The final goal of this work is to underpin novel interactions of waves with engineered nanoparticles and nanostructures that provides platforms for several interesting applications in various frequency ranges, specially at optics. For this reason I want to start by giving a brief introduction on the history of light manipulation and how it influenced the advent of metamaterials and metasurfaces. Contents of this chapter partially appeared/to appear in "Farhat, M.; Chen, P.; Guenneau, S.; Enoch, S., Transformation Wave Physics: Electromagnetics, Elastodynamics, and Thermodynamics, Pan Stanford, to be published" and " Mohammadi Estakhri, N. ; Argyropoulos, C.; Alù, A., Graded metascreens to enable a new degree of nanoscale light management. Phil. Trans. R. Soc. A 2015, 373 (2049), 20140351".

1.1 METAMATERIALS AND HISTORY OF LIGHT MANIPULATION

Light, the narrow visible portion of the electromagnetic spectrum to which the human eye is sensitive, has fascinated mankind since ancient times, and the interest in controlling and utilizing it draws back to well before the development of modern electromagnetic theory. Early scientists were able to build simple optical elements such as lenses, prisms, and mirrors to efficiently collimate, split, or redirect rays of light. Color, as the visual perception of the interaction of light with different materials, have been identified for centuries. By relying on simple empirical rules, scientists even discovered much more advanced phenomena such as plasmon resonances of nanoparticles. Since 7th century it was well-known that adding metallic salts to glass can create beautiful stained glasses that have been used in many significant building across the world [1]. However, the major progress in understanding the nature of light matter interactions, and in general the electromagnetic wave theory, started following the establishment of Maxwell's equations in the 19th century. Governing all forms of electromagnetic waves, Maxwell's equations enabled studying wave–matter interactions at spatial ranges even smaller than the wavelength scale and explained the behavior of electric and magnetic fields in relation to the properties of the background medium. This field gradually evolved toward engineering the structures' shape, orientation, and composition to enable larger degrees of molding of the electromagnetic response.

Natural materials provide the simplest way to control and tailor electromagnetic waves and have been widely utilized throughout the history of science. The intrinsic electromagnetic properties of materials are based on the shape, orientation and lattice profile of their constitutive molecules, providing a wide range of refractive indices, chirality, nonlinearity, optical activity and dichroism. This variety in bulk constitutive parameters of natural materials is at the basis of many applications in electromagnetics and optics [2]-[6]. However, at the same time, it is not often sufficient to ultimately control the wave in the desired way and fulfill the growing demand for efficiency, compactness, speed, and cost-effectiveness, particularly in advanced applications and for integrated optical devices. The need for a broader space of degrees of freedom to arbitrarily manipulate the flow of light has stimulated a large interest in metamaterials during the past years [7]-[10], with which we can achieve the desired functionalities by engineering the shape and composition of *metamolecules* or by embedding subwavelength resonances into them. The prefix "meta" comes from Greek and means "beyond", as metamaterials are artificial composites that are designed to go beyond the properties found in the natural materials. This field has been strongly advanced form many aspects, particularly owing the recent progresses in micro- and nano-fabrication methods, enabling giant light-matter interactions at the nanoscale [11]-[13].

During the past decades several new functionalities have been accomplished or greatly enhanced by incorporating metamaterials in the design of new devices, ranging from negative-refraction and super-resolving lenses [10],[14] to invisibility cloaks [15]-[16], extreme nonlinearity effects [17]-[20] and absorption enhancement [21]. Bulk metamaterials offer an enormous potential in terms of design and optimization, yet at the same time their applicability is somewhat challenged by the complicated requirements on fabrication, especially at optical frequencies [12].

Wave manipulation in three-dimensional metamaterials is typically achieved relying on the continuous propagation through these media, which is necessarily related to undesired losses and strong dispersion in metamaterial-based devices [22]. Many of these limitations and drawbacks, associated with the wave-matter interaction properties inside these artificial media, can be circumvented with metasurfaces, the two-dimensional counterparts of bulk metamaterials [23]-[25]. Metasurfaces provide a platform for efficient and largely enhanced light-matter interaction over subwavelength thicknesses, compatible with current nano-lithographic techniques. In addition, their ultrathin, planarized features are particularly appealing in the prospect of direct integration into nanophotonic systems. Important results have been recently attained in this context, and properly designed metasurfaces have been introduced to efficiently control and manipulate phase, amplitude, polarization and momentum of the optical waves at the nanoscale [26]-[31]. Single and stacked metasurfaces have been exploited to implement several optical elements, such as polarizers, compact lenses, meta reflect- and transmitarrays, optical vortex plates, optical holograms, and quarter wave plates over ultrathin volumes [27],[31]-[34].

The advent of metamaterials and metasurfaces provided new possibilities to approach, improve, and re-think many of the current scientific and technological challenges. The ongoing research in the field is also extremely multidisciplinary and entails extensive study on the physics of light-matter interaction at the nanoscale and engineering subwavelength configurations to attain various desired functionalities at the optimal level, along with theoretical studies to provide new designer tools for metamaterials and advancing the nanofabrication techniques. The focus of this work is across the first two areas: initially engineering novel nanoparticles and metamolecules that go beyond the regular response achievable from subwavelength structures —in terms of absorption, scattering, resonance bandwidth, and so on— and next, showing theoretically and experimentally how metasurfaces can improve many aspects of different technologies. In the first three chapters we discuss how engineered nanoparticles can provide unprecedented absorption and scattering properties associated with careful excitation of localized resonances in their geometries. Many of the topics studied here are relevant to a wide range of frequencies, in addition to the optical waves. For instance, inspired by the theory of minimum-scattering nanoparticles provided in chapter 4 we later design minimum-scattering microwave antennas. In the following chapters, we then discuss the main theory of wave-shaping with arrays of metamolecules forming "metasurfaces" and propose several interesting functionalities enabled and improved through local wave engineering at the subwavelength level, and that completes the subject matter of this thesis.

1.2 References

[1] https://en.wikipedia.org/wiki/Stained_glass#Origins

[2] Wu, Q., Hewitt, T. & Zhang, X. C. Two-dimensional electro-optic imaging of THz beams. Applied Physics Letters 69, 1026-1028 (1996).

[3] Wu, Q., Litz, M. & Zhang, X. C. Broadband detection capability of ZnTe electro-optic field detectors. Applied Physics Letters 68, 2924-2926 (1996).

[4] Desurvire, E. Erbium-doped fiber amplifiers: Device and System Developments. (Wiley-Interscience, 2002).

[5] Chen, C.-Y. et al. Liquid-crystal-based terahertz tunable Lyot filter. Applied Physics Letters 88, 101107-101103 (2006).

[6] Kuiper, S. & Hendriks, B. Variable-focus liquid lens for miniature cameras. Applied Physics Letters 85, 1128-1130 (2004).

[7] Engheta, N. & Ziolkowski, R. W. Metamaterials: physics and engineering explorations. (John Wiley & Sons, 2006).

[8] Smith, D. R., Padilla, W. J., Vier, D., Nemat-Nasser, S. C. & Schultz, S. Composite medium with simultaneously negative permeability and permittivity. Physical review letters 84, 4184 (2000).

[9] Joannopoulos, J. D., Johnson, S. G., Winn, J. N. & Meade, R. D. Photonic crystals: molding the flow of light. (Princeton university press, 2011).

[10] Shalaev, V. M. Optical negative-index metamaterials. Nature photonics 1, 41-48 (2007).

[11] Boltasseva, A. & Shalaev, V. M. Fabrication of optical negative-index metamaterials: Recent advances and outlook. Metamaterials 2, 1-17 (2008).

[12] Soukoulis, C. M. & Wegener, M. Past achievements and future challenges in the development of three-dimensional photonic metamaterials. Nature photonics 5, 523-530 (2011).

[13] Gates, B. D. et al. New approaches to nanofabrication: molding, printing, and other techniques. Chemical reviews 105, 1171-1196 (2005).

[14] Jacob, Z., Alekseyev, L. V. & Narimanov, E. Optical hyperlens: far-field imaging beyond the diffraction limit. Optics express 14, 8247-8256 (2006).

[15] Alù, A. & Engheta, N. Multifrequency optical invisibility cloak with layered plasmonic shells. Physical review letters 100, 113901 (2008).

[16] Schurig, D. et al. Metamaterial electromagnetic cloak at microwave frequencies. Science 314, 977-980 (2006).

[17] Argyropoulos, C., Chen, P.-Y., D'Aguanno, G., Engheta, N. & Alu, A. Boosting optical nonlinearities in ε-near-zero plasmonic channels. Physical Review B 85, 045129 (2012).

[18] Chen, P.-Y., Argyropoulos, C. & Alu, A. Enhanced nonlinearities using plasmonic nanoantennas. Nanophotonics 1, 221 (2012).

[19] Suchowski, H. et al. Phase Mismatch–Free Nonlinear Propagation in Optical Zero-Index Materials. Science 342, 1223-1226 (2013).

[20] Husu, H. et al. Metamaterials with tailored nonlinear optical response. Nano letters 12, 673-677 (2012).

[21] Avitzour, Y., Urzhumov, Y. A. & Shvets, G. Wide-angle infrared absorber based on a negative-index plasmonic metamaterial. Physical Review B 79, 045131 (2009).

[22] Shalaev, V. M. et al. Negative index of refraction in optical metamaterials. Optics Letters 30, 3356-3358 (2005).

[23] Holloway, C. L. et al. A discussion on the interpretation and characterization of metafilms/metasurfaces: The two-dimensional equivalent of metamaterials. Metamaterials 3, 100-112 (2009).

[24] Kildishev, A. V., Boltasseva, A. & Shalaev, V. M. Planar photonics with metasurfaces. Science 339 (2013).

[25] Yu, N. & Capasso, F. Flat optics with designer metasurfaces. Nature materials 13, 139-150 (2014).

[26] Yu, N. et al. Light propagation with phase discontinuities: generalized laws of reflection and refraction. Science 334, 333-337 (2011).

[27] N. Mohammadi Estakhri and A. Alu, Manipulating Optical Reflections Using Engineered Nanoscale MetaSurfaces, Physical Review B, in press (2014).

[28] Chen, P.-Y. & Alù, A. Optical nanoantenna arrays loaded with nonlinear materials. Physical Review B 82, 235405 (2010).

[29] Landy, N., Sajuyigbe, S., Mock, J., Smith, D. & Padilla, W. Perfect metamaterial absorber. Physical review letters 100, 207402 (2008).

[30] Li, G. et al. Spin-enabled plasmonic metasurfaces for manipulating orbital angular momentum of light. Nano letters 13, 4148-4151 (2013).

[31] Zhao, Y., Belkin, M. & Alù, A. Twisted optical metamaterials for planarized ultrathin broadband circular polarizers. Nature communications 3, 870 (2012).

[32] Monticone, F., Mohammadi Estakhri, N. & Alù, A. Full control of nanoscale optical transmission with a composite metascreen. Physical review letters 110, 203903 (2013).

[33] Genevet, P. et al. Ultra-thin plasmonic optical vortex plate based on phase discontinuities. Applied Physics Letters 100, 013101 (2012).

[34] Ni, X., Kildishev, A. V. & Shalaev, V. M. Metasurface holograms for visible light. Nature communications 4 (2013).

Chapter 2: Single Plasmonic Nanoparticles for Unbounded and Broadband Absorption/Gain Efficiency

In order to achieve the desired local control on the light-matter interaction, discussed in chapter 1, we start by studying basic metamolecules with strong and controllable absorption properties. In this chapter and the next, we will discuss the fundamental physics behind inducing broadband local resonances in deeply subwavelength structures with specific geometrical characteristics, namely, sharp corners. Developing a closed-form analytical solution for response of composite plasmonic double-caps enables us to uncover interesting physical phenomena associated with the broadband adiabatic focusing of surface plasmons in these nanoparticles. We will provide detailed analysis of the characteristics of our proposed metamolecules along with the shape and material effects on the bandwidth and efficiency of absorption. Throughout this chapter we will demonstrate that it is essentially possible to induce finite amount of absorption/amplification in these metamolecules even in the limit of infinitesimally small intrinsic material loss/gain. We will discuss our findings for potential applications in nonlinear optics, switching, and sensing. Numerical simulations are also presented to verify the analytical solutions. Contents of this chapter partially appeared in "Mohammadi Estakhri, N.; Alù, A., Physics of unbounded, broadband absorption/gain efficiency in plasmonic nanoparticles. Physical Review B 2013, 87 (20), 205418".

2.1 INTRODUCTION

The growing interest in the optical properties of nanoparticles [1]-[2] has led to the discovery of many counterintuitive scattering features in plasmonic nanostructures. Due to their negative real part of permittivity, these particles support surface plasmon resonances at the nanoscale that have been proposed for many exciting applications, including field concentration, sensing, nanolasing and optical guiding [3]-[8]. Different configurations have been analyzed in recent years, from simple nanospheres and core-shell structures [6]-[7] to more complicated shapes, like crescent-shaped cylinders [9]. If simple structures are known to support strong, sharp plasmon resonances, more complicated shapes may provide more complex scattering responses, such as Fano and EIT (Electromagnetically Induced Transparency) resonances [10]-[11], or broadband operation [9]. Including gain may further boost these effects and compensate the detrimental effects usually caused by losses [12]-[13]. Many of the exotic properties of these geometries, however, often appear to contradict well-established physical limitations of resonant subwavelength systems [14], and the underlying physics is often difficultly captured because of the complex interaction between multiple resonances and plasmonic effects. On the other hand, a key parameter to consider in choosing a specific plasmonic geometry is the fabrication limitations dictated by technological challenges. Particles with exotic shapes and very fine features, although showing interesting electromagnetic properties, may be impractical to realize from the experimental point of view, and to apply to real-life devices.

As an example that may shed new light into these phenomena, in this chapter we analyze the anomalous electromagnetic response of a rather simple composite nanoparticle, formed by two conjoined half-cylinders of arbitrary complex permittivity ε_1, ε_2 relative to the background permittivity, and radius a, as shown in the inset of Fig. 2.1. This geometry has been recently proposed in the special configuration $\varepsilon_1 = -\varepsilon_2$ to form a resonant optical nanocircuit and previous attempts to analytically solve its scattering properties using mode-matching analysis [15], integral transformations [16] and coordinate mapping [17] have led to nonphysical solutions and strong numerical instabilities. In this chapter we show that these challenges are associated with remarkably counterintuitive resonant phenomena, which lead to a continuous frequency range over which distributed plasmon resonances may support unbounded values of absorption or gain efficiency, i.e., finite absorption or gain even in the limit of infinitesimally small material loss/gain. By extending the analytical approach originally introduced in [17] to evaluate the polarizability of a hemicylinder, we are able to solve the complete scattering problem associated with this geometry and derive closed-form expressions for the induced fields inside and outside this composite particle. This solution provides valuable physical insights into the complex wave interaction of this particle over a broad range of frequencies, which may provide, as we discuss in the following, exciting possibilities for energy concentration, harvesting and spasers [18]-[22].

2.2 THEORETICAL FORMULATION OF QUASI-STATIC POLARIZABILITY EXTRACTION

We start by solving the scattering problem in the quasi-static limit, under the assumption $a \ll \lambda_0$. An incident monochromatic wave with electric field $\mathbf{E}_0$ illuminates the nanostructure under an $e^{j\omega t}$ time convention and the permittivities of the two half-cylinders can take arbitrary complex values, whose imaginary parts correspond to material loss or gain depending on their negative or positive sign. Due to symmetries and linearity, the problem may be split into two orthogonal excitations with respect to the common diameter of the structure. By using separation of variables in the 2D bipolar coordinate system [17], the potential distribution in each material may be written in integral form as

$$\varphi_i(u,v) = \int_0^\infty U(u)\left[C_{i1}(\lambda)\cosh(\lambda v) + C_{i2}(\lambda)\sinh(\lambda v)\right] d\lambda\,, \tag{2.1}$$

in which the subscript $i = 1,2,0$ refers to upper, lower and outer regions, respectively, λ is the continuous eigenvalue, $U(u)$ is either $\cos(\lambda u)$ or $\sin(\lambda u)$ for longitudinal and transverse polarizations respectively, and $-\infty < u < \infty$, $-\pi < v \le \pi$ are bipolar coordinate variables. The unknown coefficients $C_{ij}(\lambda)$ may be found by applying suitable boundary conditions at the various boundaries to calculate the general form of potential distribution in all space from Eq. (2.1). In [17], this integral expansion was used to determine the electric polarizability $\alpha = p / E_0$ of an isolated hemicylinder, where p is the induced electric dipole moment, evaluated using the asymptotic expression of φ_0 in the far-field.

In the present case of two conjoined hemicylinders, the normalized polarizability may be analogously derived for arbitrary relative permittivity values. For longitudinal excitation we obtain

$$\begin{aligned} \alpha_l &= \frac{\pi^2\left[-\varepsilon_2 + \varepsilon_1\left(-1+6\varepsilon_2\right)\right] + 12\left(\varepsilon_1+\varepsilon_2\right)\left(\mathrm{Li}_2\left(\varepsilon^-\right) + \mathrm{Li}_2\left(\varepsilon^+\right)\right)}{1.5\pi^2\left(\varepsilon_1+\varepsilon_2+2\varepsilon_1\varepsilon_2\right)} \\ \varepsilon^\pm &= -\frac{\left(1+\varepsilon_1\right)\left(1+\varepsilon_2\right)\left(\varepsilon_1+\varepsilon_2\right)}{\varepsilon_2 \pm \sqrt{-\left(\varepsilon_1-\varepsilon_2\right)^2\left(2+\varepsilon_1+\varepsilon_2\right)\left(\varepsilon_1+\varepsilon_2+2\varepsilon_1\varepsilon_2\right)} + \varepsilon_1\left[1+\varepsilon_2\left(4+\varepsilon_1+\varepsilon_2\right)\right]} \end{aligned} , \qquad (2.2)$$

in which $\mathrm{Li}_2(x)$ is the polylogarithm function of second order, and analogously for the transverse excitation

$$\alpha_t = \frac{\pi^2\left[\varepsilon_1+\varepsilon_2-6\right] - 12\left(\varepsilon_1+\varepsilon_2\right)\left(\mathrm{Li}_2\left(\varepsilon^-\right) + \mathrm{Li}_2\left(\varepsilon^+\right)\right)}{1.5\pi^2\left(2+\varepsilon_1+\varepsilon_2\right)} . \qquad (2.3)$$

Having derived in closed-form the polarizability of this particle, we may efficiently analyze its extinction properties as a function of the available design parameters. We start from the lossless configuration, for which all involved permittivities are purely real. Fig. 2.1(a,b) shows the calculated longitudinal polarizability for different values of ε_1 and ε_2, assuming lossless materials (real-valued ε). Since so far we have been working in the quasi-static limit, there is no radiation loss and, in the limit of no Ohmic absorption, we expect the absorbed power to be identically zero. This requires that the polarizability is purely real, as in absence of scattering loss $P_{ext} = -\omega / 2 |E_0|^2 \operatorname{Im}[\alpha] = P_{abs}$ (P_{ext} and P_{abs} are extinction and absorbed powers, respectively). On the contrary, the results in Fig. 2.1(b) highlight continuous frequency ranges over which the polarizability has an imaginary component even in this lossless limit, consistent with some of the findings in [17] for a single hemicylinder.

To gain a better understanding of the behavior of the polarizabilities and their dependency on the permittivity and excitation, Fig 2.1(c,d) also shows the longitudinal and transverse polarizabilities of the structure fixing the lower half at $\varepsilon_2 = 3$ and varying ε_1 ;yellow shades highlight the resonance regions in these plots. Since plasmonic properties require frequency dispersion, these plots may be also read as the variation of polarizability versus frequency, once an appropriate dispersion model for ε_1 is assumed, as discussed in the following section.

The paradoxical result illustrated in Fig. 2.1, for which a complex polarizability may be obtained in the static limit for lossless materials, is mathematically associated with the range of permittivities for which the arguments of Li_2 have magnitude larger than one. However, the polylogarithm function $\mathrm{Li}_N(z) = \sum_{k=1}^{\infty} \frac{z^k}{k^N}$ is strictly convergent only for $|z| < 1$, requiring that its value should be analytically continued over the whole complex plane. Two branch-cuts are associated with this range of complex solutions, and complex conjugate values are admissible solutions of (2.2) and (2.3). This implies that our geometry may be able to extract (or produce, depending on the sign of $\operatorname{Im}[\alpha]$)

power even in the case of purely lossless (or gainless) materials. In Fig. 2.1(c,d) we indicate with solid (dashed) lines the solution with $\mathrm{Im}[\alpha]<0$ ($\mathrm{Im}[\alpha]>0$), corresponding to absorbing (amplifying) nanoparticles We notice that the author of [17] arbitrarily selected one of the two admissible branches, choosing opposite signs of the imaginary part in the different ranges with complex polarizability. Mathematically there is no reason to choose one branch or the other, as both solutions satisfy all boundary conditions of the system. By choosing opposite signs, we imply that the particle absorbs and emits in the two different permittivity ranges. We notice that a similar response has been highlighted in the case of other plasmonic geometries involving sharp corners [23].

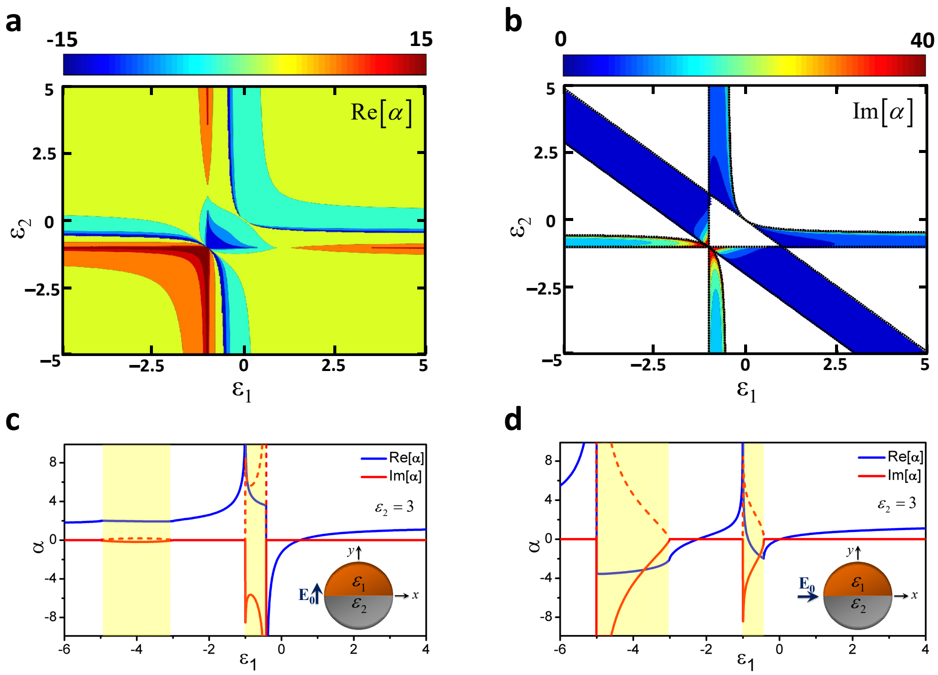

Figure 2.1: Normalized complex polarizability of two conjoined half-cylinders for different permittivity values under longitudinal excitation. (a) Real part of polarizability, (b) imaginary part. Polarizability of the structure with $\varepsilon_2=3$ (c) for longitudinal and (d) transverse excitation. Particle geometry and excitation fields are shown in the inset. Shaded regions highlight the resonant ranges of this geometry, as defined in (2.4). (Reprinted with permission from Physical Review B, Vol. 87, Issue 20, pp. 205418 (2013). Copyright 2013 American Physical Society).

2.3 SINGULARITIES AND THE ABSORPTION/GAIN PARADOX

In this section we discuss the reasons behind the paradox highlighted in the previous section. We start by looking at a simple dielectric wedge structure, which models the wave interaction at the corner region shown to be at the foundation of this phenomenon. We then present novel closed-form expressions for the polarizability and potential distribution in all regions of space, which allow us to discuss the nature of the induced electric field inside and around the particle. Finally, we study the absorption properties of the proposed geometry in the electrodynamic case and investigate how realistic considerations affect these conclusions.

As shown in the following, the counterintuitive response of the composite particle under analysis is physically associated with the singularities induced at the two corners of the structure, which have so far been assumed as ideal mathematical edges with zero curvature at the tip. In the corner proximity, the geometry may be statically modeled as a double dielectric wedge described by Laplace equation. Independent of the polarization of the applied field, eigen-solutions may be supported by the wedge configuration for some specific values of material permittivities [24]. Not surprisingly, the permittivity range over which $\mathrm{Im}[\alpha] \neq 0$ in Fig. 2.1(b) exactly corresponds to the quasi-static eigen-resonance of a $90°$ double dielectric wedge. It is possible to show, in fact, that the resonance of a $90°$ double wedge arises when

$$\begin{array}{ll}
-\varepsilon_2 - 2 < \varepsilon_1 < \min\{-\varepsilon_2, -1\}, \max\{-\varepsilon_2, -1\} < \varepsilon_1 < \dfrac{-\varepsilon_2}{1+2\varepsilon_2} & \text{for } \varepsilon_2 > 0 \\
-\varepsilon_2 < \varepsilon_1 < -\dfrac{\varepsilon_2}{2\varepsilon_2+1}, -\varepsilon_2 - 2 < \varepsilon_1 < -1 & \text{for } -1/2 < \varepsilon_2 < 0 \\
-\varepsilon_2 < \varepsilon_1 < \infty, -\infty < \varepsilon_1 < -\dfrac{\varepsilon_2}{2\varepsilon_2+1}, -\varepsilon_2 - 2 < \varepsilon_1 < -1 & \text{for } -1 < \varepsilon_2 < -1/2 \\
-\varepsilon_2 - 2 < \varepsilon_1 < -\varepsilon_2, -1 < \varepsilon_1 < -\dfrac{\varepsilon_2}{2\varepsilon_2+1} & \text{for } \varepsilon_2 < -1
\end{array} \quad .(2.4)$$

These inequalities provide, in general, two/three separate continuous resonant windows of unbounded absorption/gain efficiency, defined as the ratio $\mathrm{Im}\left[\alpha\right]/\varepsilon_i$ with ε_i being $\mathrm{Im}[\varepsilon_1]$ or $\mathrm{Im}[\varepsilon_2]$. In the permittivity range of Eq. (2.4), the corners support continuous eigenmodes that are at the basis of the anomalous response discussed in the previous section.

From the physical point of view, in this resonant range a highly oscillatory potential distribution is induced around the corner of the composite nanoparticle, with strongly enhanced electric fields. In practice, this behavior is limited by nonlocal effects and the minimum corner curvature of a realistic structure. In the special case of a hemicylinder ($\varepsilon_2 = 1$) previously studied in [15],[17], divergent or nonphysical solutions were found in the same range. Under this condition the two windows merge into $-3 < \varepsilon_1 < -1/3$, separated by a single point $\varepsilon_1 = -1$, corresponding to the special internal resonance analyzed in [25].

In the ideal lossless limit, there is no way to distinguish between the two branch-cuts, and both conjugate solutions in Fig. 2.1 are equally admissible. This implies that the boundary-value problem is not well defined, as the uniqueness theorem does not apply to an ideal lossless scenario [26]. Small losses are required to select the correct Riemann sheet and assign proper meaning to the solutions in Fig. 2.1. In order to address this issue, Fig. 2.2 shows the effect of loss/gain in ε_1 on $\mathrm{Im}\left[\alpha\right]$ for different values of $\mathrm{Re}[\varepsilon_1]$. Outside the resonance region, e.g., $\mathrm{Re}[\varepsilon_1] = -6.5$ (blue lines in Fig. 2.2), $\mathrm{Im}\left[\alpha\right]$ is a well-behaved continuous odd function of $\mathrm{Im}[\varepsilon_1]$, and it is identically zero for zero material loss. For values that lie in the continuous resonant range in Eq. (2.4), $\mathrm{Im}\left[\alpha\right]$ is still an odd function of $\mathrm{Im}[\varepsilon_1]$, but it has a discontinuity at $\mathrm{Im}\left[\varepsilon_1\right] \to 0^{\pm}$, associated with the ambiguity in selecting the correct Riemann sheet in the lossless case. By introducing an arbitrary amount of loss $\varepsilon_i < 0$ or gain $\varepsilon_i > 0$, we are able to select either the absorptive ($\mathrm{Im}[\alpha]<0$) or emissive ($\mathrm{Im}[\alpha]>0$) branch in Fig. 2.2. This implies that an arbitrarily small (but mathematically nonzero) value of loss or gain in the material can provide finite absorption or emission over a continuous bandwidth corresponding to (2.4) and in this continuous range absorption or gain efficiencies are effectively unbounded. Interestingly, smaller absorption/gain in the material can lead to larger overall absorption/gain in the nanoparticle, as the plasmonic effect at the corner is less quenched.

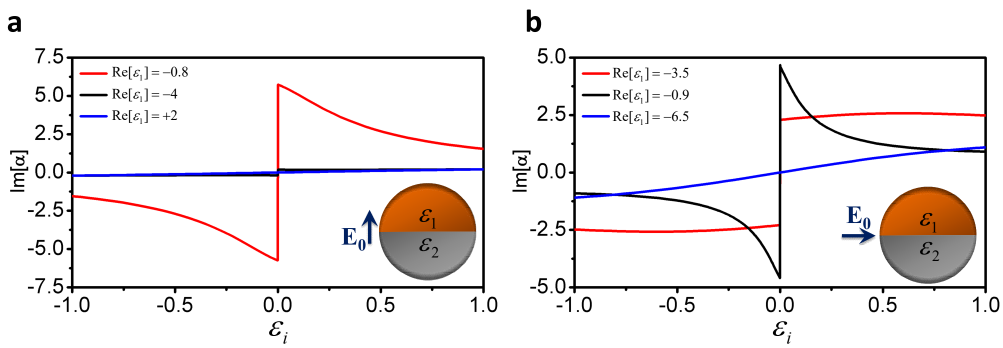

Figure 2.2: Imaginary part of polarizability versus $\mathrm{Im}[\varepsilon_1]$ for different values of $\mathrm{Re}[\varepsilon_1]$ and $\varepsilon_2 = 3$ for (a) longitudinal and (b) transverse illumination. Particle geometry and excitation fields are shown in the inset. (Reprinted with permission from Physical Review B, Vol. 87, Issue 20, pp. 205418 (2013). Copyright 2013 American Physical Society).

Power extraction or generation can arise only in regions where the quadrature component of the potential $\mathrm{Im}[\varphi_i]$ is nonzero. In the quasi-static lossless limit, we would expect φ_i to be exactly in phase with the excitation at all points, but in the resonant range of Eq. (2.4), analogous to (2.2), we need a nonzero imaginary component to justify power extraction. Our mathematical formalism allows calculating in closed-form also the imaginary part of the potential distributions in Eq. (2.1): by applying proper boundary conditions at all boundaries of the structure, the unknown coefficients $C_{ij}(\lambda)$ can be found for arbitrary values of ε_1 and ε_2, such as [17]

$$C_{01}(\lambda)=\frac{2(\varepsilon_1-\varepsilon_2)(\varepsilon_1+\varepsilon_2)}{\varepsilon_2+\varepsilon_1(1+\varepsilon_2(4+\varepsilon_1+\varepsilon_2))+(1+\varepsilon_2)(1+\varepsilon_1)(\varepsilon_1+\varepsilon_2)\cosh(\pi\lambda)}, \qquad (2.5)$$

for the longitudinal polarization. Similar expressions may be found for all the other coefficients, and for transverse excitation. Outside the resonant range in Eq. (2.4), these coefficients are continuous functions of the eigenvalue λ, and may be integrated over the entire spectrum to evaluate the potential and field distributions in Eq. (2.1) using a conventional numerical integration technique, i.e., the Euler method [27]. In this regime, the potential and fields will be real-valued at all points in space, as expected. However, in the resonant range of Eq. (2.4) the coefficients $C_{ij}(\lambda)$ have a simple pole in the denominator at

$$\lambda_p=\frac{1}{\pi}\cosh^{-1}\left(-\frac{\varepsilon_2+\varepsilon_1(1+\varepsilon_2(4+\varepsilon_1+\varepsilon_2))}{(1+\varepsilon_2)(1+\varepsilon_1)(\varepsilon_1+\varepsilon_2)}\right), \qquad (2.6)$$

implying that the coefficients, which all share the same denominator, hold a nonzero residue in this range [28]. In other words, each coefficient contains an integrable imaginary component at the pole location with Dirac-δ distribution sustaining the imaginary part of (2.1)-(2.2). The amplitude of the δ distribution may be calculated in closed-form by solving the residue problem as follows

$$C_{01}(\lambda)\Big|_{\lambda_p}=\pi j\,\mathrm{Res}\left[C_{01}(\lambda),\lambda_p\right]=j\frac{2(\varepsilon_1-\varepsilon_2)(\varepsilon_1+\varepsilon_2)}{(1+\varepsilon_2)(1+\varepsilon_1)(\varepsilon_1+\varepsilon_2)\sinh(\pi\lambda_p)}\delta(\lambda-\lambda_p), \qquad (2.7)$$

and a similar result may be derived for all the other coefficients. Therefore, the potential distribution in Eq. (2.1) may be determined everywhere without ambiguity using the Cauchy's principal value integration:

$$\begin{aligned}
\mathrm{Re}[\varphi_i(u,v)] &= \mathrm{p.v.}\int_0^{\infty} U(u)\left[C_{i1}(\lambda)\cosh(\lambda v)+C_{i2}(\lambda)\sinh(\lambda v)\right]d\lambda \\
\mathrm{Im}[\varphi_i(u,v)] &= U(u)\big|_{\lambda_p}\left[C_{i1}(\lambda_p)\cosh(\lambda_p v)+C_{i2}(\lambda_p)\sinh(\lambda_p v)\right]
\end{aligned}, \tag{2.8}$$

leading to a closed-form expression for the imaginary part of potential and field distribution. As an example in the case of conjoined hemicylinders and longitudinal excitation, the imaginary part of the potential distribution in the upper half-cylinder may be written in closed-form as:

$$\begin{aligned}
&\mathrm{Im}[\varphi_1(u,v)] = \frac{2E_0\cos(\lambda_p u)}{(\varepsilon_1+1)(\varepsilon_2+1)(\varepsilon_1+\varepsilon_2)\sinh(\lambda_p\pi)}\times \\
&\left[\begin{array}{l}
\left(-(\varepsilon_1-1)(\varepsilon_2+1)(\varepsilon_1+\varepsilon_2)\coth(\lambda_p\pi/2)+\dfrac{(\varepsilon_1-\varepsilon_2)^2}{\sinh(\lambda_p\pi)}\right)\times \\
\sinh(\lambda_p(\pi-v))+2(\varepsilon_2-\varepsilon_1)\dfrac{\sinh(\lambda_p(\pi/2-v))}{\sinh(\lambda_p\pi/2)}
\end{array}\right].
\end{aligned} \tag{2.9}$$

We recall that this component of the potential is responsible for absorption/gain, and can therefore provide interesting insights into the apparent paradox outlined in the previous section. Analogous expressions may be derived for the potential distribution at every point in space. It is quite remarkable that in this geometry we are able to derive in closed-form the imaginary component of the potential distribution everywhere in space. Similarly, we can write the imaginary part of the polarizabilities in Eqs. (2.2) and (2.3) in a simple closed-form using direct integration of the singularity in the integrand:

$$\mathrm{Im}[\alpha_l] = 8\lambda_p \mathrm{sign}\left[\frac{(\varepsilon_1+\varepsilon_2)}{\varepsilon_1+\varepsilon_2+2}\right]\times \left(\frac{(\varepsilon_1+\varepsilon_2)(\varepsilon_1\varepsilon_2-1)\coth(\lambda_p\pi/2)\sinh(\lambda_p\pi)-(\varepsilon_1-\varepsilon_2)^2}{(\varepsilon_1+1)(\varepsilon_2+1)(\varepsilon_1+\varepsilon_2)\sinh^2(\lambda_p\pi)}\right)$$

$$\mathrm{Im}[\alpha_t] = 8\lambda_p \mathrm{sign}\left[\frac{(\varepsilon_1+\varepsilon_2)}{\varepsilon_1+\varepsilon_2+2}\right]\times \left(\frac{(\varepsilon_1+\varepsilon_2)(\varepsilon_1\varepsilon_2-1)\cosh(\lambda_p\pi)+\varepsilon_1\varepsilon_2(\varepsilon_1+\varepsilon_2-2)+\varepsilon_2^2+\varepsilon_1^2-\varepsilon_1-\varepsilon_2}{(\varepsilon_1+1)(\varepsilon_2+1)(\varepsilon_1+\varepsilon_2)\sinh^2(\lambda_p\pi)}\right), \quad (2.10)$$

which allows calculating $P_{ext} = -\omega/2|E_0|^2 \mathrm{Im}[\alpha] = P_{abs}$ in closed-form. These expressions are consistent with (2.2)-(2.3) and are clearly valid only in the resonant range in Eq. (2.4), and zero elsewhere. The sign term in this last equation ensures the proper choice of the branch cut in the lossless limit. By adding an infinitesimally small amount of loss/gain the solution will automatically collapse to the correct branch, consistent with Fig. 2.2.

Figs. 2.3(a,b), as an example, show the real and imaginary parts of the potential distribution for a hemicylinder ($\varepsilon_2 = 1$) with $\varepsilon_1 = -1.1$ and longitudinal excitation. The imaginary part is calculated using our closed-form expressions, whereas the real part is obtained by numerical integration of (2.1). The imaginary component of the potential essentially represents an eigenmode of the structure, in quadrature with the impinging field and supported by plasmonic resonances at the two corners, with an amplitude linked to the value of excitation. This distribution, integrated over the nanoparticle volume, effectively sustains the extracted/generated power. Our analytical solution ensures that in the corner proximity the potential varies in the form ρ^{ν}, in which ν is purely imaginary inside the resonance region, forming a highly oscillatory distribution analogous to Figs. 2.3(a-b) around these points. It should be noted that in the ideal lossless limit this distribution is not square-integrable, as it leads to a finite value of extracted/generated power for $\varepsilon_i \to 0$ [29]. This finding, consistent with the unbounded energy density found near sharp corners in other geometries [30], explains the reason behind the non-uniqueness of our solution in the lossless limit. Figs. 2.3(c,d) show the corresponding field distributions in the same structure, calculated analytically as $\mathbf{E} = -\nabla\varphi$. Plasmonic oscillations around the corners (Figs. 2.3(a,b)) result in enhanced fields, which may become infinite at the edge point in the lossless case for an ideal corner.

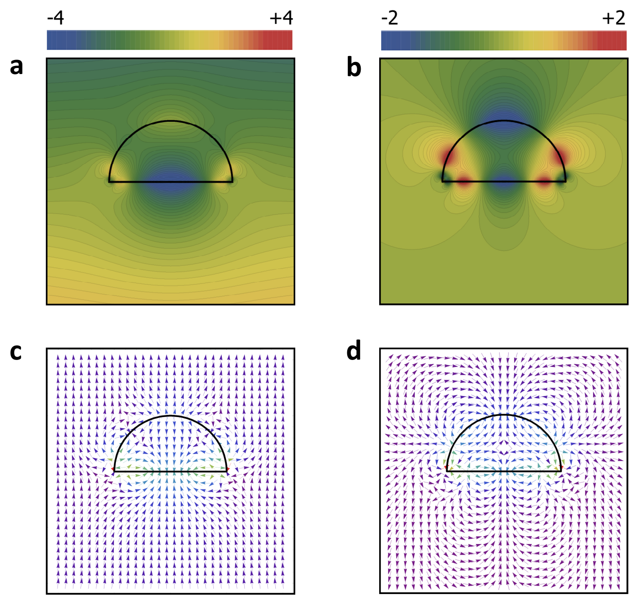

Figure 2.3: (a) Real part and (b) imaginary part of the potential distribution for a half-cylinder with permittivity $\varepsilon_1 = -1.1$ under longitudinal excitation, normalized to the impinging potential amplitude; (c) real and (d) imaginary parts of the field distribution in the particle. (Reprinted with permission from Physical Review B, Vol. 87, Issue 20, pp. 205418 (2013). Copyright 2013 American Physical Society).

Inspecting the imaginary part of the potential distribution in Fig. 2.3(b), we indeed notice strong plasmonic oscillations around the nanoparticle corners. The variation of potential along the particle diameter is plotted in Fig. 2.4(a), highlighting that the surface plasmon supported by the metal-dielectric interface is adiabatically focused towards the corners, with a finer and finer spatial variation as the corner is approached. This effect, supported over the whole resonant range in Eq. (2.4), produces broadband, largely enhanced electric fields and it sustains absorption/amplification even for infinitesimally small values of material loss/gain. Essentially, the surface plasmon is adiabatically focused towards the corner, as if it were traveling to infinity (inset of Fig. 2.4), explaining the reason why negligible losses (gain) are sufficient to sustain large absorption (amplification). Different from conventional adiabatic focusing of surface plasmons, in this geometry this effect is achieved at the nanoscale.

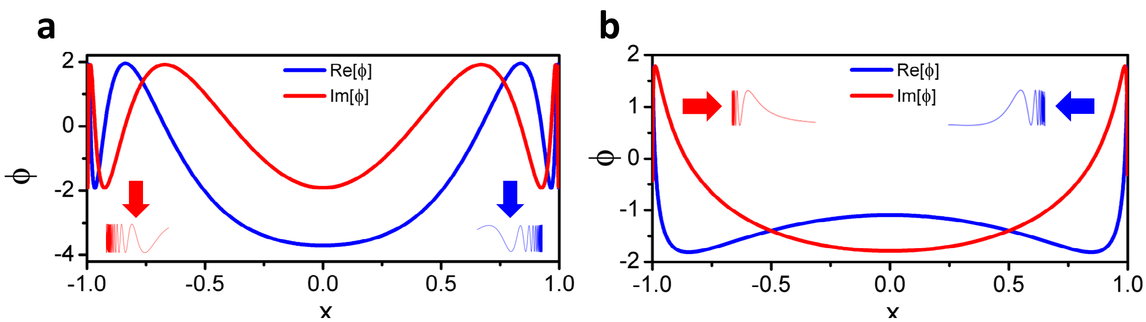

Figure 2.4: (a) Real (blue) and imaginary (red) parts of the normalized potential distribution for a half-cylinder with $\varepsilon_1 = -1.1$ under longitudinal excitation along the x-axis, (b) same distributions when $\varepsilon_1 = -2$. Closer views of the calculated potential around the corner points are shown in inset. (Reprinted with permission from Physical Review B, Vol. 87, Issue 20, pp. 205418 (2013). Copyright 2013 American Physical Society).

Fig. 2.4(b) shows the potential variation along the common diameter of the particle for a different example ($\varepsilon_1 = -2, \varepsilon_2 = 1$). The different behavior between $\varepsilon_1 = -1.1$ and $\varepsilon_1 = -2$ can be interestingly explained considering the wedge solution. For values of ε_1 near -1 the frequency of spatial oscillations is much larger compared to $\varepsilon_1 = -2$, resulting in oscillations extended farther from the corners. For these situations the field enhancement may be extended more broadly all over the particle, with interesting possibilities to more effectively enhance optical nonlinearities. These distributed resonances and adiabatic focusing have direct analogies with the resonant distribution highlighted in [9],[31]-[32], for crescent-shaped and touching plasmonic cylinders, but it is obtained here in an arguably simpler geometry over a flat surface and controllable frequency bands.

2.4 RADIATION LOSSES AND ABSORPTION CROSS-SECTION

The previous analysis highlights that the apparent paradox of unbounded absorption/gain efficiencies in the proposed nanoparticle is related to two relevant assumptions: ideal singularities in the nanoparticle geometry (perfect corners) and quasi-static solution. In the following we relax both these assumptions and analyze how these effects may be translated into realistic geometries and setups. In the long-wavelength limit, as long as the dipolar contribution dominates the scattering response, the quasi-static solution can be easily extended to the dynamic regime to include effects of radiation and retardation [33]. The dynamic Mie dipolar coefficient C_1 is related to the static polarizabilities in Eqs. (2.2) and (2.3) via $C_1 = \left(-1 + j8x_0^{-2}\alpha^{-1}/\pi\right)^{-1}$, $x_0 = k_0 a$, which includes now radiation losses. This procedure is consistent with the fact that, in the long-wavelength limit, the second-order correction to the polarizability response is due to dipolar radiation, taken into account by the additional imaginary term.

Fig. 2.5 shows the absorption cross-section normalized to the physical width of the particle for composite cylinders with $2a = 40\,\text{nm}$, compared to the case of a homogeneous cylinder of same size. In this case, in order to include also frequency dispersion and realistic material absorption, the upper half-cylinder is chosen to be silver with $\varepsilon_r = \varepsilon_\infty - \omega_p^2 \big/ \omega(\omega - j\Gamma)$, $\varepsilon_\infty = 5$, $\omega_p = 2\pi \times 2175\,\text{THz}$ and $\Gamma = 2\pi \times 4.35\,\text{THz}$ [34]. We compare the case of a silver hemi-cylinder ($\varepsilon_2 = 1$) and the case $\varepsilon_2 = 3$, which have different resonant bands following (2.4). The results confirm that absorption/gain may be largely enhanced over a continuous and controllable frequency band, significantly broadening the range and level of absorption/gain compared to a full circular rod of same material. For a half cylinder, the absorption is drastically enhanced in the frequency bands corresponding to the resonance region ($-3 < \varepsilon_1 < -1$ and $-1 < \varepsilon_1 < -1/3$), and is negligible at other frequencies. We observe that this particle shows a lower amount of absorption around the frequency for which $\varepsilon_1 = -1$, at which we actually have the highest absorption in the full cylinder case, consistent with the previous analysis. Quite counterintuitively, this absorption band does not rely on material losses and in fact is larger in the limit of zero losses, as discussed in Fig 2.2. Another example of this phenomenon, although much more limited in bandwidth, is evident in transition metamaterials [35]. Compared to a full cylinder of the same material, the absorption is drastically enhanced and its bandwidth significantly broadened. Since we can control the resonance range with ε_2 following (2.4), the structure can be designed to show high absorption efficiencies in two separate bands over the desired frequency ranges.

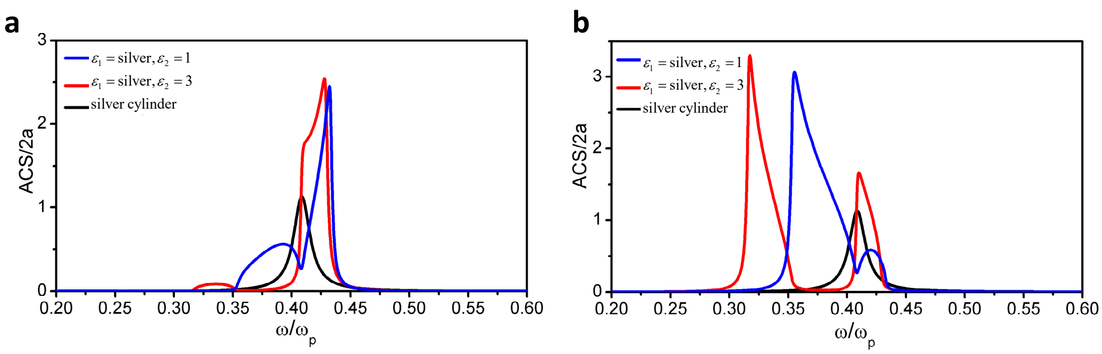

Figure 2.5: Normalized absorption cross-section for (a) longitudinal (b) transverse excitation of a composite nanoparticle with upper half-cylinder made of silver and different values of ε_2. The full cylinder case is also shown for comparison. (Reprinted with permission from Physical Review B, Vol. 87, Issue 20, pp. 205418 (2013). Copyright 2013 American Physical Society).

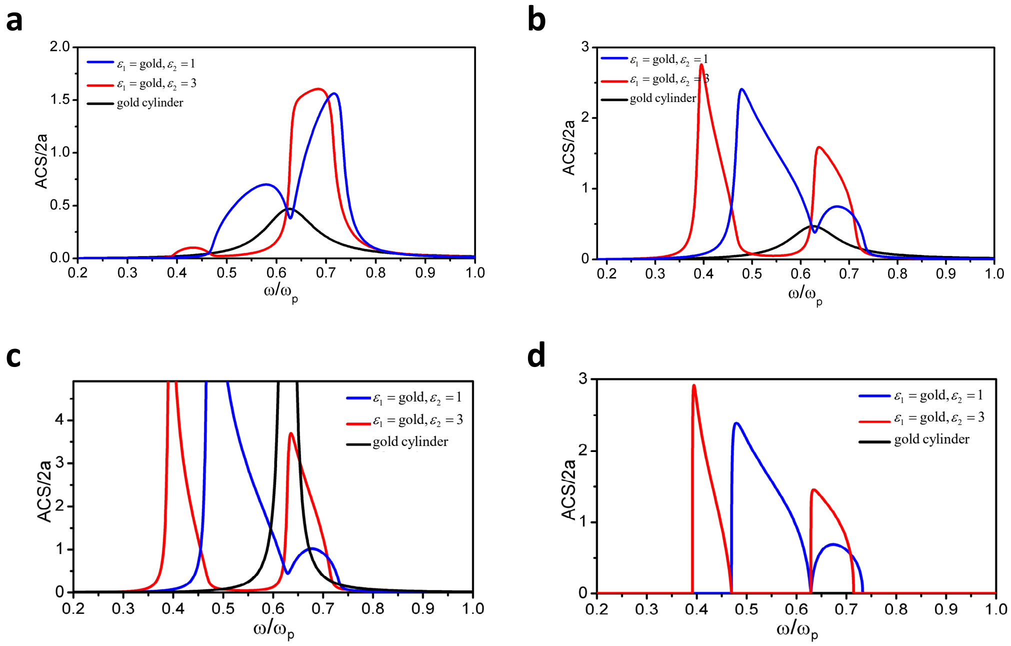

Figure 2.6: Normalized absorption cross-section for different configurations: the upper half-cylinder is gold while the lower part is either $\varepsilon_2 = 1$ (blue curves) or $\varepsilon_2 = 3$ (red curves). A full cylinder composed of gold (black curves) is also included for comparison. (a) Longitudinal excitation (b) transverse polarization. (c) Normalized absorption cross-section for transverse excitation under the quasi-static approximation; (d) same as (b), but neglecting gold losses. (Reprinted with permission from Physical Review B, Vol. 87, Issue 20, pp. 205418 (2013). Copyright 2013 American Physical Society).

In order to gain further insight into the effect of material and radiation losses on the resonance behavior of the structure, we also separately study these effects in a gold-dielectric configuration. We consider conjoined half-cylinders with diameter $2a = 40$ nm, in which now the upper half is made of gold following a Drude model with $\varepsilon_\infty = 1.53$, $\omega_p = 2\pi \times 2069\,\text{THz}$, and $\Gamma = 2\pi \times 17.64\,\text{THz}$ based on experimental measurement data [34]. Again, three configurations are studied separately: $\varepsilon_2 = 1$, $\varepsilon_2 = 3$, and a full gold cylinder for comparison. Fig. 2.6 shows the normalized absorption cross-section versus frequency for three different scenarios: in the first two panels we consider both realistic losses and retardation effects for different polarization of the impinging wave. Panel (c) shows the absorption for transverse excitation neglecting retardation but including realistic losses. Panel (d) on the other hand includes the retardation effect but assumes $\Gamma = 0$ (lossless gold).

Compared to silver (Fig. 2.5), gold provides slightly lower absorption due to damping of the plasmonic resonance near the corners in presence of a larger material and radiation losses. This can be explained also inspecting Fig. 2.6(d), in which we totally neglect material loss. In general, with conventional low-loss plasmonic materials (e.g., silver and gold), the focusing effect still dominates the absorption features of these particles. The effect of retardation can be observed in Fig.2.6(c). By including scattering loss, as expected, the absorption cross-section is broadened and dampened. It is interesting that in the case of a single full cylinder, scattering loss affects the total absorption much more drastically than in the composite configurations.

2.5 Realistic configurations

In order to demonstrate the realistic applicability of the proposed structure, we analyze now the effect of finite curvature at the corners. As discussed in Ref. [30], when a mathematical edge is replaced by one with nonzero curvature, the continuous eigen-resonance range is necessarily converted into a set of discrete resonance frequencies, which ensures that Chu's fundamental limit is satisfied [14]. The amount of realizable absorption will depend on how adiabatically surface plasmon resonances may be focused and absorbed before the edge is terminated. We used full-wave simulations to study this effect for different curvature values. Absorption cross-section of a blunted hemi-cylinder with permittivity $\varepsilon_1 = -0.529 - j\varepsilon_i$ and $2a = 40$ nm is compared in Fig. 2.7 to an ideal geometry with same parameters. The full cylinder case is also shown for comparison. We notice that the absorption phenomenon is pretty robust for finite values of material loss, and the edge bluntness effectively sets the lower level of $|\varepsilon_i|$ for which large absorption/gain may be achieved. In other words, when considering corners with finite curvature, absorption/gain efficiencies are inherently bounded and fundamentally limited by how sharp (relative to the radius of the particle), the corner may be made. Similar results are found in the case of the singular geometry simulated with finite-integration methods (blue curve), as a finite curvature is automatically introduced by numerical meshing. Our results show that significantly large and broadband absorption/gain effects may be achieved with realistic nanoparticle geometries.

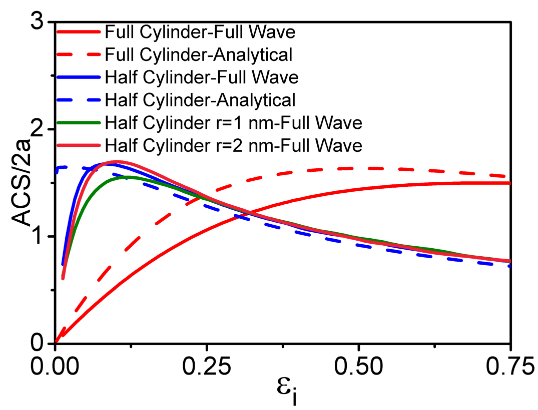

Figure 2.7: Normalized absorption cross-section vs. material loss for a hemi-cylinder with $\varepsilon_1 = -0.529 - j\varepsilon_i$ compared to full-wave simulations for 1 and 2 nm curvature radii. The full cylinder is also shown for comparison. (Reprinted with permission from Physical Review B, Vol. 87, Issue 20, pp. 205418 (2013). Copyright 2013 American Physical Society).

Our full-wave simulations confirm the robustness of this phenomenon on the corner curvature and edge bluntness, consistent with previous results for other types of plasmonic resonances [36]. For sharper edges, the number of quantized resonances increases and the overall effect gets closer to the ideal solution [37]. Figs. 2.8(a,b) show the field distribution for a silver half-cylinder having an ideal corner using our analytical solution in the quasi-static limit versus a blunted structure with $2a = 40$ nm and radius of curvature $r = 2\text{ nm}$ using full-wave simulations at $f = 925\,\text{THz}$ for longitudinal excitation. Fig. 2.8(c) also shows the power flow in the blunted structure. Interestingly, even with a relatively large edge curvature, and including scattering losses and dynamic effects, highly oscillatory fields are still induced around the corners and field enhancement is pretty comparable with the ideal case. The small asymmetry in the distribution is due to the direction of the impinging wave, but since the particle is small compared to wavelength, this effect is almost negligible. Power flow is plotted in a log100 scale, implying large power concentration inside the particle, responsible for large absorption efficiencies. In other words, under the resonance condition power is strongly concentrated inside the particle giving rise to very large absorption regardless of the small amount of material loss.

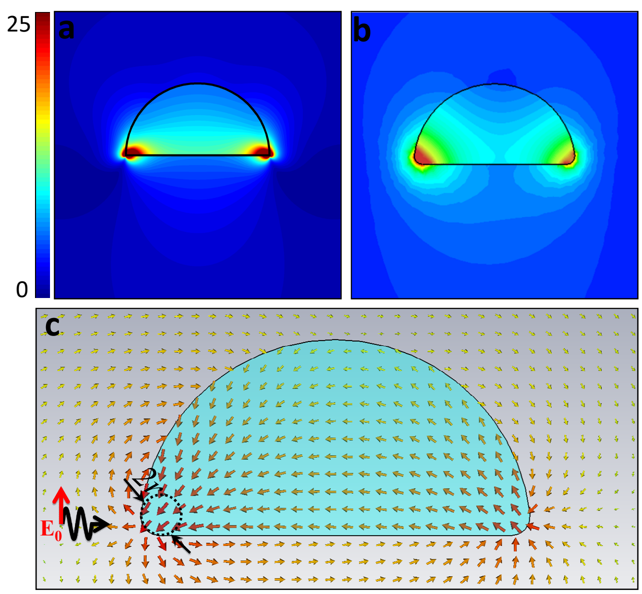

Figure 2.8: Amplitude of the electric field distribution for (a) an ideal silver half-cylinder with $\varepsilon_1 = -0.529 - 0.026j$, calculated with our analytical formulation, and (b) a blunted configuration at the corresponding frequency. (c) Power flow inside and outside the geometry under monochromatic plane wave excitation for the blunted configuration. (Reprinted with permission from Physical Review B, Vol. 87, Issue 20, pp. 205418 (2013). Copyright 2013 American Physical Society).

2.6 EFFECT OF SHAPE ON THE ABSORPTION/GAIN CHARACTERISTICS OF NANOPARTICLE

Through previous sections we have demonstrated that the anomalous resonance behavior observed in composite half-circles is related to the presence of the sharp corners, enabling excitation of localized modes that are in quadrature phase with the incident wave. In this sense, we notice that the bandwidth of enhancement is effectively controlled by the corner geometry, and sharper corners can support eigenmodes over even broader continuous bandwidths. Indeed, the simple composite particle shown in the inset of Fig. 2.1 (c) is a special case of a larger class of particles shown in Fig. 2.9, forming two conjoined cap-shaped cylinders with different corner angles. Following analogous procedure o solve Laplace equation in section 2.2 we were able to find the general form of potentials and fields (and polarizability), for an arbitrary corner angle θ. In this regard, the resonances of a double wedge with corner angle θ and $\varepsilon_2 > 0$ arises when,

$$\left(\max\{-\varepsilon_2,-1\} < \varepsilon_1 < -\frac{\varepsilon_2\theta}{2\pi\varepsilon_2+\theta-2\varepsilon_2\theta}\right) \| \left(\frac{-2\pi+2\theta-\varepsilon_2\theta}{\theta} < \varepsilon_1 < \min\{-\varepsilon_2,-1\}\right), \quad (2.11)$$

which simplifies to (2.4) for the double hemi-cylinder case.

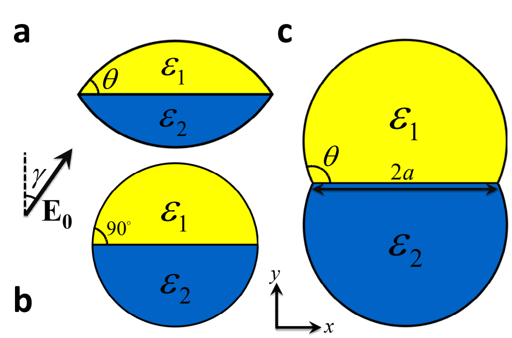

Fig. 2.9: Particle geometry and excitation field for different corner angles. The structures are infinite in z direction. Panel (b) shows conjoined hemicylinders studied in sections 2.3 through 2.5. $\gamma = 0$ degrees corresponds to the longitudinal and $\gamma = 90$ degrees corresponds to the transverse polarizations of the incident wave.

Figs. 2.10 shows the field distributions assuming the upper halves of the particles are made of realistic gold modeled by Drude model dispersion $\varepsilon_1 = \varepsilon_\infty - \omega_p^2 / \left(\omega\left(\omega - j\gamma\right)\right)$ where $\varepsilon_\infty = 1.53$, $\omega_p = 2\pi\,2069\,\mathrm{THz}$, and $\gamma = 2\pi\,17.64\,\mathrm{THz}$ [34]. The lower half is either air ($\varepsilon_2 = 1$) or silicon dioxide ($\varepsilon_2 = 2.4$) in different examples, and the fields are calculated analytically as $\mathbf{E} = -\nabla\varphi$ for $\theta = 45°, 90°, 135°$ and both input polarizations, at various sample frequencies. We notice that as we discussed previously and based on the edge solution, the oscillations may be extended all over the particle (as in Fig. 2.10(a,c)) or be focused at the corner (as in Fig. 2.10(e,f)). Plasmonic oscillations around the corners (Fig. 2.4) result in enhanced fields, which may become infinite at the edge point in the lossless case for an ideal corner.

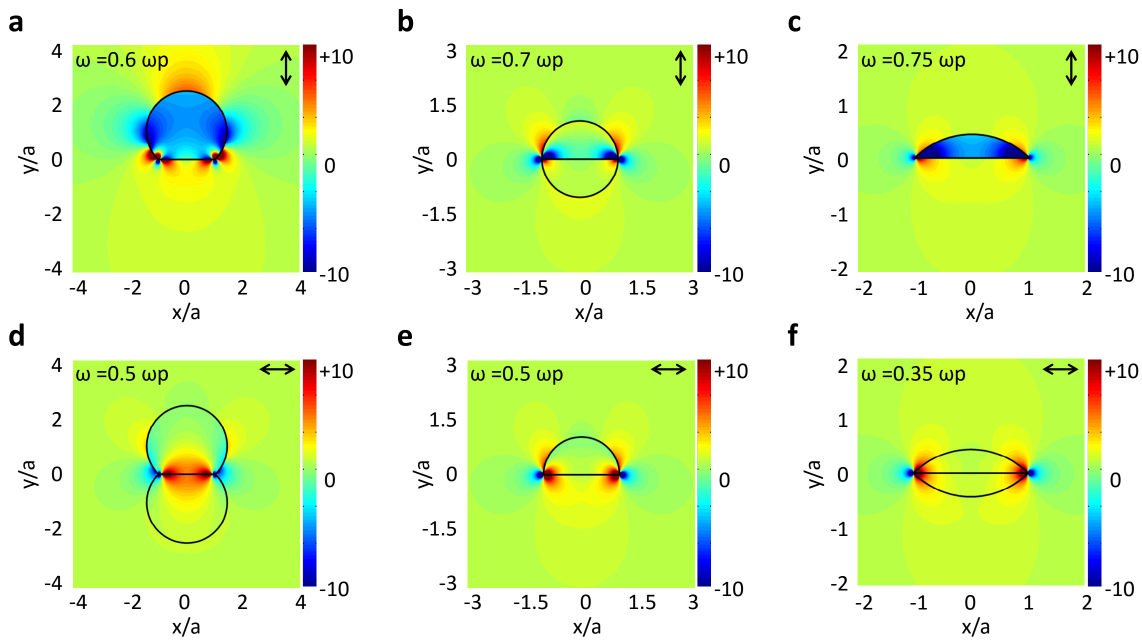

Figure 2.10: Electric field distribution (snapshot in time) in different conjoined particles. The upper half is gold, and the lower halves are either (a,c,e) air or (b,d,f) silicon dioxide. The component of the field parallel to the input direction is plotted in each case. Operation frequency and polarization are indicated in the insets. The corner angles are set at (a,d) $\theta = 135°$,(b,e) $\theta = 90°$ and (c,f) $\theta = 45°$.

Since we can control the resonance range with permittivities and θ following (2.11), the structure can be designed to show high absorption efficiencies in two separate bands over the desired frequency ranges. In order to gain further insight into the effect of material and geometry on the resonance behavior of the structure, we also separately study these effects in a gold-dielectric configuration. Fig. 2.11 shows the normalized absorption cross-section versus the corner angle and frequency of operation for the two normal exciting polarizations. The upper half is made of gold, hence it is frequency dispersive, and the lower halves are either air (a,b) or silicon dioxide (c,d). Notably, both the bandwidth and position of resonance regions can be independently controlled through edge angle and ε_2, respectively. In addition, excitation angle directly influences the resonance strength in different bands. The black dashed lines in each figure indicates the resonance region predicted from (2.11) for a lossless gold-dielectric configuration. Remarkably, owing to the robustness of the resonance modes to the material loss in this configuration, a simple lossless wedge accurately predicts the resonance bands.

2.7 Conclusion

In this chapter we have analyzed the scattering boundary-value problem of two conjoined subwavelength half-cylinders and analyzed its drastically enhanced absorption properties. We have shown that in the ideal case of perfect corners, this geometry may provide broadband light absorption or amplification in the limit of negligible material loss or gain, respectively. This absorption paradox has been shown to be associated with the singularities in the geometry and the adiabatic focusing of broadband surface plasmons supported at the corners. A closed-form solution was derived for the scattering and absorption properties of the composite nanostructure and simple conditions on the material permittivities have been derived to control the position of the absorption band.

The distributed resonances and anomalous behavior of the proposed composite nanoparticle may have many exciting applications, including enhanced energy harvesting and spasers [12],[18] based on materials with limited absorption/gain coefficients and an arguably simple configuration from the fabrication point of view. These resonances may be broadband and with a bandwidth and enhancement level controllable by geometry and design, as discussed in the previous section.

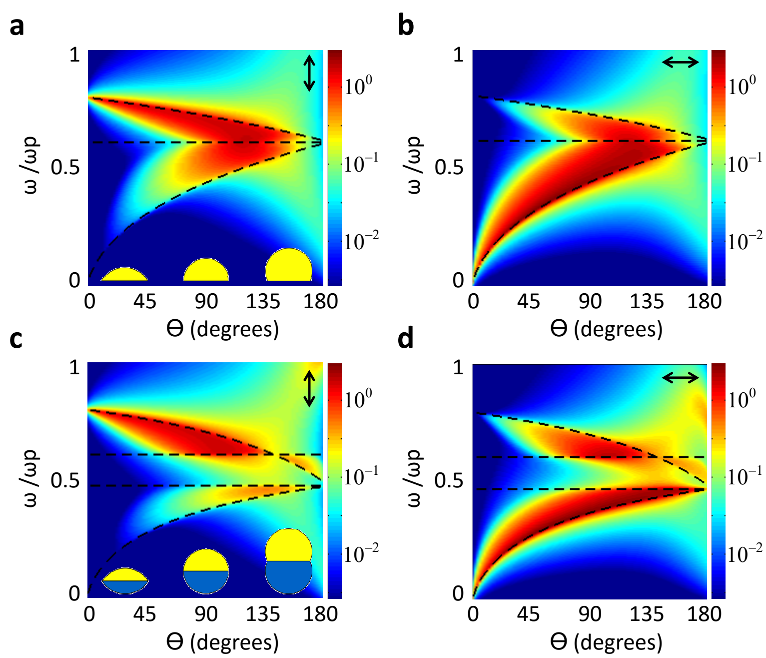

Figure 2.11: Normalized absorption cross-section vs. corner angle and frequency for $2a = 40$ nm composite particles - plotted in logarithmic scale. The upper half is gold, and the lower halves are either (a,b) air or (c,d) silicon dioxide. Input polarizations are indicated in the insets. Black dashed lines show the predicted resonance range from (2.11).

Adiabatic plasmonic focusing at the corners may be used for exciting applications such as enhanced optical nonlinear effects e.g. switching and nanomemories [11]. The field enhancement may be tailored to be extended all over the particle volume or be confined only around the corners, with exciting implications for these applications (Fig.

2.4). The rapid and sharp variation of absorption versus frequency observed in Figs. 2.5 and 2.6 can also be used for sensing [38], with sharp linewidths that are comparable to the ones associated with Fano phenomena [10]. These effects may also have a great interest in boosting the usually low values of gain coefficients in natural optical materials, of great interest for loss compensation in metamaterials and plasmonics [13],[39]-[41], as well as for efficient spasers [12],[18]-[19],[42]. Finally, these structures can provide strong switching and modulation effects at the nanoscale, which we discuss in the next chapter.

2.8 References

[1] Y. Sun, and Y. Xia, Science 298, 2176 (2002).

[2] V. Bastys, I. Pastoriza-Santos, B. Rodriguez-Gonzalez, R. Vaisnoras, and L. M. Liz-Marzan, Adv. Funct. Mater. 16, 766 (2006)

[3] W. L. Barnes, A. Dereux, and T. W. Ebbesen, Nature 424, 824 (2003).

[4] S.A. Maier, *Plasmonics: Fundamentals and Applications* (Springer, New York, 2007).

[5] A. Polman, Science 322 868 (2008).

[6] K. L. Kelly, E. Coronado, L. Zhao, and G. C. Schatz, J. Phys. Chem. B 107, 668 (2003).

[7] E. Prodan, C. Radloff, N. J. Halas, and P. Nordlander, Science 302, 419 (2003).

[8] T. Klar, M. Perner, S. Grosse, G. von Plessen, W. Spirkl, and J. Feldmann, Phys. Rev. Lett. 80, 4249 (1998).

[9] A. Aubry, D. Y. Lei, S. A. Maier, and J. B. Pendry, Phys. Rev. B 82, 125430 (2010).

[10] B. Luk'yanchuk, N. L. Zheludev, S. A. Maier, N. J. Halas, P. Nordlander, H. Giessen, and C. Chong, Nature Mater. 9, 707 (2010).

[11] C. Argyropoulos, P. Chen, F. Monticone, G. D'Aguanno,and A. Alù, Phys. Rev. Lett. 108, 263905 (2012).

[12] N. I. Zheludev, S. L. Prosvirnin, N. Papasimakis, V. A. Fedotov, Nature Photon. 2, 351 (2008).

[13] M. I. Stockman, Phys. Rev. Lett. 106, 156802 (2011).

[14] L. J. Chu, J. Appl. Phys. 19, 1163 (1948).

[15] H. Kettunen, H. Wallen, and A. Sihvola, J. Electrostatics 67, 890 (2009).

[16] A. Salandrino, A. Alù, and N. Engheta, J. Opt. Soc. Am. B 24, 3007 (2007).

[17] M. Pitkonen, J. Electromagn. Waves and Appl. 24, 1267 (2010).

[18] D. J. Bergman, and M. I. Stockman, Phys. Rev. Lett. 90, 027402 (2003).

[19] M. A. Noginov, G. Zhu, A. M. Belgrave, R. Bakker, V. M. Shalaev, E. E. Narimanov, S. Stout, E. Herz, T. Suteewong, and U. Wiesner, Nature 460, 1110 (2009).

[20] E. S. Andrianov, A. A. Pukhov, A. V. Dorofeenko, A. P. Vinogradov, and A. A. Lisyansky, Opt. Lett. 36, 4302 (2011).

[21] E. S. Andrianov, A. A. Pukhov, A. V. Dorofeenko, and A. P. Vinogradov, J. of Commun. Technol. Electron. 57 106 (2012).

[22] M. W. Tsai, T. H. Chuang, C. Y. Meng, Y. T. Chang, and S. C. Lee, Appl. Phys. Lett. 89 173116 (2006).

[23] G. W. Milton, The Theory of Composites, Cambridge Monographs on Applied and Computational Mathematics (Cambridge University Press, Cambridge, 2002).

[24] M. G. Silveirinha, and N. Engheta, Phys. Rev. B 76, 245109 (2007).

[25] A. Alù, and N. Engheta, New J. of Phys. 11, 013026 (2009).

[26] R. F. Harrington, Time-Harmonic Electromagnetic Fields (John Wiley & Sons, 2001).

[27] M. N. O. Sadiku, Numerical techniques in electromagnetics (CRC, Boca Raton, FL, 2001).

[28] J. W. Brown, and R. V. Churchill, Complex variables and applications Vol. 7 (McGraw-Hill, New York, 1996).

[29] J. Helsing, R. C. McPhedran, and G. W. Milton, New J. Phys. 13,115005 (2011).

[30] L.C. Davis, Phys. Rev. B 14, 5523 (1976).

[31] R. McPhedran, and W. Perrins, Appl. Phys. A 24, 311 (1981).

[32] A. Aubry, D. Y. Lei, S. A. Maier, and J. B. Pendry, Phys. Rev. Lett. 105, 233901 (2010).

[33] J. E. Sipe, and J. V. Kranendonk, Phys. Rev. A 9, 1806 (1974).

[34] M. A. Ordal, R. J. Bell, R. W. Alexander, Jr, L. L. Long, and M. R. Querry, Appl. Opt. 24, 4493 (1985).

[35] N. M. Litchinitser, A. I. Maimistov, I. R. Gabitov, R. Z. Sagdeev, and V. M. Shalaev, Opt. Lett., 33, 2350 (2008).

[36] Y. Luo, D. Y. Lei, S. A. Maier, and J. B. Pendry, Phys. Rev. Lett. 108, 023901 (2012).

[37] R. Fuchs, Phys. Rev. B 11, 1732 (1975).

[38] N. Liu, M. Mesch, T. Weiss, M. Hentschel, and H. Giessen, Nano Lett. 10, 2342 (2010).

[39] S. Xiao, V. P. Drachev, A. V. Kildishev, X. Ni, U. K. Chettiar, H. K. Yuan, and V. M. Shalaev, Nature (London) 466, 735 (2010).

[40] M. A. Noginov, G. Zhu, M. Bahoura, J. Adegoke, C. E. Small, B. A. Ritzo, V. P. Drachev, and V. M. Shalaev, Opt. Lett. 31, 3022 (2006).

[41] S. Anantha Ramakrishna, and J. B. Pendry, Phys. Rev. B 67, 201101(R) (2003).

[42] Y. J. Lu et al., Science 337, 450 (2012).

Chapter 3: Parity-Time Symmetry Breaking and Loss-Gain Transitions in Scattering

In the previous chapter, we discussed how the geometry and composition of nanoparticles can create strong absorption properties, even in the limit of small intrinsic material absorption. An interesting and quite unusual property of these plasmonic nanoparticles resides in the strong switching between the absorption/gain properties of the metamolecules as we switch between small amount of intrinsic loss to gain and vice versa. This property suggests a platform to implement optical nanoswitches and modulators at the single particle level. In this regard, in this chapter we look at the electromagnetic properties of composite nanoparticles that incorporate gain medium. In particular, we focus on the scattering properties of a class of active structures with balanced loss and gain, known as parity-time symmetric structures. Our studies reveal that the spontaneous real to complex spectrum transitions typically observed in large-size parity-time symmetric systems can be scaled down to the quasi-static regime by exploiting plasmonic nanoparticles, as the result of a unique form of interplay of localized plasmons at a gain-loss interface. We will provide physical insights to elucidate the underlying mechanisms involved in this parity-time induced scattering transition, occurring at the single particle level. The obtained response has ideal features for ultrafast optical switching and sensing.

3.1 Introduction

The notion of parity-time (PT)-symmetry has been recently adapted from quantum mechanics to optical systems, attracting significant attention to a range of quite extraordinary phenomena supported by PT-symmetric optical components [1]-[7]. Despite being non-Hermitian, quantum-mechanics Hamiltonians that commute with the combined parity and time-reversal operators can possess real-valued energy spectra below certain thresholds of the non-Hermiticity parameter [8],[9], and can undergo spontaneous symmetry breaking as this threshold is passed. In the context of optics, a system with balanced distribution of loss and gain, i.e. refractive index modulated, is PT-symmetric, with analogous intriguing possibilities of undergoing spontaneous symmetry-breaking transitions [2]-[4]. The direct implication for the modal characteristics of bounded and unbounded PT-symmetric systems is the presence of real-valued eigen-frequencies in the unbroken phase spectrum at which absorption and amplification are balanced in different regions of the system [3],[10]. This is in contrast with conventional lossy systems that only support decaying modes. At a certain level of non-Hermiticity, i.e., of the loss-gain coefficient, such symmetry is broken and eigen-frequencies emerge as pairs of complex-conjugate values, corresponding to modes skewed towards different parity regions [3],[10]. These unique properties have enabled several exciting applications including, loss-free propagation, directional coupling and asymmetric power transmission [3], and single mode lasing [6]. So far, however, the majority of works on optical PT-symmetric systems have been based on wavelength-scale closed systems without radiation features, and/or 1D systems with only specific radiation channels enabled by symmetries. Here, on the contrary, we show that PT-symmetric subwavelength nanoparticles with the geometry described in the previous chapter can support highly unusual optical responses in spite of their quasi-static nature.

The optical properties of open optical systems are mirrored in their scattering properties under external excitation. The scattering eigenvalues of PT-symmetric systems have been studied in a few recent works, showing that they remain unimodular provided that PT-symmetry is unbroken [4], and thus the externally excited electromagnetic fields inside the structure remain balanced. Passing an appropriate threshold for the non-

Hermiticity factor, the scattering response can undergo unimodular to inverse-moduli spectrum transitions and generate sets of joined amplifying and dissipating scattering eigen-states [4]. Previous works on PT-symmetric scattering systems have been focused on large configurations, mostly in 1D setups [4],[5],[7],[11],[12]. The large size of the structure effectively provides sufficient interaction domain for the incident wave to create perceptible loss/gain scattering effects. At optical frequencies, however, plasmonic effects offer an interesting opportunity to strongly engage light-matter interactions at deeply subwavelength scales [4]-[14]. In this chapter, we demonstrate that the scattering properties of PT-symmetric plasmonic nanoparticles can sustain highly localized PT transitions at deeply subwavelength scales. Quite contrary to wavelength-scale configurations, we show that in the symmetry-broken regime, quasi-static nanoparticles can support only one non-unimodular scattering mode, triggered by small perturbations of the ideal PT-symmetry condition.

3.2 Theoretical formulation

In the following, we explore the scattering properties of a basic PT-symmetry nanoparticle, a double hemi-cylinder with diameter $\mathrm{D} \ll \lambda_0$, where λ_0 is the free-space wavelength, and a spatially modulated permittivity that satisfies the PT-symmetry condition. As shown in the inset of Fig. 3.1, both half-cylinders have the same real permittivity ε_r, yet with a symmetric amount of loss (upper half) and gain (lower half). Intuitively, at a deeply subwavelength scale it is expected that the optical properties of the particle average out, providing zero net loss/gain in the scattering signature. In the following, however, we show that the combination of PT-symmetry and plasmonic effects can provide highly unusual scattering responses in subwavelength systems, and averaging is not possible above a certain threshold of the non-Hermiticity parameter ε_i.

Although in the quasistatic regime the nanoparticle response is still dominated by its effective dipole response [15], above such threshold the polarizability can become complex with a controllable amount of amplification or dissipation.

We formally start by solving for the quasistatic dipolar electric polarizability of the particle in Fig. 3.1. Under the $e^{j\omega t}$ time convention, the solution takes the semi closed-form presented in chapter 1 [16]

$$\alpha_e = \frac{4\pi}{S}\int_0^\infty \lambda\, C(\varepsilon_1, \varepsilon_2, \lambda)\, d\lambda \,, \tag{3.1}$$

Here, S is the particle's cross-section and λ denotes the continuous spatial frequency in the bipolar coordinates. The coefficient $C(\varepsilon_1, \varepsilon_2, \lambda)$ is analytic and in general anisotropic, i.e., it is different for excitation along x and y in Fig. 3.1. The integral equation in (3.1) may be also expressed explicitly in terms of polylogarithm functions, as a function of the permittivity coefficients [16]

$$\begin{aligned} \alpha_y &= \frac{\pi^2\left(3\varepsilon_r^2 + 3\varepsilon_i^2 - \varepsilon_r\right) + 12\varepsilon_r\left(\mathrm{Li}_2\left(\varepsilon^-\right) + \mathrm{Li}_2\left(\varepsilon^+\right)\right)}{1.5\pi S\left(\varepsilon_r^2 + \varepsilon_i^2 + \varepsilon_r\right)} \\ \alpha_x &= \frac{\pi^2\left(\varepsilon_r - 3\right) - 12\varepsilon_r\left(\mathrm{Li}_2\left(\varepsilon^-\right) + \mathrm{Li}_2\left(\varepsilon^+\right)\right)}{1.5\pi S\left(\varepsilon_r + 1\right)} \end{aligned} \,, \tag{3.2}$$

in which $\mathrm{Li}_2(.)$ is the polylogarithm function of second order and $\varepsilon^\pm = -\varepsilon_r\left(\varepsilon_i^2 + \left(\varepsilon_r + 1\right)^2\right) \Big/ \left(\varepsilon_r + \left(\varepsilon_r + 2\right)\left(\varepsilon_r^2 + \varepsilon_i^2\right) \pm 2\sqrt{\varepsilon_i^2\left(\varepsilon_r + 1\right)\left(\varepsilon_r^2 + \varepsilon_i^2 + \varepsilon_r\right)}\right)$. The scattering response of the structure, therefore, may accept multiple values for the solutions that lie upon different Riemann surfaces. The position of the branch cuts in the material space is determined by the angle of the sharp corners in the structure [16]-[17], which is fixed at $\pi/2$ in our geometry. In the absence of the branch cut, the scattering response of the particle is in phase with the incident wave, as if the particle is made of an entirely lossless material. This is consistent with the initial intuition at the quasi static limit, as the overall effects of the loss and gain portions average out in the far-field. The presence of the branch cut, however, is the indication of regions (in the material space), over which the structure supports solutions that are highly oscillatory with strong focusing effects and local field enhancements at the two corners. Subsequently, the composite particle may demonstrate significant power dissipation or power amplification depending on an infinitesimal asymmetry in the geometry or material properties. In this range the response cannot average out as it asymptotically non-square-integrable at the corners. As we demonstrated in the previous chapter, this effect is also observable in low-loss composites and nanoparticles that comprise sharp features [18]-[20].

Figure 3.1 sketches the response of the polarizability in the $(\varepsilon_r, \varepsilon_i)$ parameter-space: the white areas correspond to real-valued α_e, while the gray area corresponds to a strictly complex α_e with either a finite positive or negative imaginary component. These regions occur independent of the polarization of the excitation field. Physically, this implies that the net dissipation/amplification $\mathrm{P}_{dissipated} \propto -\lambda_0^{-1}\,\mathrm{Im}[\alpha_e]$, is non-zero in the shaded area, even in the quasi-static limit for which radiation loss are negligible. Mathematically both complex conjugate solutions are admissible for this range of parameters, i.e., the boundary value problem does not support a unique solution. Before discussing the solution to this ambiguity, we notice that Fig. 3.1 illustrates the phase diagram of the PT nanoparticle, which is found to be identical for orthogonal polarizations. The dashed lines represent the boundaries across which PT-symmetry is spontaneously broken and the scattering spectrum ceases to be real. Interestingly, this is only possible if plasmonic effects are available, for this cylindrical geometry in the range $\varepsilon_r \in (-1,0)$. In this range, the threshold non-Hermiticity factor required to break the symmetry is found to be $\varepsilon_{i,\mathrm{Th}} = \sqrt{-\varepsilon_r(1+\varepsilon_r)}$. At the boundaries of this range, for $\varepsilon_r \to -1^+$ and $\varepsilon_r \to 0^-$ the transition is threshold-less, meaning that the scattering spectrum is complex even with an infinitesimal amount of non-Hermiticity coefficient ε_i . The first of such conditions represents the quasistatic resonance of a loss-free homogeneous cylinder, and our theory shows that a negligible amount of balanced loss/gain can trigger a PT-symmetry breaking transition in the scattering spectrum. The second case corresponds to an epsilon-near-zero (ENZ) cylinder, which supports similar properties. We discuss in the following that the PT-transition in our nanoparticle can be attributed to edge modes adiabatically focusing around the interface tips. It is interesting that an ENZ PT-symmetric infinite slab also supports threshold-less guided modes at the interface of loss and gain media [22], and our geometry translates these effects to a sub-wavelength nanoparticle response.

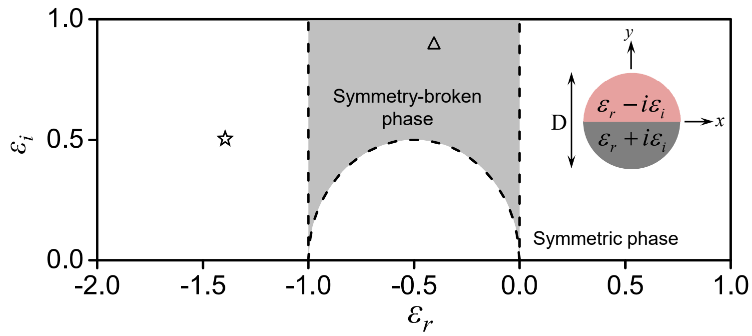

Figure 3.1: Phase diagram of scattering from the PT-symmetric double particle shown in the inset. The structure under study is a single 2D particle at the deep subwavelength limit $\mathrm{D}/\lambda_0 \to 0$, with complex-conjugate permittivities in the upper and lower halves. White areas show the PT-symmetric case where the scattering amplitude is purely real. The gray region correspond to the spontaneously-broken PT-symmetry where polarizability is in general complex and a portion of incident power is dissipated or amplified in the particle. Dashed lines show the non-Hermiticity factor threshold given by $\varepsilon_{i,\mathrm{Th}} = \sqrt{-\varepsilon_r(1+\varepsilon_r)}$. The points indicated by star $(\varepsilon_r, \varepsilon_i) = (-1.4, 0.5)$, and triangle $(\varepsilon_r, \varepsilon_i) = (-0.4, 0.9)$, correspond to the examples studied in Figs. 3.3 and 3.4, respectively.

An interesting property of the scattering system in Fig. 3.1 is the possibility of breaking PT-symmetry through variations in the real component of the permittivities. PT-symmetric optical potentials have been originally created through spatial modulations of the imaginary component of permittivity [2], in accordance to non-Hermitian quantum potentials. Therefore, it is common to break this complex continuation of the real-spectrum by increasing the non-Hermiticity factor [3],[7],[10]. However, Fig. 1 shows that PT-symmetry can be broken also for a fixed amount of loss/gain by varying ε_r.

3.3 A RESIDUE INTEGRATION APPROACH TO ANALYZE THE SCATTERING CHARACTERISTICS OF PT-SYMMETRIC NANOPARTICLES

A simple yet powerful method of evaluating the integral in (3.1) and explicitly calculate the field distribution inside and around the particle invokes residue integration [23]. The analytical properties of (3.1) in the complex plane can reveal important phenomena occurring in the nanoparticle based on the position and dynamics of the complex poles. Utilizing periodicity of the coefficient $C(\varepsilon_1, \varepsilon_2, \xi)$, with $\lambda = \mathrm{Re}\left[\xi\right]$, in the complex plane, the polarizability can be rewritten in the standard residue integration form $\alpha_e = \frac{i\pi}{2S} \oint_\Gamma \left(\xi^2 - 2i\xi\right) C(\varepsilon_1, \varepsilon_2, \xi) d\xi$. The closed contour Γ is shown in Fig. 3.2 with solid black lines, and the arrows determine the direction of integration. Quite conveniently, independent of the exact value of ε_r and ε_i, only three poles contribute to the overall response of the particle.

The first pole, p_1, is always located at $\xi = i$, associated to the geometrical shape of the particle as it is not affected by the material properties. Under the symmetric-phase condition which is inside the white regions in Fig. 3.1, if $\varepsilon_r > 0$ the additional two poles p_4 and p_5 in Fig. 3.2 are symmetrically located on the $\mathrm{Im}\left[\xi\right] = 1$ line. On the other hand, when $\varepsilon_r < 0$, both poles (p_2 and p_3) are on the imaginary axis $\mathrm{Re}\left[\xi\right] = 0$, and move toward $\xi = 0$ and $\xi = 2i$ as the permittivities approach the grey area in Fig. 3.1, and the response moves toward the broken-symmetry region. At the exact threshold line, $\varepsilon_i = \sqrt{-\varepsilon_r(1+\varepsilon_r)}$ the poles coalesce and then split on the real axis. Considering the periodicity of the kernel the poles on the real axis result on total of four poles p_6 to p_9 residing on Γ. By further increasing ε_i particle's response enters the broken-symmetry region for which the quasistatic particle supports confined modes that adiabatically focus toward the corners [16],[18]. These modes support extremely fine spatial resolutions, particularly in the vicinity of the corners. In this regime, loss and gain effects do not average out and the scattering is not unimodular. Both amplifying and absorbing modes are valid solutions of the scattering problem, and minor perturbations from the ideal geometry in Fig. 3.1, which break the ideal PT-symmetry assumption, can allow a dramatic switching between amplifying and absorbing responses.

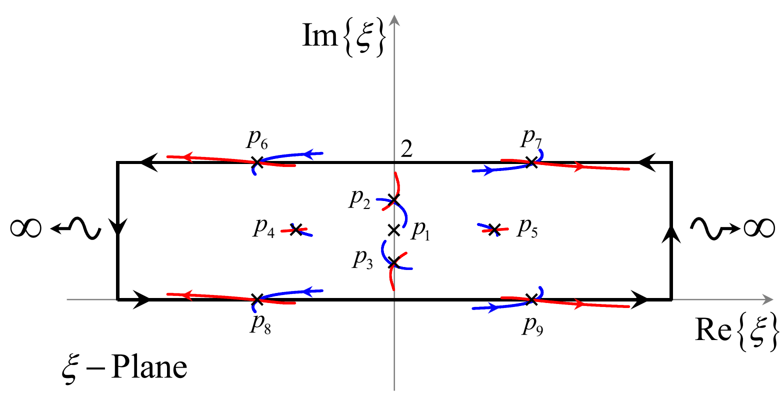

Figure 3.2: The analytic properties of the polarizability integrand in the complex ξ plane. Poles are indicated by $\times$, and each three poles correspond to a specific material distribution: p_1, p_4, p_5 for $\varepsilon_r > 0$; p_1, p_2, p_3 for $\varepsilon_r < 0, \varepsilon_i < \varepsilon_{i,\mathrm{Th}}$; and p_1, p_7, p_8 (p_1, p_6, p_9) for $\varepsilon_i > \varepsilon_{i,\mathrm{Th}}$. Poles on the real axis convey confined modes in the nanoparticle. Red (blue) lines follow the trajectory of poles when the exact PT-symmetry condition is perturbed with $\varepsilon_2 = \varepsilon_1^* + \delta$ ($\varepsilon_2 = \varepsilon_1^* + i\delta$). Arrows on $p_6 - p_9$ trajectories show that depending on the perturbation sign, different poles are located inside the integration contour Γ. Position of pole p_1 is independent of material characteristics.

In order to better understand this dynamics, we inspect in more detail the residue integration and the analytic properties of the scatterer polarizability. In the unbroken-symmetry scenario the polarizability is directly related to the sum of the residues of $\left(\xi^2 - 2i\xi\right)C(\varepsilon_1,\varepsilon_2,\xi)$ at p_1, p_2, p_3 or p_1, p_4, p_5, which are all real-valued. In the broken-symmetry scenario, instead, we must determine which of the four poles on the integration contour move inside Γ (and therefore contribute to the scattering), and which ones move outside the contour. This is to be determined by slightly perturbing the exact PT-condition of the particle. The permittivity of the lower half is modified as $\varepsilon_2 = \varepsilon_1^* + \delta$, with $\delta \to 0$ being a small perturbation. This is shown in Fig. 3.2 with red lines and corresponding arrows, indicating the trajectory of $p_6 - p_9$ in the complex plane after variations in δ. For any fixed perturbation, only two of the poles move within Γ, as a function of the sign of δ. For instance, for $\varepsilon_r = -0.4, \varepsilon_i = 0.9$, if the real permittivity of the lower half slightly decreases (increases) from the exact PT-condition, p_1, p_6, p_9 (p_1, p_7, p_8) are the contributing poles. The residue at these sets of poles have complex-conjugate values, implying that one set corresponds to a dissipative scattering state, while the complementary set supports amplification. Therefore, over this regime the scattering response of the ideal PT particle $\varepsilon_2 = \varepsilon_1^*$ violates uniqueness, associated with the quasi-static edge modes [24]. The dipolar mode, yet, can exhibit preferred non-unimodular scattering stemming from the perturbation of the PT-symmetry condition. We note that similar effects may be induced if PT-symmetry is broken on the imaginary parts of the permittivities. This is shown with blue lines in Fig. 3.2, for which we slightly vary the gain factor in the lower half. In the same figure, we also look into the variations of simple poles corresponding to the unbroken phase region, $p_2 - p_5$ upon small perturbations. As expected, the poles stay within the contour, and small perturbations do not drastically modify the overall response.

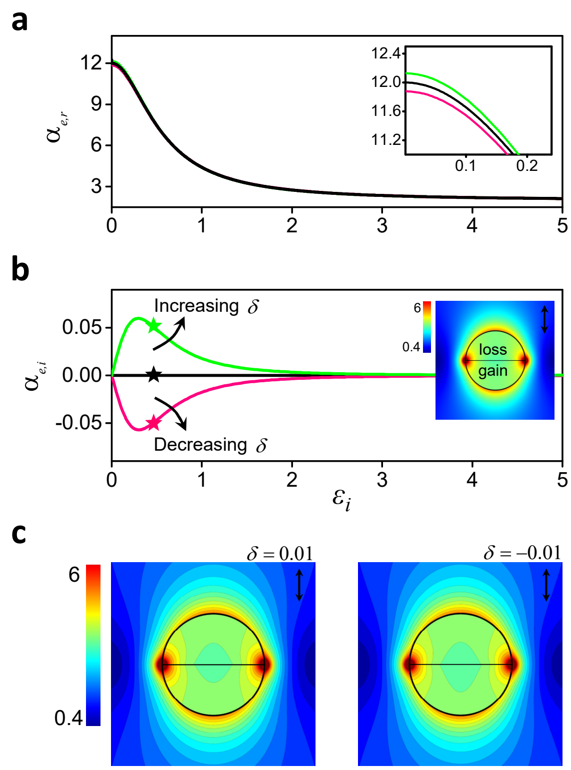

Figure 3.3: (a) Real and (b) imaginary components of α_e for the PT-symmetric particle shown in Fig. 3.1, for excitation along the y-axis, plotted for $\varepsilon_r = -1.4$ while varying the non-Hermiticity factor ε_i. Black, pink, and green lines correspond to unperturbed, $\delta = -0.01$, and $\delta = 0.01$, respectively. Pink and green curves in panel (b) monotonically converge to zero as the absolute value of δ is decreased. The inset shows the magnitude of total electric field across the particle and its close proximity for $\varepsilon_i = 0.5, \delta = 0$ (black star). (c) Magnitude of the total electric field $\left|E_x\hat{x} + E_y\hat{y}\right|$ normalized to the amplitude of the incident field, for the two cases of perturbation. Contours of constant field amplitude are plotted to highlight the small asymmetry in the field distribution. For $\delta = -0.01$ ($\delta = 0.01$) fields are slightly larger in the upper (lower) half, consistent with the negative (positive) small imaginary component of polarizability in panel (b). Field distributions are calculated based on Ref. [16] and polarizabilities are calculated utilizing the residue integration theorem discussed here.

To confirm our findings and gain further insights into the rich scattering response of these nanoparticles, in the following we discuss two examples corresponding to symmetric and symmetry-broken phase regions (indicated with a star and a triangle in

Fig. 3.1). In both examples, we fix the real part of permittivity and increase the non-Hermiticity parameter ε_i from 0 to 5. Figure 3.3 shows the case for $\varepsilon_r = -1.4$. The incident electric field is polarized along the y-axis, i.e., normal to the interface, and the real and imaginary components of the polarizability are plotted with black lines in Figs. 3.3(a) and 3.3(b). The particle is overall lossless, implying that the local loss and gain cancel out, independent of the value of non-Hermiticity factor. Indeed, as plotted in the inset of Fig. 3.3(b) for $\varepsilon_i = 0.5$, the distribution of the electric field intensity is fully symmetric between the two halves. The solution is stable around this point and after perturbing the PT-symmetry condition the polarizability and field distributions remain unaffected (see Fig. 3.3(c)). Due to the small asymmetry imposed on the material properties, field distributions slightly lean to the lower or upper half and a small amplification or absorption is induced by the asymmetry. Decreasing the absolute value of perturbation, this asymmetry converges smoothly to zero and at the infinitesimally small perturbation limit, the scattering remains unimodular. These observations are consistent with our previous discussion, highlighting the expected scattering response of a subwavelength non-resonant particle with balanced loss and gain.

The response is drastically different, however, if PT-symmetry is combined with plasmonic phenomena, and we can enter the gray-shadowed region in Fig. 3.1. Figure 3.4(a) shows the polarizability for $\varepsilon_r = -0.4$. When $\delta = 0$ (ideal PT-symmetry), the imaginary and real components of α_e are calculated for different values of ε_i. As long as $\varepsilon_i < \varepsilon_{i,\mathrm{Th}} = \sqrt{0.4 \cdot 0.6}$ (black lines), the poles lie on the imaginary axis and the polarizability is well-defined and purely real, similar to the previous example. However, beyond this threshold, the solution is not unique in the ideal PT-symmetry scenario, since we enter the broken symmetry region with supported edge modes, and complex conjugate polarizabilities are yielded. To find a unique solution, we need to slightly perturb the PT condition with $\delta = \pm 0.01$, as shown with green and pink lines in Fig. 3.4(a). First, we notice that each of the two cases yields significant amount of dissipation (amplification). These numbers should be compared with those in Fig. 3.3(b).

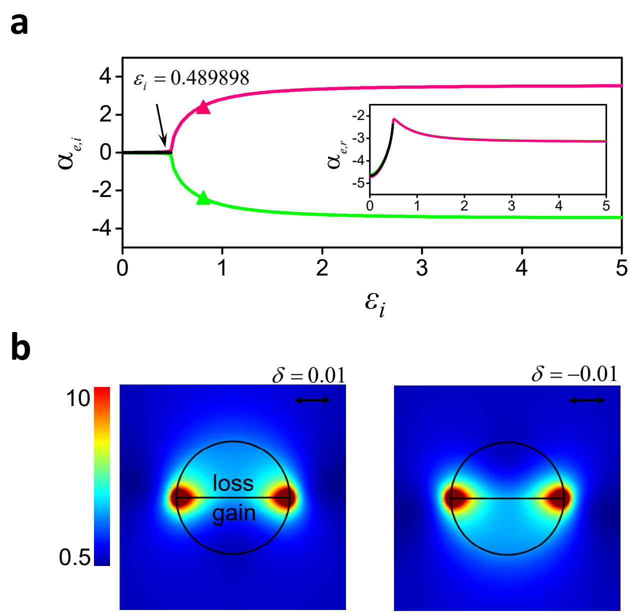

Figure 3.4: Imaginary component of α_e for the PT-symmetric particle with $\varepsilon_r = -0.4$, excited along the x-axis. Black line indicates the polarizability below threshold. Pink and green curves correspond to perturbed configuration with $\delta = -0.01$, and $\delta = 0.01$, respectively. Inset shows the real part of polarizability, almost unaffected with perturbation. (b) Magnitude of the total electric field normalized to the incident signal. Two different scattering modes are observed solely based on the sign of δ. The excited edge modes are significantly localized around corners, with very large field amplitudes, leaning toward loss (green triangle in panel a) or gain (pink triangle in panel a) elements.

More importantly, the attained $\mathrm{Im}[\alpha_e]$ is nearly independent of the amount of perturbation and even very small asymmetries would enforce the scattering to converge to one of the absorptive or amplifying branches. This is due to the contribution of poles with complex conjugate residues in Fig. 3.2, whose positions are only weakly affected by the exact perturbation amplitude. Physically, a small perturbation creates edge modes that lean toward either the loss or the gain region and due to their extreme field enhancement they produce noticeable scattering loss or gain. Quite interestingly, even at the threshold the response is not required to be continuous and it can launch from $\mathrm{Im}\left[\alpha_e\right]\to\pm\infty$ at $\varepsilon_i \to {\varepsilon_{i,\mathrm{Th}}}^{+}$ [25].

As mentioned above, this unusual scattering response is associated with resonant modes focused at the corners of the nanoparticle. This is visualized in Fig. 3.4(b) where we plot the field intensity for $\varepsilon_r = -0.4, \varepsilon_i = 0.9$, inside the broken-symmetry region. Distinct from the previous example, although panels (b) and (c) correspond to very small perturbations of an identical particle, they support modes that are specifically concentrated in one half of the cylinder, and are excited based on the sign of the perturbation. The strong super-oscillatory fields around the edges create the large absorption/ amplification effect which is absent outside the PT broken-phase region.

3.4 Conclusion

In conclusion, in this chapter we have shown that spontaneous symmetry breaking in PT-symmetric optical particles can be attained in the deeply subwavelength limit, utilizing confined plasmon polaritons. The scattering signature of the particle is found to be quite distinct from wavelength-scale or large structures, as it supports single dissipative or amplifying modes, with threshold-less symmetry-breaking in special cases. The PT symmetry-broken region corresponds to the range over which localized plasmonic modes are excited at the particle corners. It is predictable that similar scattering responses may be observed in other nanoparticle geometries, such as PT-symmetric kissing cylinders that support confined plasmonic modes [20]. Here, we have overlooked the radiation effects due to the particle's small size. However, it has been shown that radiation correction is negligible in this regime [16], and it does not affect the scattering behavior. In practice, radiation loss slightly unbalances the dissipation and amplification branches. The observed extreme localization of light along with the abrupt switching may find interesting applications in nanophotonic sensors, modulators, and optical logics.

3.5 References

[1] A. Ruschhaupt, F. Delgado, and J. Muga, J. Phys. A 38, L171 (2005).

[2] K. Makris, R. El-Ganainy, D. Christodoulides, and Z. H. Musslimani, Phys. Rev. Lett. 100, 103904 (2008).

[3] C. E. Rüter, K. G. Makris, R. El-Ganainy, D. N. Christodoulides, M. Segev, and D. Kip, Nat. Phys. 6, 192 (2010).

[4] Y. Chong, L. Ge, and A. D. Stone, Phys. Rev. Lett. 106, 093902 (2011).

[5] R. Fleury, D. L. Sounas, and A. Alù, Phys. Rev. Lett. 113, 023903 (2014).

[6] L. Feng, Z. J. Wong, R.-M. Ma, Y. Wang, and X. Zhang, Science 346, 972 (2014).

[7] H. Alaeian and J. A. Dionne, Phys. Rev. A 89, 033829 (2014).

[8] C. M. Bender and S. Boettcher, Phys. Rev. Lett. 80, 5243 (1998).

[9] C. M. Bender, D. C. Brody, and H. F. Jones, Phys. Rev. Lett. 89, 270401 (2002).

[10] L. Ge and A. D. Stone, Phys. Rev. X 4, 031011 (2014).

[11] P. Ambichl, K. G. Makris, L. Ge, Y. Chong, A. D. Stone, and S. Rotter, Phys. Rev. X 3, 041030 (2013).

[12] Z. Lin, H. Ramezani, T. Eichelkraut, T. Kottos, H. Cao, and D. N. Christodoulides, Phys. Rev. Lett. 106, 213901 (2011).

[13] S.A. Maier, Plasmonics: Fundamentals and Applications (Springer, New York, 2007).

[14] S. Eustis and M. A. El-Sayed, Chem. Soc. Rev. 35.209 (2006).

[15] C. H. Papas, Theory of Electromagnetic Wave Propagation (Dover, New York, 1988).

[16] N. Mohammadi Estakhri and A. Alù, Phys. Rev. B 87, 205418 (2013).

[17] G. W. Milton, The Theory of Composites, Cambridge Monographs on Applied and Computational Mathematics (Cambridge University Press, Cambridge, 2002).

[18] A. Aubry, D. Y. Lei, S. A. Maier, and J. B. Pendry, Phys. Rev. B 82, 125430 (2010).

[19] R. McPhedran, and W. Perrins, Appl. Phys. A 24, 311 (1981).

[20] A. Aubry, D. Y. Lei, S. A. Maier, and J. B. Pendry, Phys. Rev. Lett. 105, 233901 (2010).

[21] C. A. Balanis, Advanced Engineering Electromagnetics (Wiley, New York, 1989).

[22] S. Savoia, G. Castaldi, V. Galdi, A. Alù, and N. Engheta, Phys. Rev. B 91, 115114 (2015).

[23] J. W. Brown and R. V. Churchill, Complex Variables and Applications (McGraw-Hill, New York, 1996), Vol. 7.

[24] L.C. Davis, Phys. Rev. B 14, 5523 (1976).

[25] N. Mohammadi Estakhri and A. Alu, in CLEO: QELS_Fundamental Science, Optical Society of America, 2015, p. FTu2E. 4.

Chapter 4: Theoretical Study and Experimental Validation of Minimum-scattering Superabsorbers

Absorption and scattering are inherently related, as it is not possible to absorb power without creating a far-field shadow. In previous chapters we looked into the possibility of creating strong absorption/gain effects in plasmonic nanoparticles. In this chapter we answer a very general question: to what extent it is possible to maintain absorption properties of a receiver, while at the same time minimizing the scattering from it. We show that properly overlapped resonant modes in suitably designed receiving systems may in principle lead to arbitrarily large absorption levels, while at the same time minimizing the total scattering. We present the theoretical formulations of our analysis and provide experimental verifications at the microwave frequencies. Namely, we present the design of microwave antennas based on our theory observing over 7-dB scattering suppression without sacrificing absorption. The presented technique is of special interest for non-invasive sensing, imaging, and radar technology. Contents of this chapter partially appeared in "Mohammadi Estakhri, N.; Alù, A., Minimum-scattering superabsorbers. Physical Review B, Rapid Communications 2014, 89 (12), 121416".

4.1 INTRODUCTION

Scattering from sensors and receivers is in general unavoidable, but at the same time it is often undesired, especially in near-field sub-diffractive imaging [1]-[2] or for closely spaced receivers or energy harvesters, due to unwanted perturbations on the incoming wave. To address this problem, optimal designs for 'minimum-scattering' receiving antennas and sensors have been extensively discussed at radio-frequencies [3]-[6], yet typically producing largely sub-optimal absorption levels. A sensor or an absorber designed to maximize the amount of received power is typically required to operate under a conjugate-matched condition [7]-[9], also known in optics as coherent perfect absorption [10], but this comes at the price of scattering an equal amount of power as it receives, significantly perturbing the impinging wave [11]-[12]. It is reasonable to believe that this property is a somewhat necessary feature of good absorbers; however, and quite counterintuitively, we show in the following that it is in principle possible to design a scatterer that absorbs as much power as desired, without any minimum bound on its scattering level. In a related context, it has been recently shown that cloaking layers may be able to arbitrarily decrease the scattering from a receiving sensor [13]-[19] and efficiently form minimum-scattering designs. However, while the ratio of absorbed over scattered power may be unbounded, also here a fundamental trade-off appears between total available absorption and the amount of achievable scattering reduction [18]. To overcome this issue, arrays of impedance-matched receivers have been proposed to minimize reflections, or the scattering in specific directions, while being able to retain an optimal absorption level by increasing the scattering towards other directions [20]. It appears that all these solutions are fundamentally limited to a trade-off between maximum achievable absorption and minimum scattering signature when integrated over all angles.

4.2 MULTIPOLE SCATTERING THEORY: OPTIMAL PROPERTIES OF LOW-SCATTERING ABSORBERS

In order to devise a way to overcome these limitations, in this chapter we discuss the possibility of staggering multiple absorption channels in a single receiver in order to increase the overall absorption efficiency η_{abs}, defined as the ratio between absorbed and scattered power, while not sacrificing the accessible amount of absorption. Our theory envisions the possibility of realizing superabsorbing minimum-scattering sensors, applicable to a broad range of frequencies, ranging from radio-frequency receiving antennas to optical sensors and absorbers, with exciting possibilities in biomedical technology, security, energy harvesting, sensing and imaging.

Assuming for simplicity a spherical scatterer, its Mie coefficients $C_n^{\mathrm{TM,TE}}$, fully describing its scattering and absorption properties as a function of its geometry, may be written under an $e^{-i\omega t}$ time convention in the form

$$C_n^{\mathrm{TM,TE}} = \left(-1 + i\zeta_n^{\mathrm{TM,TE}}\right)^{-1}. \tag{4.1}$$

These coefficients relate the impinging transverse-electric (TE) and transverse-magnetic (TM) spherical harmonic amplitudes to the scattered ones, and expressions for the case of layered spheres may be found in closed-form [21]. In the limit of no absorption, ζ_n is a real number, which determines the strength of the corresponding scattered spherical harmonic: for $\zeta_n = 0$, in particular, we hit the n-th harmonic resonance in the lossless limit, which maximizes the associated scattering. In the case of loss, it is easy to prove that $\zeta_{nR} = \mathrm{Re}[\zeta_n]$ specifies the modal dispersion and reactive response, while $\zeta_{nI} = \mathrm{Im}[\zeta_n] > 0$ for passive inclusions is directly related to the level of absorption.

The total absorption cross-section of the sphere is generally given by

$$\begin{aligned}\sigma_{abs} &= \frac{-\lambda_0^2}{2\pi}\left(\sum_{n=1}^{N}(2n+1)\left(\mathrm{Re}\left[C_n^{\mathrm{TM}}\right]+\left|C_n^{\mathrm{TM}}\right|^2\right)+\sum_{m=1}^{M}(2m+1)\left(\mathrm{Re}\left[C_m^{\mathrm{TE}}\right]+\left|C_m^{\mathrm{TE}}\right|^2\right)\right)\\ &= \sum_{n=1}^{N}\sigma_{abs,n}^{\mathrm{TM}}+\sum_{m=1}^{M}\sigma_{abs,m}^{\mathrm{TE}}\end{aligned}, \tag{4.2}$$

in which we assumed that only the first N TM and M TE harmonics are of practical relevance, since the summations over all harmonics are convergent series.

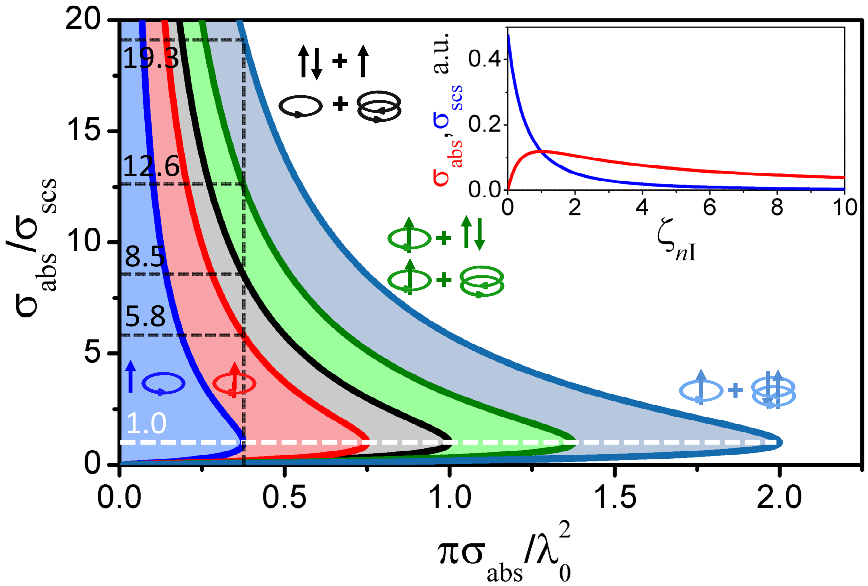

Figure 4.1: Absorption efficiency versus normalized absorbed cross-section for an arbitrary passive receiver, considering TM_1 or TE_1 (blue region), $TM_1 \& TE_1$ (red region), $TM_1 \& TM_2$ or $TE_1 \& TE_2$ (black region), $TM_{1,2} \& TE_1$ or $TE_{1,2} \& TM_1$ (green region), $TM_{1,2} \& TE_{1,2}$ (dark blue region) spherical harmonics to contribute to the total scattering signature. Solid-lines limiting each region correspond to the balanced resonance condition (4.3). Conjugate matched points, corresponding to maximum absorption, all lie along $\eta_{abs} = 1$ (dashed white line) and the black dashed lines indicate the achievable values of absorption efficiency for a given level of absorption. A typical absorption/scattering cross-section diagram is shown in the inset as a function of the level of loss ζ_{nI} for a resonant harmonic $\zeta_{nR} = 0$. (Reprinted with permission from Physical Review B, Vol. 89, Issue 12, pp. 121416 (2014). Copyright 2014 American Physical Society).

The partial absorption cross-section associated with each harmonic reaches its maximum $\sigma_{abs,n}^{\max} = (2n+1)\lambda_0^2 / 8\pi$ under the condition $\zeta_{nR} = 0, \zeta_{nI} = 1$, which corresponds to ideal conjugate matching, i.e., to the case in which the reactive energy is balanced (resonance) and the radiation and absorption resistances are equal. Conventional antennas [22] are typically tuned to hit this condition, at the price of producing a scattering cross-section equal to the absorption cross-section, $\sigma_{sca} = \sigma_{abs}\big|_{\zeta_{nR}=0,\, \zeta_{nI}=1}$ [6], as illustrated in the inset of Fig. 4.1, showing the variation of absorption and scattering as a function of the amount of loss (ζ_{nI}) in a scatterer at resonance $\zeta_{nR} = 0$. As expected, at the crossing between red (σ_{abs}) and blue (σ_{sca}) lines absorption is maximized.

Passivity ($\zeta_{nI} > 0$) poses inherent restrictions on the allowed values of total absorption efficiency $\eta_{abs} = \sigma_{abs} / \sigma_{sca}$ achievable for a given level of total absorption. This is shown in Figure 4.1, which plots the absorption efficiency versus normalized absorption cross-section for various receiving systems. The blue shaded region refers to the common situation in which the scattering is dominated by only one dipolar ($n = 1$) harmonic, either electric or magnetic, usually the case for small absorbers and receivers. The plot confirms that it is not possible in this scenario to absorb more than $\sigma_{abs,1}^{\max}$, which corresponds to the right-most point of the blue shadowed region, for which $\eta_{abs} = 1$ (conjugate matched absorber). For lower levels of absorption, η_{abs} is necessarily bounded between a maximum and minimum value, as indicated by the solid blue line ($\zeta_{1R} = 0$), and a value of $\eta_{abs} > 1$ may only be achieved trading off some absorption [18].

A way to overcome these inherent limitations is to consider the possibility of exciting at the same time more than one harmonic: for instance, the limit on maximum possible absorption may be overcome by staggering a few resonant harmonics, realizing a super-absorber [23] in some sense analogous to the super-scatterer concept originally introduced in [24]. Higher-order scattering harmonics may be excited by increasing the electrical size of the object [25]. The different shaded regions in Fig. 4.1 correspond to different combinations of consecutive scattering orders for $n, m = 1, 2$: the red region corresponds to the combination of electric and magnetic dipolar scattering, the black region to the combination of one dipolar and one quadrupolar mode, the green region to two dipolar and one quadrupolar, and finally the dark blue region to the combination of two dipolar and two quadrupolar modes, as indicated by the symbols in the figure. It is seen that, as we consider the contributions of different scattering harmonics, it is possible to push the maximum available σ_{abs} to larger values, and the maximum absorption for spherical scatterers is generally given by $\sigma_{abs}^{\max} = \left(N^2 + 2N + M^2 + 2M\right)\dfrac{\lambda_0^2}{8\pi}$.

Also in this case unitary absorption efficiency (white line) is obtained at these maxima, when all scattering harmonics are independently conjugate matched. Operating such superabsorbing system, however, is challenging in practice, especially when considering nanoparticles, because the Q-factor and corresponding inverse bandwidth of a subwavelength resonant system grows very fast with n for fixed volume, and therefore the available bandwidth and sensitivity of such designs would be inherently limited [25]-[26]. This explains why practical realizations of small sensors and absorbers are typically limited to one or two resonant dipolar modes and do not involve higher-order resonances.

Figure 4.1, however, provides useful insights into the possibility of staggering various harmonics in order to minimize the scattering, while keeping the absorption at a desired large level α_{abs}. Imagine, for instance, that our goal is to absorb $\alpha_{abs} = \sigma_{abs,1}^{\max} = 3\lambda_0^2 / \left(8\pi\right)$, i.e., the maximum absorption available with one dipolar harmonic (vertical dashed line in Fig. 4.1). The figure indicates that, by staggering a few harmonics, we can attain in principle any arbitrary value of absorption efficiency, without sacrificing absorption. For example, by operating with one dipolar and one quadrupolar order (black shadowed region), we may be able to achieve an absorption efficiency as high as 8.55 while absorbing α_{abs}. Two dipolar and two quadrupolar modes (cyan region) may achieve a scattering almost twenty times lower than the absorption, for the same α_{abs}. For a given level of absorption, it is found that scattering is minimized if and only if

$$\zeta_{nR}^{\mathrm{TM}} = \zeta_{mR}^{\mathrm{TE}} = 0;\ \zeta_{nI}^{\mathrm{TM}} = \zeta_{mI}^{\mathrm{TE}} = -1 + \frac{[N(N+2)+M(M+2)]\lambda_0^2}{4\pi\alpha_{abs}} \times \left(1+\sqrt{1-\frac{8\pi\alpha_{abs}}{\lambda_0^2[N(N+2)+M(M+2)]}}\right) = \zeta_{\mathrm{opt}}^{M,N} \quad (4.3)$$

Interestingly, substituting these values into the expressions for scattering and absorption cross-sections, we find that the corresponding maximum absorption efficiency has the identical value $\eta_{\max} = \zeta_{\mathrm{opt}}^{M,N}$. Equation (4.3) shows, as expected, that for $\alpha_{abs} = \sigma_{abs}^{\max}$ we get $\eta_{\max} = 1$, which is obtained when all coefficients are conjugate matched, i.e., all $\xi_n = i$. For smaller α_{abs}, however, still equal or larger than $3\lambda_0^2/(8\pi)$, large absorption efficiencies are accessible. To achieve maximum efficiency, according to condition (4.3) each harmonic has to be at resonance $\zeta_{nR}^{\mathrm{TE,TM}} = 0$, but they should be all largely mismatched, at the same level $\zeta_{nI}^{\mathrm{TE,TM}} \gg 1$. All contributing harmonics, under this condition, provide an amount of absorption proportional to their order, proving that the optimal strategy is to combine various mismatched harmonics, all balanced together to realize an optimal superabsorber with minimized visibility. Even more remarkably, the excitation of higher-order harmonics does not introduce in this scenario relevant constraints on the bandwidth of operation, since each mode is largely mismatched, lowering the Q-factor and sensitivity, and broadening the overall bandwidth.

This result is perfectly consistent with the optical or forward-scattering theorem [27]: large absorption is directly associated to a proportional amount of real-valued scattered fields in the forward direction (a far-field shadow behind the object produced by a polarization current in phase with the impinging field) [28] and all other residual scattering does not directly impact power conservation. For this reason, a directive scattering pattern in phase with the impinging field and pointing towards the forward direction is ideal to minimize the overall scattering of the object [4], and this may be only realized by relying on higher-order scattering harmonics. There is in principle no limit on absorption efficiency, independent of the level of desired absorption, as long as we can rely on the suitable excitation of higher-order scattering harmonics to generate this directive pattern. Eq. (4.3) determines the optimal excitation based on the suitable interference of $N+M$ spherical orders.

4.3 PLASMONIC CORE-SHELL NANOPARTICLES TO IMPLEMENT OPTICAL MINIMUM-SCATTERING ABSORBERS

To provide further insights into this finding, we propose in the following a few examples of minimum-scattering superabsorbers in the form of layered nanospheres, as schematically shown in the inset of Fig. 4.2. We optimize the geometry of all our absorbers to operate at the operating wavelength $\lambda_0 = 500\,\text{nm}$. We stress that this choice of operating frequency is completely arbitrary and the proposed concept is applicable to different classes of sensors and absorbers, ranging from simple loaded wire antennas at radio-frequencies to nanoparticle sensors and absorbers at optical frequencies. In the next section we will look into the loaded wire antenna example in more details.

In our first example, the structure consists of a low-loss dielectric core with permittivity $\varepsilon_1/\varepsilon_0 = 3.5 + i0.3$ and a concentric shell made of a plasmonic metal, i.e., gold, modeled with Drude permittivity $\varepsilon_p/\varepsilon_0 = \varepsilon_\infty - \dfrac{\omega_p^2}{\omega(\omega + i\Gamma)}$ with $\varepsilon_\infty = 1.53$, $\omega_p = 2\pi\,2069\,\text{THz}$ and $\Gamma = 2\pi\,17.64\,\text{THz}$ [29]. We fix the outer radius of the nanoparticle to be subwavelength, $a = 0.15\lambda_0$ (second row in Table 1), and explore the possibility of simultaneously exciting the first two electric harmonics $\text{TM}_1\,\&\,\text{TM}_2$, corresponding to the shaded black region in Fig. 4.1. We set our desired absorption level to the maximum achievable with a single dipolar resonance $\alpha_{\text{abs}} = \dfrac{3\lambda_0^2}{8\pi}$, black dashed line in Fig. 4.1, and tune the ratio $a_c/a = 0.83$ to satisfy conditions (4.3).

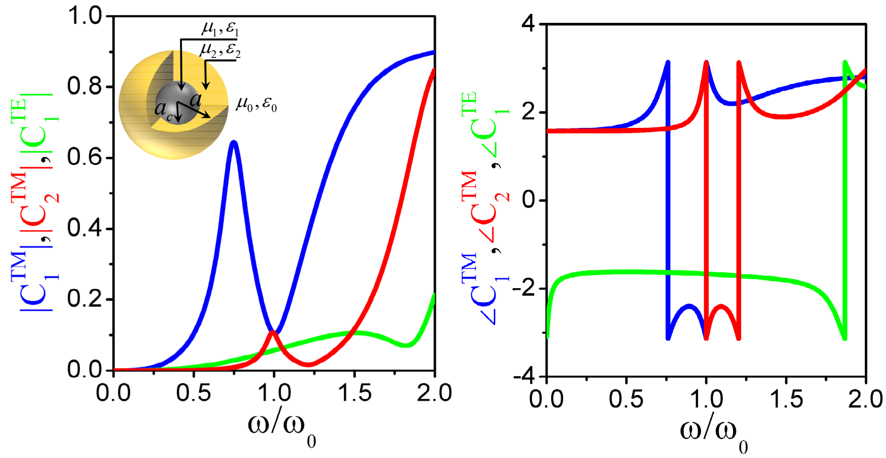

Figure 4.2: Amplitude and phase spectra of the first three scattering harmonics for the proposed superabsorber. The core-shell nanoparticle consists of a nonmagnetic dielectric core with permittivity $\varepsilon_1/\varepsilon_0 = 3.5 + i0.3$ and radius $a_c = 0.126\lambda_0$, and a plasmonic gold shell with outer radius $a = 0.15\lambda_0$, designed to operate at $\lambda_0 = 500$ nm. A schematic plot of the core-shell nanoparticle is shown in the inset. (Reprinted with permission from Physical Review B, Vol. 89, Issue 12, pp. 121416 (2014). Copyright 2014 American Physical Society).

Table 4.1. Design parameters and performance characteristics of the proposed optical superabsorber designs. (Reproduced with permission from Physical Review B, Vol. 89, Issue 12, pp. 121416 (2014). Copyright 2014 American Physical Society).

Contributing Harmonics and Number of layers	Radiuses and Permittivities	Peak absorption efficiency	Efficiency Q-factor
TM_1 & TE_1 3 layers	$\{a_{c1}, a_{c2}, a\} = \{0.13, 0.16, 0.194\}\lambda_0$ $\varepsilon_1/\varepsilon_0 = 1.29 + i0.01$ $\varepsilon_2 : Ag,\ \varepsilon_3/\varepsilon_0 = 8.4 + i2.33$	7.1	6.9
TM_1 & TM_2 2 layers	$\{a_c, a\} = \{0.126, 0.15\}\lambda_0$ $\varepsilon_1/\varepsilon_0 = 3.5 + i0.3,\ \varepsilon_2 : Au$	7.9	10.4
$TM_{1,2}$ & TE_1 3 layers	$\{a_{c1}, a_{c2}, a\} = \{0.25, 0.28, 0.31\}\lambda_0$ $\varepsilon_1/\varepsilon_0 = 1.25 + i0.03$ $\varepsilon_2 : Ag,\ \varepsilon_3/\varepsilon_0 = 8.6 + i0.96$	13.5	17

The spectral dependence of the first three scattering coefficients for this optimized superabsorber is shown in Fig. 4.2. Around the central frequency, both amplitude and phase of $\mathrm{TM}_1 \& \mathrm{TM}_2$ coefficients match each other: $\zeta_{1R}^{\mathrm{TM}} \approx \zeta_{2R}^{\mathrm{TM}} \approx 0$, $\zeta_{1I}^{\mathrm{TM}} \approx \zeta_{2I}^{\mathrm{TM}} \approx 8.51$, in excellent agreement with condition (4.3). The corresponding scattering coefficients become purely real, with value $C_1^{\mathrm{TM}} = C_2^{\mathrm{TM}} = -0.105$, guaranteeing the most directive scattering pattern in the forward direction that can be supported by the interference of these two harmonics and suppressing the unwanted out of phase component of the scattering. As seen in the plots, in this regime the next scattering coefficient, TE_1, is negligible.

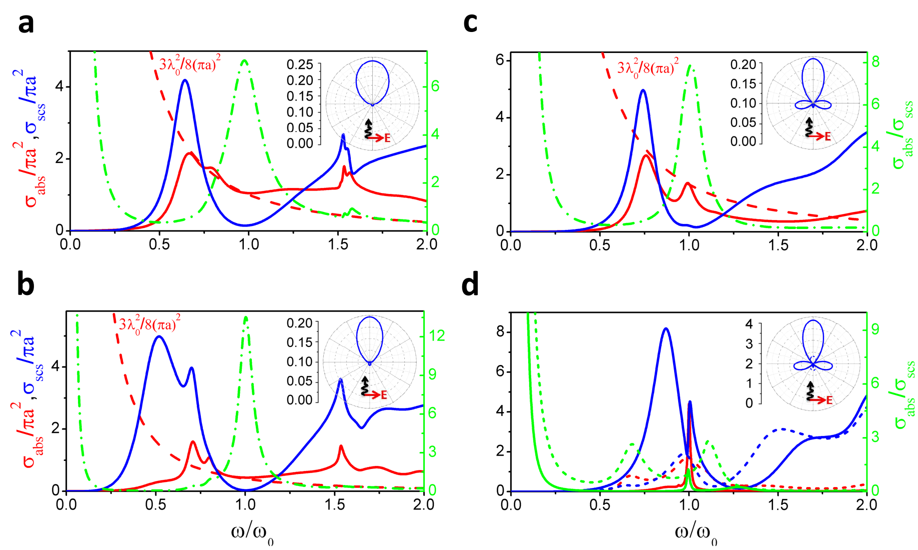

Figure 4.3: (a)-(c) Absorption (red line) and scattering (blue line) cross-sections of optimal minimum-scattering superabsorbers relying on $\mathrm{TM}_1 \& \mathrm{TE}_1$ (a), $\mathrm{TM}_{1,2}$ (b), and $\mathrm{TM}_{1,2} \& \mathrm{TE}_1$ (c) harmonics, consistent with the geometries in Table 4.1. The absorption cross-section of a conjugate matched dipole is also plotted for comparison in each panel (red dashed line). The E-plane scattering pattern is shown in each inset at the central frequency ω_0. The absorption efficiency of the sensor is shown in each panel by green lines. (d) Absorption (red) and scattering (blue) cross-sections of conjugate matched absorbers with one (solid lines) and two (dashed lines) harmonics and outer radius $a = 0.15\lambda_0$. (Reprinted with permission from Physical Review B, Vol. 89, Issue 12, pp. 121416 (2014). Copyright 2014 American Physical Society).

By increasing the number of layers it is possible to further increase the available degrees of freedom in our design, and study the evolution of this response as a function of the number of involved scattering orders. Figures 4.3(a-c) show the scattering and absorption efficiencies versus frequency of different nanoparticles optimized to meet conditions (4.3) for two harmonics ($\mathrm{TM}_1 \& \mathrm{TE}_1$, panel a), ($\mathrm{TM}_{1,2}$, panel b, consistent with Fig. 4.2), and three harmonics ($\mathrm{TM}_{1,2} \& \mathrm{TE}_1$, panel c), with design parameters summarized in Table 4.1, respectively first to third row. In each panel we also show for comparison the maximum absorption attainable from a conventional dipolar absorber with same size (dashed red line), and the frequency dispersion of the calculated absorption efficiency (green dash-dot line). In the insets, we also show the scattering pattern from each particle in the E-plane at the central frequency, showing a progressively more directive response as the number of modes and corresponding η_{abs} are increased.

We note various interesting features in these plots: first, despite the subwavelength features of all these designs, higher-order resonances can be excited quite straightforwardly with realistic parameters and materials since each harmonic is deeply mismatched by an intentionally large level of absorption resistance, bringing down the Q-factor of each resonance. In particular, $\left|C_n\right| = 0.146, 0.105, 0.07$ for the three examples in Fig 4.3(a-c), respectively, significantly far from the conjugate matched condition $\left|C_n\right| = 1$. This implies that the bandwidth is not significantly worsened, even after increasing the number of harmonics and their resonant order. To highlight this point, we calculated an effective Q-factor (inverse fractional bandwidth) for the dispersion of the absorption efficiency, reported in the last column of Table 4.1, indicating that the Q-factor grows linearly with the absorption efficiency, remaining manageable even if a few higher-order harmonics are involved and the nanoparticle is still deeply subwavelength.

This property is in stark contrast with the example in Figure 4.3d, which shows for comparison the case of conjugate-matched resonant nanoparticles with the same size as the superabsorber of Fig. 3b, but now designed to support a dipolar (dashed lines) or a combined $TM_{1,2}$ conjugate matched resonances. It is found that in this case the Q-factor drastically increases from 3 to 45 moving from one to two harmonics, while the absorption is increased by only a factor of three. Our optimized minimum-scattering superabsorbers show the same absorption as an ideally conjugate-matched resonant dipole, or a coherent perfect absorbing dipole, while scattering 7 to 13 times less, over a reasonable bandwidth and with realistic materials and robustness to imperfections in realization. The proposed balanced design may be practically implemented with considerable tolerance on the design parameters. In the following, we study the effect of variations on these parameters on the scattering and absorption response of the system. As we discussed previously, the multipoles contributing to scattering and absorption are intentionally designed to be deeply mismatched in order to satisfy the optimum criteria of Eq. (4.3). As a result of working in this regime we predict low sensitivity of the response to the material or geometrical parameters as well. Also, we note that at the optimum design condition the scattering strength of the contributing harmonics should be low (specifically $\left|C_n\right| = 0.146, 0.105, 0.07$ for the three examples in Fig 4.3(a-c)), which implies that any dielectric and plasmonic material with realistic dispersion can be used and we are still guaranteed to excite weak higher order harmonics to maintain the main features of the response.

The results presented in the chapter have been analytically derived based on Mie theory for scattering from spherical objects (see e.g. Ref. [25]), which allows us to accurately study the effect of parameter variations on the scattering and absorption spectrum. As an example, we show in Fig. 4.4 (a-b) the effect of 20% variation in the material properties of the two-mode superabsorber (row two in Table 4.1 and Fig. 4.3(b)) on the absorption and scattering cross-sections. Apart from minor variations, the main features of the response, including low scattering and high absorption at the design frequency are totally preserved. As expected, the variation of scattering and absorption cross-sections is minimal around the design point. Besides practical implementation, the robustness of the design to material variations further confirms the Q factor sustainability of the structure to the intrinsic dispersion of constitutive materials.

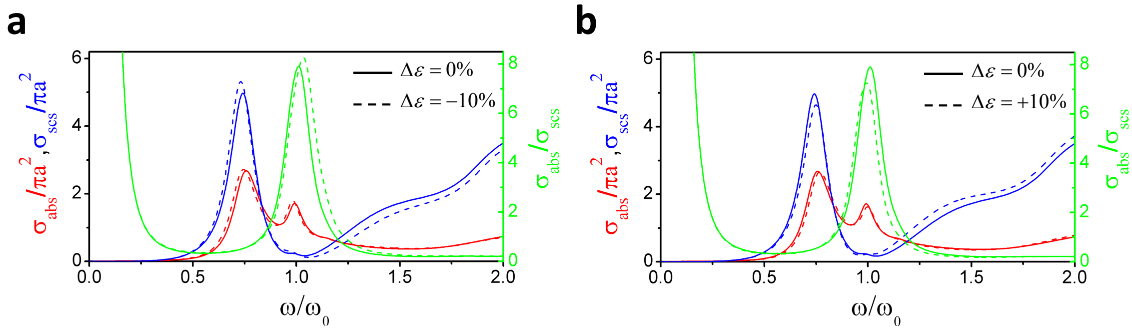

Figure 4.4: Sensitivity of the scattering and absorption cross-sections to perturbations in the material properties ($\pm 10\%$ from the values reported in Table 4.1, column 4-row 2). The other parameters are kept the same. (Reprinted with permission from Physical Review B, Vol. 89, Issue 12, pp. 121416 (2014). Copyright 2014 American Physical Society).

Some of the material parameters of the dielectric layers considered in the previous examples may not be directly available at the frequency of interest. While variations around these optimal values do not significantly affect the overall performance, we stress that significantly more flexibility on the choice of materials may be attained by adding degrees of freedom to the geometry, such as considering asymmetric shapes, or compact clusters of nanoparticles. In this case, it may be possible to realize the optimal condition (4.3) with a wide variety of available materials. In fact, suitably chosen asymmetric geometries may allow coupling different scattering channels together, further boosting the described effect.

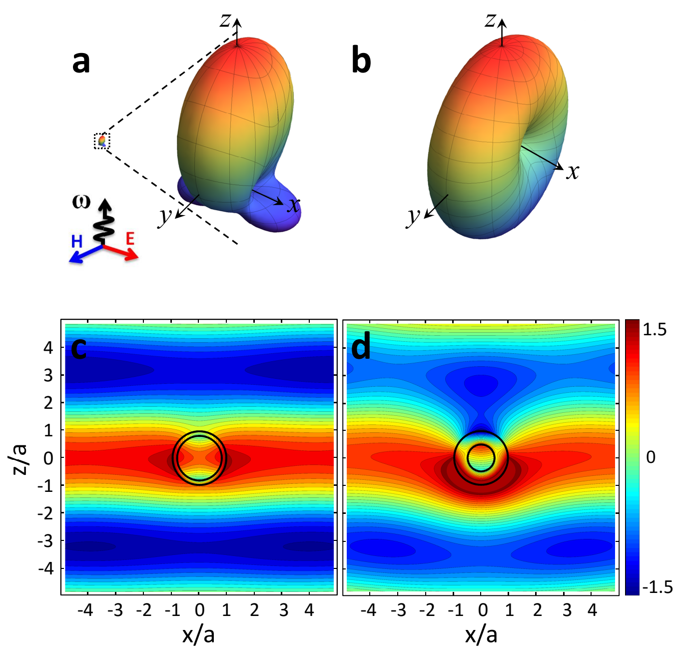

Figure 4.5: Far-field scattering pattern of (a) the designed invisible absorber shown in Fig. 4.2 compared to (b) a similar configuration when filling ratio is changed to $a_c/a = 0.5$. Plots are in the same scale and a closer image of the invisible particles pattern is shown on the right panel. (c)-(d) Total magnetic field distribution (a snapshot in time) in the xz plane (E-plane). Field distribution is normalized to the amplitude of the incident plane wave and the black circles indicate the position of the core-shell nanoparticles. (Reprinted with permission from Physical Review B, Vol. 89, Issue 12, pp. 121416 (2014). Copyright 2014 American Physical Society).

It is also worth emphasizing that this is not simply the result of scattering cancellation, but it requires the careful excitation of various resonant modes in a balanced multi-modal absorber. To demonstrate the importance of balanced excitation in the minimum-scattering superabsorber concept, we consider here two core-shell nanoparticles with geometry shown in the inset of Fig. 4.2. One of the particles is designed to operate at the $TM_1 \& TM_2$ balanced point with geometrical and material parameters provided in the second row of Table 4.1, consistent with the results in Fig. 4.2 and 4.3(b). The second nanoparticle, on the other hand, is composed of the same materials and same overall size of $a = 0.15\lambda_0$, but the filling ratio is changed to $a_c/a = 0.5$ moving farther from the optimal design point. Figures 4.5(a,b) compare the far-field scattering pattern of these two particles. The real part of the total near-field distribution at $\lambda_0 = 500\,\text{nm}$ is also plotted for both cases, assuming an incident plane-wave polarized in the x direction and propagating along z axis (Fig. 4.5(c,d)).

While our superabsorbing sensor is essentially transparent to the impinging wave, the second particle significantly perturbs the wave propagation, with scattering cross section equal to $\sigma_{scs} = 0.35\lambda_0^2$ approximately 22 times larger than the invisible sensor. At the same time, the absorption cross section of the balanced sensor is 9 times larger. The residual small scattering of the superabsorber design is directed along the z axis, consistent with our previous discussions [4].

4.4 EXPERIMENTAL IMPLEMENTATION OF LOW-SCATTERING, SUPERABSORBING MICROWAVE SENSORS

At microwaves, antennas are the essential components to bridge signals from sources to distant detectors/receivers. Throughout the last century, special interest has been devoted to their design, resulting in comprehensive techniques and design methods for various applications [22]. For various applications, such as noninvasive sensing and closely packed antenna systems, it is of special importance that the receiver picks up the incoming electromagnetic signal without affecting its original distribution, acting as an invisible 'eye' that is capable of seeing the surrounding medium without being detectable by an external observer. A rather straightforward approach to suppress the unwanted scattering is to place the antenna inside an electromagnetic cloak. Such a possibility has been discussed in the past few years, incorporating antennas in transformation-optics and scattering cancellation cloaks [4],[6]. However, the antennas' capability to collect the incident energy directly relies on how strongly they can interact with the incident signal. As we discussed in the previous sections, by reducing this interaction with an electromagnetic cloak, the power absorbed by the antenna is also expected to drop, indicating that it is not possible to extract energy from a wave without creating some sort of distortion or shadow, which is also a direct consequence of the optical theorem [4].

Interestingly, however, we have proved in the first part of this chapter [30], that staggering different absorption channels in a receiver provides a venue to relax these constraints. We discussed the possibility of designing low-scattering optical nanoparticles with large absorption, based on the proper excitation of multiple scattering modes in section (4.3). In the following, we extend this theory to radio-frequency (RF) antennas, designing and implementing a poof-of-concept low-scattering sensor based on this principle. The power absorbed by the realized antenna is larger than the one of an ideally resonant conjugate-matched dipole antenna, yet the scattering signature is reduced by over 75% across the operation bandwidth.

4.4.1 Design of low-scattering RF sensors

The field distribution around the antenna of interest may be also expanded into the orthogonal base of spherical harmonics, each one excited with an amplitude and phase related to the antenna shape, size and loading. In general, the complex Mie scattering coefficients C_n^{TM} and C_m^{TE} correspond to the excited n-th electric and m-th magnetic multipolar modes. For instance, the contribution of the $n=1$ mode dominates the response of a linear wire antenna, while other higher-order harmonics are negligible. In a wire loop antenna, on the contrary, the $m=1$ or magnetic dipolar mode dominates the response of the system. Studying the total scattered P_{scs} and absorbed P_{abs} powers of a generic antenna, we proved in Eq. (4.3) that, for a fixed amount of desired P_{abs} (proportional to the detected signal), minimal P_{scs} can be achieved by designing the antenna so that all contributing modes are excited with equal amplitude and phase. For instance, in the simplest scenario we consider a receiving antenna supporting two modes, electric and magnetic dipole moments. We note that this corresponds to the core-shell nanoparticle example of Fig. 4.3(a). The optimal scattering coefficients for such antenna to minimize P_{scs} while absorbing the desired value P_{abs} for incident power intensity $\mathrm{P}_{in} = 1\ \mathrm{W/m^2}$ equals

$$C_1^{\mathrm{TM}} = C_1^{\mathrm{TE}} = -\frac{2\pi\,\mathrm{P}_{abs}}{\lambda_0\left(3\lambda_0 + \sqrt{-12\pi\,\mathrm{P}_{abs} + 9\lambda_0^2}\right)}. \tag{4.4}$$

Conveniently, Eq. (4.4) can be translated into the dipolar polarizabilities of the low-scattering sensor, $\alpha_e = j\,6\pi\varepsilon_0 / k_0^3\, C_1^{\mathrm{TM}}$ and $\alpha_m = j\,6\pi\mu_0 / k_0^3\, C_1^{\mathrm{TE}}$. To compare our antenna with conventional receiving dipoles, we fix P_{abs} to the maximum value available in a resonant dipole antenna, i.e., $\mathrm{P}_{abs} = 3\lambda_0^2/(8\pi)$ per unit incident power intensity. In a conventional single mode antenna, this amount of absorption is achieved at the conjugate matched condition (see Fig. 4.1), for which the scattered power necessarily equals absorption, i.e., $\mathrm{P}_{scs} = \mathrm{P}_{abs}$. Yet, considering an additional scattering mode and applying (4.4), a decrease of 7.65 dB on the total scattering of the antenna can be expected for the same level of absorbed power.

4.4.2 Sensor realization and measurement

Based on the optimal polarizabilities for the two-mode antenna derived in Eq. (4.4), we implement the low-scattering sensor as the combination of two symmetrically-loaded printed antennas, an electric dipole and a magnetic loop, shown in Fig. 4.6(a).

Based on the availability of discrete loading elements (SMT 0603), the center frequency is set at 2.85 GHz and the two dipoles are designed to satisfy Eq. (4.4) through an accurate analytical modeling [31]. Interestingly, since the optimal conditions require each mode to be weakly excited, the antenna dimensions are deeply subwavelength and the designed low-scattering receiver fits in a $10.5\,\mathrm{mm}\times 11.7\,\mathrm{mm}\times 9.6\,\mathrm{mm}$ volume. The scattering and absorption properties of the sensor are calculated through a retrieval method adapted from [32], in which the antenna is placed at the center of a rectangular waveguide (WR284) and the S-parameters are measured across the range 2.5-3.1 GHz. The measurement is calibrated with four known scatterers, two electric and two magnetic dipoles, shown in Fig. 4.6(b) together with the waveguide used for the retrieval. In summary, the general relation between the electric and magnetic fields across ports 1 and 2 of the waveguide and the local fields at the position of the known dipolar particles can be written as [32],

$$
\begin{aligned}
&\begin{bmatrix} p_x \\ m_y \end{bmatrix} = \begin{bmatrix} \alpha_x^e & 0 \\ 0 & \alpha_y^m \end{bmatrix} \begin{bmatrix} E_x^{loc} \\ H_y^{loc} \end{bmatrix} \\
&\begin{bmatrix} E_{1x}^- \\ E_{2x}^- \end{bmatrix} = \begin{bmatrix} 0 & 1 \\ 1 & 0 \end{bmatrix} \begin{bmatrix} E_{1x}^+ \\ E_{2x}^+ \end{bmatrix} + \begin{bmatrix} K_{xx}^p & -K_{xy}^m \\ K_{xx}^p & K_{xy}^m \end{bmatrix} \begin{bmatrix} p_x \\ m_y \end{bmatrix} \quad . \\
&\begin{bmatrix} E_x^{loc} \\ H_y^{loc} \end{bmatrix} = \begin{bmatrix} 1 & 1 \\ -Y_0 & Y_0 \end{bmatrix} \begin{bmatrix} E_{1x}^+ \\ E_{2x}^+ \end{bmatrix} + \begin{bmatrix} C_{xx}^e & 0 \\ 0 & C_{yy}^m \end{bmatrix} \begin{bmatrix} p_x \\ m_y \end{bmatrix}
\end{aligned}
\tag{4.5}
$$

Following the definition of scattering parameters and after some simplifications it can be shown that the four unknown parameters $K_{xx}^p, K_{xy}^m, C_{xx}^e$, and C_{yy}^m, associated with the geometry of the waveguide, are uniquely determined from scattering parameters of our four independent dipolar calibrating particles. For an unknown particle with polarizability matrix of $\underline{\underline{\alpha}} = \left[\alpha_x^e, 0; 0, \alpha_y^m\right]$, polarizability is then retrieved from the measured full scattering matrix $\underline{\underline{S}} = \left[S_{11}, S_{12}; S_{21}, S_{22}\right]$ as,

$$\underline{\underline{\alpha}}^{-1} = \underline{\underline{C}}^a \cdot \underline{\underline{S}}^{\text{mod}} + \underline{\underline{C}}^b \quad , \tag{4.6}$$

in which

$$\begin{aligned} &\underline{\underline{C}}^a = \begin{bmatrix} K_{xx}^p & K_{xy}^m \\ K_{xx}^p Y_0 & K_{xy}^m Y_0 \end{bmatrix}, \underline{\underline{C}}^b = \begin{bmatrix} C_{xx}^e & 0 \\ 0 & C_{yy}^m \end{bmatrix} \\ &\underline{\underline{S}}^{\text{mod}} = \begin{bmatrix} \dfrac{2 + S_{11} - S_{12} - S_{21} + S_{22}}{-1 + S_{12} + S_{21} - S_{12}S_{21} + S_{11}S_{22}} & \dfrac{\left(S_{11} - S_{12} + S_{21} - S_{22}\right)}{-1 + S_{12} + S_{21} - S_{12}S_{21} + S_{11}S_{22}} \\ \dfrac{S_{11} + S_{12} - S_{21} - S_{22}}{-1 + S_{12} + S_{21} - S_{12}S_{21} + S_{11}S_{22}} & \dfrac{\left(-2 + S_{11} + S_{12} + S_{21} + S_{22}\right)}{-1 + S_{12} + S_{21} - S_{12}S_{21} + S_{11}S_{22}} \end{bmatrix}. \end{aligned} \tag{4.7}$$

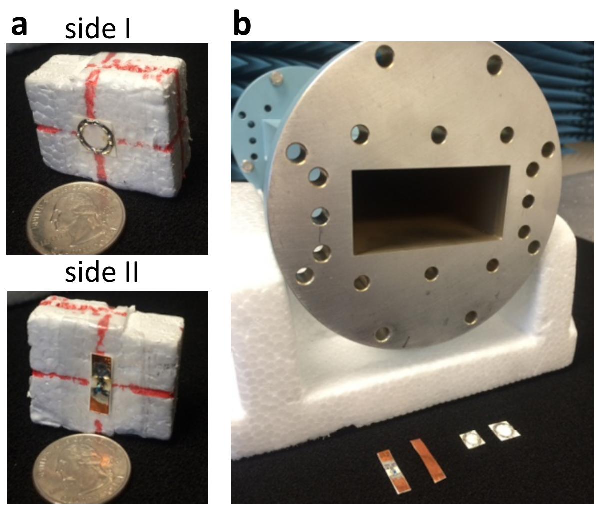

Figure 4.6: (a) The designed two-mode low-scattering antenna consisting of adjacent electric and magnetic dipoles mounted on two sides of a 9.6 mm thick Styrofoam fixture. (b) Four calibrating particles and the WR284 waveguide used for polarizability retrieval.

After retrieval of $\underline{\underline{\alpha}}$, we can calculate the scattering coefficients C_1^{TM} and C_1^{TE}, as shown in Fig. 4.7 (a), and the total absorbed and scattered powers of the low-scattering sensor, as shown in Fig. 4.7(b) with solid red and blue lines, respectively. The power levels are normalized to an incident power intensity $P_{in} = 1\ \mathrm{W/m^2}$, and in the same figure the maximum reachable absorption by a single dipole is shown with the dark gray line. Our measurements in Fig. 4.7 demonstrate the successful implementation of a low-scattering sensor that is able to absorb comparable power to a conjugate matched dipole, yet with significantly reduced scattering signature. Interestingly, the bandwidth of operation is comparable to a resonant dipole antenna of similar size, despite the improved performance in terms of scattering, which is due to the detuning of each scattering channel. In other words, the strong reduction in scattering does not require a strong narrowing of the involved resonances. Fig. 4.8(a) also shows the ratio of absorbed and scattered powers for the realized sensor, compared to full-wave simulations, and to the theoretical limits for a conjugate matched dipole and of a two-mode sensor based on Eq. (4.4). The small discrepancy between measured and simulated curves is associated to the difference between nominal and realistic values of the loading elements, as well as to fabrication errors.

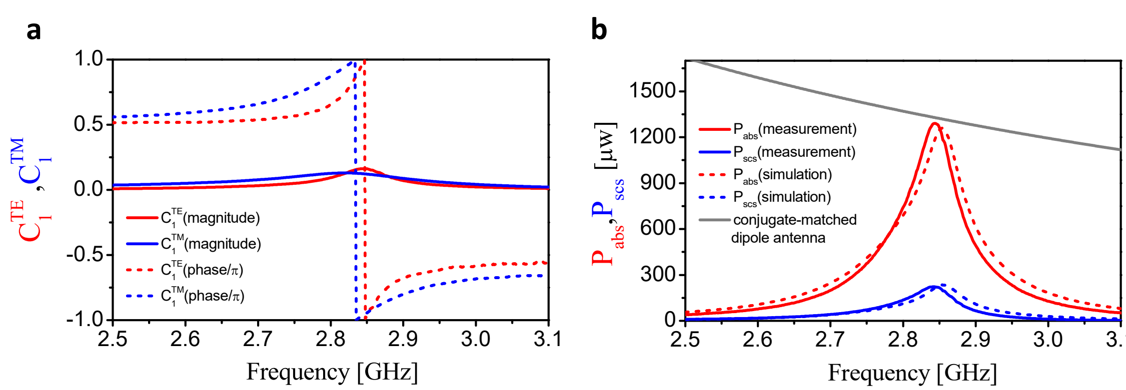

Figure 4.7: (a) Amplitude (solid) and phase (dashed) of the complex Mie scattering coefficients C_1^{TM} and C_1^{TE}. (b) Total scattered (blue) and absorbed (red) power levels: measurement (simulation) results are shown with solid (dashed) curves. The gray line indicates the maximum absorption attainable from a wire dipole at the conjugate matched condition.

It is also insightful to look into the scattering pattern of the designed sensor at the frequency of operation. The excitation of balanced electric and magnetic dipoles implies that the residual scattering has a Huygens-like pattern (Fig. 4.8(b)), consistent with the optical theorem requirement that a minimum-scattering antenna has a directive scattering distribution pointing in the forward direction. The pattern is also consistent with or previous studies of layered nanoparticles with analogous scattering and absorption properties (see inset of Fig. 4. 3(a)) [4],[25].

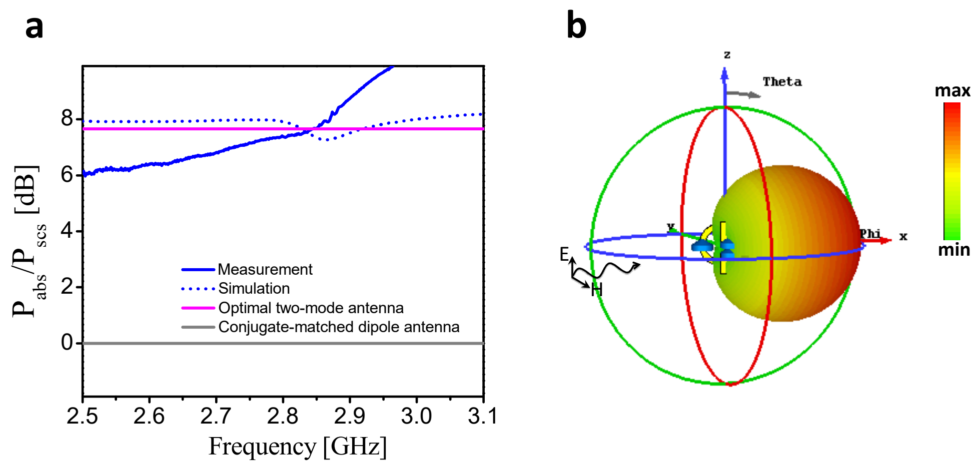

Figure 4.8: (a) Ratio of total absorbed and scattered powers for the measured (solid blue) and simulated (dashed blue) low-scattering sensor. A conjugate-matched dipole is shown in gray for comparison. The pink line indicates the optimal ratio theoretically achievable by a two-mode antenna. (b) 3D scattering pattern of the antenna under plane-wave excitation.

4.5 Conclusion

In conclusion, in this chapter we have shown that there is a possibility to independently control the scattering and absorption properties of a receiver. Our analytical, full-wave simulations and experimental results confirm that the judicious excitation of multiple absorption channels in a suitably designed sensor can produce large total scattering reductions without sacrificing the overall absorption, compared to conventional single-mode conjugate matched antennas. The balanced resonant design and minimum-scattering superabsorbing response described here may have exciting applications, including subdiffractive near field imaging [1]-[2] and optimal absorbers with minimal impact on the impinging field distribution. We have shown in fact that, with proper design, both absorption and absorption efficiency can be made in principle arbitrarily large over a moderate yet reasonable bandwidth. These findings also relax the constraints on absorption of minimum-scattering antennas, providing an exciting venue to minimize the mutual coupling between closely packed receiving antennas. Probably the most striking feature of this concept resides in the moderate values of Q-factor associated with it, making the proposed designs realistic and quite robust to fabrication tolerances, as verified by our experiment.

4.6 References

[1] D. W. Pohl, W. Denk, and M. Lanz, Appl. Phys. Lett. 44, 651 (1984).

[2] B. Hecht, B. Sick, U. P. Wild, V. Deckert, R. Zenobi, O. J. F. Martin, and D. W. Pohl, J. Chem. Phys. 112, 7761 (2000).

[3] W. K. Kahn, and H. Kurss, IEEE Trans. Antennas Propag. 13, 671 (1965).

[4] J. B. Andersen, and A. Frandsen, IEEE Trans. Antennas Propag. 53, 2843 (2005).

[5] M. Gustafsson, C. Sohl, and G. Kristensson, Proc. R. Soc. A 463, 4632007 (2007).

[6] D. H. Kwon, and D. M. Pozar, IEEE Trans. Antennas Propag. 57, 3720 (2009).

[7] A. Kurs, A. Karalis, R. Moffatt, J. D. Joannopoulos, P. Fisher, and M. Soljacic, Science 317, 83 (2007).

[8] J. Lee, and S. Nam, IEEE Trans. Antennas Propag. 58, 3442 (2010).

[9] D. M. Pozar, Microwave Engineering (John Wiley & Sons, New York, 1997).

[10] Y. D. Chong, Li Ge, Hui Cao, and A. D. Stone, Phys. Rev. Lett. 105, 053901 (2010).

[11] R. Green, IEEE Trans. Antennas Propag. 14, 17 (1966).

[12] A. Alu, and S. Maslovski, IEEE Trans. Antennas Propag. 58, 1436 (2010).

[13] A. Alù and N. Engheta, Phys. Rev. Lett. 102, 233901 (2009).

[14] G. Castaldi, I. Gallina, V. Galdi, A. Alù, and N. Engheta, J. Opt. Soc. Am. B, 27, 2132 (2010).

[15] A. Greenleaf, Y. Kurylev, M. Lassas, and G. Uhlmann, Phys. Rev. E 83, 016603 (2011).

[16] A. Alù and N. Engheta, Phys. Rev. Lett. 105, 263906 (2010).

[17] P. Y. Fan, U. K. Chettiar, L. Y. Cao, F. Afshinmanesh, N. Engheta, and M. L. Brongersma, Nat. Photonics 6, 380 (2012).

[18] R. Fleury, J. Soric, A. Alù, Phys. Rev. B 89, 045122 (2014).

[19] A. Alù and N. Engheta, Phys. Rev. E 72, 016623 (2005).

[20] A. Karilainen and S. Tretyakov, IEEE Trans. Antennas Propag. 60, 3471 (2012).

[21] A. Alù and N. Engheta, J. Appl. Phys. 97, 094310 (2005).

[22] C. A. Balanis, Antenna Theory (Wiley, New York, 1996).

[23] S. A. Mann and E. C. Garnett, Nano Lett. 13, 3173 (2013).

[24] Z. Ruan and S. Fan, Phys. Rev. Lett. 105, 013901 (2010).

[25] C. F. Bohren and D. R. Huffman, Absorption and Scattering of Light by Small Particles (Wiley, New York, 1983).

[26] A. Alù and N. Engheta, IEEE Trans. Antennas Propag. 55, 3027 (2007).

[27] A. Ishimaru, Wave Propagation and Scattering in Random Media (Academic, New York, 1978).

[28] A. Alu and N. Engheta, J. Nanophot. 4, 041590 (2010).

[29] M. A. Ordal, R. J. Bell, R. W. Alexander, Jr, L. L. Long, and M. R. Querry, Appl. Opt. 24, 4493 (1985).

[30] N. Mohammadi Estakhri and A. Alu, Phys. Rev. B 89, 121416 (2014).

[31] S. Tretyakov, Analytical modeling in applied electromagnetics (Artech House, 2003).

[32] L. Jelinek, and J. Machac, IEEE Antennas Wireless Propag. Lett., IEEE 13 (2014).

Chapter 5: Theory of Wave Transformation with Gradient Metasurfaces

Throughout chapters 2-4 we introduced methods to design and implement metamolecules with engineered absorption and scattering properties. In this and following chapters we will discuss how thin arrays of suitably arranged metamolecules, known as metasurfaces, can enable a new degree of wavefront control, suitable for many applications ranging from cloaking to energy harvesting. In this chapter, we present the theoretical analysis of gradient (i.e. nonperiodic) metasurfaces as a platform to generate arbitrary wavefronts and will derive general requirements of an ideal metasurface to perform functionalities such as beam steering, lensing, and free-space to bounded mode coupling beyond the scope of ray-optics. We furthermore outline the inherent limitations of passive gradient metasurfaces and will introduce several techniques to improve the efficiency of arbitrary wave manipulation over ultrathin surfaces. The theoretical formulation presented in this chapter will be used in the following chapters to design and implement practical metasurfaces for several applications. The contents of this chapter partially appeared/to appear in "Mohammadi Estakhri, N.; Alu, A., Wavefront Transformation with Gradient Metasurfaces, under review" and "Mohammadi Estakhri, N.; Argyropoulos, C.; Alù, A., Graded metascreens to enable a new degree of nanoscale light management. Phil. Trans. R. Soc. A 2015, 373 (2049), 20140351".

5.1 Introduction

Devising physical systems that grant full control of the distribution of electromagnetic waves has been an emerging area of research in the past decades. Photonic crystals [1] and metamaterials [2] represent the two major milestones in this direction, and several unusual wave phenomena have been put forward based on these artificially engineered structures, most notably negative refraction and perfect lensing, improved optical fibers, extreme wave localization, and invisibility cloaks [3]-[6]. One of the long-standing challenges in this context, originally considered at radio frequencies (RF), is to come up with practical and efficient techniques to arbitrarily mold the emerging wavefront of an antenna or a localized source. Conventional methods to solve this problem date back to glass lenses and prisms, which rely on engineering the gradual accumulation of phase delay as the wave propagates in the device, reshaping the scattered wavefront and beam profile at will. In the context of metamaterials, transformation optics has become a paradigm to realize arbitrary wave manipulation in volumetric devices [7]-[9]. On top of the unavoidable loss induced along the propagation path, often substantial when metamaterial components are considered [10], these devices suffer from bulky profiles and are typically at least several wavelengths thick. A relevant question we address in this chapter is whether it would be possible to realize a transformation platform similarly capable of molding wave propagation at will, but with a much thinner and low-profile geometry, in other words over a metasurface.

At RF, low-profile devices for wavefront patterning are available in the form of arrays of printed antennas, also known as reflect- and transmit-arrays, which are used to modify the spatial distribution of reflected and transmitted waves over deeply subwavelength thicknesses [11]-[13]. In contrast to the gradual transformation of the wave in a volumetric component, these printed structures create a transversely inhomogeneous impedance profile that imposes an effective field discontinuity, controlling the transverse phase distribution over a surface. Such impedance surfaces can be designed with extremely subwavelength thickness, forming the foundation for a transformation-optics paradigm over two dimensions. Passive printed antenna arrays are at the basis of planar microwave lenses and mirrors that can replace inconvenient bulky mirrors in reflector antennas and, at the same time, can enable fully-electric beam steering by exploiting appropriately engineered surface resonances. The simplicity of surface-based wave manipulation at RF has inspired scientists to extend these concepts to shorter wavelengths, up to the infrared and visible spectrum, using artificial arrays of subwavelength polarizable particles, or metasurfaces [14]-[17]. In analogy to RF patterned surfaces, optical metasurfaces can be fruitfully modeled with a local averaged surface impedance [18]. However, different from their RF counterparts, metasurfaces can largely benefit from plasmonic effects, allowing their surface constituents, i.e., nanoantennas [19], to resonate over spatial scales much smaller than the free-space wavelength, providing a route to a much larger control of the transverse spatial resolution. Plasmonic metasurfaces have enabled the concept of reflect- and transmit-arrays to shorter wavelengths, under the assumption that a suitably tailored transverse phase discontinuity profile imparted over an ultrathin surface may redirect an impinging wave toward a new direction, depending on the lateral phase gradient [20]-[22]. The abrupt phase shift introduced by nanoantennas is exploited to compensate for the phase difference between the incident and desired wave profile, e.g., linear, circular, and hyperbolic scattering phases, to create tilted waves, vortex beams, and focusing lenses. The prospect of full control on the distribution of the scattered wave with a single ultrathin patterned surface has created excitement in the scientific community, and the initial proposals have been now extended to different frequency ranges, and numerous optimized surface elements have been studied to provide efficient (i.e. with almost unitary amplitude) full phase coverage in both reflection and transmission scenarios [23]-[27].

In this chapter, we raise the fundamental question of to what extent a phase gradient on a metasurface is sufficient to guarantee an ultimate control of its scattering signature. First, it is obvious that, different from volumetric metamaterials, a metasurface can transform a wavefront to another one only provided that both fields are solutions of the source-free wave equation in the background medium. With rigorous treatment, in this paper we show that it is not possible to funnel the incident wavefront into an arbitrary solution of choice if we are limited to using passive metasurfaces, and even basic functionalities, such as wave deflection, have fundamental limitations on the overall efficiency of the transformation process in the ultrathin limit. Second, we show that the optimal phase distribution that maximizes the transformation efficiency in the case of a passive surface drastically deviates from the simple phase correction recipe stemming from ray optics, and widely used in the current literature. This is particularly important for extreme cases, such as large-angle beam deflection or near-field focusing, for which metasurfaces can outperform conventional volumetric devices or gratings.

5.2 BEAM STEERING WITH IDEAL METASURFACES: ACTIVE VERSUS PASSIVE

5.2.1 General formulation

We start by considering the general problem of EM wave interactions with a transversely inhomogeneous metasurface of arbitrary profile, as shown in Fig. 5.1(a). We assume that the surface thickness is deeply subwavelength, $d/\lambda_0 \to 0$, where $\lambda_0 = 2\pi/k_0$ is the free space wavelength and k_0 is the corresponding wave number. The subwavelength thickness of the structure allows to describe it, in a local sense, by equivalent transverse surface electric and magnetic currents $\mathbf{J}_s$ and $\mathbf{M}_s$, forming local electric admittance $\mathbf{J}_s = \underline{\underline{\mathbf{Y}}}_e(\mathbf{r}) \cdot \mathbf{E}_t$, and magnetic impedance $\mathbf{M}_s = \underline{\underline{\mathbf{Z}}}_m(\mathbf{r}) \cdot \mathbf{H}_t$ tensors, related to the tangential components of the local fields over the surface [14],[18]. For simplicity, in the following we assume that the symmetries of the problem allow us to consider scalar impedances Y_e and Z_m for the excitation of interest. It is possible to characterize the surface also by its local reflection ($R = r(\mathbf{r})e^{j\phi_r(\mathbf{r})}$) and transmission ($T = t(\mathbf{r})e^{j\phi_t(\mathbf{r})}$) coefficients, defined assuming a uniform surface built with such local impedances and excited at normal incidence. As shown in Eq. (5.1), these quantities are directly related to Y_e and Z_m [28], and ϕ_r and ϕ_t are the phase distributions imparted on the reflected and transmitted waves at the metasurface interface, respectively. A lossless ultrathin surface has locally $r^2 + t^2 = 1$ or, equivalently, Y_e and Z_m are purely imaginary.

$$R = -\frac{2\left(\eta_0{}^2 Y_e - Z_m\right)}{\left(2+\eta_0 Y_e\right)\left(2\eta_0 + Z_m\right)}, T = -\frac{\left(-2+\eta_0 Y_e\right)}{\left(2+\eta_0 Y_e\right)} + \frac{2\left(\eta_0{}^2 Y_e - Z_m\right)}{\left(2+\eta_0 Y_e\right)\left(2\eta_0 + Z_m\right)}. \tag{5.1}$$

In order to highlight the potential and limitations of a gradient metasurface for wave transformation, we first consider an ideal planar metasurface whose elements can be engineered to locally provide unitary transmission, zero reflection, and a full control on the transmission phase, so that $\phi_t(\mathbf{r})$ can take any value between 0 and 2π over the surface. This implies that the metasurface can in principle impart any phase profile to the transmitted wave, with 100% local efficiency. In order to transform a normally incident plane wave $\mathbf{E}_i = \hat{y}E_0 e^{jk_0 z}$ into an obliquely transmitted wave $\mathbf{E}_t = \hat{y}E_0 e^{jk_0(-\sin(\theta_t)x+\cos(\theta_t)z)}$ propagating toward the angle θ_t in the xz -plane (anomalous refraction, a common target for gradient metasurfaces), the available literature has so far considered designs based on phase compensation, which requires that the metasurface provides a constant phase gradient $\phi_t(x) = -k_0 \sin(\theta_t)x$ [20]-[22]. This is at the basis of the so-called ‘generalized Snell’s law of refraction’, which allows challenging the usual refraction response at a transversely homogeneous interface.

We show in the following that this picture is inherently approximate, as it does not consider the relevance of impedance matching in the scattering process [29].

Changing the refraction angle from normal to oblique implies a different ratio of the transverse components of electric and magnetic fields on the surface, which in turn requires that the local transmission coefficient t should be different for local tangential electric and magnetic fields. In other words, contrary to the common assumptions in recent metasurface works, a passive-lossless surface whose sole role is to imprint a locally engineered linear momentum to the scattered wave, necessarily fails to generate a plane wave tilted toward an arbitrary direction with unitary efficiency, and the impedance mismatch is expected to grow for steeper angles. This is consistent with earlier papers analyzing linear gradient metasurfaces (see, e.g., [30]), which have commonly found a degradation of coupling efficiency as the steering angle grows away from the normal.

It is possible to rigorously derive the impedance requirements for a single ultrathin metasurface to transform an arbitrary impinging wavefront $(\mathbf{E}_i, \mathbf{H}_i)$ into the scattered waves $(\mathbf{E}_{1s}, \mathbf{H}_{1s})$ in region 1 and $(\mathbf{E}_{2s}, \mathbf{H}_{2s})$ in region 2, with the only assumption that all three field distributions are valid solutions of source-free Maxwell's equations in the respective regions. The averaged induced current distributions on the metasurface should be suitably designed to compensate for the field discontinuity across the interface [28], and surface admittance and impedance need to satisfy the boundary condition at each point on the surface [23],[31],

$$\begin{aligned} \hat{n} \times \left(\mathbf{H}_2 - \mathbf{H}_1\right)\Big|_S &= \frac{1}{2} Y_e \left(\mathbf{E}_{2t} + \mathbf{E}_{1t}\right)\Big|_S \\ \hat{n} \times \left(\mathbf{E}_2 - \mathbf{E}_1\right)\Big|_S &= -\frac{1}{2} Z_m \left(\mathbf{H}_{2t} + \mathbf{H}_{1t}\right)\Big|_S \end{aligned} . \tag{5.2}$$

Assuming that impinging and scattered fields are known, Eq. (5.2) formulates the exact isotropic metasurface boundary condition that allows converting the impinging wavefront into the desired reflected and transmitted waves, and the formulation may straightforwardly be extended to the anisotropic case when polarization coupling is present [32]-[33]. The subscript t represents the tangential field components in each region. The extracted electric admittance and magnetic impedance from (5.2) can be directly used in (5.1) to calculate the local reflection and transmission coefficients along the metasurface.

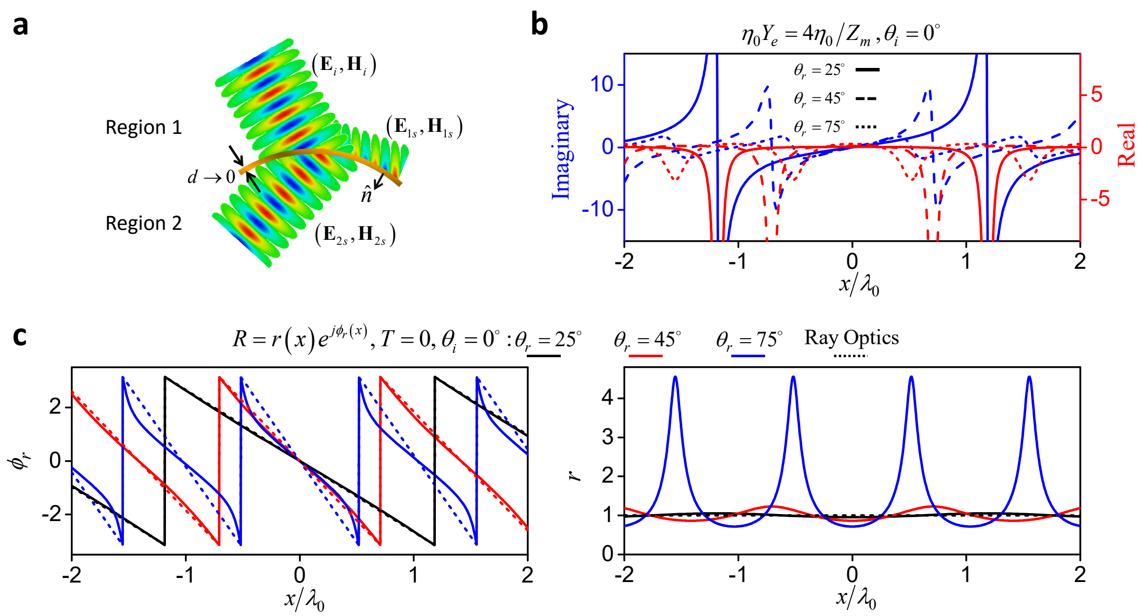

Figure 5.1 (a) An arbitrary incident wavefront is transformed into the desired scattering profile employing a transversely inhomogeneous metasurface with local distribution of loss and gain. (b) Metasurface impedance profile and (c) local reflection coefficient $R(x) = r(x)e^{j\phi_r(x)}$ required to convert a normally incident wave ($\theta_i = 0$ degrees) into refracted waves at $\theta_r = 25, 45, 75$ degrees. In each example, the amplitude of the reflected plane wave is $|A_r| = \sqrt{\cos\theta_i} / \sqrt{\cos\theta_r}$ to ensure that total incident and reflected powers are equal towards the normal direction. The real component of the surface admittance in panel (b) and non-unitary local reflection amplitudes in panel (d) indicate the requirement of loss/gain modulation of the surface.

In the particular case of a wave-bending metasurface, the incident and scattered fields are plane waves propagating in specified directions. As a basic example, we look into the case of redirecting an impinging plane wave toward the desired direction in reflection, with zero transmission. Incident and scattered fields are linearly polarized transverse-electric (TE) plane waves with wave vectors $\mathbf{k}_i = k_0\left(-\sin\left(\theta_i\right)\hat{x}+\cos\left(\theta_i\right)\hat{z}\right)$ and $\mathbf{k}_r = -k_0\left(\sin\left(\theta_r\right)\hat{x}+\cos\left(\theta_r\right)\hat{z}\right)$ in region 1, whereas the total fields are enforced to be zero in region 2 (Fig. 5.1(a)). The metasurface is located in the xz-plane as shown in the inset of Fig. 5.4(b). Following (5.2), the required electric surface admittance and surface magnetic impedance to realize this scattering signature are

$$\begin{aligned} Y_e &= 2\left.\frac{\hat{x}\cdot\left(\mathbf{H}_i+\mathbf{H}_{1s}\right)}{\hat{y}\cdot\left(\mathbf{E}_i+\mathbf{E}_{1s}\right)}\right|_{z=0} = \frac{2}{\eta_0}\frac{\cos\left(\theta_i\right)e^{-jk_0\sin(\theta_i)x}-A_r\cos\left(\theta_r\right)e^{-jk_0\sin(\theta_r)x}}{e^{-jk_0\sin(\theta_i)x}+A_r e^{-jk_0\sin(\theta_r)x}} \\ Z_m &= 2\left.\frac{\hat{y}\cdot\left(\mathbf{E}_i+\mathbf{E}_{1s}\right)}{\hat{x}\cdot\left(\mathbf{H}_i+\mathbf{H}_{1s}\right)}\right|_{z=0} = 2\eta_0\frac{e^{-jk_0\sin(\theta_i)x}+A_r e^{-jk_0\sin(\theta_r)x}}{\cos\left(\theta_i\right)e^{-jk_0\sin(\theta_i)x}-A_r\cos\left(\theta_r\right)e^{-jk_0\sin(\theta_r)x}} \end{aligned}, \tag{5.3}$$

in which A_r is the amplitude of the electric field in the reflected plane wave, normalized to the incident one. Based on the general condition (5.2), it is possible to show that total reflection is possible if and only if $Y_e Z_m = 4$ which is indeed satisfied by (5.3). In this regard we notice that with the intention of arbitrarily manipulating the reflected wave with zero transmission, Eq. (5.2) reduces to,

$$\begin{aligned} \hat{n}\times\left(\mathbf{H}_1\right)\Big|_S &= -\frac{1}{2}\underline{\underline{\mathbf{Y}}}_e\cdot\left(\mathbf{E}_{1t}\right)\Big|_S \\ \hat{n}\times\left(\mathbf{E}_1\right)\Big|_S &= \frac{1}{2}\underline{\underline{\mathbf{Z}}}_m\cdot\left(\mathbf{H}_{1t}\right)\Big|_S \end{aligned}, \tag{5.4}$$

with the total fields set at zero inside region 2. We set the local right-handed coordinate system on the surface as $\left(\hat{n},\hat{t}_1,\hat{t}_2\right)$, with $\hat{n}$ indicating the normal unit vector as shown in Fig. 5.1(a), and $\left(\hat{t}_1,\hat{t}_2\right)$ are the two orthogonal transverse unit vectors along the surface. In the most general format, the surface may be anisotropic with admittance dyadic profile

$\underline{\underline{\mathbf{Y}}}_e = Y_{e,t_1}\hat{t}_1\hat{t}_1 + Y_{e,t_2}\hat{t}_2\hat{t}_2$ and impedance dyad of $\underline{\underline{\mathbf{Z}}}_m = Z_{m,t_1}\hat{t}_1\hat{t}_1 + Z_{m,t_2}\hat{t}_2\hat{t}_2$. Rewriting and decomposing Eq. (5.4) we get,

$$\begin{aligned} Y_{e,t_2} &= -2\frac{\hat{t}_1 \cdot \mathbf{H}_1}{\hat{t}_2 \cdot \mathbf{E}_1}, Z_{m,t_1} = -2\frac{\hat{t}_2 \cdot \mathbf{E}_1}{\hat{t}_1 \cdot \mathbf{H}_1} \\ Y_{e,t_1} &= +2\frac{\hat{t}_2 \cdot \mathbf{H}_1}{\hat{t}_1 \cdot \mathbf{E}_1}, Z_{m,t_2} = +2\frac{\hat{t}_1 \cdot \mathbf{E}_1}{\hat{t}_2 \cdot \mathbf{H}_1} \end{aligned} . \tag{5.5}$$

Equation (5.5) demonstrates the relation $Y_{e,t_2} Z_{m,t_1} = Y_{e,t_1} Z_{m,t_2} = 4$ between electric and magnetic properties of a general surface operating in reflection mode. In an isotropic surface, this condition simplifies to $Y_e Z_m = 4$, as noted. Under this condition, the local transmission coefficient T , as defined in Eq. (5.1), is also zero along the surface.

Fig. 5.1(b) shows the required distribution of Y_e and Z_m along the metasurface that ensures anomalous reflection with unitary power efficiency, plotted for normal incidence and various reflection angles. Following the periodicity of the incident and scattered waves, the attained surface holds a superlattice periodicity X along the x-axis, as shown in Fig. 5.1(b), related to the incident and reflection angles by $X = \left|\lambda_0 / \left(\sin\theta_r - \sin\theta_i\right)\right|$ [24]. The reflected wave, hence, corresponds to the first diffraction order of the gradient metasurface. To ensure unitary efficiency, the relative amplitude of the reflected wave should also be $\left|A_r\right| = \sqrt{\cos\theta_i} \big/ \sqrt{\cos\theta_r}$ in (5.3), so that incoming and outgoing power flows are equal, i.e. $\hat{z} \cdot \mathbf{P}_{incident} = -\hat{z} \cdot \mathbf{P}_{reflected}$.

In this regard we notice that a regular homogenous interface, such as the boundary between two plain dielectrics, supports simple specular reflection. This means that, when illuminated by a plane wave, any percentage of power reflected by such interface is funneled into the single wave propagating away from the surface in the mirror direction. This wave is highlighted as the $n = 0$ arrow in Fig. 5.2. When the interface is not homogenous, the scattered wave is in general a combination of all plane waves in the radiation continuum, and for a periodic structure, their integral sum straightforwardly reduces to discrete waves propagating toward specific directions (the discrete diffraction orders). As pointed out previously, a surface designed to transform an incident plane wave into another plane wave with different wave vector is inherently periodic. Therefore, one appropriate measure to determine the performance of the surface is to calculate the percentage of power coupled to each of these diffraction orders when illuminating the structure. This is applied to later examples in this and next chapters. For instance in Fig. 5.4 we summed over all undesired orders and compared it to the power coupled into the intended one . In our frequency range of interest, each surface couples non-negligible power to a maximum of three orders $n = 0, \pm 1$, with $n = +1$ referring to the desired plane wave (solid arrows in Fig. 5.4(b) and Fig. 5.2).

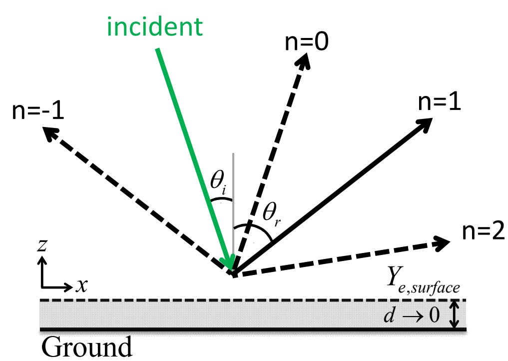

Figure 5.2: Trajectory of a plane wave illuminating a periodic gradient metasurface with incident wave vector $\mathbf{k}_i = k_0\left(-\sin\left(\theta_i\right)\hat{x} + \cos\left(\theta_i\right)\hat{z}\right)$, and the desired reflected plane wave (solid arrows) with wave vector $\mathbf{k}_r = -k_0\left(\sin\left(\theta_r\right)\hat{x} + \cos\left(\theta_r\right)\hat{z}\right)$. Dashed arrows indicate other allowed scattering directions in such configuration. The metasurface is realized as an electric admittance surface mounted in a subwavelength distance from the ground plane.

The required surface properties are extracted from Eq. (5.2) and Eq. (5.4), considering the appropriate distribution of incident and scattered waves as,

$$\begin{aligned}
\left(\mathbf{E}_i, \mathbf{H}_i\right) &= \left(\hat{y}, \frac{\hat{x}\cos\theta_i + \hat{z}\sin\theta_i}{\eta_0}\right) E_0 e^{-j\sin\theta_i k_0 x} e^{j\cos\theta_i k_0 z} \\
\left(\mathbf{E}_{1s}, \mathbf{H}_{1s}\right) &= A_r \left(\hat{y}, \frac{-\hat{x}\cos\theta_r + \hat{z}\sin\theta_r}{\eta_0}\right) E_0 e^{-j\sin\theta_r k_0 x} e^{-j\cos\theta_r k_0 z}
\end{aligned}, \tag{5.6}$$

where the term $A_r = \sqrt{\cos\theta_i} / \sqrt{\cos\theta_r}$ takes care of ensuring that the power reflected in the direction normal to the surface is equal to the impinging power, assuming TE illumination. The averaged total power supplied to the surface can be expressed as $\overline{\mathrm{P}}_{surface} = -\frac{1}{2X}\int_X \left(Y_e^* \left|\mathbf{E}_t\right|^2 + Z_m \left|\mathbf{H}_t\right|^2\right) dx$ [34], in which $X = \left|\lambda_0 / \left(\sin\theta_r - \sin\theta_i\right)\right|$ is the surface superlattice. After some algebraic simplification, the supplied electric and magnetic power can be written in terms of the incident and scattered angles as,

$$\overline{\mathrm{P}}_{surface,e} = \overline{\mathrm{P}}_{surface,m} = -\frac{E_0^2}{4\eta_0 X}\int_X \sqrt{\cos\theta_i \sec\theta_r}\left(\cos\theta_i e^{-\frac{2j\pi x}{X}} - \cos\theta_r e^{\frac{2j\pi x}{X}}\right) dx, \tag{5.7}$$

both equal to zero. This property further verifies that the metasurface as a whole does not pump any power into the scattered wave or absorb any part of it, but rather transforms the incident wave to the desired field by proper, locally distributed, balanced absorption/gain. The averaged net power emerging from the surface is equivalently zero in this scenario:

$$\overline{\mathrm{P}}_{surface} = \frac{1}{X}\int_X \left(\mathrm{Re}\left(\hat{z}\cdot\mathbf{P}_{total}\right)_{z\to 0^+}\right) dx = -\frac{E_0^2\left(\cos\left(\theta_i\right) - \left|A_r\right|^2\cos\left(\theta_r\right)\right)}{2\eta_0} = 0. \tag{5.8}$$

Equation (5.8) also verifies that for $\left|A_r\right| = \sqrt{\cos\theta_i} / \sqrt{\cos\theta_r}$, the net power generated by the surface is zero and wave bending efficiency is 100%.

Interestingly, the required surface to achieve unitary efficiency always involves local loss and gain (passive and active portions correspond to simultaneous positive and negative values of both $\mathrm{Re}\left[Y_e\right]$ and $\mathrm{Re}\left[Z_m\right]$ in Fig. 5.1(b)), and it is not passive in a local sense, consistent with Huygens transmit-arrays introduced in [23]. This is expected, since the total power emerging right above the metasurface, $\mathrm{Re}\left(\hat{z}\cdot\mathbf{P}_{total}(x)\right) = -1/2\,\mathrm{Re}\left(E_y H_x^*\right)\Big|_{z\to 0^+}$, can be explicitly calculated from the required field distribution, superposition of the impinging and reflected waves,

$$\mathrm{Re}\left(\hat{z}\cdot\mathbf{P}_{total}(x)\right) = \frac{E_0^2}{2\eta_0}\times$$
$$\left[\left|A_r\right|^2\cos(\theta_r)-\cos(\theta_i)+\left|A_r\right|\left(\cos(\theta_r)-\cos(\theta_i)\right)\cos\left(\angle A_r + k_0\left(\sin(\theta_i)-\sin(\theta_r)\right)x\right)\right] \quad ,(5.9)$$

whose value oscillates from positive to negative values along x. The only exception is $\theta_r = \pm\theta_i$ or accordingly for the specular and retro-reflection, for which $\mathrm{Re}\left(\hat{z}\cdot\mathbf{P}_{total}(x)\right) = 0$ everywhere. This is expected, as the incident and reflected local impedances are matched for these special cases, and interestingly a passive-lossless metasurface is sufficient to fully transform the incident wave (see Eq. (5.17)). Apart from this condition, the optimal surface described by Eq. (5.2) necessarily requires that the local power absorption/gain oscillates around zero along x. Note that by optimal, here and in the following, we mean the surface that allows realizing conversion to the desired wavefront with unitary efficiency.

It follows that the only way to keep a unitary conversion efficiency towards the desired direction with a steering ultrathin metasurface is to locally absorb and pump a portion of the incident power in different regions within the superlattice. At the same time, as we mentioned the surface remains globally lossless, in the sense that the averaged net power supplied by the surface $\overline{\mathrm{P}}_{surface} = -\frac{1}{2S}\int_S Y_e^*\left|\mathbf{E}_t\right|^2 ds + \int_S Z_m\left|\mathbf{H}_t\right|^2 ds$ is identically zero, as required by the choice of $\left|A_r\right|$ to ensure unitary power efficiency. This raises interesting connections with the field of parity-time symmetry and balanced loss and gain [35]-[37], a feature that has been recently shown to open exciting opportunities in optics. Highly efficient steering metasurfaces appears to also require a specific balance of loss and gain. After transforming the derived impedance profile into local reflection and transmission coefficients using (5.1), we find the local phase and amplitude profiles required to create the desired wavefront deflection with an ultrathin metasurface,

$$R(x) = r(x) e^{j\phi_r(x)} = -1 + \left. \frac{2\hat{y} \cdot (\mathbf{E}_i + \mathbf{E}_{1s})}{\hat{y} \cdot (\mathbf{E}_i + \mathbf{E}_{1s}) + \eta_0 \hat{x} \cdot (\mathbf{H}_i + \mathbf{H}_{1s})} \right|_{z=0}, T = 0. \quad (5.10)$$

These are visualized in Fig. 1(c), which shows the local reflection phase $\phi_r(x)$ and amplitude $r(x)$ at the metasurface, highlighting alternating regions with local loss and gain, with $r > 1$ and $r < 1$, respectively. While unitary power conversion efficiency is possible only using local gain and loss elements, it is interesting that also the phase requirements are quite different from the simple linear distribution predicted by ray optics.

Eqs. (5.9)-(5.10) and Fig. 5.1 show the first important conclusion of our analysis: efficient beam steering towards arbitrary angles with an ultrathin surface cannot be achieved using passive-lossless linear phase profiles. Interestingly, when the anomalous reflection angle is close to specular reflection, linear phase compensation along the surface provides a very good approximation for the optimal surface. However, as we increase the deflection angle, and we get into the regime in which metasurfaces can outperform conventional gratings in terms of efficiency, thanks to their subwavelength control of the transverse resolution, our rigorous solution significantly deviates both in amplitude and phase from the linear phase approximation commonly used in the literature.

5.2.2 All-electric implementation of metasurfaces

Prior to this point, we have assumed ideal metasurfaces with negligible thickness that possess simultaneous electric and magnetic surface properties. In general, the desired reflection profile $R(x)$ and zero transmission may be implemented without relying on a series impedance distribution $Z_m\left(x\right)$, which would inherently require magnetic effects, by simply using a gradient non-magnetic surface admittance backed by a ground plane [24],[30]-[31], as schematically shown in Fig. 5.2. It is possible to prove that in the limit of subwavelength thickness, $d/\lambda_0 \to 0$, a grounded isotropic surface with $Y_{e,surface} = Y_e/2 + j\,n_{sub}\cot\left(n_{sub}k_0 d\right)/\eta_0$ is equivalent to a reflecting isotropic magneto-electric interface. Here n_{sub} is the refractive index of substrate material shown by gray color in Fig. 5.2. To prove this property we notice that in addition to its local surface admittance and impedance, any surface can be equivalently characterized by its local reflection and transmission coefficients, R and T, defined in (5.1) for an isotropic surface. These scattering parameters are defined for a strictly periodic metasurface and under normal plane wave illumination. For an strictly reflecting metasurface (5.1) further simplifies to

$$R_{\mathrm{TE}} = 1 - \frac{4\eta_0}{2\eta_0 + Z_{m,xx}}, R_{\mathrm{TM}} = 1 - \frac{4\eta_0}{2\eta_0 + Z_{m,yy}}, T_{\mathrm{TE}} = T_{\mathrm{TM}} = 0, \tag{5.11}$$

in which we generalized the surface to be anisotropic along x and y directions. The grounded metasurface shown in Fig. 5.2 can be analogously described by its local scattering parameters following conventional transmission-line analysis. The scattering parameters for normal incidence of this surface can be written as,

$$
\begin{aligned}
R_{surface,\mathrm{TE}} &= \frac{1-\eta_0 Y_{e,surface,yy} + jn_{sub}\cot\left(n_{sub}k_0 d\right)}{1+\eta_0 Y_{e,surface,yy} - jn_{sub}\cot\left(n_{sub}k_0 d\right)} \\
R_{surface,\mathrm{TM}} &= \frac{1-\eta_0 Y_{e,surface,xx} + jn_{sub}\cot\left(n_{sub}k_0 d\right)}{1+\eta_0 Y_{e,surface,xx} - jn_{sub}\cot\left(n_{sub}k_0 d\right)}
\end{aligned}
, \tag{5.12}
$$

and it can be straightforwardly shown that the grounded structure is equivalent to free-standing magneto-electric metasurface under the general condition ,

$$
\begin{aligned}
Y_{e,surface,yy} &= \frac{Y_{e,yy}}{2} + j\frac{n_{sub}\cot\left(n_{sub}k_0 d\right)}{\eta_0} \\
Y_{e,surface,xx} &= \frac{Y_{e,xx}}{2} + j\frac{n_{sub}\cot\left(n_{sub}k_0 d\right)}{\eta_0}
\end{aligned}
. \tag{5.13}
$$

which simplifies to $Y_{e,surface} = Y_e/2 + j\,n_{sub}\cot\left(n_{sub}k_0 d\right)/\eta_0$ if the surface is isotropic. Provided that the grounded structure has deeply subwavelength thickness, it effectively models a single physical interface, and its in-plane characteristics are fully described by means of normal reflection and transmission coefficients [15], as illustrated in (5.12). Yet, it is important to evaluate the effects of finite thickness of the structure, which allows out-of-plane polarizability under oblique excitations. In this regard, we update Eq.(5.12) for an arbitrary oblique illumination when the incident plane wave is tilted by an angle ϑ from the normal direction. For TE illumination R and T read,

$$
R_{surface,\mathrm{TE}}\left(\vartheta\right) = \frac{\cos\vartheta - \eta_0 Y_{e,surface,yy,yy} + jn_{sub}\cot\left(n_{sub}k_0 d\cos\vartheta\right)\cos\vartheta}{\cos\vartheta + \eta_0 Y_{e,surface,yy,yy} - jn_{sub}\cot\left(n_{sub}k_0 d\cos\vartheta\right)\cos\vartheta}. \tag{5.14}
$$

Correspondingly, we calculate the scattering parameters of the infinitely thin magneto-electric surface under same oblique illumination,

$$
R_{\mathrm{TE}}\left(\vartheta\right) = 1 - \frac{4\eta_0}{2\eta_0 + Z_{m,xx}\cos\vartheta}. \tag{5.15}
$$

Solving (5.14) and (5.15) for electric sheet admittance of the grounded structure we straightforwardly get,

$$Y_{e,surface,yy} = \frac{Y_{e,yy}}{2} + j\frac{n_{sub}\cot\left(n_{sub}k_0 d\cos\vartheta\right)\cos\vartheta}{\eta_0}, \tag{5.16}$$

which simplifies to the angle-independent solution $Y_{e,surface,yy} = Y_{e,yy}/2 + j/\left(\omega\mu_0 d\right)$ after replacing the cotangent function with its Laurent expansion in the small argument limit (i.e. $d \ll \lambda_0/n_{sub}$). In other words, when (5.13) satisfied, the two systems with magneto-electric metasurface and all-electric grounded metasurface follow the same scattering response under arbitrary illumination, and the effects of finite thickness are negligible for TE polarized waves. For TM illumination, the conditions are more stringent. Following a similar procedure, the orthogonal components of the sheet electric admittance becomes $Y_{e,surface,xx} = Y_{e,xx}/2 + j/\left(\omega\mu_0 d\cos^2\vartheta\right)$, and the surface profile is in general angle-dependent. This condition is the result of enhanced light-matter interactions at the PEC interface for an oblique TM wave (which has a large magnetic component parallel to surface), and can be addressed by replacing the PEC mirror in Fig. 5.2 with a metamaterial perfectly magnetic (PMC) mirror [38]. It can be straightforwardly shown that by employing the PMC mirror, the required electric admittance of the surface becomes angle-independent and equals $Y_{e,surface,xx} = Y_{e,xx}/2 - j\omega\varepsilon_0 d n_{sub}^2$.

After calculating $Y_{e,surface}$ based on the derived formulas the grounded structures are simulated in COMSOL Multiphysics 4.4 in a periodic setup to calculate the percentage of power coupled to each Floquet harmonic or the scattering field distribution under arbitrary illumination. In the simulations in this chapter no frequency dispersion is embedded in $Y_{e,surface}$, i.e., $Y_{e,surface}$ is assumed constant over the entire spectral range.

This technique would significantly facilitate the synthesis of the desired response in a practical design, especially in the optical range for which magnetic responses are typically weak. We also note that there is a wide range of metasurface configurations that may physically implement high-resolution surface elements in various setups, from microwave to infrared and optical frequencies. Plasmonic and dielectric nanoantennas, composite particles, printed circuits, multilayered meta-atoms, and wire antennas [20],[23]-[26],[39]-[41] provide a fertile ground for local phase (and also amplitude) manipulation. We will extensively look into plasmonic-dielectric metamolecules in the next chapter. In addition, in section 5.3.2 we will implement one of our metasurfaces based on grounded, microwave capacitor-inductor pairs.

5.2.3 Passive metasurfaces

In the following, we focus on passive metasurfaces in order to avoid the requirement of active elements, which may be difficult to realize and may introduce challenging stability limitations. First, it is interesting to notice that, while the previous analysis shows that balanced gain and loss is necessary to achieve ideal energy steering with a metasurface, it may still be possible to route all the scattered energy towards a preferred direction with proper design. The requirement of unitary power efficiency implies that the power density steered towards the desired angle grows as $\cos\theta_i / \cos\theta_r$, simply following the projection of the wave vector to the surface normal. If we allow the scattered power in the normal direction to be less than the incident one, the surface will provide a net absorption, $\mathrm{Re}\left(\overline{\mathrm{P}}_{surface}\right) < 0$, up to the point for which the ideal surface would exhibit only lossy components (i.e., at all points $r \leq 1$), implementing a distributed loss pattern over the surface similar to [42].

Interestingly, as we show in the following, selective coupling to the desired diffraction order can be achieved with a passive-lossy surface, provided that the relative amplitude of the reflected wave is equal or lower than $|A_r|_{\max} = \min\left(1, \cos(\theta_i)/\cos(\theta_r)\right)$, valid for both TE and TM waves.

To prove this formula we notice that the local passivity of the metasurface can be enforced considering either its local admittance, i.e., $\forall x, \mathrm{Re}\left(Y_e(x) \,\&\, Z_m(x)\right) > 0$, or the local emerging power, i.e., $\forall x, \mathrm{Re}\left(\hat{z}\cdot\mathbf{P}_{total}\right)_{z\to 0^+} < 0$. The first condition implies that, if the surface possesses any resistive component, it must be positive to avoid local power generation. The second condition, equivalently, requires that at no point along the surface, the total power flows toward the outgoing direction from the surface. This means that, locally, the metasurface is either lossless (corresponding to $r = 1$), or absorptive (corresponding to $r < 1$). The local emerging power on the surface is found in (5.9). Enforcing $\mathrm{Re}\left(\hat{z}\cdot\mathbf{P}_{total}\right)_{z\to 0^+} < 0$ and solving (5.9), the maximum acceptable reflection amplitude is found to be $|A_r|_{\max} = \min\left(1, \cos(\theta_i)/\cos(\theta_r)\right)$. The conversion efficiency of the surface under this condition may be found by calculating the incident and reflected power along the z-direction

$$\eta = \frac{\mathrm{Re}\left(\hat{z}\cdot\mathbf{P}_{reflected}\right)}{\mathrm{Re}\left(-\hat{z}\cdot\mathbf{P}_{incident}\right)} = \frac{\cos\theta_r}{\cos\theta_i}|A_r|^2 = \min\left(\frac{\cos\theta_r}{\cos\theta_i}, \frac{\cos\theta_i}{\cos\theta_r}\right), \tag{5.17}$$

consistent with the reciprocity theorem [43]. A similar argument holds for TM waves where we have

$$\begin{aligned}\left(\mathbf{E}_i, \mathbf{H}_i\right) &= \left(-\hat{x}\cos\theta_i - \hat{z}\sin\theta_i, \frac{\hat{y}}{\eta_0}\right) E_0 e^{-j\sin\theta_i k_0 x} e^{j\cos\theta_i k_0 z} \\ \left(\mathbf{E}_{1s}, \mathbf{H}_{1s}\right) &= A_r\left(\hat{x}\cos\theta_r - \hat{z}\sin\theta_r, \frac{\hat{y}}{\eta_0}\right) E_0 e^{-j\sin\theta_r k_0 x} e^{-j\cos\theta_r k_0 z}\end{aligned}, \tag{5.18}$$

with $A_r = \sqrt{\cos\theta_i} / \sqrt{\cos\theta_r}$. The general format of power, as presented in equations (5.7) through (5.8), also holds for the TM polarization of incident and scattered waves with same upper bounds on the scattering amplitude.

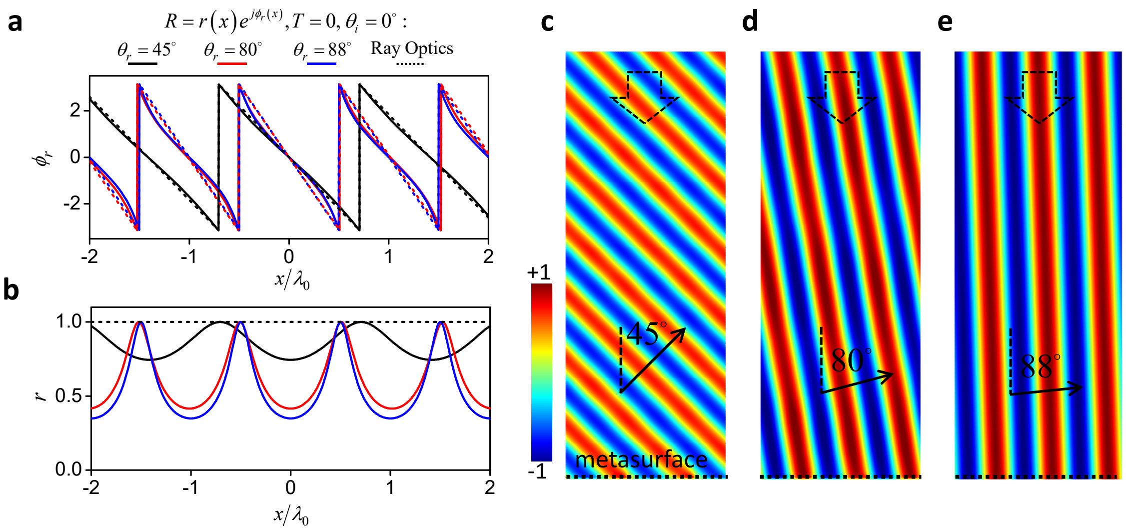

Figure 5.3: (a)-(b) Local reflection coefficient $R(x) = r(x)e^{j\phi_r(x)}$ required to convert a normally incident wave ($\theta_i = 0$ degrees) into (a) refracted waves at $\theta_r = 45, 80, 88$ degrees while preserving its amplitude, i.e. $|A_r| = 1$. Distribution of the scattered magnetic field H_z, for $\theta_i = 0$ and (c) $\theta_r = 45,\ d = \lambda_0/20$, (d) $\theta_r = 80,\ d = \lambda_0/20$, (e) $\theta_r = 88,\ d = \lambda_0/200$, for the passive-lossy surfaces illustrated in (a) and (b). Parts (c)-(e) correspond to overall efficiencies of 70.7, 17.36, and 3.49%, respectively. All plots are normalized to the amplitude of the incident magnetic field and the metasurfaces are realized in an all-electric grounded setup, as shown in the inset of Fig. 5.4(b).

This analysis indicates that, using Eq. (5.3), it is possible to design a passive-lossy surface that steers a normally incident beam exclusively to an arbitrary direction of choice, while preserving the amplitude of electric and magnetic fields, i.e., $|A_r| = 1$. This surface would necessarily lose a portion of the impinging power since the outgoing power is less than the impinging one, but scattering to other diffraction orders can be made identically zero at the cost of efficiency. Figures 5.3(a,b) illustrate the required reflection phase and amplitude for three reflection angles in this scenario. As expected, the local reflection amplitude varies along the surface, yet, its maximum value is limited to unity, $r_{\max} = 1$. In accordance to our previous discussion, as the reflection angle increases, the required local reflection phase along the surface departs from the linear approximation.

Using the calculated local reflections in Fig. 5.3(a,b) and based on the implementation approach described in section 5.2.2, Fig. 5.3(c,e) show the corresponding normal component of the magnetic field distribution (which is present only in the reflected beam), showing full coupling towards the desired direction, and zero scattering toward unwanted directions. The synthesis of amplitude modulation along the surface, as in Fig. 2b, may be achieved either by varying locally absorbing elements, or by using anisotropic inclusions and modulating the cross-polarization coupling or loss, as recently suggested in [42] and [44], to simultaneously realize desired amplitude and phase modulation with a metasurface.

The designs of Fig. 5.3 provide the maximum coupling efficiency to achieve exclusive scattering in a desired direction of choice with a passive-lossy metasurface. As described in the caption, the efficiency may become drastically low for large steering angles (an efficiency of 3.49% is available for a steering angle of 88 degrees), which may not be desirable or practical. These results, however, show again the relevance of going beyond the ray optics approximation, and properly tailor amplitude and phase of the local reflection coefficient to design efficient gradient metasurfaces. Yet, in several applications it may be important to maximize the amount of power coupled towards the desired direction with a lossless surface, even though this may require coupling a small portion of it towards other diffraction orders [45]. Since we proved that no passive metasurface can achieve unitary power efficiency beam steering in near- and far-field, we explore next what impedance profile is needed to boost its overall coupling. In such case, loss over the surface should be avoided, and we focus therefore on lossless impedance profiles.

Considering normal incidence, Fig. 5.4 shows the simulated power distribution scattered from lossless surfaces designed to steer towards $\theta_r = 45, 80, 88$ degrees at the design frequency ω_0, while the response considers the natural frequency dispersion of the grounded metasurface related to the finite distance between the surface and ground plane. Solid lines indicate the percentage of incident power coupled into the desired diffraction order, while dashed lines indicate the portion of power scattered into other orders, based on the superlattice periodicity of the beam steering surface (Fig. 5.1(b,c)). The black lines refer to the case in which the structure is designed to impart the phase profile extracted from (5.10), as in Fig. 5.1(c), while the local reflection amplitude is unitary, i.e. $R = 1e^{j\phi_r(x)}$. As we discussed above, the imparted phase gradient in this case is different from the phase difference between incident and reflected waves, especially for steep deflection angles. The blue curves refer to the case in which the metasurface is designed by simply discarding the real part of the impedance profiles in Fig. 5.1 (b), i.e., $Y_{e,surface}$ is replaced with $j\,\mathrm{Im}\left[Y_{e,surface}\right]$, and thus the reflection amplitude is once more unitary. Finally, the red curves refer to the case when the linear phase predicted from ray-optics is imprinted over the surface, as in most conventional metasurface designs.

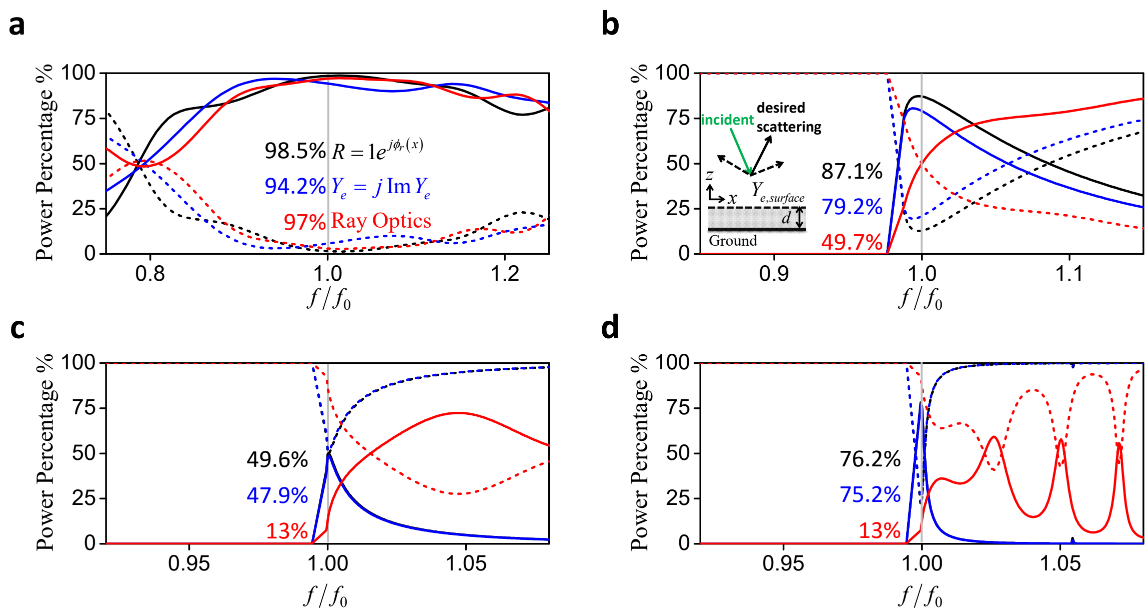

Figure 5.4: Frequency variation of the power reflected into the desired diffraction order for $\theta_i = 0$ and (a) $\theta_r = 45,\ d = \lambda_0/20$, (b) $\theta_r = 80,\ d = \lambda_0/20$, (c) $\theta_r = 88,\ d = \lambda_0/50$, (d) $\theta_r = 88,\ d = \lambda_0/200$. The inset shows the geometry of an all-electric grounded metasurface. Solid lines indicate the percentage of power coupled into the desired direction. All examples correspond to passive-lossless metasurfaces with different approximations indicated in the inset of panel (a).

Quite predictable from our previous discussions, for a deflection angle $\theta_r = 45$ degree, the constraints on loss/gain are moderate, and all cases provide very large conversion efficiencies. Yet, as the deflection angle increases, the linear phase approach fails to follow the desired scattering profile, and at $\theta_r = 80$ degrees and 88 degrees only 50% and 13% of power is coupled to the desired directions, respectively. With the phase profile retrieved from Eq. (5.10), on the other hand, more than 87% and 50% efficiency can be attained. Pushing down the thickness of the structure, the reflecting surface better mimics a metasurface, and the coupling efficiency to $\theta_r = 88$ degree grows to over 76%, as shown in Fig. 3d. Despite the clear difference between the approximate phase profile and our approach, both profiles are quite smoothly varying

(Fig. 5.1(c)) and the coupling efficiency is predicted to be robust to spatial discretization of the surface profile, even for large deflection angles, as we study in the next section. Clearly, for larger angles the superlattice footprint shrinks and proper quantization requires smaller surface granularities to maintain high efficiency. While no passive ultrathin surface may provide unitary power efficiency, a design that considers the impedance mismatch of the deflected wave makes indeed possible to steer a significant portion of the impinging wave towards an arbitrary angle, in both near- and far-fields, well beyond the limits of conventional gratings.

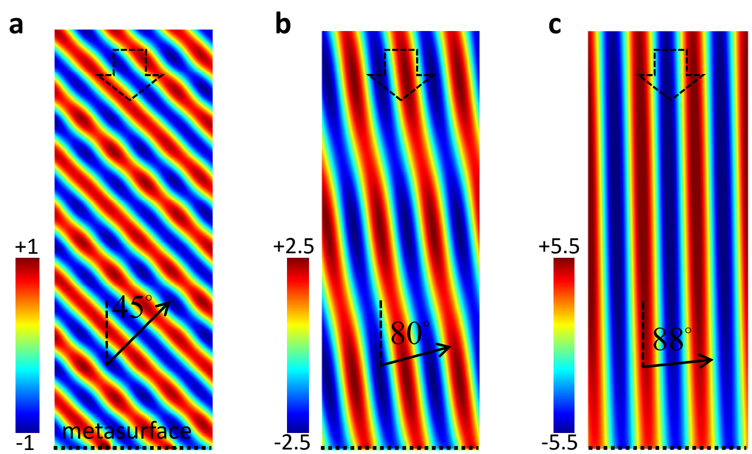

Figure 5.5: Distribution of the scattered magnetic field H_z, for $\theta_i = 0$ and (a) $\theta_r = 45,\ d = \lambda_0/20$, (b) $\theta_r = 80,\ d = \lambda_0/20$, (c) $\theta_r = 88,\ d = \lambda_0/200$, for the lossless approximation scenario. All plots are normalized to the amplitude of the incident magnetic field and parts (a)-(c) correspond to overall power conversion efficiencies of 98.5, 87.1, and 76.2%, respectively. The loss/gain profile of the optimal metasurface is approximated by its local reflection phase, i.e. $R(r) = 1e^{j\phi_r(x)}$.

The striking features of the proposed wave shaping metasurfaces may be better appreciated by investigating the field distributions plotted in Fig 5.5, corresponding to the designs in Fig. 5.4(a,b,d). Still relying on lossless gradient metasurfaces, and without ad-hoc optimization but simply following Eq. (5.2) and neglecting the amplitude modulation, we are able to efficiently rotate the incident wave vector (normal) toward extremely oblique angles, with minimal unwanted scattering. The key factor to achieve these close-to-optimal efficiencies is to go beyond the ray approximation and linear phase gradients, and instead to engineer the phase distribution following the previous formulation.

Imparting the phase profile extracted from (5.10) also allows us to go beyond the maximum efficiencies attainable from multimode Huygens metasurfaces [29],[40]. Multimode metasurfaces rely on the presence of one or more additional scattering modes to ensure surface passivity, and they may suffer from low efficiencies and a large number of evanescent modes close to the metasurface, particularly at large deflection angles. Designing the metasurface in the near-field, however, allows us to create efficient wave-shaping metasurfaces that maintain their performance even in the proximity of the surface. This property allows achieving complex near-field operations, such as near-field focusing, as discussed in section 5.5.

5.3 EFFECT OF REALISTIC APPROXIMATION OF THE IDEAL METASURFACE PROFILE

5.3.1 Discretization

The nonlinear, relatively fast-varying phase profiles in Fig. 5.1(c) raise important questions regarding the stability of the response to surface discretization, which may be necessary in a practical implementation. To investigate this effect, we design, based on the previous formulation, a metasurface reflect-array to convert a normally incident plane wave into a plane wave propagating towards $\theta_r = 75$ degrees, with minimal coupling to spurious modes in near- and far-field. The reflection phase and amplitude of this surface are shown as solid blue lines in Figs. 5.1(c,d). Each period of the surface is then divided into N_Q segments, where we set $N_Q = 4,8,16$, and we enforce unitary local reflection coefficient, implementing a passive lossless approximation of the ideal metasurface. Fig. 5.6(a) illustrates the spatial distribution of the surface electric admittance $Y_{e,surface}$ over one period of the grounded metasurface (shown in Fig. 5.4(b)), calculated for $N_Q = 8$ and $d = \lambda_0/20$. The corresponding continuous and quantized local reflection phases on the surface are also shown in Fig. 5.6(b). Analogous to the examples provided in section 5.2, full-wave simulations of the periodic setup are used to evaluate the percentage of power coupled toward each Floquet harmonic, shown in Fig. 5.6(c). For easier comparison, we also report the efficiency of the continuous (non-quantized) surface in the same panel with dashed lines.

We observe over 94%, 90% (shown in Fig. 5.6(c)), and 87% coupling efficiency toward the desired direction, respectively for $N_Q = 4, 8 \,\&\, 16$. Quite interestingly, the original continuous gradient surface provides 85% overall efficiency and the quantized profiles appears to be closer to the best possible profile for a passive lossless wave-bending metasurface. This improved performance is associated with the elimination of singular impedance values due to the discretization of the impedance profile, and it appears quite favorable for experimental implementation of these surfaces. In addition, the stability of the response to a rough discretization implies that, with the implementation of the local impedances in a realistic setup, one can expect increasingly improved performance for metasurfaces designed based on our analytical solution in comparison to those designed based on the ray optics approximation.

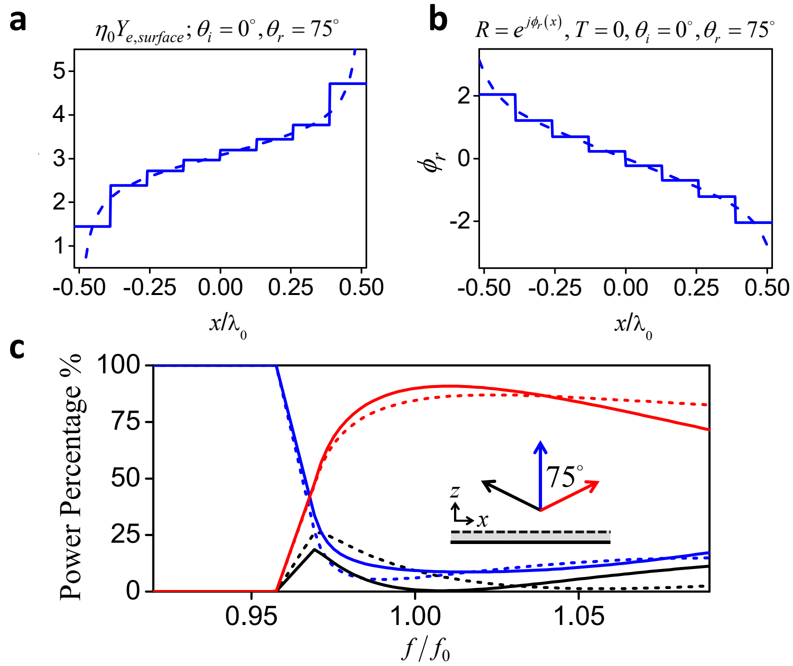

Figure 5.6: (a) Spatial distribution of admittance profile and (b) local reflection coefficient of the grounded metasurface designed to redirect a normal TE incident plane wave towards $\theta_r = 75$ degrees. The admittance layer is at $d = \lambda_0/20$ distance from the ground plane and the passive, lossless approximation is considered, i.e., $R(x) = 1e^{j\phi_r(x)}$. The amplitude of the reflected plane wave is set at $|A_r| = 1/\sqrt{\cos 75^\circ}$ in Eq. (5.3). Solid lines show the discretized profiles for $N_Q = 8$ and dashed line correspond to the original continuous pattern. (c) Frequency variation of the power reflected into different diffraction orders of the quantized metasurface. $n = +1, 0, -1$ correspond to $\theta_r = 75, 0, -75$ degrees at the center design frequency $f = f_0$. Dashed lines indicate the coupling efficiency of the continuous metasurface.

5.3.2 RF implementation

We demonstrate these findings by implementing the structure studied in Fig. 5.6 in a realistic setup, designed for operation at 1 GHz. Each of the eight admittance/phase steps in Figs. 5.6(a,b) are realized using four individual inductor-capacitor (LC) series-resonators, placed on a 10 mm thick ($= \lambda_0/30$) Eccostock®PP foam [46], as shown in Fig. 5.7(a). Each period of the gradient metasurface, thus, contains thirty-two surface resonators in the x-direction and one resonator in the y-direction. The LC components are electrically connected through metallic patches placed on the foam and the entire structure is grounded at the back surface. To design the gradient metasurface, we first calculate the local reflection phase on the top surface of each building block for commercially available chip inductors and capacitors [47], in a periodic setup. Subsequently, the element values are appropriately selected in accordance to Fig. 5.6(b). Columns two and three in Table 5.1 list the final design parameters. For comparison, we also repeated the same procedure to design another metasurface based on the ray optics approximation, i.e., using a linear local reflection phase (Columns four and five, Table 5.1), as commonly done in conventional gradient metasurface designs.

The overall performance for the two cases are evaluated through full-wave simulations, and the percentage of total incident power coupled into each propagating Floquet harmonic is shown in Fig. 5.7(b). As expected, the performance of the metasurface designed based on our analytical approach significantly outperforms the metasurface designed based on the linear phase approximation (shown with dashed lines in Fig. 5.7(b)), using similar discretization. Specifically, at the center frequency, our technique provides around 89% coupling from a normally incident wave to the $n=1$ Floquet mode, while ray optics provides only around 59% efficiency. It is quite fascinating that, although we implement each admittance/phase step with only four elements, our realistic metasurface design provides comparable performance to a quantized surface implemented with ideal surface profile (Fig. 5.6). In this regard, the predicted efficiency of an ideal quantized surface with similar substrate material and overall thickness is 90% (59%) for our approach (the ray optics) solution.

Table 5.1. Design parameters for the wave-bending metasurface to redirect a normal TE incident plane wave toward $\theta_r = 75$ degrees. Metasurface consists of thirty-two surface series-resonators and is designed at $1\,\mathrm{GHz}$. The lossless approximation is considered here as and the ray optics approximation is implemented with the linear local phase $R(x) = 1e^{-j2\pi x/X}$. All local phases are calculated on top of the surface. Capacitor and inductor values are specified in pico-Farad and nano-Henry, respectively.

Element types and numbers	Local phase for $R(x) = 1e^{j\phi_r(x)}$	Element values $R(x) = 1e^{j\phi_r(x)}$	Local phase for $R(x) = 1e^{-j2\pi x/X}$	Element values $R(x) = 1e^{-j2\pi x/X}$
(C_{1-4}, L_{1-4})	117.1°	$(1.1, 10)$	157.5°	$(0.1, 2.2)$
(C_{5-8}, L_{5-8})	69.5°	$(1.7, 4.7)$	112.5°	$(1.5, 4.3)$
(C_{9-12}, L_{9-12})	39.7°	$(1.3, 10)$	67.5°	$(1.8, 3.9)$
(C_{13-16}, L_{13-16})	13°	$(1.9, 4.3)$	22.5°	$(1.2, 12)$
(C_{17-20}, L_{17-20})	-13°	$(1.9, 4.7)$	-22.5°	$(1.3, 11)$
(C_{21-24}, L_{21-24})	-39.7°	$(1.6, 7.5)$	-67.5°	$(1.8, 6.2)$
(C_{25-28}, L_{25-28})	-69.5°	$(1.5, 9.1)$	-112.5°	$(1.5, 10)$
(C_{29-32}, L_{29-32})	-117.1°	$(2.2, 4.7)$	-157.5°	$(3.6, 2.2)$

Following these results, it is expected that, with appropriate implementation of the surface impedance, and even with quite rough discretization of $N_Q = 4, 8$, it is possible to design highly efficient metasurfaces for wavefront transformation. For instance, for the aforementioned example of bending a normally incident beam toward 75 degrees, at $\lambda_0 = 500\,\mathrm{nm}$ and $N_Q = 4$, each surface element is approximately $130\,\mathrm{nm}$ wide, which can be practically implemented using subwavelength high-index nanoparticles. Over visible wavelengths, the strong mutual interactions between adjacent particles (which can be calculated analytically for dissimilar surface components [48]), and the enhanced local density of states combined with low absorption, make high-index dielectric metasurfaces an excellent choice, with the intriguing prospect of tunability [41],[49]-[50].

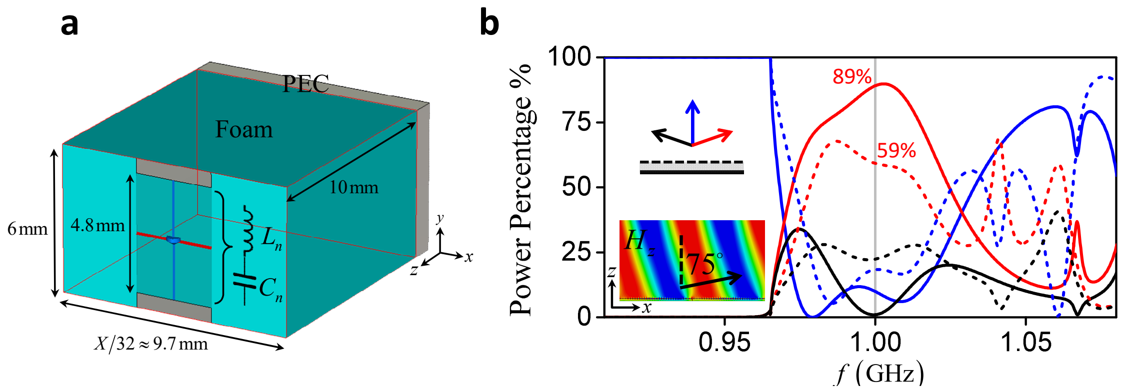

Figure 5.7: (a) Schematic of the microwave building block to implement gradient metasurfaces designed to redirect a normal incident plane wave toward $\theta_r = 75$ degrees at $1\,\text{GHz}$. Each block consists of a grounded $10\,\text{mm}$ thick Eccostock®PP foam with relative permittivity $\varepsilon_r = 1.06$. Elements are assumed to be passive and lossless, and the local reflection phase on top of each element is controlled by varying the surface capacitors and inductors. Thirty-two blocks are utilized in order to implement one supercell period of the intended gradient metasurfaces, and $X = \left|\lambda_0 / (\sin\theta_r - \sin\theta_i)\right|$ $\approx 310.6\,\text{mm}$. (b) Distribution of the reflected power toward different Floquet harmonics. Solid lines indicate the performance of the gradient metasurface designed based on the passive, lossless approximation of our analytical solution, i.e., $R(x) = 1e^{j\phi_r(x)}$, and the dashed lines demonstrate analogous results for the metasurface designed based on the ray optics approximation, i.e., $R(x) = 1e^{-j2\pi x/X}$. Except for the LC surface components listed in Table 1, all physical properties of the two metasurfaces are similar. Red lines indicate the percentage of power successfully redirected in the direction of the first Floquet harmonic, i.e., $\theta_r = 75$ degrees at $f = 1\,\text{GHz}$. The inset shows a time-snapshot of H_z at $1\,\text{GHz}$ for the metasurface designed based on our approach, demonstrating the clean scattered wave profile even in close proximity to the surface. The field amplitude is normalized to the incident plane wave.

In this line, we study beam steering metasurfaces in chapter 7. Another particularly interesting scenario is the case of graphene ribbons or patches, which may be able to model atomically-thick tunable impedance sheets at terahertz frequencies. Graphene-based metasurfaces may be an ideal implementation of the structure envisioned in Fig. 5.2, and may be fabricated with deeply subwavelength resolution and rigorously designed based on our accurate analytical model [51]. For instance, at $1\,\text{THz}$ and for

$N_Q = 16$, each surface element is over $19\,\mu\text{m}$ wide, which is well above the state of the art fabrication resolution for graphene metasurfaces [52]-[53].

5.4 METASURFACE COUPLERS

An extreme example of beam steering is the case in which we aim at converting a propagating wave into a bound state, as in a surface coupler, which corresponds to the case of complex θ_r in our previous formulation. As θ_r approaches 90 degrees, the reflection wave vector $\vec{k}_r = -k_0\hat{x}$ will be solely along the tangential direction, with transverse momentum equal to the free-space wave number. Beyond this point, the wave vector is larger than k_0, which can be conveniently modeled by a complex reflection angle $\theta_r = 90 + j|\alpha_r|$. This problem has been approached in the literature using gratings or linear phase gradient metasurfaces, providing the required momentum mismatch between incident and guided waves [54]-[58]. Artificial symmetry-breaking in the scattering properties of the graded surface, along with proper optimization of the coupling structure, has been exploited to enhance the coupling efficiency [59]-[60]. However, following the previous discussion, we can rigorously explore the conditions to achieve optimal coupling with a gradient metasurface, and we expect a linear phase gradient to be far from optimal. Similar to (5.3), given the incident and scattered wave profiles,

$$\begin{aligned}
\left(\mathbf{E}_i, \mathbf{H}_i\right) &= \left(\hat{y}, \frac{\hat{x}}{\eta_0}\right) E_0 e^{jk_0 z} \\
\left(\mathbf{E}_{1s}, \mathbf{H}_{1s}\right) &= A_r \left(\hat{y}, \frac{\hat{x}\beta_z - \hat{z}\beta_x}{k_0\eta_0}\right) E_0 e^{j\beta_x x} e^{j\beta_z z}
\end{aligned}, \tag{5.19}$$

the required surface impedances to couple a normally incident plane wave into a guided mode along the x-direction with transverse momentum $\beta_x = -k_0 \cosh\left(\alpha_r\right)$ equals

$$Y_e = \frac{2}{\eta_0} \frac{k_0 + A_r k_z e^{jk_x x}}{A_r k_0 e^{jk_x x} + k_0}, Z_m = 4/Y_e, \tag{5.20}$$

in which $\beta_z = j\left|\sqrt{\beta_x^2 - k_0^2}\right| = j\cosh\left(|\alpha_r|\right)$. The required surface impedance is in this case complex, with alternating regions of loss and gain depending on the relative amplitude of the guided wave A_r. Notice that this infinite surface coupler is an extreme example, inherently ill-posed, presented here to confirm the generality of our proposed theory: while the gradient metasurface supports the desired guided mode along the surface, the normal incident power $\hat{z} \cdot \mathbf{P}_{incident}$ cannot contribute to the power propagating in the lateral direction, since the power flowing along the surface is constant for a guided mode over an infinite periodic structure. Indeed, in the infinite metasurface coupler described by (5.20), the net power absorbed by the surface $\mathrm{Re}\left(-\overline{\mathrm{P}}_{surface}\right)$ over each superlattice period is equal to the incident power, independent from A_r

$$\mathrm{Re}\left(-\overline{\mathrm{P}}_{surface}\right) = \mathrm{Re}\left[\frac{1}{2X}\int_X \left(Y_e^* \left|\mathbf{E}_t\right|^2 + Z_m \left|\mathbf{H}_t\right|^2\right) dx\right] = \frac{E_0^2}{2\eta_0}, \tag{5.21}$$

with $X = 2\pi/\beta_x$. The graded surface absorbs the entire incident power independent of the amplitude of the scattered bound states A_r, consistent with the power conservation. The surface inhomogeneous loss/gain profile is then responsible for generating the desired guided mode under the excitation of such plane wave. For a beam of finite cross-section, on the other hand, we can expect efficient coupling to the desired modal profile, using Eq. (5.2).

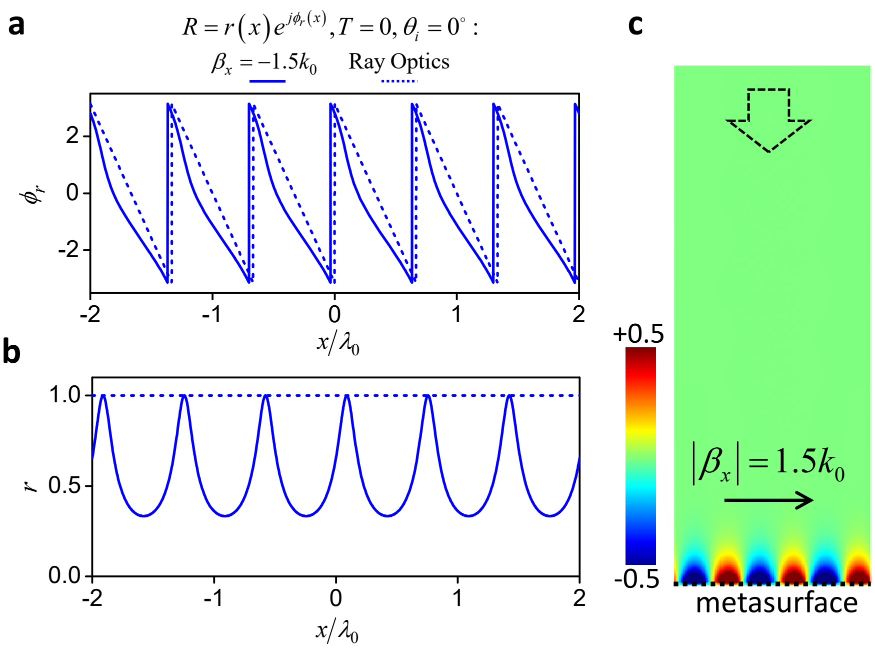

Figure 5.8: (a)-(b) Metasurface local reflection coefficient $R(x) = r(x)e^{j\phi_r(x)}$, required to convert a normally incident wave ($\theta_i = 0$ degrees) into a guided wave with $\beta_x = -1.5k_0$, in a passive-lossy metasurface, i.e. $|A_r| = k_0/|\beta_x|$. (c) Distribution of the scattered magnetic field H_z, for $\theta_i = 0$ and $\beta_x = -1.5k_0$, $d = \lambda_0/20$, for the all-passive surface illustrated in Fig 5.8 (a,b). The field is normalized to the amplitude of the incident magnetic field.

Interestingly, even limiting ourselves to passive surfaces, the required surface scattering phase is far from linear, as shown in Fig. 5.8(a) for $\beta_x = -1.5k_0$. Here, the relative amplitude of the guided mode is chosen to assure passivity of the surface, following the previously discussed approach (Fig. 5.8(b)). To ensure passivity of the gradient metasurface, the reflection amplitude $|A_r|$ is chosen so that the local emerging power on the surface is always negative, i.e. $\forall x$, $\mathrm{Re}(\hat{z} \cdot \mathrm{P}_{total})_{z\to 0^+} < 0$. Following (5.19), the local emerging power on the surface can be simplified as,

$$\mathrm{Re}(\hat{z} \cdot \mathbf{P}_{total})_{z\to 0^+} = -\frac{E_0^2}{4\pi\eta_0}\left[2\pi + |A_r|\beta_x\lambda_0 \sin\left(\angle A_r + \beta_x x - \tan^{-1}\left(k_0/|\beta_z|\right)\right)\right]. \quad (5.22)$$

Enforcing $\mathrm{Re}\left(\hat{z}\cdot\mathbf{P}_{total}\right)_{z\to0^+}<0$, the maximum tolerable reflection amplitude is found to be $\left|A_r\right|_{\max}=k_0/\beta_x$. A linear scattering phase approximation may allow coupling a portion of incident power to a guided wave with parallel wave vector [56]-[58], similar to a conventional grating. However, it fails to provide the optimal surface profile to maximize the coupling efficiency [55]. Conversely, as shown in Fig. 5.8(c), the rigorous formulation described here is capable of creating a pure secondary guided wave with the desired distribution using a metasurface, and zero coupling into other scattering orders.

We conclude this section noting that this approach can be extended to the practical problem of the design of finite-sized surface couplers. In this case, the excitation field is not an infinite plane wave, but the finite incident beam profile that excites the coupler. At the same time, the desired scattered wave should be a gradually growing surface wave that adiabatically matches the mode profile of the fed waveguide. Quite distinct from infinite couplers, the total power carried by the incident wave is finite in this case, and it matches the total guided mode power. In addition, the normal component of the incident wave directly feeds the guided mode. Interestingly, a ray-optics approach is unable to provide any adaptation on the size or profile of the coupler based on these specifications, and is thus limited in overall efficiency and in impedance matching to the fed waveguide. Consequently, ray-optics based couplers are typically limited to low conversion efficiencies, analogous to traditional grating based couplers [55].

5.5 Metasurface lensing and focusing

The approximations of the ray-optics approach highlighted in the previous section are not limited to wave bending and coupling. Here, we examine the design of an ultrathin planar lens with extreme focusing properties. Reducing the volumetric size of a dielectric lens into a single patterned surface is of great interest in nano-optics and integrated photonics, and the local phase compensation approach has been incorporated in the designs of numerous flat focusing structures [27],[62]. To generate a spherical outgoing phase front from an incident plane wave, ray-optics suggests a hyperboloidal phase profile to be imprinted over the surface (i.e., all normally incident rays will be redirected towards the desired direction and collimate at the focal point). However, the previous results suggest that this approach would provide a reasonable performance only in the limit of small numerical apertures (NA), and when the focal point is located far from the lens. Under such condition, the rays traced from the corner of the lens, which experience the largest local deflection angle, are far from the grazing angle and the phase difference between scattered and incident waves is close to the phase (and amplitude) profile of the optimal surface. For $\mathrm{NA} < 0.96$ the cone angle of the lens is smaller than 73 degrees and, as illustrated in Fig. 5.9(a), the hyperboloidal interfacial phase pattern (dashed line) mimics the exact surface profile (solid lines) with about 35 degrees error range, while the ideal reflection amplitude oscillates around unity. As we increase the numerical aperture to ranges that are not achievable with conventional diffraction elements, the line shape of the optimal phase drastically deviates from a simple hyperbolic pattern and we find over 70 degrees error range for $\mathrm{NA} = 0.998$. To design the optimal surface in accordance to (5.2), a normally incident plane wave is transformed into an outgoing cylindrical wave. The scattered wave can be considered as the time reverse of the wave radiated by a line source (point source in a two-dimensional lens), and fields take the general format [61],

$$
\begin{aligned}
&(\mathbf{E}_i, \mathbf{H}_i) = \left(\hat{y}, \frac{\hat{x}}{\eta_0}\right) E_0 e^{jk_0 z} \\
&\mathbf{E}_{1s} = \frac{-I_0 k_0 \eta_0}{4} H_0^{(1)}\left[k_0 \sqrt{x^2 + (z-f)^2}\right]\hat{y} \\
&\mathbf{H}_{1s} = \frac{-jI_0 k_0}{4} H_1^{(1)}\left[k_0 \sqrt{x^2 + (z-f)^2}\right]\left(\frac{\hat{x}(z-f)}{\sqrt{x^2+(z-f)^2}} - \frac{\hat{z}x}{\sqrt{x^2+(z-f)^2}}\right)
\end{aligned} \quad . \tag{5.23}
$$

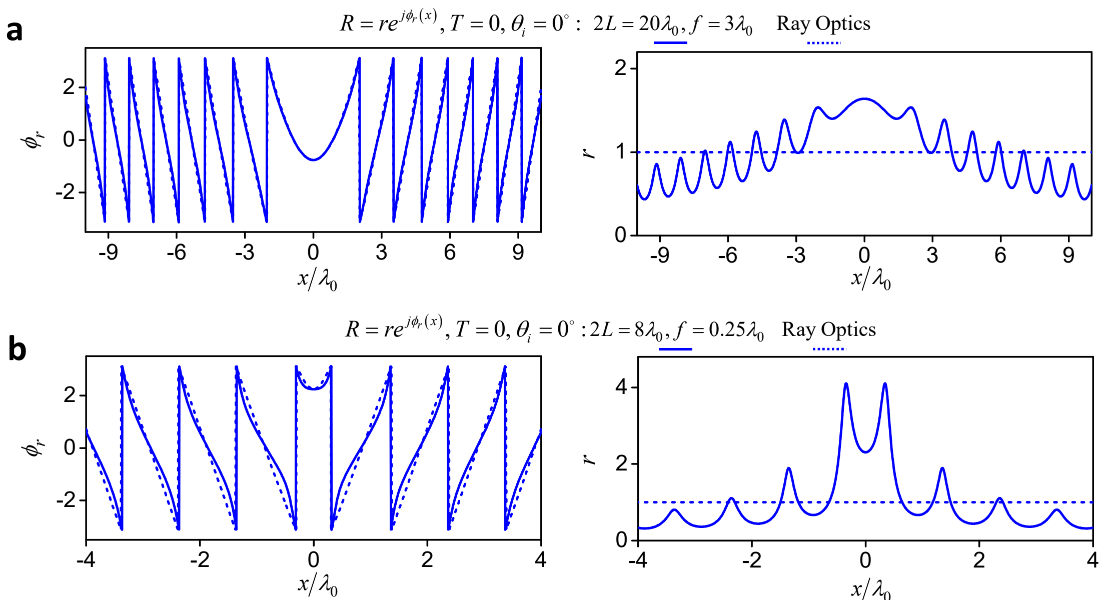

Figure 5.9: Comparison between the scattering properties of ideal (solid lines) and ray-optics based (dashed lines) metasurface reflecting lenses with local distribution of loss and gain and (a) $\mathrm{NA} = 0.9578$ and (b) $\mathrm{NA} = 0.9981$. Amplitude and phase of the local reflection coefficient $R(x) = r(x)e^{j\phi_r(x)}$ are plotted along the lens surface for (a) $\alpha = \pi$ and (b) $\alpha = \pi/2$. Metasurface lenses are extended between $x = (-L, L)$, excited by a plane wave propagating along $-z$ direction.

We note that the field distributions in (5.23) are accurate if an ideal drain, i.e. the time-reversed equivalent of the line source, is also positioned in the focal point. In practice, the absence of such point may reduce the overall performance of the designed lens. The metasurface lens is placed in the xz-plane with focal point at $z = f$ and

$H_n^{(1)}[r]$ refers to the Hankel function of type 1 with order n. Assuming a finite length of $2L$ for the lens, power conservation determines the relation between E_0 and I_0, so as the surface on the whole is lossless,

$$
\begin{aligned}
&-\left|\mathbf{P}_{incident}\right| = -\frac{E_0{}^2}{2\eta_0}2L \\
&\left|\mathbf{P}_{reflected}\right| = \frac{\tan^{-1}\left(L/f\right)}{\pi}\times\left(\text{Power radiated by current I}_0\right) = \frac{I_0{}^2 k_0\eta_0}{8\pi}\tan^{-1}\left(L/f\right)
\end{aligned}
\quad , \qquad (5.24)
$$

which simplifies to the relation $\left|E_0\right| = \left|I_0\right|\eta_0\sqrt{\frac{\tan^{-1}\left(L/f\right)}{\pi}\frac{k_0}{8L}}$. The relative phase of the fields is determined by the focusing properties of the surface. In fact, any relative phase between E_0 and I_0, $\alpha = \angle E_0 - \angle I_0$, transforms the incident plane wave into the cylindrical wave with the corresponding phase. However, since we are working in reflection, we want to create a hot spot for the total field, and not only the scattered field. This means that, for a given α, the scattered cylindrical beam can constructively or destructively add to the incident wave at the focal point. To achieve the sharpest focus, we theoretically predict the optimal phase difference for the design process. The total power flowing toward the focal point in its vicinity equals $\mathrm{P}_\kappa = \hat{\kappa}\cdot\mathbf{P}_{total}\left(x = \delta\cos\gamma, z = f + \delta\sin\gamma\right)\big|_{\delta\to 0, -\pi<\gamma<0}$, in which we define $\hat{\kappa}$ as the radial unit vector around the focal point. After some mathematical simplification and replacing Hankel functions by their approximation around zero, derivative of P_κ versus α is found to be proportional to $\frac{d\,\mathrm{P}_\kappa}{d\alpha} \propto -4\sin\left(k_0 f + \alpha\right)$. The local power toward the focal point is then maximized for $\alpha = \pi - k_0 f$. This optimum value of α is valid for a lossy/gainy metasurface lens and when we approximate the surface as lossless (by ignoring the amplitude modulation), the best value of α changes. To account for this lossless approximation, the finite thickness of the lens, and also the absence of a sink at the focal point, in Fig. 5.10 we tuned this relative phase in Eq. (5.23) to maximize the total power at the focal point.

As we move toward higher numerical apertures, as expected, the optimal surface requires extremely localized loss and gain segments, and the scattering phase significantly diverges from the hyperboloidal approximation. We stress that these limitations are independent of the resolution of the gradient metasurface, and a surface designed based on local phase compensation inevitably exhibits unwanted spherical aberrations and fails to create focusing effects in the near-field region.

In accordance to the previous results on wave bending, the optimal active/passive surface can be approximated by its passive-lossless counterpart to preserve the ideal phase pattern, and provide an improved passive-lossless low-aberration, high numerical aperture lens design, by sacrificing a small portion of the focused energy. This is illustrated in Fig. 5.10, where we compare two lenses with overall lengths of $20\,\lambda_0$ and $8\,\lambda_0$, designed to focus the incident wave at $f_1 = 3\lambda_0$ and $f_2 = 0.25\lambda_0$, with numerical apertures $\mathrm{NA} = 0.958$ and $\mathrm{NA} = 0.998$, respectively. Both lenses are lossless, and implemented with grounded all-electric metasurfaces, shown in Fig. 5.4(b). The first column illustrates the power distribution above the reflecting lenses that are designed based on the optimal phase distribution on the surface. The second column shows the power distribution when a hyperbolic phase distribution is imprinted over the surface. As expected, for a small numerical aperture and reasonably large focal distance, ray optics provides a very good approximation of the exact solution, yet it fails to create near-field focusing effects (Fig. 5.10(d)). On the contrary, the passive-lossless metasurface lens, designed based on our analytical solution, provides strong near-field focusing effects, as shown in Fig. 5.10(c). Compared to the ideal lens, the focal point is slightly shifted from the intended position (less than $0.06\,\lambda_0$), toward +z direction. This minor deviation is associated with the lossless approximation of the ideal lens, as well as the absence of an active drain at the focal point [63]. Quite interestingly, we also found that the half power beam width of the focal image is similar in both approaches, and it is approximately $0.32\,\lambda_0$ (Fig. 5.10(e,f)).

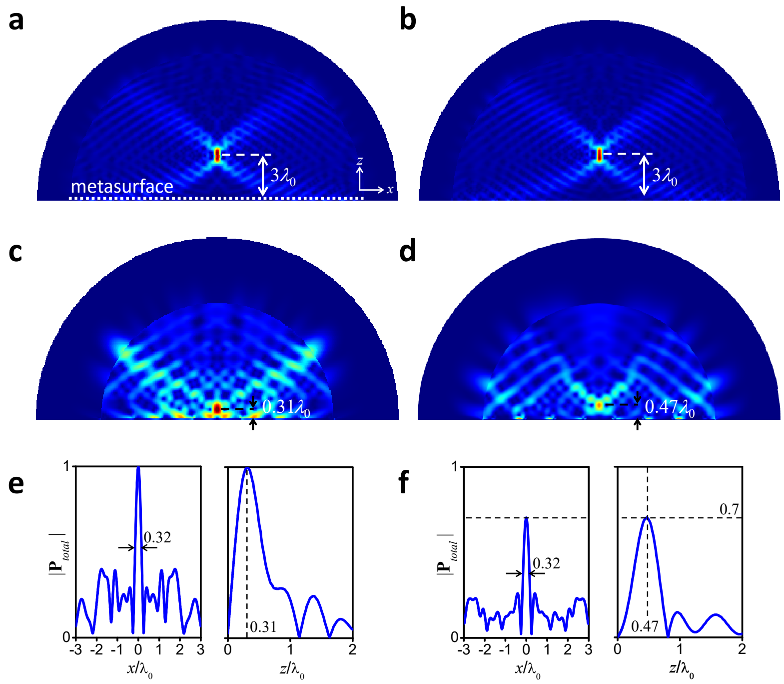

Figure 5.10: Comparison between the power distribution in passive-lossless planar lenses with optimal (a, c), and hyperbolic (b, d) lateral phase profiles. Plots in the same row have the same color bar, and all metasurfaces have equal thickness $d = \lambda_0/50$. Imparted local reflection coefficients $R(x) = 1e^{j\phi_r(x)}$ calculated for (a) $\alpha = \pi$ and (c) $\alpha = 4.4$ radians. Metasurface lenses in panels (a, b) and (c, d) are designed to collimate the normally incident plane wave at $f_1 = 3\lambda_0$ and $f_2 = 0.25\lambda_0$, respectively. (e, f) Field profile along the x- and z- directions across the focal points corresponding to panels (c) and (d), respectively. For better comparison, the plots are all normalized to the same value.

5.6 Conclusion

In this chapter, we have investigated the theoretical limitations and potentials of passive gradient metasurfaces for arbitrary wave manipulation. Our study is based on a rigorous treatment of the wave equation, which allows deriving relevant results for the field of gradient metasurfaces and wave manipulation over a surface. First, we proved that wave transformations over an ultrathin surface, even in their simplest form, e.g., for beam steering, inherently require the presence of balanced loss and gain to achieve unitary efficiency. Then, we derived a bound on the maximum coupling efficiency that allows exclusively coupling to the desired diffraction order, and we derived a path towards maximizing the coupling efficiency to the wavefront of choice, showing the inaccuracy of conventional ray optics approximations commonly used in the literature to realize wave transformations not achievable with conventional diffraction gratings.

We inspected practical examples of anomalous wave deflection, coupling from propagating waves to surface bounded modes, and lenses, showing that passive-lossless metasurfaces following the derived gradient profiles can significantly outperform designs based on conventional design rules derived from ray optics. We further studied the effect of surface quantization on the overall performance of the device and provided a realistic implementation of a gradient metasurface at microwave frequencies, designed following our analytical derivation. Our findings confirm a considerable improvement of 30% to the overall efficiency for an extreme-angle wave-bending metasurface, compared to a similar metasurface designed using the conventional ray-optics approach. For simplicity, here we considered two-dimensional reflection scenarios, yet, similar restrictions may be derived for three dimensions, polarization coupling surfaces, and transmitting metasurfaces. Our results shed light into the physical limitations of passive metasurfaces and provide a practical route toward highly efficient wave shaping metasurfaces, beyond the extent attainable from current techniques based on ray optics.

5.7 REFERENCES

[1] J. D. Joannopoulos et al., Photonic crystals: molding the flow of light (Princeton university press, 2011).

[2] N. Engheta, and R. W. Ziolkowski, Metamaterials: physics and engineering explorations (John Wiley & Sons, 2006).

[3] J. B. Pendry, Phys. Rev. Lett. 85, 977 (2000).

[4] P. Russell, Science 299, 358 (2003).

[5] S. McCall et al., Microwave propagation in two-dimensional dielectric lattices, Phys. Rev. Lett. 67, 2017 (1991).

[6] D. Schurig et al., Metamaterial electromagnetic cloak at microwave frequencies, Science 314, 3966 (2006).

[7] U. Leonhardt, Optical conformal mapping, Science 312, 1777 (2006).

[8] J. B. Pendry, D. Schurig, and D. R. Smith, Controlling electromagnetic fields, Science 312, 1780 (2006).

[9] S. Maci, G. Minatti, M. Casaletti, M. Bosiljevac, Metasurfing: Addressing waves on impenetrable metasurfaces, IEEE Antenn. Wireless Propag. Lett. 10, 1499 (2011).

[10] A. A. Houck, J. B. Brock, and I. L. Chuang, Experimental observations of a left-handed material that obeys Snell's law, Phys. Rev. Lett. 90, 137401 (2003).

[11] R. E. Munson, H. A. Haddad, and J. W. Hanlen, Microstrip reflectarray for satellite communication and radar cross-section enhancement or reduction, (US Patent 4684952, 1987).

[12] D. Pozar, Flat lens antenna concept using aperture coupled microstrip patches, Elect. Lett. 32, 2109 (1996).

[13] D. M. Pozar, S. D. Targonski, and H. Syrigos, Design of millimeter wave microstrip reflectarrays, IEEE Trans. Antennas and Propag. 45, 287 (1997).

[14] E. F. Kuester et al., Averaged transition conditions for electromagnetic fields at a metafilm, IEEE Trans. Antennas and Propag. 51, 2641 (2003).

[15] C. L. Holloway et al., An overview of the theory and applications of metasurfaces: The two-dimensional equivalents of metamaterials, IEEE Antennas Propag. Magazine 54, 10 (2012).

[16] A. Papakostas et al., Optical manifestations of planar chirality, Phys. Rev. Lett. 90,107404 (2003).

[17] Y. Zhao, and A. Alu, Manipulating light polarization with ultrathin plasmonic metasurfaces, Phys. Rev. B 84, 205428 (2011).

[18] Y. Zhao, N. Engheta, and A. Alù, Homogenization of plasmonic metasurfaces modeled as transmission-line loads, Metamaterials 5, 90 (2011).

[19] L. Novotny, Effective wavelength scaling for optical antennas., Phys. Rev. Lett. 98, 266802 (2007).

[20] N. Yu et al., Light propagation with phase discontinuities: generalized laws of reflection and refraction, Science 334, 333 (2011).

[21] X. Ni et al., Broadband light bending with plasmonic nanoantennas, Science 335, 427 (2011).

[22] F. Aieta et al., Out-of-plane reflection and refraction of light by anisotropic optical antenna metasurfaces with phase discontinuities, Nano Lett. 12, 1702 (2012).

[23] C. Pfeiffer and A. Grbic, Metamaterial Huygens' surfaces: tailoring wave fronts with reflectionless sheets, Phys. Rev. Lett. 110, 197401 (2013).

[24] N. Mohammadi Estakhri, and A. Alù, Manipulating optical reflections using engineered nanoscale metasurfaces, Phys. Rev. B 89, 235419 (2014).

[25] N. Yu, and F. Capasso, Flat optics with designer metasurfaces, Nat. Mater. 13, 139 (2014) and the references within.

[26] F. Monticone, N. M. Estakhri, and A. Alù, Full control of nanoscale optical transmission with a composite metascreen, Physical Review Letters 110, 203903 (2013).

[27] A. Pors et al., Broadband focusing flat mirrors based on plasmonic gradient metasurfaces, Nano Lett. 13, 829 (2013).

[28] C. L. Holloway et al., Reflection and transmission properties of a metafilm: With an application to a controllable surface composed of resonant particles, IEEE Trans. Electromagn. Compat. 47, 853 (2005).

[29] A. Epstein, and G. V. Eleftheriades, Passive Lossless Huygens Metasurfaces for Conversion of Arbitrary Source Field to Directive Radiation, IEEE Trans. Antennas and Propag. 62, 11 (2014).

[30] S. Sun et al., High-efficiency broadband anomalous reflection by gradient meta-surfaces, Nano Lett. 12, 6223 (2012).

[31] N. Mohammadi Estakhri, C. Argyropoulos, and A. Alù, Graded metascreens to enable a new degree of nanoscale light management, Philos. Trans. R. Soc. London, A. 373, 20140351 (2015).

[32] C. Pfeiffer, A. Grbic, Bianisotropic metasurfaces for optimal polarization control: Analysis and synthesis, Phys. Rev. Applied 2, 044011 (2014).

[33] M. Selvanayagam, G. Eleftheriades, Polarization control using tensor Huygens surfaces, IEEE Trans. Antennas and Propag. 62, 6155 (2014).

[34] Harrington R. F., Time-Harmonic Electromagnetic Fields. (John Wiley & Sons, 2001).

[35] C. M. Bender and S. Boettcher, Real spectra in non-Hermitian Hamiltonians having P T symmetry, Phys. rev. lett. 80, 5243 (1998).

[36] C. E. Rüter et al., Observation of parity–time symmetry in optics, Nat. Phys. 6, 192 (2010).

[37] L. Feng et al., Experimental demonstration of a unidirectional reflectionless parity-time metamaterial at optical frequencies, Nat. mater. 12, 108 (2013).

[38] M. Esfandyarpour et al., Nat. nanotechnol. 9, 7 (2014).

[39] M. A. Al-Joumayly, and N. Behdad, A generalized method for synthesizing low-profile, band-pass frequency selective surfaces with non-resonant constituting elements, IEEE Trans. Antennas and Propag. 58, 4033 (2010).

[40] M. Selvanayagam, and G. V. Eleftheriades, Discontinuous electromagnetic fields using orthogonal electric and magnetic currents for wavefront manipulation, Opt. Express 21, 14409 (2013).

[41] L. Zou et al., Dielectric resonator nanoantennas at visible frequencies, Opt. Express 21, 1344 (2013).

[42] M. Kim, A. M. Wong, G. V. Eleftheriades, Optical Huygens' Metasurfaces with Independent Control of the Magnitude and Phase of the Local Reflection Coefficients, Phys. Rev. X 4, 041042 (2014).

[43] G. M. Whitman and F. Schwering, Reciprocity identity for periodic surface scattering, IEEE Trans. Antennas and Propag. 27 252 (1979).

[44] L. Liu et al., Broadband metasurfaces with simultaneous control of phase and amplitude, Adv. Mater. 26 (2014).

[45] A. Epstein, G. V. Eleftheriades, Floquet-Bloch analysis of refracting Huygens metasurfaces, Phys. Rev. B 90, 235127 (2014).

[46] http://www.eccosorb.com

[47] Chip inductors from Murata Manufacturing Co., and multi-layer high-Q capacitors from Johanson Technology.

[48] A. Alù et al., Coupling of optical lumped nanocircuit elements and effects of substrates," Opt. express 15, 13865 (2007).

[49] D. Lin, P. Fan, E. Hasman, M. L. Brongersma, Dielectric gradient metasurface optical elements, Science 345, 298 (2014).

[50] J. Sautter et al., Active Tuning of All-Dielectric Metasurfaces, ACS nano 9, 4308 (2015).

[51] J. S. Gomez-Diaz et al., Hyperbolic plasmons and topological transitions over uniaxial metasurfaces, Phys. Rev. Lett 114, 233901 (2015).

[52] F. J. Garcia de Abajo, Graphene plasmonics: challenges and opportunities, ACS Photonics 1, 135 (2014).

[53] J. Cai et al., Atomically precise bottom-up fabrication of graphene nanoribbons, Nat. 466, 470 (2010).

[54] D. Taillaert, P. Bienstman, and R. Baets, Compact efficient broadband grating coupler for silicon-on-insulator waveguides, Opt. Lett. 29, 2749 (2004).

[55] S. Sun et al., Gradient-index meta-surfaces as a bridge linking propagating waves and surface waves, Nat. Mater. 11, 426 (2012).

[56] J. Wang et al., High-efficiency spoof plasmon polariton coupler mediated by gradient metasurfaces, Appl. Phys. Lett. 101, 201104 (2012).

[57] F. Ding et al., Unidirectional surface plasmon polariton coupler in the visible using metasurfaces, in CLEO: QELS Fundamental Science (2014).

[58] A. Pors et al., Efficient unidirectional polarization-controlled excitation of surface plasmon polaritons, Light: Science & Applications 3 (2014).

[59] A. Baron et al., Compact antenna for efficient and unidirectional launching and decoupling of surface plasmons, Nano Letters 11, 4207 (2011).

[60] D. Taillaert et al., Grating couplers for coupling between optical fibers and nanophotonic waveguides, Japanese J. Appl. Phys. 45, 6071 (2006).

[61] Balanis C. A., Advanced Engineering Electromagnetics. (John Wiley & Sons, 1989).

[62] F. Aieta et al., Aberration-free ultrathin flat lenses and axicons at telecom wavelengths based on plasmonic metasurfaces, Nano Lett. 12, 4932 (2012).

[63] Y. G. Ma et al., Evidence for subwavelength imaging with positive refraction. New J. Phys. 13, 033016 (2011).

Chapter 6: Design of Composite Plasmonic Nanoparticles as Building Blocks of Metasurfaces to Manipulate Local Light Scattering

In the previous chapter we illustrated that a complex beam-forming task can be simplified to the design of a spatially modulated reactive surface, and local capacitive and inductive elements are essential to ensure effective wave manipulation in such configuration. In view of these finding on ideal, zero-thickness metasurfaces, in this chapter we will study practical metamolecules suitable to implement passive metasurfaces at optical frequencies. To physically realize such metasurfaces we get inspiration from RF concepts. One of the main reasons behind the rapid and widespread development of the microelectronic technology at radio frequencies is the modularization of lumped circuit elements. Basic building blocks such as chip resistors, capacitors, and inductors are readily available in this range and combined to synthesize complex functionalities, which subsequently build large operational circuits at radio frequencies. Optical and IR designs, on the other hand, are conventionally performed at the physical level where the complex light–matter interactions are directly exploited via different methods to achieve the desired effect. Here we utilize a nanocircuit paradigm to modularize surface elements creating local nanoresonators with controllable reactances based on the combination of two different materials. We will also study performance of these subwavelength metamolecules in terms of bandwidth, tunability and loss. These surface elements are used in the following chapters to physically implement wave shaping metasurfaces at optical frequencies. Contents of this chapter partially appeared/to appear in "Farhat, M.; Chen, P.; Guenneau, S.; Enoch, S., Transformation Wave Physics: Electromagnetics, Elastodynamics, and Thermodynamics, Pan Stanford, to be published" and "Mohammadi Estakhri, N.; Alù, A., Manipulating optical reflections using engineered nanoscale metasurfaces. Physical Review B 2014, 89 (23), 235419".

6.1 NANORESONATORS AS OPTICAL PHASE ELEMENTS

Quite recently, a comprehensive nanocircuit paradigm has been proposed to bridge the design gap between optics and microwaves and to extend the conventional circuit theory to shorter wavelengths [1]. This paradigm allows to quantitatively describe subwavelength nanoparticles in terms of equivalent lump circuit elements, proposing an ideal solution for what we are seeking for the gradient metasurfaces. As the wavelength shrinks, the contribution of the conduction current versus the displacement current in the material drops down rapidly and eventually becomes negligible. Based on this phenomenon, nanocircuit theory defines an intrinsic equivalent optical impedance for subwavelength particles as the ratio of the E effective optical voltage $V = |\mathrm{E}|h$ across the particle, and the flux of the electric displacement current $I = |\mathrm{J}_{\mathrm{d}}|S$ flowing through it. In analogy to circuit theory, the voltage is related to the local electric field across the particle and height of the nanoparticle along this field (h), while retardation effects are neglected in view of the small size of the structure (quasi-static approximation). Similarly, the displacement current density $J_{\mathrm{d}} = j\omega\varepsilon\mathrm{E}$ integrated over the transverse cross section of the particle, S, sustains the total flux of the electric displacement current, which is in quadrature phase with the effective voltage when the material is lossless (i.e., real permittivities). Based on this concept, a dielectric nanoparticle, $\varepsilon > 0$, has a capacitive effective impedance while a plasmonic one, $\varepsilon < 0$, is characterized by an inductive effective impedance. In the presence of loss (i.e., complex permittivities) a resistive component is added to the impedance, taking absorption into account.

Alongside modeling the scattering response of quasi-static nanoparticles, the nanocircuit paradigm allows translating various low-frequency concepts to IR and visible range. For instance, the input impedance is one of the characterizing parameters of RF antennas, typically utilized to match the antenna to arbitrary feeding networks and tuning its resonance frequency. In a similar fashion, nanocircuit theory allows defining an effective optical voltage, current, and impedance for nanoantennas (e.g., a plasmonic dipole) and adjust their scattering dispersion employing nanoloads [2].

The contribution of the nanocircuit modeling in realizing of gradient wave-shaping surfaces is evident now. Particles with different equivalent impedances need to be arranged properly on the surface to realize the electric surface reactance profiles derived in Eq. (5.13). These particles are inherently subwavelength in this quasi-static regime, guaranteeing a satisfactory transverse resolution on the surface. For the capacitive portion (i.e., $\mathrm{Im}[Y_{e,surface}] > 0$), dielectric particles may be utilized, and for the inductive elements ($\mathrm{Im}[Y_{e,surface}] < 0$), plasmonic nanoparticles are required, both widely available at IR and visible range. To tailor the value of the impedance, the shape of nanoparticle (i.e., h and S) may be modified or different materials can be employed. Besides, nanoparticles may be combined to create more complex impedance responses.

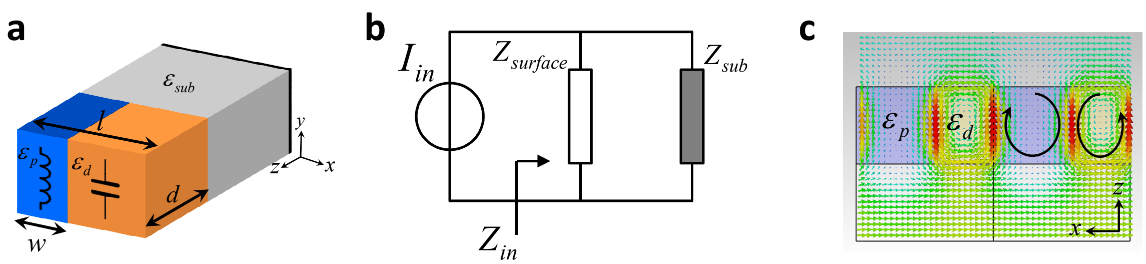

Figure 6.1: Spatial phase modulator. (a) Basic element of the metasurface made of alternated plasmonic (blue) and dielectric (orange) materials deposited on a grounded substrate layer (gray). The element lies in the xy plane and is invariant along the y axis. (b) Equivalent circuit model for the structure shown in (a). The metasurface layer is modeled by the appropriate shunt electric surface impedance $Z_{surface}$, and Z_{sub} includes the effect of the substrate and ground plane. (c) Magnetic field distribution in a sample periodic metasurface composed of the elements shown in (a) and excited with a plane wave $\left(\mathrm{E}_y, \mathrm{H}_x\right)$ along the –z direction. The opposite direction of rotation of the magnetic field indicates a reverse sign of local reactance in each portion.

We explore here the idea of implementing lumped nanoresonators on the surface, realized with pairs of local inductors and capacitors connected in series/parallel. In the simplest format, Fig. 6.1(a) illustrates a 2D cubical nanoresonator ($l \ll \lambda_0$) consisting of two materials with permittivities $\varepsilon_p < 0$ and $\varepsilon_d > 0$, deposited on a grounded substrate. We will later apply these elements to implement a variety of gradient surfaces in the following chapters. Employing such hybrid particles to realize the required surface impedance, rather than a homogenous dielectric or plasmonic nanoparticle, brings out several advantages. First, the equivalent impedance of the particle cluster now depends on the ratio between the size of the inductive and capacitive elements (i.e., $w/(l-w)$) rather than their absolute geometrical size l [3]. This enables us to shrink the footprint of the resonator arbitrarily, basically as far as fabrication techniques allow us. Second, two materials would be essentially sufficient to sweep the entire impedance spectrum. Here, the surface impedance can be easily controlled through changing the filling ratio along the surface, rather than employing a range of different materials at different points, which is relatively impractical.

The electromagnetic response of the fundamental element shown in Fig. 6.1(a) can be accurately modeled employing simple transmission-line concepts together with the nanocircuit paradigm [1]. When arranged in a periodic fashion, these elements create an effective, homogenous surface impedance $Z_{surface}$ associated to the corresponding impedance of each nanoparticle cluster. In this regard, if the flux of the electric displacement current is continuous between the two particles, that is, $\mathrm{E} = |\mathrm{E}|\hat{x}$, the particles form a series connection and $Z_{surface} = Z_p^s + Z_d^s$, in which $Z_{p,d}^s$ are equivalent series impedances of the plasmonic and dielectric portions. Alternatively, if analogous voltages are induced across the particles, that is, $\mathrm{E} = |\mathrm{E}|\hat{y}$, they form a parallel connection and $Z_{surface} = Z_p^p \| Z_d^p$, where now $Z_{p,d}^p$ indicate the parallel equivalent impedance of the two particles (see Fig. 6.1(b,c)).

For the 2D configuration considered here, these unit length impedances can be easily found as [4],

$$\begin{aligned} Z_p^s &= w\left(j\omega d(\varepsilon_p - \varepsilon_0)\right)^{-1}, Z_d^s = \left(l - w\right)\left(j\omega d(\varepsilon_d - \varepsilon_0)\right)^{-1} \\ Z_p^p &= \left(j\omega w d(\varepsilon_p - \varepsilon_0)\right)^{-1}, Z_d^p = \left(j\omega\left(l - w\right)d(\varepsilon_d - \varepsilon_0)\right)^{-1} \end{aligned}, \quad (6.1)$$

which are purely imaginary in the lossless case. Equation (5.12) already showed that if $Z_{surface} = \left(Y_{surface}\right)^{-1}$ can be designed arbitrarily at each point on the surface, the local reflection phase is also arbitrarily controllable. With an embedded resonance in $Z_{surface}$, we expect to be able to efficiently control its magnitude by means of common optical dielectrics and metals. In fact, it is clear from Eq. (6.1) that if the total length of the element, l, is fixed, by simply changing the filling ratio of the plasmonic portion we move from a capacitive surface to an inductive surface, and a broad range of impedances is accessible. For a specific filling ratio, a resonance is achieved (i.e., $Z_{surface} = 0$ in series connection, and $Z_{surface} = \infty$ in the parallel case) around which a rapid variation of impedances and reflection phases are expected.

As an example of a practical implementation of such surface in the visible range ($\lambda_0 = 500\text{ nm}$), the equivalent surface impedance of this hybrid particle is plotted in Fig. 6.2(a) as a function of the width of the plasmonic portion. To construct the capacitive and inductive portions we select an optical semiconductor and silver as the constitutive materials, and particle dimensions are set at $l = \lambda_0/16 = 31.25\text{ nm}$ and $d = 40\text{ nm}$. At optical frequencies silver follows a Drude type dispersion, $\varepsilon_p = \varepsilon_\infty - f_\mathrm{p}^2 / f\left(f - j\gamma\right)$, with $\varepsilon_\infty = 5$, plasma frequency of $f_\mathrm{p} = 2175$ THz and collision frequency $\gamma = 4.35$ THz

[5]. The real part of the permittivity of silver takes negative values in optical regime and at the same time it shows relatively low intrinsic loss, which makes it a suitable candidate for the inductive element. We note that due to the realistic losses included in this model, the equivalent inductor calculated from Eq. (6.1) is now complex with a resistive component. For the dielectric portion an optical semiconductor with relative permittivity of $\varepsilon_d = 12$ [6], is employed. Semiconductors are particularly appealing at optical frequencies due to negligible loss, high refractive index, and the possibility of tuning the permittivity through proper doping. Another option is to use Titanium dioxide to construct the metasurface, which we look into in chapter 7.

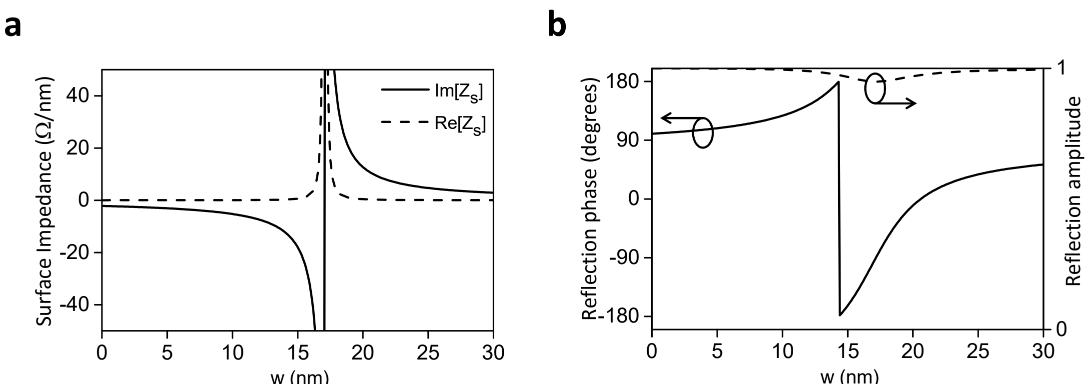

Figure 6.2: (a) Surface reactance and resistance per unit length as a function of the width of the plasmonic portion for the structure shown in Fig. 6.1(a). Material and geometry specifications are included in the main text. (b) Corresponding reflection coefficient. Parallel combination of the nanoelements is considered. (Reproduced with permission from Physical Review B, Vol. 89, Issue 23, pp. 235419 (2014). Copyright 2014 American Physical Society).

Figure 6.2(a), which is plotted for a parallel combination of nanoresonator elements —i.e. incident electric field is along the y axis and $Z_{surface} = \left(Y_{e,surface,yy}\right)^{-1}$— demonstrates the capability of the proposed composite particle to achieve any arbitrary local impedance on the surface. Around the resonance, which occurs approximately at

$w = 17$ nm in this example, both ranges of inductive and capacitive elements can be easily obtained by varying the filling ratio. It is particularly important that such wide range of variation of impedance is obtained over only 31.25 nm lateral dimension of the unit cell, 40 nm depth of the surface, and simply employing two materials. This implies that if embedded in a nonperiodic and gradient metasurface, these elements are capable of practically controlling the local impedance at each point, with an ultrathin depth along the direction of the propagation of wave (z axis). As the result of wave matter interaction over a surface, effect of loss is also negligible. Evident from Fig. 6.2(a), except around the resonance point where an inevitable surface resistance is created, the hybrid particle is effectively reactive. We will specifically look at the effect of material absorption on the performance of the metasurface in section 6.2.

The corresponding scattering coefficient, that is, $R_{surface,\mathrm{TE}}$, when such impedance surface is loaded over a ground plane with $d = 100$ nm spacing and $n_{sub} = 1$, is plotted in Fig. 6.2(b) (setup shown in Fig. 5.2). Unsurprisingly, we successfully cover almost the entire 360° phase variation due to the artificial in-plane resonance created with the composite nanoparticle. This effect is clearly independent of the gap size between the metasurface and the back mirror because we don't rely on the propagation effects in this region to provide the required phase variation. Changing the gap distance will simply shift the entire phase curve [4]. The performance of the proposed metasurface regarding the covered spectrum of impedance, ultrathin thickness, spatial resolution, and efficiency, is far superior to other proposals at IR and optical frequencies [7]-[10]. In the following, we will refer to these surface elements as spatial phase modulators.

6.2 TUNABILITY, FREQUENCY DISPERSION, AND EFFECT OF LOSS

When a gradient metasurface is implemented based on the general class of conjoined nanoparticles with deeply subwavelength size, introduced in the previous section, we theoretically predict very large conversion efficiency to the desired scattered wave. In practice, however, several parameters may affect the ideal performance of the metasurface, including loss, deviation from center design frequency, surface granularity, and fabrication defects. Here and in the following sections we will qualitatively look into these imperfections and nonidealities to estimate their effect on the performance of the phase modulator and gradient metasurfaces. In addition, we investigate the possibility of including tunability in the design, envisioning a broader set of applications for switchable and reconfigurable wave-manipulating optical elements.

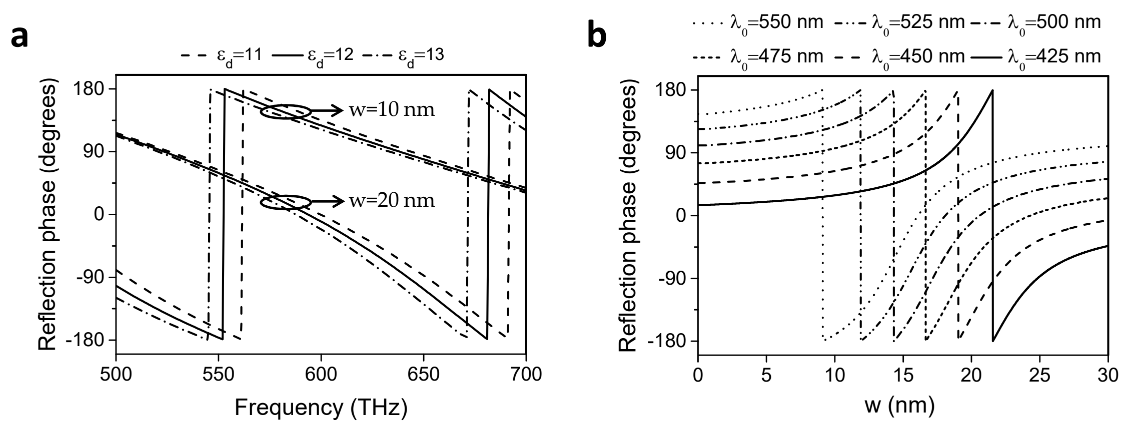

Figure 6.3: Tunability and intrinsic dispersion. (a) Reflection phase from a periodic metasurface with unit cells shown in Fig. 6.1(a). Dielectric permittivity is swept from $\varepsilon_d = 11$ to $\varepsilon_d = 13$ to tune the frequency response. (b) Evolution of the reflection phase with the wavelength. (Reproduced with permission from Physical Review B, Vol. 89, Issue 23, pp. 235419 (2014). Copyright 2014 American Physical Society).

Examining Eq. (6.1), there is an interesting possibility to add tunability to the introduced spatial phase modulator through controlling the material properties of the particle. This control may be attained in various manners such as varying temperature, external bias, intensity (when nonlinear materials are included), or doping. Figure 6.3(a) illustrates the effect of the dielectric permittivity on the phase response of the element. Dimensions and the inductive portion are kept unchanged compared to the example in Fig. 6.2, however, we assume that through one of the aforesaid methods we are capable of slightly varying the capacitive element, that is, the permittivity of the dielectric portion. Altering the nanocapacitor, the surface resonance frequency is expected to slightly shift. Indeed, as shown in Fig. 6.3(a), reflection phase which is a direct function of the surface impedance (via Eq. (5.12)) is moving along the frequency axis for different values of ε_d. Two sample filling ratios are shown here to demonstrate the tunability of the operational frequency. Such tunability may be incorporated in many applications such as a beam deflecting surface to adjust the operational frequency of the surface.

The bandwidth of operation of a gradient metasurface implemented with hybrid nanoelements depends on the frequency dispersion of the constitutive materials, as well as the dispersive propagation effect in the substrate (or spacing layers between transmitting metasurfaces). Such frequency-dependent constituents anticipate a narrow-band behavior for gradient metasurfaces that are realized with these building blocks. However, and quite surprisingly, the proposed spatial phase modulators, exhibit an exceptional frequency response that makes them a suitable choice for a wide range of radiation engineering applications. This effect resides in the rather stable frequency dispersion of the effective impedance surface when a parallel nanoresonator is utilized. Inspecting Eq. (6.1), the equivalent local reactance of the surface can be written in the general format $Z_{surface} \propto \left(\omega(\varepsilon_p + \varepsilon_d)\right)^{-1}$. In reality, and especially at shorter wavelengths, both dielectric and plasmonic permittivities are decreasing toward higher frequencies and, thus, Z_{surface} exhibits suppressed frequency dispersion compared to its constitutive materials. The remaining phase variation in the surface impedance as well as the contributing propagation in the thin substrate create a relatively linear dispersion, as verified in Fig. 6.3(b). Here, we are inspecting the variations in the reflection phase signature of the particle cluster in Fig. 6.2(b), but now for various operating wavelengths. Interestingly, although the absolute scattering phase is frequency dependent, its gradient is more or less dispersion-less. In other words, if we rely on the gradient of the scattering phase for a specific radiation pattering purpose, the operation is expected to be broadband. This is in fact the condition of interest for many applications including moderate-angle beam steering, mid- and far-field focusing, and so on. We note that this is not necessarily the case if we employ a series nanoresonator. In general, the nanoblock configuration must be chosen in view of the intrinsic material properties and the application of interest. As the proposed unit cell is simple and can be accurately and efficiently modeled with nanocircuit concepts, it is straightforward to predict the dispersion behavior of the surface and to select appropriate set of materials and geometrical combinations (parallel vs. series) to tailor the dispersion in the desired way.

Exploiting a resonant unit cell for the metasurface may rise concerns on the effects of ohmic loss in the response. This is particularly important at IR and optical frequencies as plasmonic metals typically show considerable losses over these regimes. Intrinsic material losses, however, only marginally affect the response since they are very much concentrated around the resonant point (e.g., in Fig. 6.2(a)). In addition, the interaction of the metasurface with the impinging wave is over a subwavelength thickness (e.g., $d = 40\,\mathrm{nm}$ in the previous example) which furthermore reduces the effect of the surface resistance on the reflection efficiency. This is the reason behind very high reflectivity of the metasurface even around the resonance point, as plotted in Fig. 6.2(b). Typically, less than 6% of the input power is absorbed in a gradient metasurface constructed with silver-based spatial phase modulators [4]. Employing even more lossy plasmonic metals does not drastically affect the performance. Figure 6.4(a) exemplifies the effect of higher intrinsic loss in the surface. Reflection coefficient is plotted here when we purposefully increase the collision frequency from the one of silver (low-loss metal) to moderate ($\gamma_{\mathrm{Ag}} \times 2$) and high plasmonic losses ($\gamma_{\mathrm{Ag}} \times 5$). Interestingly, the reflection phase is very stable to the surface absorption while the amplitude is also reasonably high even incorporating large plasmonic losses.

The second source of unwanted absorption in a reflecting metasurface is a non-ideal back-plane mirror. Up until here, we assumed perfect reflection from the ground plane which is modeled with a perfect electric conductor (PEC) surface. A more realistic scenario is to employ a real metal, such as silver or gold to more accurately estimate the amount of absorption due to the penetration of the fields inside the metal. Figure 6.4(b) illustrates the effect of the back-plane material on the reflection from the silver-semiconductor metasurface in Fig. 6.2. Due to the low concentration of power around this surface (as the tangential component of the electric field vanishes on the metal) an imperfect ground only slightly increases the absorbed power. The reflection phase, on the other hand, may shift down a little bit since the permittivity of the metallic plane is now a realistic finite value. It is important to underline that with the recent advances in film synthesis, it is in fact possible to realize plasmonic surfaces with absorption even less than conventional silver films [11]. In general, the total effect of loss in plasmonic metasurfaces is relatively insignificant for these effects.

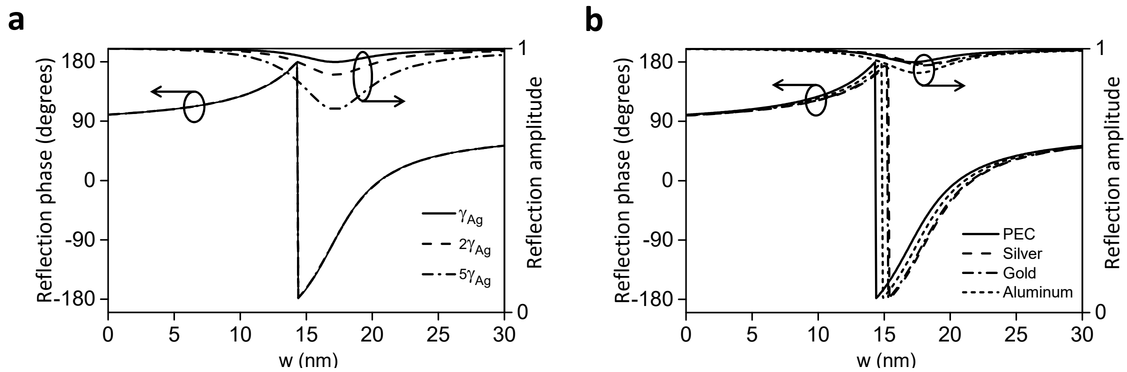

Figure 6.4: Effect of loss. Amplitude and phase of the reflection coefficient for the unit cell shown in Fig. 6.1(a) with different amounts of intrinsic loss in the plasmonic portion and (b) replacing the back mirror with realistic optical metals.

6.3 POLARIZATION CONTROL IN OPTICAL LUMPED RESONATORS

One of the rather challenging problems in the design of gradient metasurfaces is the one of providing a suitable control on their polarization response. We discussed earlier that to grant an acceptable control over the local scattering phase, some sort of resonance needs to be embedded on the surface constituents, for instance employing plasmonic nanoantennas or the proposed lumped nanoresonators. Quite remarkably, the artificial quasi-static resonance we create on the surface enables perfect control on the polarization response of the structure. We are capable of designing nanoresonators with strong polarization preference (i.e., $Y_{e,surface,xx}$ and $Y_{e,surface,yy}$ are drastically different) or, on the contrary, with the minimum sensitivity to the excitation axis, that is, $Y_{e,surface,xx} = Y_{e,surface,yy}$. Clearly, geometrically symmetric nanoresonators, such as plasmonic posts embedded in a dielectric substrate, will operate without any polarization preference. The 2D example of Fig. 6.1(a), on the other hand, can be feasibly designed to operate under a specific polarization of the incident wave.

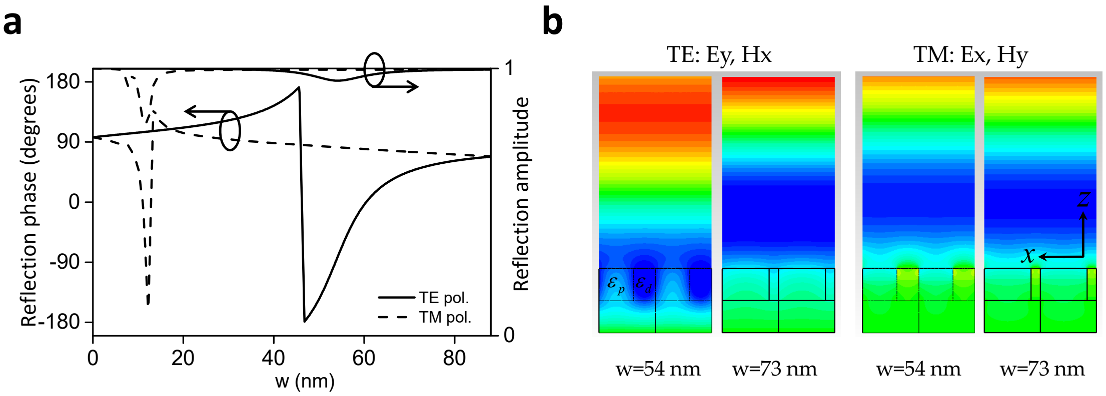

Figure 6.5: Polarization response. (a) Reflection coefficient from a grounded metasurface with the unit cell shown in Fig. 6.1(a) under two orthogonal excitations. (b) Effect of the geometry and incident polarization on the distribution of electric field over the metasurface. Two adjacent unit cells from the periodic metasurface are shown.

It is interesting to underline that this freedom in working with different polarizations is the result of exploiting lumped circuit elements. We can arbitrarily move around these circuit components on the surface to artificially create different effects for opposite polarizations (i.e., linearly polarized waves) or vice versa. This is not the case for plasmonic nanoantennas that naturally work only for the incident wave polarized along the antenna rod.

One exciting application for controllable polarization response is to create completely different effects toward opposite excitation directions. For instance, the unit cell proposed in Fig. 6.1(a) may be tailored to provide 0° to 360° phase variation under y-polarized illumination, while the same structure creates a constant scattering phase for an x-polarized wave. We designed such elements based on Eq. (6.1), and intentionally created very distinct phase signatures for parallel and series nanoresonators. The operation wavelength is $\lambda_0 = 500\,\text{nm}$ and silver-semiconductor nanoresonators are utilized in this case. The particle dimensions are set at $l = \sqrt{2}\,\lambda_0/8 = 88.4\,\text{nm}$, $d = 50\,\text{nm}$, and the metasurface is deposited on a $50\,\text{nm}$ grounded quartz (

$SiO_2, n = 1.55$) substrate. Figure 6.5(a) shows the reflection coefficient under TE (y-polarized) and TM (x-polarized) illuminations versus the width of the plasmonic portion in the cell. In the range between $w = 20$ nm and $w = 88$ nm, the resonance condition is hit under the TE illumination and a large span of scattering phase is therefore attainable. On the other hand, the TM resonance is confined around $w = 15$ nm and, over the same region, less than 20° variation is created by the metasurface for this polarization. Different interactions of the input wave and the metasurface elements are also highlighted in Fig. 6.5(b). Changing the filling ratio does not affect TM waves but it drastically modifies the TE reflection phase. The designed element can be used to realize interesting devices, such as ultrathin polarization beam splitters, which we will investigate in the next chapter.

In other scenarios, it may be of interest to realize more isotropic, and polarization-independent, devices. The concept of optical nanocircuits can be applied again in this context: it is possible to consider three-dimensional elements, as shown in Fig. 6.6, in such a way to realize polarization-independent building blocks with similar phase control features. We used numerical full-wave simulations [12] in Fig. 6.6 to demonstrate these structures, shown in the inset, are able to cover almost the entire 2π range by changing the filling ratio of the plasmonic portion over a lateral dimension of $l = \lambda_0/16$.

6.4 TRANSMITTING METAMOLECULES

To conclude this chapter we briefly discuss transmitting metamolecules that are appropriate for molding the transmitted wave from the metasurface. For such purpose, It has been shown that rather than a single metasurface, a symmetric stack of three impedance surfaces is required to provide the necessary control on the phase of the transmitted wave [13], while keeping unitary transmission amplitude. Following our discussions in this chapter, each of these layers may be straightforwardly implemented employing nanoresonator structures shown in Fig. 6.1(a). The filling ratio and spacing between different layers can be then tuned to provide the necessary requirements on the local amplitude and phase of transmission. More discussion can be found in [13].

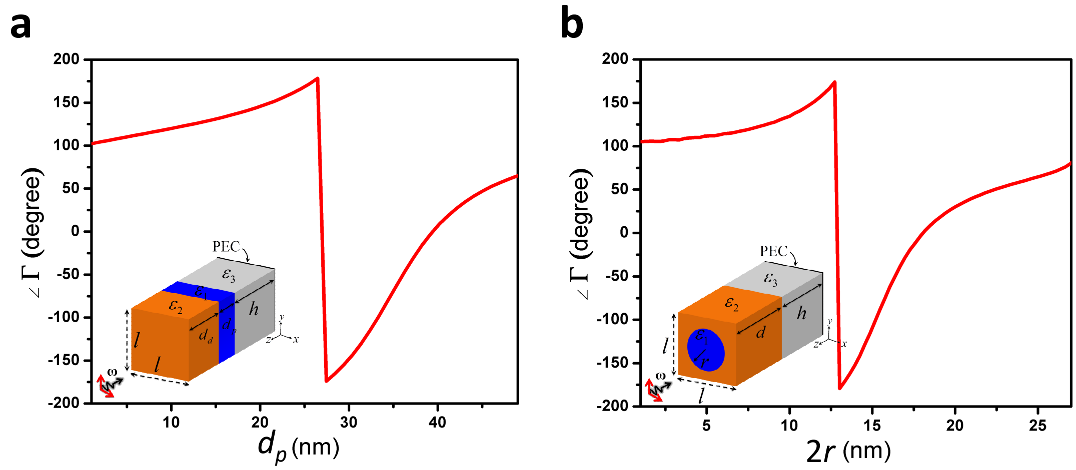

Figure 6.6: Polarization management. (a) Reflection phase variation for two dimensional periodic metasurfaces composed of the unit cell shown in the inset as a function of thickness d_p of the plasmonic segment. Dimensions are set at $h = 50$ nm, $d = d_d + d_p = 50$ nm, and $l = 31.25$ nm. The phase is calculated at $\lambda_0 = 500$ nm using full-wave numerical simulation and the permittivities of constitutive materials are $\varepsilon_1 \approx (-8.14 - 0.095j)\varepsilon_0$ (silver), $\varepsilon_2 = 12\varepsilon_0$ (Aluminum Arsenide), and $\varepsilon_3 = \varepsilon_0$ at the center frequency. (b) Same as in (a) for the concentric nano-block shown in the inset. Dimensions are set at $h = 100$ nm, $d = 40$ nm, and $l = 31.25$ nm; the diameter of the nanorods are changed to span the entire phase spectrum. All phases are calculated at a plane 300 nm above the metasurface. (Reprinted with permission from Physical Review B, Vol. 89, Issue 23, pp. 235419 (2014). Copyright 2014 American Physical Society).

6.5 References

[1] Engheta, N. (2007). Circuits with light at nanoscales: optical nanocircuits inspired by metamaterials, Science, 317(5845), 1698-1702.

[2] Alu, A., and Engheta, N. (2008). Tuning the scattering response of optical nanoantennas with nanocircuit loads, Nat. Photonics., 2(5), 307-310.

[3] Engheta, N. (2002). An idea for thin subwavelength cavity resonators using metamaterials with negative permittivity and permeability, IEEE Antennas Wireless Propag. Lett., 1(1), 10-13.

[4] Mohammadi Estakhri, N., and Alù, A. (2014). Manipulating optical reflections using engineered nanoscale metasurfaces, Phys. Rev. B, 89(23), 235419.

[5] Ordal, M. A., Bell, R. J., et al. (1985). Optical properties of fourteen metals in the infrared and far infrared: Al, Co, Cu, Au, Fe, Pb, Mo, Ni, Pd, Pt, Ag, Ti, V, and W, Appl. Opt., 24(24), 4493-4499.

[6] Adachi, S. (1985). GaAs, AlAs, and AlxGa1− xAs: Material parameters for use in research and device applications, J. Appl. Phys., 58(3), R1-R29.

[7] Yu, N., P. Genevet, et al. (2011). Light propagation with phase discontinuities: generalized laws of reflection and refraction, Science, 334(6054), 333-337.

[8] Sun, S., He, Q., et al. (2012). Gradient-index meta-surfaces as a bridge linking propagating waves and surface waves, Nat. Mater.,11(5), 426-431.

[9] Grady, N. K., Heyes, J. E., et al. (2013). Terahertz metamaterials for linear polarization conversion and anomalous refraction, Science, 340(6138), 1304-1307.

[10] Pors, A., Nielsen, M. G., et al. (2013). Broadband focusing flat mirrors based on plasmonic gradient metasurfaces, Nano Lett., 13(2), 829-834.

[11] Wu, Y., Zhang, C., et al. (2014). Intrinsic optical properties and enhanced plasmonic response of epitaxial silver, Adv. Mater., 26(35), 6106-6110.

[12] http://www.CST.com.

[13] Monticone, F., Mohammadi Estakhri, N., et al. (2013). Full control of nanoscale optical transmission with a composite metascreen, Phys. Rev. Lett., 110(20), 203903.

Chapter 7: Gradient Metasurfaces for Improved Ultrathin Optical Devices

The fundamental building blocks proposed in the previous chapter provide us with the appropriate tool to manipulate the scattering phase over a surface. The general method introduced in chapter 5 indicates that if it is possible to do so on a subwavelength scale, it is also possible to mold the outgoing wave at will. In chapter 5 we provided examples of ideal (zero-thickness) gradient metasurfaces along with a microwave reflectarray based on LC resonators. Throughout the current and the following chapter we look into various realistic devices employing this technique to imprint the desired pattern on the output, yet at optical frequencies.

To realize gradient metasurfaces and satisfy the requirements on the local scattering phase, each element is individually selected from a periodic metasurface with the appropriate scattering phase. Throughout this process we implicitly assume that the mutual coupling between neighboring elements (which are dissimilar in the gradient device) does not significantly affect their scattering properties. In other words, each nanoblock can individually provide a local scattering phase on its surface as if it is arranged in a periodic fashion. This is an acceptable assumption due to small coupling between neighboring elements in properly designed thin metasurfaces. Moreover, the subwavelength nature of inclusions we employ here to synthesize the surface allows strong field localization to implement smooth phase variations across several elements with minimum mutual coupling. The contents of this chapter partially appeared/to appear in "Mohammadi Estakhri, N.; Neder, V.; Knight, M.; Polman, A.; Alu, A., Wide-Angle, Broadband Graded Metasurface for Back Reflection, under review", "Mohammadi Estakhri, N.; Argyropoulos, C.; Alù, A., Graded metascreens to enable a new degree of nanoscale light management. Phil. Trans. R. Soc. A 2015, 373 (2049), 20140351", and

"Farhat, M.; Chen, P.; Guenneau, S.; Enoch, S., Transformation Wave Physics: Electromagnetics, Elastodynamics, and Thermodynamics, Pan Stanford, to be published".

7.1 Optical Reflectarray and Transmitarray

In analogy to microwave reflectarrays and transmitarrays, gradient metasurfaces may be suitably designed to efficiently steer the direction of the outgoing wave (anomalous reflection or refraction), realizing arbitrary beam-steering functionality. This is somewhat similar to the operation of a blazed grating which, at one specific wavelength, is able to transfer the incident energy to one of its diffraction orders. Yet, distinct from conventional blazed gratings, here the desired outgoing beam is reconstructed on the surface with very high spatial resolution enabling near-field operation, steering at very steep angles, as well as broad bandwidth (see section 5.3.2). We have studied these structures in the ideal form in chapter 5, where we realized reflectarrays through zero-thickness impedance surfaces (section 5.2). Here we look into realistic realization of these structures at optical frequencies exploiting the nanoresonator building blocks introduced in the previous chapter.

To realize anomalous reflection (or refraction) on a metasurface, the outgoing wave must follow a linear phase variation over the surface, separate from the phase profile of the excitation wave. As discussed through Fig. 5.1, for moderately small deflection angles the required surface properties can be attained with a simple ray approximation and a linear scattering phase $\angle R(x) = \alpha x$ must be enforced along the metasurface. Here, the relation between the incident angle θ_i and reflected angle θ_r is $\pm\alpha\lambda_0 = 2\pi\left(\sin\theta_r - \sin\theta_i\right)$ and x denotes the bending axis toward the surface (a 2D setup is assumed). The scattering phase profile is plotted in Fig. 7.1(b), assuming $\theta_i = 0$ and $\theta_r = -45$ degrees (in accordance to Fig. 5.1). To implement this surface, we quantize the phase profile into steps of lateral size $l = \sqrt{2}\,\lambda_0/8$, indicated by stars in Fig. 7.1(b). We notice that due to the periodicity of the required phase pattern, the profile repeats itself over each 8 elements as well. In other words, the surface exhibits a superlattice periodicity of $L = \left|\lambda_0/\left(\sin\theta_r - \sin\theta_i\right)\right| = \sqrt{2}\lambda_0$. This, however, is not an inherent requirement and we may realize the exact same scattering phase profile employing a fully nonperiodic surface. Here, to execute each phase step under TE illumination, we exploit the nanoblocks designed in Fig. 6.5, as shown in Fig. 7.1(b), lower panel.

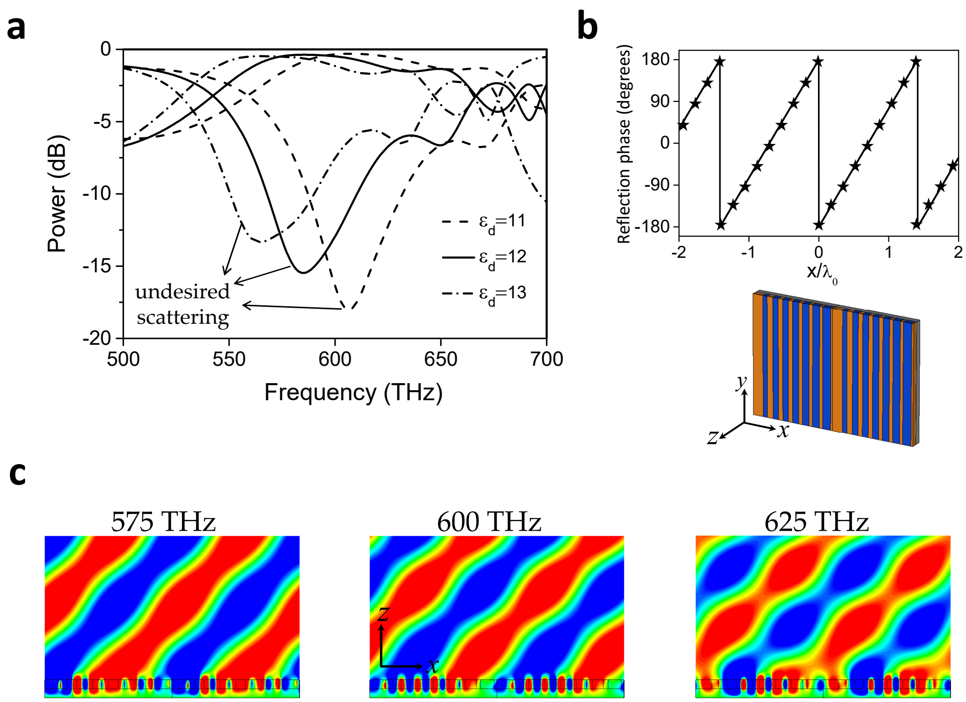

Figure 7.1: Tunable beam steering. (a) Normalized reflected power toward the desired direction when a TE-polarized plane wave illuminates the gradient metasurface shown in (b) toward the –z direction. Permittivity of the dielectric portion of the surface nanoblocks is swept from $\varepsilon_d = 11$ to $\varepsilon_d = 13$ to tune the frequency response. (b) Linear phase function to bend a normal impinging wave by 45°. Quantized phases are shown by stars on the curve, and the corresponding metasurface is shown in the lower panel. (c) Distribution of the scattered field on the incident plane (xz) at three frequencies.

Figure 7.1 illustrates the wave bending performance of the designed metasurface. After imparting the linear phase profile on the scattered wave, a normally incident wave is successfully deflected toward –45° at $600\ \mathrm{THz}$. It is important to underline the effect of subwavelength wave reconstruction in this technique. As demonstrated through the near-field plots in Fig. 7.1(c), the outgoing plane wave is generated right above the surface elements with minimal undesired evanescent waves in the surface proximity. This is the direct consequence of satisfying exact boundary conditions of Eq. (5.2) over the surface. Following the superlattice periodicity of the implemented surface, the scattered wave may be also viewed as summation of multiple scattering orders, that is, $n = 0, \pm 1, \pm 2, \ldots$ Floquet modes, of a periodic structure. Enforcing a plane wave toward $\theta = \theta_r$ (similar to Eq. (5.6)) as the ideal scattered wave is subsequently equivalent to entail the corresponding amplitude of all spatial orders to be zero, except for the $n = +1$ mode which is the plane wave toward the desired direction. In this regard the efficiency of the anomalous reflection (as opposed to specular reflection) can be defined as the ratio of the input power coupled to the first diffractive order (–45° in this example) to the total incident power. Figure 7.1(a) shows the normalized power coupled to the first diffractive order in comparison to the all other directions, versus excitation frequency. At the center design frequency $600\ \mathrm{THz}$ around 90% of the total power redirects toward –45°, 5% is scattered to unwanted spatial orders, and the rest get absorbed in the metasurface. We recall here that for simplicity of implementation, the lossy/gain portions of the surface response are forced to zero from the ideal scenario in Fig. 5.1, yet conversion efficiency above 90% is achieved. The performance of the surface is also very stable with frequency and sustains over 20% bandwidth (–3 dB bandwidth). We point out that a wave-squinting effect is naturally present owing to the dispersion of the Floquet modes. As a result, the reflection angle slightly varies over frequency, yet still the dominant portion of the input wave couples to the first diffraction order in this regime. The broadband operation of the surface is predictable if we inspect the nature of the process: an additional linear phase is imparted on the input, but, the absolute value of the phase is not a parameter in this process and the curve in Fig. 7.1(b) may have any arbitrary offset on the vertical axis. We discussed in Section 6.2 that the plasmonic-dielectric nanoblock maintains a stable phase profile over broad bandwidths and it merely adds a dispersive phase offset to the surface (Fig. 6.3(b)), which results in a broadband response for beam-steering applications. We underline again that the total wave manipulation process is accomplished here simply employing a single gradient metasurface with $50\ \mathrm{nm} \approx \lambda/10$ thickness, and composed of two alternating materials.

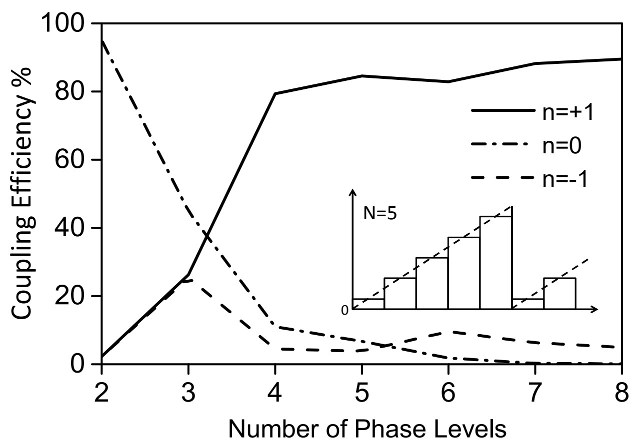

Figure 7.2: Discretization effect. Coupling efficiency to the propagating diffraction orders as a function of quantization levels for the phase profile shown in Fig. 7.1(b). Inset illustrates the case of $N = 5$.

There is a possibility to tune the frequency response of the surface by tailoring the properties of the nanoresonators. We looked at this option for the nanoblocks in Section 6.2 and here we examine this concept at the device level. As shown in Fig. 7.1(a), maximum coupling range can be effectively tuned along the frequency by changing the permittivity of the dielectric portion of nanoresonators. In practice, the permittivity may be altered with temperature, optical tuning or via nonlinear effects. Tunable, or reconfigurable beam-steering surfaces are envisioned based on this effect, with which we may efficiently control the frequency signature (i.e., color) of the steered beam with external bias. While we looked into practical implementation of reflectarrays at optical frequencies, we note that the building blocks introduced in section 6.4 can be used to implement similar functionalities in transmission. In this regard, the scattering phase of a moderate-angle transmitarray is enforced to be linear to deflect the wave as the wave pass through the surface. More details on transmitting beam-steering metasurfaces can be found in [1].

To conclude this section, we investigate the effect of surface granularity on the performance of a gradient metasurface. Clearly, it is not possible to realize the required phase with infinite resolution and we always need to somehow quantize the phase pattern. Intuitively, more quantization levels appear to provide larger conversion efficiency to the desired scattering pattern (see section 5.3.1 for a discussion on the effect of quantization of ideal surface profile). To gain a quantitative rule for our design, we study the effect of discretization on the performance of the beam-steering example. A gradient metasurface is designed to deflect a normally incident plane wave toward –45 degrees at $\lambda_0 = 500\ \mathrm{nm}$. The superlattice periodicity (Fig. 7.1(b)) equals $\sqrt{2}\lambda_0 = 707\ \mathrm{nm}$ which is now filled with $\mathrm{N} = 2,3,...,8$ different phase units (The previous example considered the case of $\mathrm{N} = 8$). For each discretization number, the appropriate unit cell is designed employing silver-semiconductor resonators with $d = 50\ \mathrm{nm}$ thickness, deposited on $50\ \mathrm{nm}$ quartz substrate. Figure 7.2 indicates the distribution of the power to different diffraction orders for these gradient metasurfaces. The incident power essentially couples to three propagating Floquet modes, where $n = +1$ indicated the desired direction of –45°. As expected, the efficiency of conversion to this mode increases as the discretization gets finer and finer. For $\mathrm{N}=2$ and 3, the surface exhibits odd, and even scattering symmetries and thus equal amount of power couples to $n=\pm 1$ modes. For $\mathrm{N}>3$ an artificial directional preference is obtained on the surface and therefore efficiency of coupling to $n=+1$ increases rapidly. Above $\mathrm{N}=4$, which represents a unit cell size of $l=176\ \mathrm{nm} \approx \lambda_0/2.8$, we attain a reasonable performance from the structure. It must be noted that in this particular example, the metasurface exhibits a superlattice profile which in return creates a collective grating effect on top of the local phase management of the nanoresonators. In other applications, and to create a strong sense of local variation, a unit cell size of at least $\lambda_0/5$ is desirable. The minimum size of the surface element is a technological consideration related to the limitations of the considered fabrication methods; the composite nanorasonator block considered here can inherently provide a very large spatial resolution [2].

7.2 EXPERIMENTAL IMPLEMENTATION OF PLANAR NEGATIVE REFLECTION

In this section, we discuss the design of a specific kind of optical metasurfaces that are tailored to couple the majority of the incident energy toward the first negative diffraction order. These devices are typically known as Littrow gratings, which we implement here using subwavelength textured metasurfaces. We devise the metasurface to provide optimal retroreflection for an off-axis angle, and relying on the broadband and non-resonant nature of the wave transformation from the gradient surface we achieve negative reflection over considerably large bandwidth.

7.2.1 Design of ideal metasurface backreflector

Following the general approach in chapter 5, we focus first on the design of an ideal gradient metasurface that reflects back all the impinging energy for a specific frequency and angle. We will then study a practical realization obtained by simplifying the design for fabrication. Fig. 7.3(a) shows the concept and a schematic of the fabricated structure. While an ideal homogeneous mirror as shown in Fig. 7.3(b), reflects the impinging light towards the specular direction due to momentum conservation, an ideal metasurface with tailored gradient of the reflection phase as shown in Fig. 7.3(c), can impart a suitable additional negative transverse momentum to the impinging wave, reflecting the entire impinging light flux back to the source.

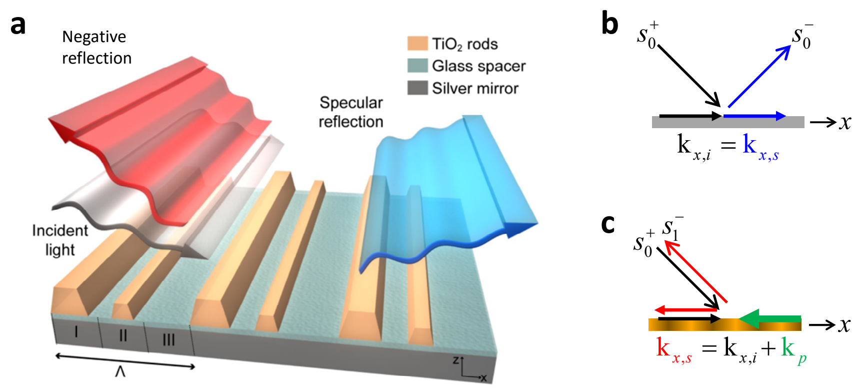

Figure 7.3: Operation principle of a metasurface backreflector. (a) Schematic illustration of negative reflection from a gradient metasurface. (b,c) Illustrative representation of scattering channels. (b) Specular reflection from an ideal mirror: incident light (s_0^+,black) is specularly reflected (s_0^-,blue) from an ideal mirror due to momentum conservation at the interface. (c) Backreflection from a gradient metasurface: incident light is reflected back (s_1^-,red) toward the source due to the transverse momentum imparted by the inhomogeneous interface. The additional negative momentum k_p (green) is introduced by a tailored gradient of the reflection phase. Momenta in the x-direction are shown by $k_{x,i}$ and $k_{x,s}$ for incident and reflected waves, respectively.

The analytical expression of the local reflection coefficient that an ultrathin metasurface needs to support to achieve retroreflection with unity efficiency for illumination angle θ_0 in the $x-z$ plane, where $\hat{z}$ is the normal to the surface, reads

$$R(x) = \frac{-1+\cos\theta_0 - e^{\frac{2i\pi x}{\Lambda}}\left(1+\cos\theta_0\right)}{-1-\cos\theta_0 + e^{\frac{2i\pi x}{\Lambda}}\left(-1+\cos\theta_0\right)}. \tag{7.1}$$

As we discussed in chapter 5, for the special case of retroreflection the required reflection coefficient is unitary all across the surface, implying that it can be achieved with a fully passive interface with inhomogeneous phase profile $\phi(x)$, shown in Fig. 7.4(a) for $\theta_0 = 35.7$ degrees, with period $\Lambda = \frac{\lambda}{2\sin\theta_0}$, where λ is the wavelength of operation in free-space. This phase profile compensates for the momentum mismatch between the incoming and the desired retroreflected waves (Fig. 7.3(c)).

For an ideal continuously modulated metasurface with local reflection in (7.1), given the periodicity of the reflection phase, the reflected power can couple to only two propagating diffraction orders, the specular reflection s_0^- and the backreflection order s_1^-. The numerically calculated coupling efficiency to these orders as a function of illumination angle is shown in Fig. 7.4(b) for the surface with phase profile in Fig. 7.4(a).We implemented the phase profile following the method described in section 5.2.2. The variation in the phase of the local reflection coefficient is effectively implemented by varying the surface admittance at a subwavelength distance from an ideal mirror (a perfect electric conductor). The obtained surface profile is modeled as a sheet admittance in COMSOL, with $d = \lambda/20 = 35\,\text{nm}$ for the distance between the sheet admittance $Y_{e,surface}$ and the ground plane. The relation between the local phase and the admittance is $\eta_0 Y_{e,surface} = -i\tan\left(\phi(x)/2\right) + i\cot k_0 d$ where $\phi(x) = \angle R(x)$ and η_0 is the free-space characteristic impedance [2].

As expected, we obtain 100% coupling efficiency at $\theta_0 = 35.7$ degrees, i.e., $\left|s_1^-\right|^2 = 1$. In addition, the figure shows that the angular response is considerably robust, and for the angular range $11 < \theta_{in} < 80$ degrees over half of the incident power is redirected into the non-specular direction. This broad angular response is associated with the fact that the momentum imparted by the surface does not change with the incidence angle [13], and it is sufficiently negative to ensure that the angle of the emerging reflected beam stays negative over a very broad angular range. The negative reflection angle varies as a function of impinging angle following the grating equation for first-order diffraction $\theta_{retro} = \sin^{-1}\left(\sin\theta_{in} \mp \frac{\lambda}{\Lambda}\right)$, where the $\mp$ sign refers to $\theta_{in} > 0$ and $\theta_{in} < 0$ respectively, as plotted in Fig. 7.4(c). Yet, the scattered beam always lies in the same half-plane as the incident one. The lower cut-off for $\theta_{in} = 11$ degrees is simply determined by the cut-off of s_1^- for close-to-normal incidence.

An interesting feature evident in Fig. 7.4(b) is the inherent symmetry in response of the backreflective surface, a symmetry that arises despite the fact that its geometric profile, is asymmetric and tailored for a specific oblique illumination. This symmetry is not limited to this particular configuration, but it is a general result stemming directly from reciprocity [3]-[4]. More specifically, if the surface is designed to backreflect with unity efficiency for the impinging angle θ_0, it ensures zero coupling to the specular direction. Reciprocity then ensures that, when illuminating the surface from the specular direction, no power can be coupled back towards θ_0, indicating that there is no trade-off between directionality and efficiency in this metasurface. As we described in section 6.2 and discuss in the following section, the angular robustness of the metasurface response, associated with its non-resonant performance properties, is also reflected in an inherently broadband operation [2], and in strong robustness to variations in the spatial profile of Fig. 7.4(a).

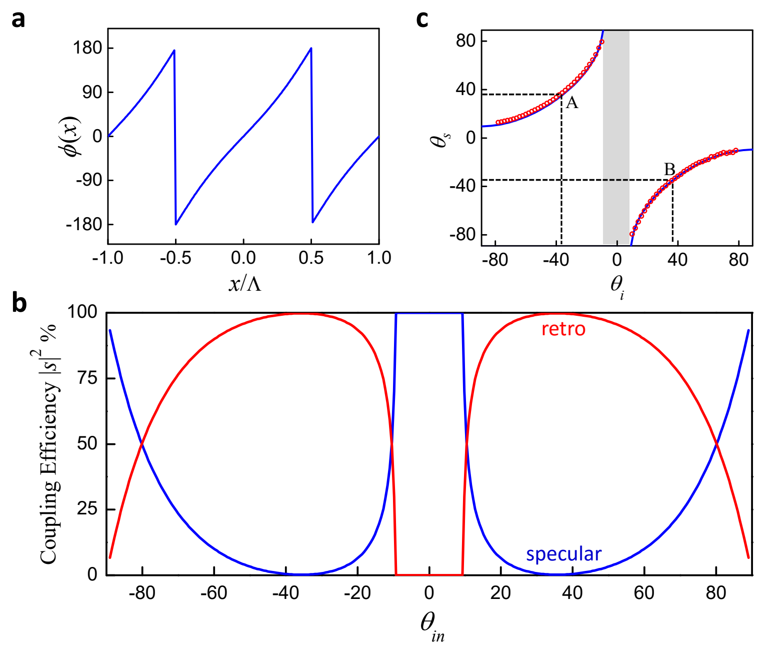

Figure 7.4: Wide angle operation of an ideal negative reflection metasurface (a) Calculated local phase profile of the ideal surface $\phi(x) = \angle R(x)$, designed for an incoming angle $\theta_0 = 35.7$ degrees following (7.1), with surface period $\Lambda = \lambda/(2\sin\theta_0)$. (b) Numerically calculated coupling efficiency of the ideal surface in panel (a) for different incident angles and for s-polarized illumination. Blue and red curves show the percentage of power coupled toward the specular direction (s_0^-) and first diffraction order (s_1^-), respectively. (c) Calculated (solid black line), and measured (yellow circles) angular dispersion of the gradient surface for the ± 1 diffraction orders. The black lines correspond to the ideal surface in panel (a) and the yellow circles are analogous results measured at $\lambda = 700$ nm for the fabricated sample. A and B correspond to the ideal retroreflection points where $\theta_{retro} = -\theta_{in} = \pm 35.7$ degrees. Inside the highlighted gray region, the non-specular diffraction orders are evanescent.

7.2.2 Practical implementation of the metasurface

In order to practically realize the metasurface with a nanostructured surface, we need to discretize the ideal profile. Assuming an equal discretization of the ideal phase profile into N phase steps, the coupling efficiency to the retroreflected order gets closer to 100% as the number of steps increases. Interestingly, however, even a coarse discretization, i.e., a phase profile with same period but only two discretization steps, yields a retroreflection efficiency larger than 75%. Compared to Fig. 7.2, we notice that here the surface supports only two propagating diffraction modes and thus we get large coupling even with two phase steps.

We realized the device characterized in Fig. 7.4(a) using a nanostructured dielectric metasurface (Fig. 7.5(a,b)) with subwavelength thickness $t = 100\,\mathrm{nm}$, made of TiO_x trapezoidal rods on top of an Ag mirror via e-beam lithography and evaporation. An schematic of the fabricated structure is shown in Fig. 7.3(a). The dielectric nature of TiO_x, and its relative high index, are ideal to minimize absorption and provide enhanced phase control over an ultrathin thickness. We designed the structure with three phase discretization steps, $\mathrm{N} = 3$, for operation at $\lambda = 700\,\mathrm{nm}$, tailored for s-polarized excitation. The phase variation of the local reflection coefficient in the first two elements is achieved by controlling the geometry of the nanorods, so that they impart the required reflection phase uniformly over their width, while for the third segment we simply employed the bare back-mirror (Fig. 7.5(a)).

For fabrication, a 1-mm-thick Si wafer was coated with 200 nm of Ag and 20-30 nm of SiO_x by thermal evaporation. This protected mirror was then spin-coated with ZEP520a, a high-resolution negative tone resist and Espacer 300z to improve the conductivity of the sample. Then the asymmetric grating was written by E-beam lithography using a 20 keV beam. The patterned area was $1.5 \times 1.5\,\mathrm{mm}^2$ square, comprised of stitched $100 \times 100\,\mu\mathrm{m}^2$ write fields. Afterwards, the sample was rinsed 30 seconds in water to remove the Espacer and developed in pentylacetate for 45 seconds, rinsed 15 seconds in a mixture of methyl isobutyl ketone and isopropanol (MIBK:IPA,9:1), dipped into IPA and transferred to ethanol. To prevent collapse of the fragile resist patterns the sample was dried at the critical point. The lines were then filled with 100 nm of TiO_x by e-beam evaporation followed by lift-off which was done by dissolving the resist for 10 minutes in an ultrasonic bath in anisole.

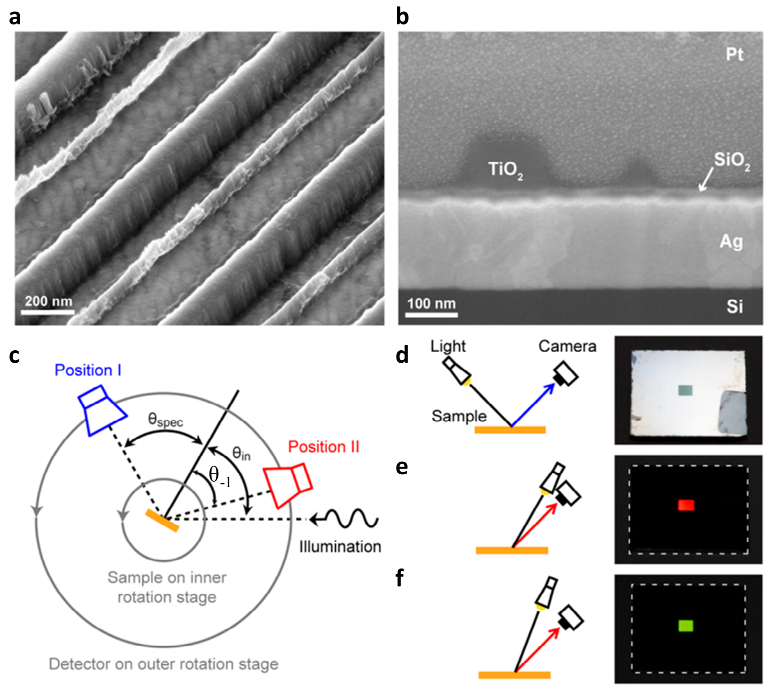

Figure 7.5: Fabricated structure and measurement setup (a) SEM image (top view, under 40% tilt) and (b) cross section of the fabricated sample. One unit cell of the structure is composed of three regions: two TiO_x nanorods and the bare mirror. See Methods section for detailed geometry information. The Pt layer on top of the sample was added in the cross-section fabrication process to get a clean cross-section. (c) Schematic of the measurement setup: Angle of illumination θ_{in} can be changed by rotating the sample on the inner rotation stage while the illumination arm is kept fixed. The coupling intensity to the different diffraction orders is measured by independently rotating the detector on the outer rotation stage to positions I to measure θ_{spec} or position II to measure θ_{-1}. Illumination and detection planes are slightly tilted horizontally to allow retroreflection measurements without blocking the illumination. (d)-(f) Photographs of the fabricated structure on the right ($1.5 \times 1.5\,\mathrm{mm}^2$ square in the center of $12 \times 12\,\mathrm{mm}^2$ silver mirror, bare Si residual from fabrication process in left lower corner) and schematic of photography setup on the left. (d) Specular response under illumination from the back with a commercial flashlight: observing no reflection in the specular direction from the structure (dark square in the middle). (e)-(f) Negative reflection response of the sample when illuminated with a commercial flashlight for different angles. The angle between light and camera was increased in (f) compared to (e).

TiO_x was also evaporated directly on a Si wafer to allow a determination of the TiO_x dielectric function using spectroscopy ellipsometry, fitting the data using a Gaussian-Cauchy model. Completed dimensions were measured using a focused ion beam (FIB, FEI Helios Nanolab 600) to cut cross sections, with dimensions measured by electron micrographs. The metasurface consisted of repeating in unit cells with a periodicity of 605 nm. The taller line had a height of 100 nm, a bottom width of 180 nm and a top width of 100 nm. The narrower line, separated from the tall line by a gap of 123 nm, had a height of 50 nm with bottom and top widths of 70 nm and 20 nm respectively [5].

7.2.3 Measurement and performance characterization

We excited the fabricated structure with a weakly converging beam to allow a well-defined excitation angle, and we measured the reflected intensity in the same half-plane as the incident beam using an optical power meter. By measuring the total beam power, the absolute reflectance was then determined. The sample was mounted in the center and the power meter on the outer ring of a rotating stage, while the illumination direction was held constant. This enabled independent control of excitation and sampling angles, as depicted in the schematic of the measurement setup in Fig. 7.5(c). We chose $\Lambda = 605\,\text{nm}$ to enable efficient retroreflection in the free-space wavelength range $\lambda = 490 - 940\,\text{nm}$.

Fig. 7.5(d-f) visualizes the negative and specular reflection efficiency of our fabricated sample from the practical observer standpoint. The photographs of the samples can be seen next to the schematic of the photography setup. In Fig. 7.5(d) the bright specular reflection of the Ag mirror around the structure is visible while the dark square in the middle of the sample where the metasurface is placed indicates that specular reflection is almost absent. In contrast, the center of the sample is noticeably bright for an observer sitting close to the excitation source, as can be seen in Fig. 7.5(e,f) for different incoming angles. The bright color that can be observed in negative reflection depends on the angle of observation and illumination.

The efficiency of negative reflection is quantitatively demonstrated in Fig. 7.6. Owing to the scattering symmetry of the device imposed by reciprocity, the measurement process could be reduced to only half of the angular range, but to confirm our theoretical results we performed measurements across the entire angular spectrum. In the figure, we compare the specular reflection to the measurements obtained using a flat silver mirror, similar to the ground plane utilized in our device, allowing a direct comparison that provides a quantitative calibration of the measured efficiency. The grey circles in Fig. 7.6(a) present the measured angular response of the silver mirror when illuminated with s-polarized light at $\lambda = 700\,\mathrm{nm}$. We observe that around 10% of the incident power is absorbed in the silver or lost through diffused scattering as a result of the sample roughness and disorder. The measured response of the silver mirror is slightly lower than the simulated one, also shown in Fig. 7.6(a). This is due to the roughness of the surface by evaporation and other fabrication defects. With the dielectric metasurface in place, specular reflection significantly drops over a wide angular region around the retroreflective angle $\theta_0 = 35.7$ degrees. The scattered power is focused toward the backward diffraction channel (s_1^- in Fig. 7.3(c)), yielding a coupling efficiency of 88% under illumination at $\theta_0 = 35.7$, and with less than 10% of the impinging power being absorbed or diffusely scattered at the design frequency under illumination from all angles, except around the Wood's anomaly, consistent with the absorption levels obtained from the bare silver back-mirror.

7.2.4 Numerical simulations

For comparison, the solid lines in Fig. 7.6(a) show the calculated coupling to the two scattering orders obtained using full-wave simulation for a structure with the same geometry as the fabricated device. Numerical simulations were carried out by the 2D finite-element software COMSOL Multiphysics in the frequency-domain radio-frequency module. To model the fabricated device, we used the SEM images in Figs. 7.5(a,b) and estimated the dimensions as described in the fabrication process. All materials are modeled as dispersive and lossy and we used realistic values for the permittivities of silver and SiO_x from experimentally retrieved data sets [6]-[7]. For TiO_x, we measured the refractive index for a sample of TiO_x on a Si wafer by spectroscopic ellipsometry. Maximum element size of 20 nm is used for high-index TiO_x rods and the remaining parts are meshed with maximum element size of 28 nm. Silver layer with thickness of 200 nm is used as the back reflector which we truncated with perfectly matched layer to model a semi-infinite ground plane. The scattering parameters of the port are used to calculate the percentage of the power coupled toward each channel. The simulated results agree very well with our experiment, even though a slightly lower cut-off at large angles is observed in the measured data compared to the calculated curves. This is due to the small size of our sample, as the area where the measurement beam hits the structure increases with higher incoming angles and exceeds the structure area for $|\theta_{in}| > 60$ degrees. In this angular range, part of the light is specularly reflected by the bare mirror next to the structure.

To further investigate the frequency dispersion of the surface, we also determined the amplitude dispersion of the coupling to the two scattering modes for a structure with the dimensions of the fabricated device through full-wave simulations for all incident angles. As expected, the designed metasurface operates over an extremely broad half-power wavelength range $\lambda = 490 - 940$ nm in terms of retroreflection efficiency. We verified our simulations with experimental measurements at multiple wavelengths, in addition to the $\lambda = 700$ nm case, and as expected, they are in good agreement at all measured wavelengths.

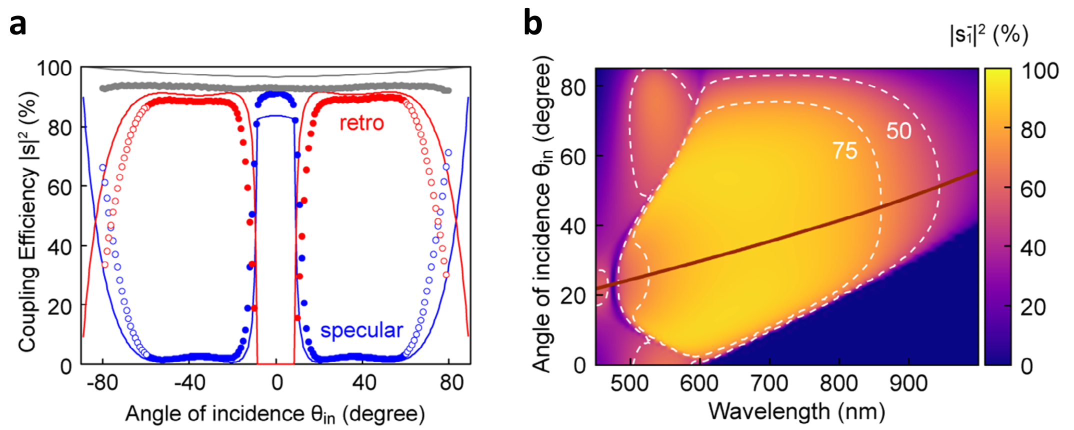

Figure 7.6: (a) Angular response at $\lambda = 700$ nm. Comparison between measurements (circles) and numerical simulations (solid lines). Coupling efficiencies for the specular reflection s_0^- and the first-order negative reflection s_1^-, are shown with blue and red colors, respectively. The empty circles indicate reflection measurements for angles above $|\theta_{in}| = 60$ degrees, for which the spot size of the beam is larger than the structure and part of the beam is specularly reflected by the mirror next to the structure. The measurements and simulations of the bare mirror are depicted in grey. The homogenous surface supports specular reflection with approximately 10% absorption across all angles. (b) Numerical simulation results of the angular/frequency dispersion of the structure with the fabricated dimensions, showing the coupling efficiency toward the first-order negative reflection s_1^- and highlighting the 75 %-power and 50 % - power operation regions. The dark red line indicates the retroreflective loci, for which the incoming and the reflected wave are aligned. More than 50% retroreflection is achieved across $\lambda = 490 - 940$ nm and $\theta_{in} = 24 - 51$ degrees.

7.3 Flat Lens

Figure 7.7 shows another planar device based on gradient metasurfaces: a flat ultrathin lens. In the ray optics regime, flat lenses impart a quadratic phase distribution (as shown in Fig. 7.7(b)) on the outgoing wave so that an incident normal plane wave efficiently converts to a spherical wave. Gradient metasurface-based lenses exhibit many advantages in terms of compact size, conformability, and the possibility of direct integration into optical systems. Through appropriately engineering the dispersion of unit cells, it is also possible to reduce the typical aberration effects present in conventional lenses [8]. These features make gradient metasurfaces an appealing choice to realize electromagnetically thin lenses over wide range of frequencies (see, for example, Refs. [1]-[2],[8]-[10]). The most interesting property of this technique, however resides in the ability of tailoring the outgoing wavefront with high spatial resolution. This enables us to set the focal point arbitrarily close to the surface and realize lenses with very high numerical apertures (see section 5.5).

Here we construct a mirror lens at $\lambda_0 = 500\,\mathrm{nm}$ exploiting the nanoblocks characterized in Fig. 6.2, assuming a 2D variation on the surface and TE polarization of the incident wave. With the focal point at $f_\mathrm{L} = 2\lambda_0$, the required phase distribution along the surface can be estimated with ray optics and as (see Fig. 5.9),

$$\angle R(x) = 2\pi/\lambda_0 \left(\sqrt{x^2 + f_\mathrm{L}^2} - f_\mathrm{L}\right), \tag{7.2}$$

which is implemented in the form of a graded metasurface after proper discretization, as shown in Fig.7.7(b). Owing to the relative value of the scattered phase, we expect broadband focusing behavior from the structure, as demonstrated in Fig. 7.7(a,c). While the surface is designed at $600\,\mathrm{THz}$, it exhibits remarkable focusing properties over more than 30% fractional bandwidth.

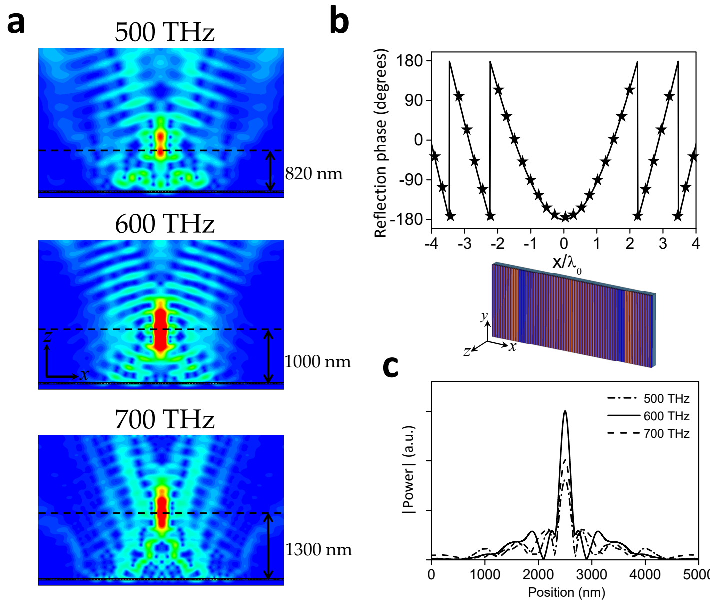

Figure 7.7: Broadband beam collimation. (a) Power density distribution of a flat mirror lens at three sample frequencies. The metasurface is illuminated along the –z axis with a Gaussian beam profile and under TE polarization. (b) Quadratic phase function to focus the impinging wave at distance $2\lambda_0$ from the surface. Quantized phases are shown by stars, and the corresponding metasurface is shown in the lower panel. The numerical aperture of the lens is 0.9. (c) Power density along the focal plane, indicated by dashed lines in (a).

7.4 Polarization beam splitter

A polarization beam splitter is an optical device intentionally designed to distinguish different polarization states of an unpolarized optical beam. Conventionally, natural birefringent materials, such as calcite crystals, may grant such functionality through creating beam displacement between orthogonal polarizations or by reflecting one polarization state while fully transmitting the other. These effects are yet naturally weak and entail long-distance propagation of the optical beam inside the birefringent crystal to accumulate the desired levels of extinction ratio. Graded metasurfaces offer a potential solution to these inherent limitations, as the metasurface elements can be designed to exhibit a drastically polarization-dependent scattering signature as discussed through section 6.3.

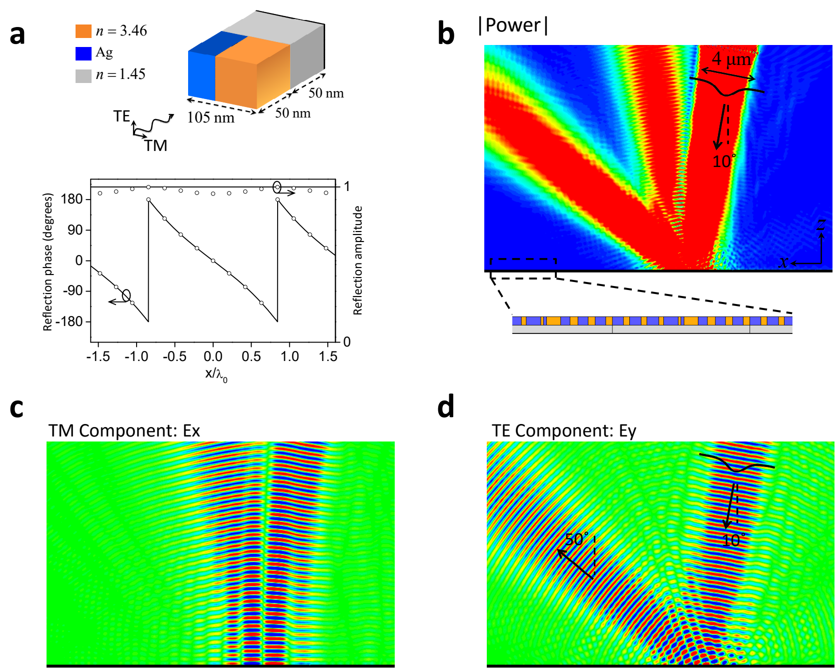

Figure 7.8: (a) Upper panel: surface admittance units used to realize the graded beam splitting metasurface. The filling ratio between dielectric and plasmonic portions are varied to imprint the desired surface pattern. Lower panel: local reflection coefficient along the surface to deflect an incident TE plane wave (solid lines). Circles indicate physically implemented elements, with each superlattice period divided into eight steps. (b) Power density distribution when the metasurface is illuminated with a Gaussian circularly polarized beam at $\lambda_0 = 500$ nm . The illumination angle is $\theta_i = 10°$ and the reflection angles are designed at $\theta_{r,\mathrm{TE}} = 50°$ and $\theta_{r,\mathrm{TM}} = 10°$. Time snapshot of the (c) TM and (d) TE components of the total electric field. (Reprinted with permission from Philosophical Transactions A, Vol. 373, Issue 2049, pp. 20140351 (2015). Copyright 2015 The Royal Society Publishing).

With the proper choice of surface admittance, graded metasurfaces can be designed to enforce distinct functionalities based on the polarization of the excitation field, e.g., to steer incident light into different directions under TE or TM illuminations [11]. To further outline our proposed point-by-point scattering management technique introduced in chapter 5, in this section we design and implement a beam steering surface to redirect an obliquely incident TE plane wave illuminating the surface at $\theta_i = 10°$ toward $\theta_{r,\mathrm{TE}} = 50°$ while the TM wave experiences a specular reflection and $\theta_{r,\mathrm{TM}} = 10°$. The metasurface creates an abrupt birefringence with 40 degrees divergence angle at the design wavelength of 500 nm, emulating the functionality of a Wollaston prism over an ultrathin profile, with the potential of integrability into nanophotonic systems and polarization control at the subwavelength scale.

The required local reflection coefficient of the surface is analytically calculated and plotted in Fig. 7.8(a) (solid lines). For a physical implementation of the structure, the surface profile is divided into eight equally sized segments within each supercell, which we then realize using the conjoined particle illustrated in Fig. 7.8(a) (upper panel). In this case we consider a substrate thickness $d = 50\,\mathrm{nm}$ and $n_{\mathrm{sub}} = 1.45$. The parallel sheet admittance $Y_{e,surface,yy}$ is effectively controlled by varying the filling ratio of the plasmonic portion. Over this range, $Y_{e,surface,xx}$ is approximately constant and the variations in the TM reflection phase $R_{surface,\mathrm{TM}}$ is less than 30 degrees, ensuring efficient specular reflection for this polarization. Incident and scattered TE waves are expressed analytically as,

$$\begin{aligned}\left(\vec{E}_i, \vec{H}_i\right) &= \left(\hat{y}, \frac{\hat{x}\cos 10 + \hat{z}\sin 10}{\eta_0}\right) E_0 e^{-j\sin 10 k_0 x} e^{j\cos 10 k_0 z} \\ \left(\vec{E}_s, \vec{H}_s\right) &= \left(\hat{y}, \frac{-\hat{x}\cos 50 + \hat{z}\sin 50}{\eta_0}\right) \sqrt{\frac{\cos 10}{\cos 50}} E_0 e^{-j\sin 50 k_0 x} e^{-j\cos 50 k_0 z}\end{aligned}, \qquad (7.3)$$

where a scaling factor $\sqrt{\cos 10 / \cos 50}$ is added to the scattered wave to ensure power conservation in the normal direction (i.e. along z-axis). Eq. (5.10) is then solved for the local reflection coefficient of the ideal surface as plotted in Fig. 7.9(a). Since both incident and scattered waves are plane waves, the acquired surface is periodic with fundamental period of $L = \lambda_0 / (\sin 50 - \sin 10) = 844\ \text{nm}$. The local surface properties are in general complex, as in this example, and as the result reflection magnitude is non-unitary. In fact, the ideal surface hold alternative lossy/gainy portions as indicated by $|R|<1/|R|>1$ in Fig. 7.9(a). To obtain the passive approximation of the structure, in this example we simply enforced $|R|=1$ while keeping the ideal reflection phase profile at eight discrete points in each period (shown by circles in Fig. 7.8(a)). Figure 7.9(b), moreover, shows the variation of reflection coefficient under TE illumination for the composite particle in Fig. 7.8(a), sweeping the filling ratio of silver in each cell (solid lines). The circles correspond to picked dimensions for each element and the triangles show the reflection phase for the exact same structure, under TM illumination (amplitude is ≈ 1). As discussed earlier, surface properties are almost constant under TM incidence while the TE wave is deflected based on (7.3).

The discrete points on Fig. 7.8(a) indicate the physically realized local reflection coefficients for the graded metasurface, also schematically shown in Fig. 7.8(b). Numerical simulations [12] of the designed surface under plane wave illumination confirm that over 91% of the incident TE component, and less than 0.19% of the TM component, are redirected toward $\theta_r = 50°$ direction, while 98% of the incident TM wave and less than 1% of the TE polarized wave is reflected toward $\theta_r = 10°$. We further examine the performance of the designed structure when illuminated by a finite size, circularly polarized Gaussian beam, as shown in Fig. 7.8(b). The incident wave clearly splits into two branches, which we verified to be TE and TM in the field plots presented in Fig. 7.8(c,d). In addition, the considered plasmonic-dielectric composite particles have been demonstrated to have a stable frequency dispersion (section 6.2). While the scattering properties of each building block may change with frequency, the reflection phase from the surface maintains an approximately constant profile, as all elements experience similar phase variations and dispersion. In a periodically arranged graded metasurface (which is the case for polarization beam splitter), the absolute phase center is arbitrary and hence, the device operation is predicted to be relatively broadband. Our numerical simulations confirm more than 15% fractional bandwidth, ranging between 560-660 THz, over which at least -3db of the incident wave is coupled to the desired modes (half power bandwidth). We note that the fixed periodicity of the surface, imposes an additional wave squinting along frequency and the direction of the TE wave varies between $\theta_{r,\mathrm{TE}} = 53.9°$ and $\theta_{r,\mathrm{TE}} = 45.4°$ as we move from 560 to 660 THz.

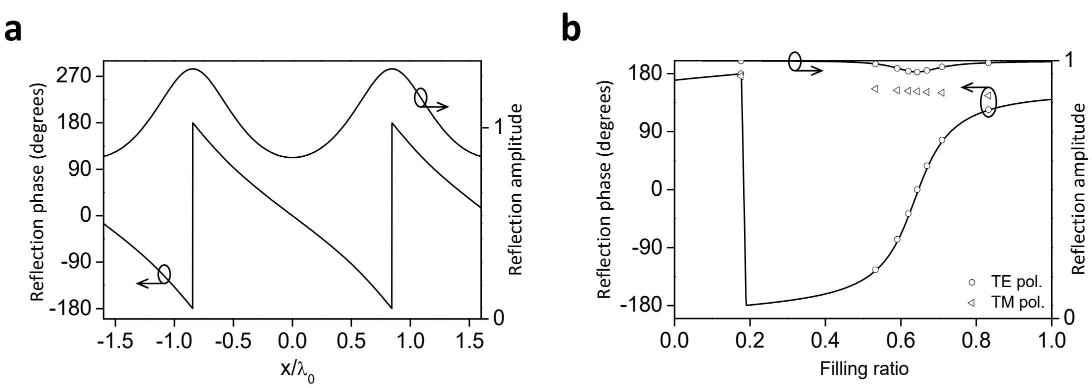

Figure 7.9: (a) Ideal local reflection coefficient on the graded surface to deflect obliquely incident TE wave toward $\theta_{r,\mathrm{TE}} = 50°$. (b) Reflection coefficient from a periodic metasurface with surface elements shown in Fig. 6.1(a), under TE illumination, varying the filling ratio of plasmonic metal (solid lines). Circles indicate the realized element and triangles show the reflection phase of the same surface if illuminated by a TM plane wave. (Reprinted with permission from Philosophical Transactions A, Vol. 373, Issue 2049, pp. 20140351 (2015). Copyright 2015 The Royal Society Publishing).

7.5 Broadband energy harvesting

Due to weak light matter interactions inside its absorbing material, a thin film solar cell intrinsically absorbs only a small percentage of the incoming wave, proportional to its physical thickness. However, around the natural Fabry-Perot resonances of the film, a strong vertical standing wave is created inside the slab and relatively high absorption levels may be attained from the structure. Here, we present a way to employ graded metasurfaces as ground planes for thin film photovoltaic cells in order to artificially create large standing waves in the lateral direction and increase the optical path of the impinging beam inside the cell. We show that the generated local hot spots inside the active layer can significantly improve the absorption properties of the film, and this effect may be induced over broad bandwidths.

Figure 7.6(a) schematically illustrates the proposed technique: a weakly absorbing thin film is coupled to a graded metasurface back-reflector, and the whole configuration is tailored to redirect the impinging wave toward a new direction (i.e., 45 degrees off-normal, as shown in Fig. 7.10(a)). Wave deflection, which is equivalent to impose a constant transverse momentum along the surface [13], enforces multiple partial internal reflections inside the active layer, owing to the refractive index contrast between the dielectric film and free space. This process successfully creates lateral standing waves inside the semiconductor layer that are anticipated to increase carrier collection efficiency due to enhanced light-matter interactions.

In order to demonstrate the proposed light trapping scheme, we consider a thin-film active layer with refractive index $n \approx \sqrt{3}$ and absorption length ranging from 0.9 to 5.7 μm (between 450-1100 THz). The optical properties of the thin film are shown in Fig. 7.10(c) (inset). The semiconductor layer is assumed to be 180 nm thick and it is placed on top of a graded metareflector composed of conjoined composite particles. The structure is then designed to impart a transverse momentum able to bend the wave impinging from normal incidence by an angle of 45 degrees at 500 nm. Analogous to the polarization beam splitting surface, this functionality is realized with a superlattice periodicity, suitable for large-scale solar cell designs. The required profile periodicity is discretized into eight steps, and in each segment the filling ratio of the plasmonic portion (Ag) is tailored to replicate the calculated ideal reflection phase from the structure. We set the metasurface thickness at $d = 50$ nm and the entire structure is deposited on a thin layer of $d = 30$ nm silicon-dioxide ($n_{\text{sub}} = 1.45$) backed by a PEC ground plane, shown in Fig. 7.10(b). In this example the meta-reflectarray is designed for a one-dimensional set-up, tuned for TE polarized impinging waves. A similar concept can be easily extended into a 2D matrix in order to provide an isotropic response for all input polarizations, for instance by employing the concentric graded metasurface shown in Fig. 6.6(b).

Figure 7.6(c) shows the numerically calculated absorption spectra of the solar cell, highlighting the overall absorption enhancement [14]. The shaded area represents the additional absorption attained by patterning the back reflector, indicating an improvement factor of 2.6 at the design frequency. As predicted, while the total structure aims at coupling the impinging wave to the first Floquet order (i.e. $\theta_r = 45°$), the higher refractive index in the semiconductor allows multiple internal reflections inside the dielectric, ensuring an overall longer propagation distance inside the thin-film active layer (Fig. 7.10(d)). Notably, the coupling efficiency to the first scattering order (i.e., wave bending) using graded metasurfaces is very high over a relatively broad range of frequencies. This phenomenon resides in the inherently broadband response of the exploited composite nanoparticles, and accordingly allows to predict that this light trapping mechanism can be broadband, as verified in Fig. 7.10(d). The reflections build up to ensure strong light concentration and trapping inside the cell, consequently increasing the total collected photocurrent, except possibly in the vicinity of Fabry-Perot resonances of the original configuration (occurring around 720 THz). In addition, depending on its thickness, the film may support a number of guided optical modes [15]-

[17]. Typically, a substantial light trapping effect may also be achieved at the resonant frequency of these modes (around 540 and 1000 THz in the current example), over narrow spectral widths of few nanometers. However, these resonances are considerably broadened in our configuration and, combined with the broadband background absorption enhancement produced by the gradient metareflector, they significantly boost the overall efficiency, which is particularly important in the frequency bands where the original material fails to properly harness the solar radiation.

7.6 CONCLUSION

In this chapter we applied the concept of local wave-shaping metasurfaces, introduced in chapter 5, to a few relevant examples at optical frequencies. Exploiting the nanoresonator metamolecules introduced in chapter 6, we have shown that a single electrical metasurface with deeply subwavelength thickness can be used to fully control the scattering signature of optical elements such as thin-film solar cells and polarization beam splitters and drastically boost their performance, while minimizing the size of the device and improve the robustness to losses. In addition, we have designed graded metasurfaces to perform functionalities such as beam steering and focusing over large bandwidths and with small insertion losses. Finally we provided an experimental realization of a highly efficient beam steering surface at optical frequencies.

Due to their conformal profile and the fact that our designs are all based on the alternation of commonly available optical materials, the proposed optical films may be directly integrated into nanophotonic devices. These applications may also be scaled up to longer wavelengths to realize ultra-thin infrared, terahertz or microwave elements. The described control and manipulation of optical scattering through metasurfaces, along with their compatibility with standard lithographic techniques and on-chip fabrication technologies, may pave the way to several applications in optics, and open up a new route to design compact, planarized optical devices.

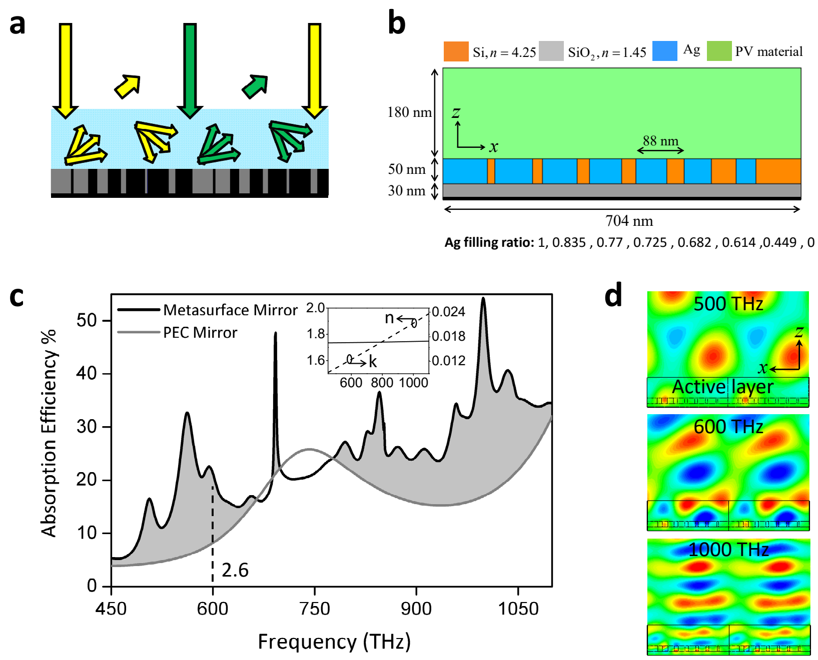

Figure 7.10: (a) Schematic illustration of light trapping inside an organic PV solar cell. The active layer is backed by a metasurface imparting the desired linear momentum to the impinging wave. Green arrows indicate the process of light trapping within one unit cell. (b) sketch of one period of the thin film absorbing structure. Dimensions and material properties are indicated in the figure. The PV material characteristics are shown in the inset of panel c.(c) Absorption spectrum for normally incident light on a 180 nm organic material without nanoscale metasurface (gray line), in comparison to a metasurface-backed solar cell with same thickness (black line). The structure is designed to redirect the outgoing field by 45 degrees. Each unit-cell is 88 nm wide, partially filled with silicon (n=4.25) and silver. Metasurface and substrate (SiO_2, $n_{sub} = 1.45$) thicknesses are $h = 50$ nm and $d = 30$ nm, respectively. The impinging electric field is polarized parallel to the cubic nano-rods on the surface, along the y-axis. Complex refractive index of the absorbing layer is also depicted in the inset. (d) Time snapshot of the normalized electric field distribution for three sample frequencies at 500, 600 (center design frequency), and 1000 THz. The metasurface and active region are included in the field plots. (Reprinted with permission from Philosophical Transactions A, Vol. 373, Issue 2049, pp. 20140351 (2015). Copyright 2015 The Royal Society Publishing).

7.7 REFERENCES

[1] Monticone, F., Mohammadi Estakhri, N., et al. (2013). Full control of nanoscale optical transmission with a composite metascreen, Phys. Rev. Lett., 110(20), 203903.

[2] Mohammadi Estakhri, N., and Alù, A. (2014). Manipulating optical reflections using engineered nanoscale metasurfaces, Phys. Rev. B, 89(23), 235419.

[3] V. H. Rumsey, "Reaction concept in electromagnetic theory." Physical Review 94.6 (1954): 1483.

[4] G. M. Whitman, and F. Schwering. "Reciprocity identity for periodic surface scattering." IEEE Transactions on Antennas and Propagation 27 (1979): 252-254.

[5] N. Mohammadi Estakhri, V. Neder, M. Knight, A. Polman, and A. Alu, under review.

[6] I. H. Malitson, "Interspecimen Comparison of the Refractive Index of Fused Silica" JOSA 55.10 (1965): 1205-1209.

[7] A. D. Rakić, et al. "Optical properties of metallic films for vertical-cavity optoelectronic devices." Applied optics 37.22 (1998): 5271-5283.

[8] Aieta, F., Genevet, P., et al. (2012). Aberration-free ultrathin flat lenses and axicons at telecom wavelengths based on plasmonic metasurfaces, Nano Lett., 12(9), 4932-4936.

[9] Pors, A., Nielsen, M. G., et al. (2013). Broadband focusing flat mirrors based on plasmonic gradient metasurfaces, Nano Lett., 13(2), 829-834.

[10] Li, X., Xiao, S., et al. (2012). Flat metasurfaces to focus electromagnetic waves in reflection geometry, Opt. Lett., 37(23), 4940-4942.

[11] Farmahini-Farahani M, Mosallaei H. 2013 Birefringent reflectarray metasurface for beam engineering in infrared. Opt. Lett. 38, 462–464.

[12] http://www.CST.com.

[13] Yu, N., P. Genevet, et al. (2011). Light propagation with phase discontinuities: generalized laws of reflection and refraction, Science, 334(6054), 333-337.

[14] N. Mohammadi Estakhri, C. Argyropoulos, and A. Alù, Graded metascreens to enable a new degree of nanoscale light management, Philos. Trans. R. Soc. London, A. 373, 20140351 (2015).

[15] Bermel P, Luo C, Zeng L, Kimerling LC, Joannopoulos JD. 2007 Improving thin-film crystalline silicon solar cell efficiencies with photonic crystals. Opt. Expr. 15, 16 986–17 000.

[16] Yu Z, Raman A, Fan S. 2010 Fundamental limit of nanophotonic light trapping in solar cells. Proc. Natl Acad. Sci. USA 107, 17 491–17 496.

[17] Pala RA, White J, Barnard E, Liu J, Brongersma ML. 2009 Design of plasmonic thin film solar cells with broadband absorption enhancements. Adv. Mater. 21, 3504–3509.

Chapter 8: Unidirectional Carpet Cloaks and Wavefront Reconstruction with Gradient Metasurfaces

In addition to rather simple functionalities implemented with metasurfaces in chapter 7, in this chapter we demonstrate that it is possible to design graded metasurfaces to perform more complex functionalities. Wave reconstruction over a single textured surface can provide an exciting platform for ultrathin carpet cloaking. In the previous chapters, we described the process of creating arbitrary scattering distributions by accurately engineering the profile of the surface to satisfy the required boundary conditions in Eq. (5.2). Through this process, the ultrathin metasurface is tailored to operate as a structure that scatters the incident wave in the predesignated manner. For instance, the flat lens presented in section 7.3 operates analogous to a concave mirror or the reflectarray presented in section 7.1 imitate a tilted mirror's functionality. Interestingly, we can likewise reverse this process and create a non-planar gradient metasurface that scatters resembling a flat mirror. This indeed creates an ideal camouflage for any object put beneath such a surface so it can't be identified by an external observer who inspects the scattered wave from such surface. We apply this concept to hide electrically large 2D and 3D objects through several examples. Both ideal and physical implementations of metasurface-based cloaks are discussed. The presented graded metasurface-based cloaks may find interesting applications as low-profile, tunable covers for low-observability and noise reduction in wireless commutation systems. The contents of this chapter partially appeared in "Mohammadi Estakhri, N.; Argyropoulos, C.; Alù, A., Graded metascreens to enable a new degree of nanoscale light management. Phil. Trans. R. Soc. A 2015, 373 (2049), 20140351", and "Mohammadi Estakhri, N.; Alu, A., Ultra-thin unidirectional carpet cloak and wavefront reconstruction with graded metasurfaces. Antennas and Wireless Propagation Letters, IEEE 2014, 13, 1775-1778".

8.1 Introduction

Metamaterials and artificial materials with effective properties that may be controlled to a large degree, have been at the basis of exciting schemes for wave manipulation, particularly well suited to hide an object from electromagnetic waves. To realize practical invisibility cloaks, transformation electromagnetics methods [1] and scattering cancellation techniques [2] are currently the most popular approaches, and simplified versions of these proposals have been implemented and examined in recent years (see e.g. [3]-[5]). TE-based cloaks exploit the fundamental connection between spatial material properties of the surrounding medium and a suitable coordinate space transformation, conserving the same format of Maxwell's equations while effectively isolating target object from the incoming wave. This paradigm inherently requires specific profiles of anisotropy and inhomogeneity, which may be approximately implemented employing metamaterials. Applying a quasi-conformal mapping can minimize the required anisotropy under specific circumstances, such as in the case of carpet cloaking, for which a reflecting surface with a bump appears as a flat mirror after covering the bump with a suitably tailored transformation electromagnetics medium [6]. In contrast, scattering cancellation techniques do not directly manipulate the field distribution around an object; instead, the dominant multipolar scattering orders are suppressed by a cover which may be typically made with an isotropic metamaterial. Similar effects may also be achieved employing isotropic metasurfaces (e.g., a frequency selective surface (FSS) at radio frequencies [7], or a graphene monolayer at terahertz [8]) wrapped around the object of interest. These cloaking techniques have distinctly different approaches to conceal an object, yet they both rely on the collective response of artificially engineered materials (or surfaces) enclosing the target structure, in order to attain the desired response.

In this chapter, we propose a different approach of cloaking applied to an arbitrarily shaped object placed over a ground plane, inspired from point-by-point wave reconstruction technique introduced in chapter 5. We show that a single, inhomogeneous metasurface is sufficient to guarantee directional invisibility with no lower limit on the overall thickness of the cloaking layer. After covering the target with a suitably designed graded metasurface, an exterior observer will perceive the whole system as a flat reflector, with several interesting advantages compared to transformation electromagnetics based carpet cloaks in terms of ease of implementation, low-profile, and conformability to the geometrical shape of the object. We investigate the performance of the proposed method through several ideal and realistic examples, and demonstrate successful concealment of electrically large 2D and 3D structures at optical wavelengths, along with high angular stability in the cloaking performance. This technique may bring cloaking devices one step closer to their practical implementation, especially at radio frequencies where there is the additional advantage of straightforward reconfigurability.

8.2 CONCEPT OF WAVEFRONT RECONSTRUCTION

We aim at hiding an object over a reflecting surface similar to a unidirectional carpet cloak. Let us first consider an empty region with a ground plane, as depicted in Fig. 8.1(a). When illuminated by a plane wave, the ground plane generates a specularly reflected wave, producing total electric and magnetic fields of $(\mathbf{E}_1, \mathbf{H}_1)$ everywhere. Our goal is to create a region (delimited by ∂V) above this mirror in which we can put an arbitrary obstacle without deforming this original field distribution (see. Fig. 8.1(b)), so that any observer placed above ∂V would perceive the same field $(\mathbf{E}_1, \mathbf{H}_1)$, assuming the excitation direction is known. To attain this goal, we exploit the well-established equivalence principle, based on the uniqueness theorem of Maxwell's equations [9].

Based on this general principle, two physical systems, as shown in Fig. 8.1, will have the same field solution above ∂V, provided that the exact same distribution of tangential electric (or magnetic) field is imposed on the domain boundaries, i.e.,

$$\left(\mathbf{E},\mathbf{H}\right)_{2t}\Big|_{\partial V}=\left(\mathbf{E},\mathbf{H}\right)_{1t}\Big|_{\partial V}. \tag{8.1}$$

This implies that, as long as we satisfy the boundary condition in (8.1), an external observer cannot distinguish between these two systems and $\left(\mathbf{E}_2,\mathbf{H}_2\right)=\left(\mathbf{E}_1,\mathbf{H}_1\right)$. To replicate the primary field distribution in the presence of an obstacle, we employ an ultrathin grounded metasurface, coating the structure along ∂V. The metasurface needs to be transversely inhomogeneous —direct consequence of (8.1)— and its composition is tailored at each point to locally imitate the desired specularly reflected beam along ∂V, assuming a specific plane wave excitation.

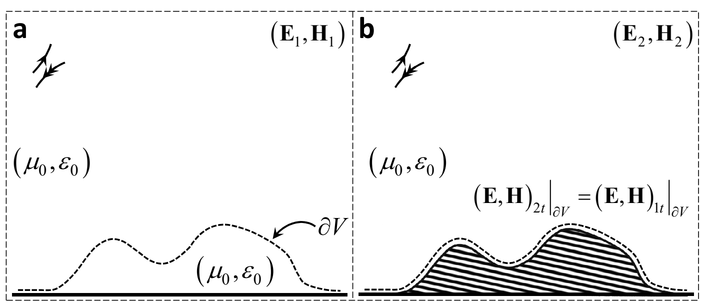

Figure 8.1: Reconstruction of initial field distribution in the presence of an obstacle. Based on the equivalence principle, the fields are uniquely determined by the electromagnetic field distribution over the surface enclosing the obstacle. (Reprinted with permission from AWPL, Vol. 13, pp. 1775 - 1778 (2014). Copyright 2014 IEEE).

We note that this representation is equivalent to Eq. (5.2), when the scattered field is replaced by the specular reflection of the incident wave. As we extensively discussed in chapter 5, for moderate wavefront shaping the constraints on the metasurface profile can be simplified to a requirement on the phase of the local reflection coefficient of an inhomogeneous surface (i.e. ray-optics approximation). This requires that the chosen surface profile smoothly varies in the scale of a wavelength, and the incident and reflected waves can be locally approximated by plane waves [10]. In practice, the ideal plane wave excitation may be replaced by a finite size beam, as long as the incident and reflected waves sufficiently overlap on the object surface. If the impinging beam is not a uniform plane wave and it covers only a small portion of the object, however, condition (8.1) would translate into a nonlocality requirement (i.e., it would require the response of the surface at a given point to depend on the excitation at another point), or alternatively into the necessity of introducing active elements in the metasurface. In the following we will examine an ideal cloaking surface including the local loss and gain, and approximate passive cloaks based on local phase compensation.

Anyhow, it is relevant to point out that this cloaking method does not necessitate prior information on the input signal to set up the cloak. This is in contrast to Huygens-based active cloaking approaches, for which surface currents must be induced based on the formerly known magnitude and phase of input beam [11]. Here, the geometrical shape of the object univocally determines the deviation of the local reflected phase (and amplitude) from the ideal scenario (Fig. 8.1(a)), which can be then corrected employing the metasurface cloak, provided that the incidence angle is known.

8.3 IDEAL LOCAL SCATTERING CANCELLATION

In this section, we demonstrate the ideal metasurface-based cloaking technique through a comprehensive example. We aim at concealing the object between the metasurface and a ground plane, such that the whole system mimics a flat reflecting surface. For simplicity, let us first assume a 2D configuration illuminated by a TE polarized Gaussian beam at $\lambda_0 = 500\,\text{nm}$, as depicted in Fig. 8.2(a). A triangular PEC bump with lateral size $L = 10\,\lambda_0$ and center height $H = 1.6\,\lambda_0$ is placed on the PEC ground and illuminated at 45 degrees. The presence of the bump results in total deformation of the input wave, as expected, and the incident beam experiences a new boundary condition at each point on the surface of the obstacle, observable in Fig. 8.2(c). The metasurface to cloak the object is readily characterized following equations (5.2) and (5.13), by inserting the incident and desired scattered waves, implying that condition (8.1) is exactly satisfied at each point on the surface. The admittance profile is calculated assuming $d = \lambda_0/10$ and $n_{sub} = 1$, as plotted in Fig. 8.2(b).The excitation field is a TE-polarized plane wave propagating in xz-plane at an angle of $45°$ toward the x-axis and the scattered wave is the ideal specularly reflected wave assuming a perfect mirror at $z = 0$, shown in Fig. 8.2(b),

$$\begin{aligned}
\left(\mathbf{E}_i, \mathbf{H}_i\right) &= \left(-\hat{y}, \frac{-\hat{x}\cos 45 - \hat{z}\sin 45}{\eta_0}\right) E_0 e^{-j\sin 45 k_0 x} e^{j\cos 45 k_0 z} \\
\left(\mathbf{E}_s, \mathbf{H}_s\right) &= \left(\hat{y}, \frac{-\hat{x}\cos 45 + \hat{z}\sin 45}{\eta_0}\right) E_0 e^{-j\sin 45 k_0 x} e^{-j\cos 45 k_0 z}
\end{aligned} \quad . \tag{8.2}$$

We design the cloaking layer conformal to the obstacle to follow its line shape. Consequently, the surface covering the triangular object in Fig. 8.2(a) has a constant normal vector $\hat{n} = \left(-2H\hat{x} + L\hat{z}\right)\big/\sqrt{4H^2 + L^2}$ on side 1 and $\hat{n} = \left(2H\hat{x} + L\hat{z}\right)\big/\sqrt{4H^2 + L^2}$ on side 2. Magneto-electric properties of the surface are then found following Eq. (5.2),

$$Y_{e,yy} = \frac{4}{Z_{m,xx}} = 2\frac{b\left(H_{ix} + H_{sx}\right) - a\left(H_{iz} + H_{sz}\right)}{\left(E_{iy} + E_{sy}\right)}, \tag{8.3}$$

where $a = \hat{n}\cdot\hat{x}, b = \hat{n}\cdot\hat{z}$. E_0 is an arbitrary constant complex number, which does not influence the acquired surface properties in (8.3).This indicates that the designed metasurface cloaks are independent of the absolute phase and amplitude of the excitation signal. The magneto-electric surface properties are then exploited to characterize the equivalent non-magnetic surface admittance $Y_{e,surface,yy}$ following (5.13). The sheet admittance of the grounded metasurface for $H = 800\ \text{nm}$, $L = 5000\ \text{nm}$, $d = 50\ \text{nm}$, and $n_{sub} = 1$, at $\lambda_0 = 500\ \text{nm}$ is shown in Fig.8.2(b,c).

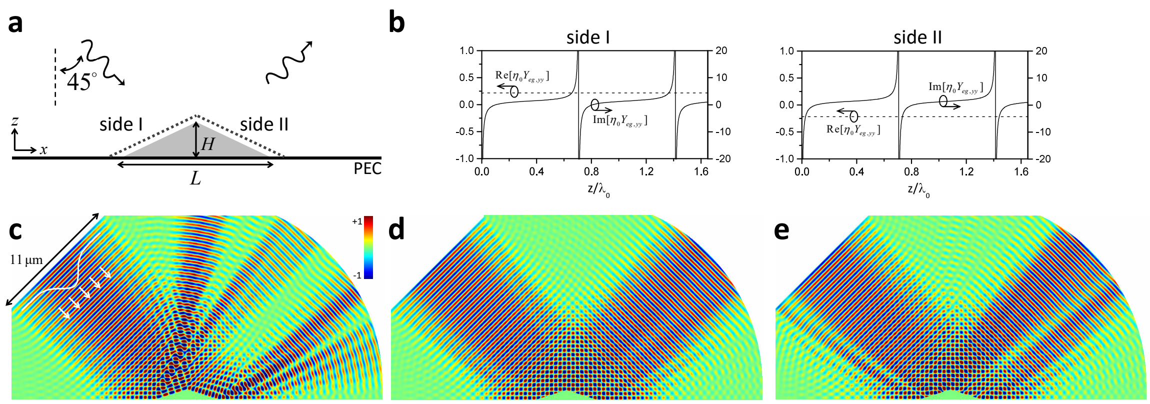

Figure 8.2: (a) Illustration of the cloaking setup. A PEC triangular obstacle with lateral size L and center height H is placed on a PEC ground plane. The excitation signal is a TE polarized plane wave ($\mathbf{E} = \hat{y}\,\mathrm{E}_0$), illuminating the structure at the angle of 45 degrees toward the x-axis. The gradient metasurface is shown with a dashed line, covering the structure on both sides. (b) Electric surface admittance of the cloaking metasurface plotted versus local distance to the ground plane, with $\lambda_0 = 500\ \text{nm}$. The physical dimensions of the obstacle are set at $H = 800\ \text{nm}$ and $L = 5\ \mu\text{m}$. The metasurface substrate is 50 nm thick with $n_{\text{sub}} = 1$. Snapshot in time of the electric field distribution when the structure is illuminated by a Gaussian beam: (c) free-standing obstacle; (d) obstacle covered with a graded metasurface characterized in panel (b); (e) cloaking metasurface approximated by its reactive components. (Reprinted with permission from Philosophical Transactions A, Vol. 373, Issue 2049, pp. 20140351 (2015). Copyright 2015 The Royal Society Publishing).

For cloaking, the optimal surface admittance is generally complex and, interestingly, the requirement on the surface admittance is to have lossy elements (i.e. $\text{Re}[Y_{e,surface,yy}] > 0$) on one edge and active components (i.e. $\text{Re}[Y_{e,surface,yy}] < 0$) on the opposite side, while the reactive portions are symmetric. This shares interesting analogies with the recently proposed PT-symmetric cloaking configurations in which a balanced combination of loss and gain may create unidirectional cloaking in various setups [12]-[14]. The distribution of the electric field around the obstacle is shown in Fig. 8.2(d), when the cloaking layer illustrated in panel (b) is applied at the predesignated position around the object. The presence of the cloak successfully enforces the desired specular reflection pattern, with negligible residual scattering associated to the finite thickness of the configuration ($d = 50\,\text{nm}$). Next, we relax the requirement on spatially distributed loss/gain over the surface and replace the exact complex admittance of Fig. 8.2(b) with its reactive portion, i.e. $Y_{e,surface,yy} = j\,\text{Im}[Y_{e,surface,yy}]$. Shown in Fig. 8.2(e) is the corresponding electric field distribution of the passive cloak, clearly displaying sub-optimal performance compared to the exact solution. Yet, even with the approximate passive cloak, the unwanted scattering is largely suppressed, which is particularly interesting considered the large dimensions of the obstacle compared to the operation wavelength. The residual scattering can be minimized by further optimizing the passive cloaking layer, which we do in the next examples, physically implementing a surface cloak based on the admittance elements shown in Fig. 6.1(a). The results presented in this example have been performed via full-wave simulations in COMSOL Multiphysics [15].

8.4 Realization of 2D and 3D ultrathin carpet cloaks

In the previous section, the reactance profile presented in Fig. 8.2(b) is imposed on the metasurface in a continuous fashion and with infinite spatial resolution. It would be insightful to physically implement a metasurface-based cloak and study its performance under realistic conditions. For this purpose, here we implement a graded metasurface to effectively conceal a PEC triangle with physical dimensions of $L = 1500\,\text{nm}$ and $H = 200\,\text{nm}$ at $\lambda_0 = 500\,\text{nm}$ and under 45 degrees TE illumination.

The metasurface thickness is set at $h = \lambda_0/10$ to ensure accurate sheet approximation, and we choose $d = 100\,\text{nm}$ and $n_{\text{sub}} = 1$. The metasurface elements are the conjoined dielectric-plasmonic particles shown in Fig. 6.1(a) and are made of combinations of a high index dielectric ($n = 3.46$) and a plasmonic metal (Ag). Silver dispersion and realistic losses are taken into account considering the Drude type permittivity model $\varepsilon_{Ag} = \varepsilon_\infty - \omega_p^2/\omega(\omega - j\gamma)$, with $\varepsilon_\infty = 5$, $\omega_p = 2\pi \times 2175\,\text{THz}$ and $\gamma = 2\pi \times 4.35\,\text{THz}$ based on experimental data [16]. The surface admittance is discretized into 13 elements on each side, elements 1 to 8 with lateral size of 97 nm and elements 9-13 with lateral size of 112 nm (approximately $\lambda_0/5$), to guarantee an acceptable resolution at 500 nm. These choice of dimensions follow geometrical specifications of the obstacle (8 equally sized elements to cover the object and 5 equally sized elements to cover the corners). As shown in Fig. 8.3(a), elements 9-13 are polygonic, rather than an exact rectangular shape.

The complex computed sheet admittance is approximated with its reactive portion for ease of implementation, i.e. $Y_{e,surface,yy} = j\,\text{Im}[Y_{e,surface,yy}]$. Surface admittance of the composite dielectric-plasmonic nanoparticles have been shown to be widely controllable by varying the filling ratio between the two materials (see section 6.2). Here, in order to extract the properties of each element, first, we calculated the reflection coefficient of the designed passive surface on each of the 13 segments using Eq. (5.12). The composite particles are then simulated in CST full-wave electromagnetic solver and the required reflection coefficients mapped to the filling ratio between the two materials in the cell. The obtained parameters are reported in Table 8.1-second column. Figure 8.3(b) shows the eclectic field distribution around the obstacle applying such analytically designed cloak. As we discussed in the previous section, mutual coupling between adjacent elements may modify their local admittance while assembled in the graded surface. In addition, the polygonal shape of corners and surface granularity will also affect the performance, since the admittance is inevitably averaged on each portion. However, and in spite of all these non-idealities and the passive approximation, the covered obstacle restores the original field distribution to very good extent (uncloaked case in Fig. 8.4(a)).

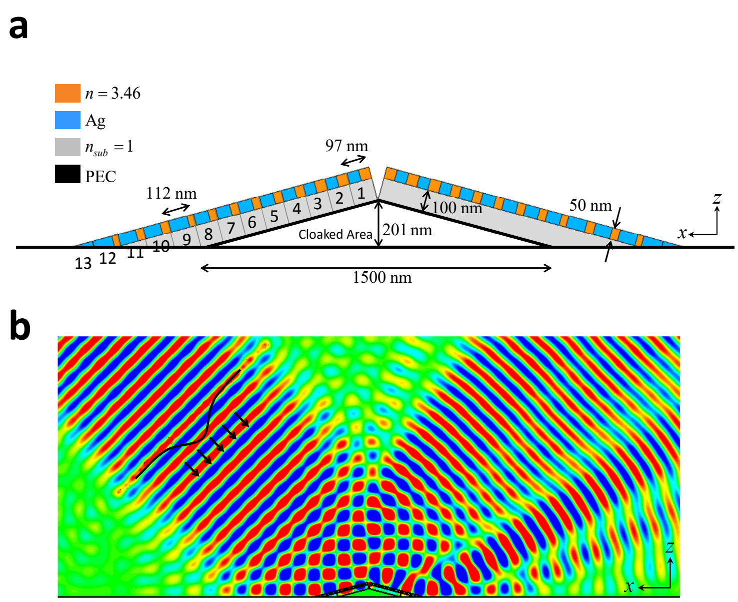

Figure 8.3: (a) Physical implementation of the carpet cloak. Designed surface admittance is implemented by varying filling ratio of silver inside each element (data provided in Table 8.1). (b) Time snapshot of the electric field distribution when the object is covered with the analytically designed metasurface with parameters given in Table 8.1-second column. (Reprinted with permission from Philosophical Transactions A, Vol. 373, Issue 2049, pp. 20140351 (2015). Copyright 2015 The Royal Society Publishing).

To eliminate the remaining undesired effects, we further fine tuned the surface to restore the local electric field over a hypothetical line with 20 nm spacing on the metasurface and effectively realize our analytically calculated surface admittance, now including all mutual couplings, discretization effects, and the approximation of neglecting the resistive portion of the impedance. Optimized filling ratios of the silver portion are reported in Table 8.1-third column and the distribution of electric field around the optimized cloak are shown in Fig. 8.4(b). Comparing these two sets of data reveals the stability of the design to variations of surface parameters as well. A 3D sketch of the final setup is shown in Fig. 8.4(c).

Table 8.1. Calculated and optimized silver filling ratio in each surface element of the cloak shown in Fig. 8.3(a). Based on reciprocity, in this passive limit the metasurface is symmetric on the two sides. (Reprinted with permission from Philosophical Transactions A, Vol. 373, Issue 2049, pp. 20140351 (2015). Copyright 2015 The Royal Society Publishing).

Element Number	Calculated Filling Ratio	Optimized Filling Ratio
1	0.518	0.525
2	0.585	0.505
3	0.614	0.505
4	0.632	0.587
5	0.645	0.608
6	0.655	0.628
7	0.666	0.634
8	0.676	0.639
9	0.706	0.732
10	0.723	0.661
11	0.756	0.688
12	0.828	0.759
13	1	0.991

Figures 8.4(a,b) compare the electric field distribution in the incidence plane, when the bare and optimized cloaked objects are illuminated by a Gaussian beam at 45 degrees (the design angle). As desired, the cloaked set-up scatters like a flat ground plane and the near field around the scatterer is fully restored. This is quantitatively shown in Fig. 8.43(d), in which we plot the total electric field (i.e. $\hat{y} \cdot \mathbf{E}$) along a hypothetical line placed 20 nm above the surface. Incorporating a single 50 nm thick graded surface, both amplitude and phase of the electric field are successfully reconstructed at each point to those of a reference flat mirror. Due to the subwavelength thickness of the metasurface

and small lateral foot-print of the elements, the metasurface response is stable with respect to the angle of incidence [17]-[18].

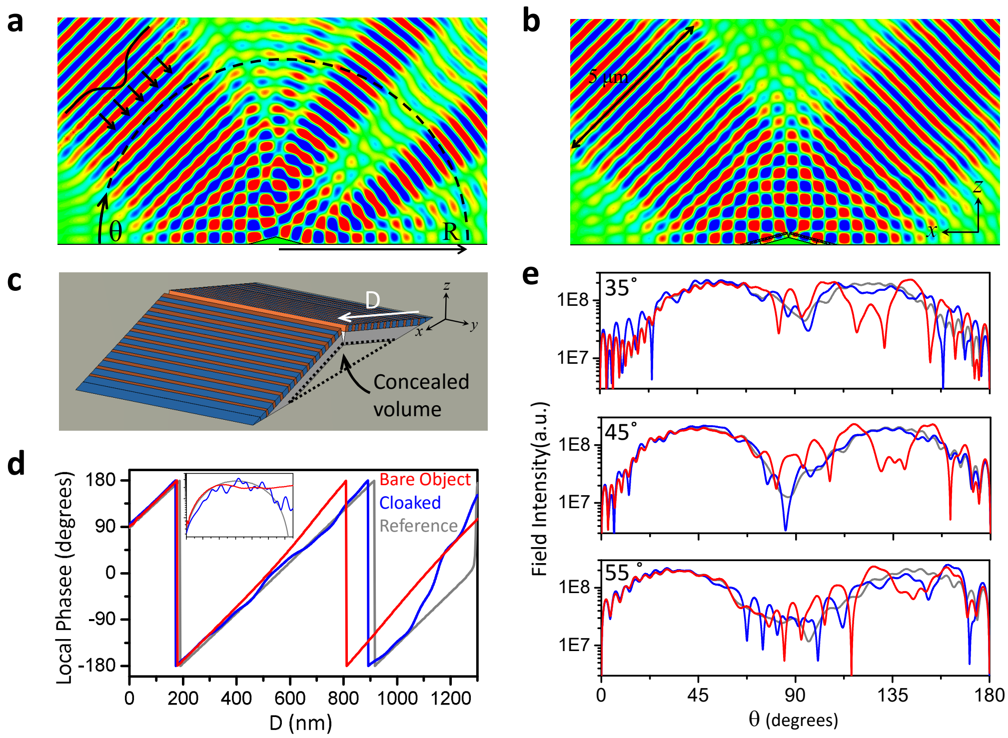

Figure 8.4: (a) A time snapshot of the electric field distribution when the object (without cloak) is illuminated by a 45° Gaussian beam. The ground plane and the scatterer are made of PEC material, and the length and height of the object are $L = 1500$ nm and $H = 200$ nm. (b) Electric field distribution when the object is covered with the designed metasurface (cloaked). The metasurface thickness is $h = 50$ nm, placed on top of the original object and conformally following its shape with $d = 100$ nm spacing. (c) 3D sketch of the deigned cloaking set-up. (d) Phase of the total electric field on a hypothetical boundary placed at 20 nm distance above the metasurface, as indicated by the white arrow in panel (c). The corresponding amplitude is also shown in the inset. (e) Angular dependence of the carpet cloak metasurface: the total field intensity along a half circle enclosing the system (dashed-line in panel a) is shown for three different incident angles. Blue and red curves refer to cloaked and uncloaked cases, and the gray curve indicates the reference response in the absence of any surface bump. All fields are calculated through full-wave simulations of the entire setup [19]. (Reprinted with permission from Philosophical Transactions A, Vol. 373, Issue 2049, pp. 20140351 (2015). Copyright 2015 The Royal Society Publishing).

This is further studied in Fig. 8.4(e), in which we excite the object under different incident angles and record the field magnitude on a half-circle placed at $R = 10\,\lambda_0$ (indicated in Fig. 8.4(a) by a dashed line). The numerical simulations confirm the angular stability of the designed cloak over more than ± 10 degrees range [19].

8.4.1 Realization of ray-optic based carpet cloaks

As we discussed in the beginning of this chapter, the exact requirements on the surface admittance and local phase/amplitude compensation may be simplified to merely a local phase compensation as long as the chosen surface profile smoothly varies in the scale of a wavelength. In addition, we notice that ultimately, and in order to eliminate the effects of mutual coupling and passive approximation of an ideal surface cloak, fine tuning of the initial metasurface design is usually necessary. Consequently, it is reasonable to design regular surface cloaks based on ray-optics, where the role of the metasurface is to compensate for the phase difference between the reflection from a flat mirror and reflection from an elevated point on the object. In this section, we design two surface-cloaks based on this simple ray-optics approach. As we will discuss, we obtain very good cloaking performance relying on thin, conformal, and passive cloaking blankets. In addition, and in contrast to the previous example, here we also exploit polarization insensitive surface elements (as in Fig. 6.6(b)) to hide 2D and 3D objects.

As the first example, we design a carpet cloak to conceal a PEC cylindrical dome, as shown in the inset of Fig. 8.5(e). The dome is a circular segment, infinite in the y-direction and lying in the xy-plane, with length of 1300 nm and height of 150 nm, respectively. An incident perpendicularly polarized Gaussian beam (electric field along the y-axis) illuminates the obstacle at $45°$, as illustrated in Fig. 8.5(c). Again, as expected, the presence of the bump distorts the original field pattern and a large shadow is formed in the forward direction, also highlighted in Fig. 8.5(e), where we plot the field intensity along a quarter-circle trajectory in the far-field of the obstacle (red line). In comparison to the reference beam (specular reflection, gray), the fields are diffracted and scattered by the object.

In order to cloak the dome, we conformally cover it with a graded metasurface composed of nanoblocks shown in Fig. 8.5(a). The metasurface follows the circular line shape of the dome, so the unit cells are "curved sectors" rather than exact cubical units. This, however, only minorly affects the estimated reflected field, as the radius of curvature is large compared to the size of each nanoblock. The metasurface may also follow simpler shapes, such as planar, triangular or smooth bell-shaped surfaces, and does not necessarily have to be conformal to the object. Here we chose to keep the exact shape of target to minimize the profile, and minor effects of unit cell approximation are eliminated by fine tuning the design. The graded metasurface is discretized into 17 segments in the xz-plane (each with approximate length of 100 nm), repeated in the y-direction with a 100 nm period, as shown in the inset of Fig. 8.5(e). The rod's radii are theoretically determined to follow condition (8.1), and then optimized through a series of simulations of the entire setup to account for mutual coupling between adjacent blocks, their slightly different slopes, and fairly rough discretization of the field profile ($\lambda_0/5$). Due to reciprocity, the geometrical symmetry of obstacle imposes a symmetry condition on the cloak [20] that reduces the overall number of optimization variables to just nine.

Figure 8.5(b) shows the obtained phase and amplitude distribution of the total electric field along a circular line above the metasurface (at 20 nm distance), as shown in Fig. 8.5(e)-inset. Black curves indicate the near-field distribution around the cloaked dome while red and gray curves represent the cases of an uncloaked dome and a flat mirror, respectively. As expected, the metasurface successfully repairs the phase distortion caused by the obstacle, and it restores the near-field as if the object were not there, Accordingly, Fig. 3d shows a snapshot of the electric field distribution with the dome covered by the optimized cloak. The small residual scattering is associated to the metasurface granularity. Even with just five nanoblocks per wavelength, we achieve a very good level of scattering reduction.

Interestingly, our method also eliminates the inevitable lateral shift occurring in isotropic realizations of transformation electromagnetic carpet cloaks [21], associated to their transverse homogeneity and finite thickness. As shown in Fig. 8.5(e), the main beam is reconstructed to its original shape, employing a single 60 nm thick inhomogeneous metasurface. The ultrathin profile is in direct contrast to transformation electromagnetic based carpet cloaks, for which electrically large metamaterial covers must be placed around the target even for unidirectional cloaking [3],[5], typically larger than the obstacle itself. Metasurface cloaks, however, can have deeply subwavelength thicknesses, and eliminate the requirement for precise control of 3D anisotropy.

Similar to the previous study, in this example we designed the cloak for an incident angle of $45°$; however, the cloaking performance is stable to variations in angle as long as we employ a thin, gradually inhomogeneous surface. This is easily explained considering that, in order to compensate the phase distortion imposed by the object, the local reflection phase at each point on the metasurface is approximated as $\angle R_{desired}$ = $\pi - 2k_0 h\cos\theta$, with k_0 and h indicating the free-space wave number and local height of the obstacle, and θ being the incident angle. At the same time, the reflection phase from a lossless normalized surface impedance jX_s placed at distance $d \ll \lambda_0$ from a ground plane, and illuminated at an angle θ by a perpendicularly polarized plane wave can be approximately written as $\angle R \approx \pi - 2k_0 d X_s \cos\theta / \left(X_s + k_0 d\right)$. Comparing the two expressions, we see that, as we tune the surface impedance to operate for a specific incident angle, it essentially maintains its performance for other angles. In practice, finite thickness and slight angular dependence break this assumption for large variations in θ; yet, as illustrated in Fig. 8.5(f), the cloaking performance is maintained to a very good extent over at least $\pm 10°$ variations from the original angle.

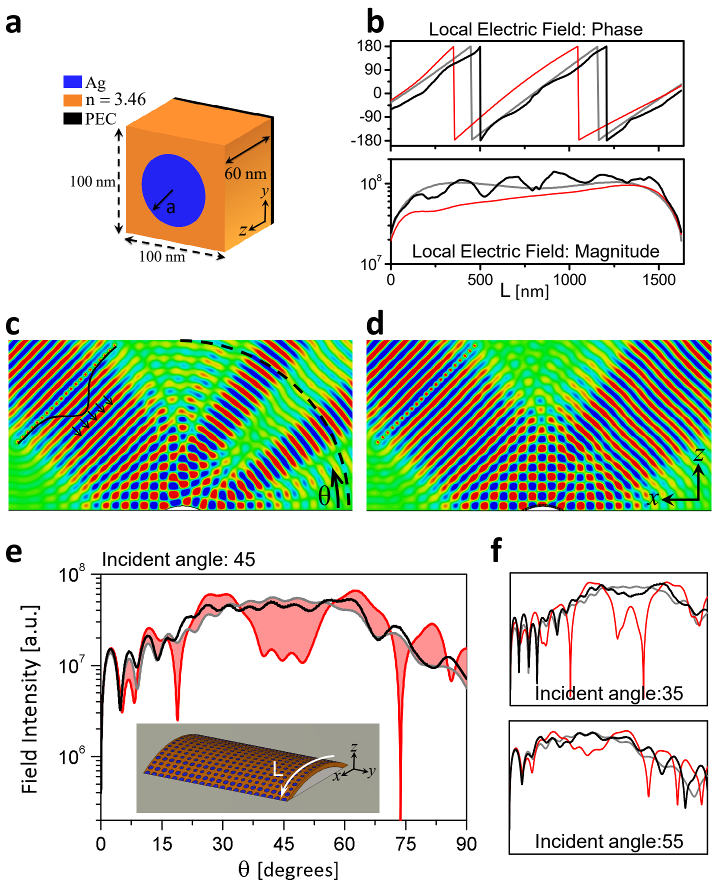

Figure 8.5: (a) Schematic of the concentric nanoresonator used to implement metasurface cloak. (b) Electric field distribution along the cloak surface (white arrow in panel (e)-inset) when the object is illuminated at 500 nm with a Gaussian beam. An ideal mirror, bare object, and cloaked object cases are shown in gray, red, and black, respectively. (c)-(d) Time snapshot of the electric field distribution without and with the cloaking surface. (e) Field intensity along the dashed line in panel (c) for the three cases. Deviation of scattering signature for the bare obstacle from the ideal scenario is highlighted in red. Inset shows a 3D view of the dome and cloaking surface. (f) Same as (e) when the angle of incident is changed by $\pm 10°$. (Reprinted with permission from AWPL, Vol. 13, pp. 1775 - 1778 (2014). Copyright 2014 IEEE).

Finally, and in analogy with the previous example, we applied the same technique to a 3D obstacle, shown in Fig. 8.6(a). The target now is a PEC spherical dome with height and length of 150 nm and 1300 nm, illuminated with a 2D Gaussian beam at $45°$. The metasurface elements are kept unchanged compared to the design in Fig. 8.5, however, in order to account for the 3D geometry, the elements are arranged so that the surface is axially symmetric (Fig. 8.6(a)-inset). This assumption provides a good approximation of the ideal cloaking surface in view of the angular stability of the design (Fig. 8.5(f)). While the optimized 3D cloak is not required to be axially symmetric, as the incident polarization and angle are slightly different for adjacent elements, this assumption significantly reduces the computational cost and post-optimization steps.

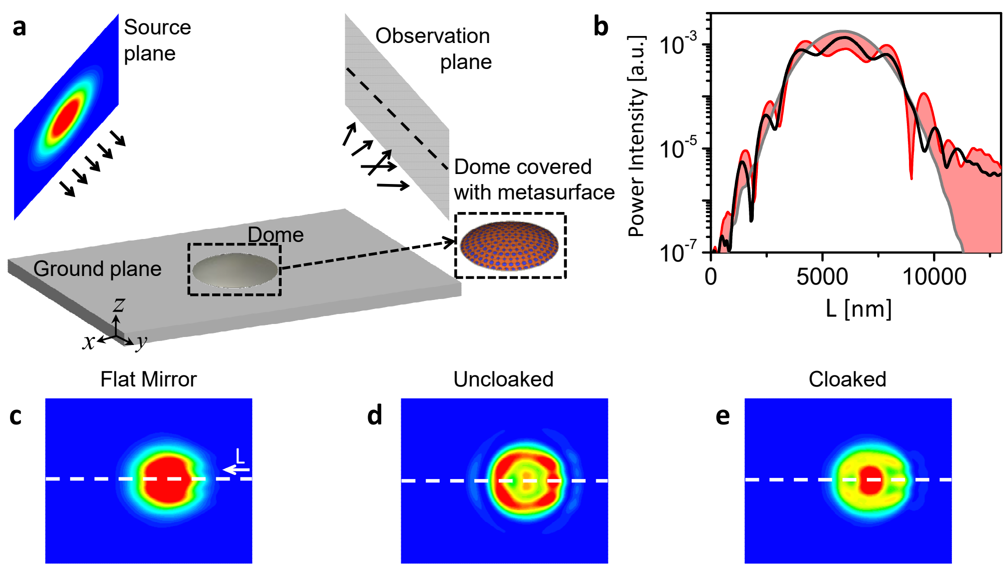

Figure 8.6: (a) The 3D cloaking setup. A spherical PEC dome is placed on a semi-infinite ground plane, illuminated by a Gaussian beam at 500 nm, at $45°$ angle. Observation plane is set in the mirror-symmetric position of excitation plane. Inset shows the graded metasurface wrapped on the dome. (b) Power intensity along dashed line in panel (a). Gray, red, and black lines indicate flat surface, uncloaked, and cloaked dome cases, respectively. (c)-(e) Power intensity on the observation plane. All plots are in same scale. (Reprinted with permission from AWPL, Vol. 13, pp. 1775 - 1778 (2014). Copyright 2014 IEEE).

Figures 8.6(c,e) show the intensity distribution of the scattered power on the observation plane. Compared to the case of a simple flat mirror, for which the Gaussian profile is preserved, the bare object creates a funnel-shaped scattering pattern with a distinct null at its center. Employing the cloaking metasurface, however, drastically reduces these scattering lobes and restores the main beam. For a clearer comparison, the trajectory of power flow along the dashed line is also shown in Fig. 8.6(b). Our study indicates that also this 3D cloak maintains a good performance over $\pm 10°$ variations in incidence angle.

8.5 CONCLUSION

In this chapter, we have introduced the concept of unidirectional carpet cloaking based on ultrathin graded metasurfaces, showing that, by engineering the local field distribution on the surface of an obstacle, we can realize ultrathin cloaks for arbitrary structures. Practical examples have been presented at optical frequencies and the cloaking performance has been shown to be stable to surface discretization, incident angle, and polarization. The reflection signature of the proposed metasurfaces may be locally managed with external signals for various applications such as, switching between cloaked/uncloaked modes, or creating scattering illusions to deceive the observer [22]. Temperature control and nonlinear effects at optical frequencies, gate voltage in graphene-based terahertz metasurfaces, and varactor loading in FSSs, are among possible approaches to add tunability in this design. As we discussed, by considering nonlocal or active metasurfaces, it will be possible to create ideal and excitation-independent carpet cloaks. With the advantage of easier implementation and simple design methodology, we envision a broad range of application for this concept, in camouflaging, switchable invisibility, noise reduction in wireless communication systems, and specially in the context of cloaking electrically large objects, with potential controllability and reconfigurability [23]-[25].

8.6 References

[1] J. B. Pendry, et al., "Controlling electromagnetic fields," Science, vol. 312, pp. 1780-1782, 2006.

[2] A. Alù and N. Engheta, "Achieving transparency with plasmonic and metamaterial coatings," Physical Review E, vol. 72, p. 016623, 2005.

[3] D. Schurig, et al., "Metamaterial electromagnetic cloak at microwave frequencies," Science, vol. 314, pp. 977-980, 2006.

[4] D. Rainwater, et al., "Experimental verification of three-dimensional plasmonic cloaking in free-space," New Journal of Physics, vol. 14, p. 013054, 2012.

[5] N. Landy and D. R. Smith, "A full-parameter unidirectional metamaterial cloak for microwaves," Nature Materials, vol. 12, pp. 25-28, 2013.

[6] J. Li and J. Pendry, "Hiding under the carpet: a new strategy for cloaking," Physical review letters, vol. 101, p. 203901, 2008.

[7] A. Alù, "Mantle cloak: Invisibility induced by a surface," Physical Review B, vol. 80, p. 245115, 2009.

[8] P.-Y. Chen and A. Alù, "Atomically thin surface cloak using graphene monolayers," ACS nano, vol. 5, pp. 5855-5863, 2011.

[9] R. F. Harrington, Time-harmonic electromagnetic fields. John Wiley & Sons, 2001, pp. 100–103.

[10] D.M. Pozar, S. D. Targonski, and H. Syrigos, " Design of millimeter wave microstrip reflectarrays," Antennas and Propagation, IEEE Transactions on 45, 287-296, 1997.

[11] M. Selvanayagam and G. V. Eleftheriades, "An Active Electromagnetic Cloak Using the Equivalence Principle," IEEE Antennas and Wireless Propagation Letters, vol. 11, pp. 1226-1229, 2012.

[12] Lin, Z. et al. Unidirectional invisibility induced by PT-symmetric periodic structures. Physical Review Letters 106, 213901 (2011).

[13] Zhu, X., Feng, L., Zhang, P., Yin, X. & Zhang, X. One-way invisible cloak using parity-time symmetric transformation optics. Optics letters 38, 2821-2824 (2013).

[14] D. L. Sounas, R. Fleury, A. Alù, Unidirectional Cloaking and Super-Stealth with Parity-Time Symmetric Metasurfaces. under review (2014).

[15] http://www.comsol.com/comsol-multiphysics.

[16] Ordal, M. A., et al. Optical properties of fourteen metals in the infrared and far infrared: Al, Co, Cu, Au, Fe, Pb, Mo, Ni, Pd, Pt, Ag, Ti, V, and W. Applied optics 24, 4493-4499 (1985).

[17] Mohammadi Estakhri, N. & Alù, A. Manipulating optical reflections using engineered nanoscale metasurfaces. Physical Review B 89, 235419 (2014).

[18] Al-Joumayly, M. A. & Behdad, N. A generalized method for synthesizing low-profile, band-pass frequency selective surfaces with non-resonant constituting elements. Antennas and Propag IEEE Transactions on 58, 4033-4041 (2010).

[19] http://www.cst.com/

[20] D. Sounas, and A. Alù, “Extinction symmetry for reciprocal objects and its implications on cloaking and scattering manipulation,” Optics Letters, vol. 39, No. 13, pp. 4053-4056, June 27, 2014.

[21] B. Zhang, T. Chan, and B.-I. Wu, "Lateral shift makes a ground-plane cloak detectable," Physical Review Letters, vol. 104, p. 233903, 2010.

[22] Lai, Y. et al. Illusion optics: the optical transformation of an object into another object. Physical review letters 102, 253902 (2009).

[23] N. Mohammadi Estakhri, and A. Alù "Ultra-thin unidirectional carpet cloak and wavefront reconstruction with graded metasurfaces." Antennas and Wireless Propagation Letters, IEEE 13 (2014): 1775-1778.

[24] X. Ni, Z. J. Wong, M. Mrejen, Y. Wang, and X. Zhang, “An ultrathin invisibility skin cloak for visible light,” Science, vol. 349, no. 6254, pp. 1310–1314, 2015.

[25] B. Orazbayev, N. Mohammadi Estakhri, M. Beruete, and A. Alù, “Terahertz carpet cloak based on a ring resonator metasurface,” Phys. Rev. B, vol. 91, no. 19, p. 195444, 2015.

Chapter 9: Conclusion and Future Directions

9.1 Conclusions

In this study we investigated that to what extent it is possible to engineer the scattering, absorption, and local wave-matter interactions of metamolecules, which are the basic building-blocks of metamaterials, as well as the possibility of wave manipulation by two-dimensional assembles of them, known as metasurfaces. First, we proposed a novel nanoparticle geometry with tailored complex absorption signature. We demonstrated that these plasmonic-based nanostructures can be engineered to provide unprecedented absorption efficiency over broad and controllable bandwidths, specifically in the optical frequency range. Later, and based on these composite nanoparticles, we proposed a nanoscale optical switch with strong sensitivity and tunability. Next, we demonstrated the theoretical limitations of a furtive sensor and provided a proof of the concept implementation of minimum-scattering superabsorbers at optical and microwave frequencies. Our analysis provided the physical limitations imposed on cloaking general absorbing bodies, which we also explored via an experimental realization of a low-scattering microwave receiver. Finally, we proposed a new approach for controlling the propagation and scattering of light through gradient or non-periodic metasurfaces. We provided a comprehensive theoretical method to design wave-shaping metasurfaces that are capable of performing complex functionalities over ultrathin surfaces. Based on our full analytical approach, we underlined the inherent limitations and wide range of capabilities of metasurfaces, and proposed novel techniques to significantly improve their efficiency. We then investigated our proposed concept of local wave manipulation for several practical applications in beam steering, improved energy harvesting, and cloaking arbitrary obstacles.

9.2 FUTURE DIRECTIONS AND OUTLOOKS

In spite of the significant developments in the field of metamaterials and metasurfaces, there are several challenges that may hinder the technological advent of these fields. For instance, many of metasurface configurations exploit localized plasmon resonances that are known to be very lossy. Thanks to the advances in nanofabrication techniques, recently, epitaxially grown plasmonic metals have been realized with the lower levels of intrinsic loss [1]. In addition, exploiting high index low-loss dielectric metamolecules in place of plasmonic elements is aimed to reduce the intrinsic loss of metasurfaces [2]-[3]. Exploring other possibilities to reduce the insertion loss of metasurfaces is an important direction of future works in this area. Besides the available analytical techniques, numerical and approximate methods to optimize metamolecules and metasurfaces are of significant importance. To be of broader interest, there are also many efforts on engineering novel infrared and THz metamolecules. Advancing the current nanofabrication techniques in order to achieve higher resolutions at the nanoscale is of fundamental importance as well. Finally, adding tunability and reconfigurability into wave shaping metasurfaces is highly desirable as it enables dynamic spatial light modulation over an ultrathin surface.

9.3 REFERENCES

[1] Wu, Y.; Zhang, C.; Estakhri, N. M.; Zhao, Y.; Kim, J.; Zhang, M.; Liu, X. X.; Pribil, G. K.; Alù, A.; Shih, C. K., Intrinsic optical properties and enhanced plasmonic response of epitaxial silver. Advanced Materials 2014, 26 (35), 6106-6110.

[2] D. Lin, P. Fan, E. Hasman, M. L. Brongersma, Dielectric gradient metasurface optical elements, Science 345, 298 (2014).

[3] Arbabi, A.; Horie, Y.; Bagheri, M.; Faraon, A., Dielectric metasurfaces for complete control of phase and polarization with subwavelength spatial resolution and high transmission. Nature nanotechnology 2015.

Bibliography

Adachi, S., GaAs, AlAs, and AlxGa1− xAs: Material parameters for use in research and device applications. Journal of Applied Physics 1985, 58 (3), R1-R29.

Aieta, F.; Genevet, P.; Kats, M. A.; Yu, N.; Blanchard, R.; Gaburro, Z.; Capasso, F., Aberration-free ultrathin flat lenses and axicons at telecom wavelengths based on plasmonic metasurfaces. Nano letters 2012, 12 (9), 4932-4936.

Aieta, F.; Genevet, P.; Yu, N.; Kats, M. A.; Gaburro, Z.; Capasso, F., Out-of-plane reflection and refraction of light by anisotropic optical antenna metasurfaces with phase discontinuities. Nano Letters 2012, 12 (3), 1702-1706.

Alaeian, H.; Dionne, J. A., Parity-time-symmetric plasmonic metamaterials. Physical Review A 2014, 89 (3), 033829.

Al-Joumayly, M. A.; Behdad, N., A generalized method for synthesizing low-profile, band-pass frequency selective surfaces with non-resonant constituting elements. Antennas and Propagation, IEEE Transactions on 2010, 58 (12), 4033-4041.

Alù, A., Mantle cloak: Invisibility induced by a surface. Physical Review B 2009, 80 (24), 245115.

Alù, A.; Engheta, N., Achieving transparency with plasmonic and metamaterial coatings. Physical Review E 2005, 72 (1), 016623.

Alù, A.; Engheta, N., Cloaked near-field scanning optical microscope tip for noninvasive near-field imaging. Physical Review Letters 2010, 105 (26), 263906.

Alù, A.; Engheta, N., Cloaking a sensor. Physical Review Letters 2009, 102 (23), 233901.

Alù, A.; Engheta, N., Enhanced directivity from subwavelength infrared/optical nano-antennas loaded with plasmonic materials or metamaterials. Antennas and Propagation, IEEE Transactions on 2007, 55 (11), 3027-3039.

Alu, A.; Engheta, N., How does zero forward-scattering in magnetodielectric nanoparticles comply with the optical theorem? Journal of Nanophotonics 2010, 4 (1), 041590-041590-17.

Alù, A.; Engheta, N., Multifrequency optical invisibility cloak with layered plasmonic shells. Physical Review Letters 2008, 100 (11), 113901.

Alù, A.; Engheta, N., Optical nanoswitch: an engineered plasmonic nanoparticle with extreme parameters and giant anisotropy. New Journal of Physics 2009, 11 (1), 013026.

Alù, A.; Engheta, N., Polarizabilities and effective parameters for collections of spherical nanoparticles formed by pairs of concentric double-negative, single-negative, and/or double-positive metamaterial layers. Journal of Applied Physics 2005, 97 (9), 094310.

Alu, A.; Engheta, N., Tuning the scattering response of optical nanoantennas with nanocircuit loads. Nature Photonics 2008, 2 (5), 307-310.

Alu, A.; Maslovski, S., Power relations and a consistent analytical model for receiving wire antennas. Antennas and Propagation, IEEE Transactions on 2010, 58 (5), 1436-1448.

Alù, A.; Salandrino, A.; Engheta, N., Coupling of optical lumped nanocircuit elements and effects of substrates. Optics Express 2007, 15 (21), 13865-13876.

Ambichl, P.; Makris, K. G.; Ge, L.; Chong, Y.; Stone, A. D.; Rotter, S., Breaking of P T Symmetry in Bounded and Unbounded Scattering Systems. Physical Review X 2013, 3 (4), 041030.

Andersen, J. B.; Frandsen, A., Absorption efficiency of receiving antennas. Antennas and Propagation, IEEE Transactions on 2005, 53 (9), 2843-289.

Andrianov, E.; Pukhov, A.; Dorofeenko, A.; Vinogradov, A., Spaser operation in the presence of external optical field. Journal of Communications Technology and Electronics 2012, 57 (1), 106-116.

Andrianov, E.; Pukhov, A.; Dorofeenko, A.; Vinogradov, A.; Lisyansky, A., Dipole response of spaser on an external optical wave. Optics letters 2011, 36 (21), 4302-4304.

Arbabi, A.; Horie, Y.; Bagheri, M.; Faraon, A., Dielectric metasurfaces for complete control of phase and polarization with subwavelength spatial resolution and high transmission. Nature nanotechnology 2015.

Argyropoulos, C.; Chen, P.-Y.; D'Aguanno, G.; Engheta, N.; Alu, A., Boosting optical nonlinearities in ε-near-zero plasmonic channels. Physical Review B 2012, 85 (4), 045129.

Argyropoulos, C.; Chen, P.-Y.; Monticone, F.; D'Aguanno, G.; Alu, A., Nonlinear plasmonic cloaks to realize giant all-optical scattering switching. Physical review letters 2012, 108 (26), 263905.

Aubry, A.; Lei, D. Y.; Maier, S. A.; Pendry, J., Broadband plasmonic device concentrating the energy at the nanoscale: The crescent-shaped cylinder. Physical Review B 2010, 82 (12), 125430.

Aubry, A.; Lei, D. Y.; Maier, S. A.; Pendry, J., Interaction between plasmonic nanoparticles revisited with transformation optics. Physical review letters 2010, 105 (23), 233901.

Avitzour, Y.; Urzhumov, Y. A.; Shvets, G., Wide-angle infrared absorber based on a negative-index plasmonic metamaterial. Physical Review B 2009, 79 (4), 045131.

Balanis, C. A., Advanced Engineering Electromagnetics. John Wiley & Sons: 1989.

Balanis, C. A., Antenna theory: analysis and design. John Wiley & Sons: 1996.

Barnes, W. L.; Dereux, A.; Ebbesen, T. W., Surface plasmon subwavelength optics. Nature 2003, 424 (6950), 824-830.

Baron, A.; Devaux, E.; Rodier, J.-C.; Hugonin, J.-P.; Rousseau, E.; Genet, C.; Ebbesen, T. W.; Lalanne, P., Compact antenna for efficient and unidirectional launching and decoupling of surface plasmons. Nano letters 2011, 11 (10), 4207-4212.

Bastys, V.; Pastoriza Santos, I.; Rodríguez González, B.; Vaisnoras, R.; Liz Marzán, L. M., Formation of silver nanoprisms with surface plasmons at communication wavelengths. Advanced Functional Materials 2006, 16 (6), 766-773.

Bender, C. M.; Boettcher, S., Real spectra in non-Hermitian Hamiltonians having P T symmetry. Physical Review Letters 1998, 80 (24), 5243.

Bender, C. M.; Brody, D. C.; Jones, H. F., Complex extension of quantum mechanics. Physical Review Letters 2002, 89 (27), 270401.

Bergman, D. J.; Stockman, M. I., Surface plasmon amplification by stimulated emission of radiation: quantum generation of coherent surface plasmons in nanosystems. Physical review letters 2003, 90 (2), 027402.

Bermel, P.; Luo, C.; Zeng, L.; Kimerling, L. C.; Joannopoulos, J. D., Improving thin-film crystalline silicon solar cell efficiencies with photonic crystals. Optics Express 2007, 15 (25), 16986-17000.

Bohren, C. F.; Huffman, D. R., Absorption and scattering of light by small particles. John Wiley & Sons: 1983.

Boltasseva, A.; Shalaev, V. M., Fabrication of optical negative-index metamaterials: Recent advances and outlook. Metamaterials 2008, 2 (1), 1-17.

Brown, J. W.; Churchill, R. V.; Lapidus, M., Complex variables and applications. McGraw-Hill New York: 1996; Vol. 7.

C. H. Papas, C. H., Theory of Electromagnetic Wave Propagation. Dover, New York: 1988.

Cai, J.; Ruffieux, P.; Jaafar, R.; Bieri, M.; Braun, T.; Blankenburg, S.; Muoth, M.; Seitsonen, A. P.; Saleh, M.; Feng, X., Atomically precise bottom-up fabrication of graphene nanoribbons. Nature 2010, 466 (7305), 470-473.

Castaldi, G.; Gallina, I.; Galdi, V.; Alù, A.; Engheta, N., Power scattering and absorption mediated by cloak/anti-cloak interactions: A transformation-optics route toward invisible sensors. JOSA B 2010, 27 (10), 2132-2140.

Chen, C.-Y.; Pan, C.-L.; Hsieh, C.-F.; Lin, Y.-F.; Pan, R.-P., Liquid-crystal-based terahertz tunable Lyot filter. Applied physics letters 2006, 88 (10).

Chen, P.-Y.; Alù, A., Atomically thin surface cloak using graphene monolayers. ACS nano 2011, 5 (7), 5855-5863.

Chen, P.-Y.; Alù, A., Optical nanoantenna arrays loaded with nonlinear materials. Physical Review B 2010, 82 (23), 235405.

Chen, P.-Y.; Argyropoulos, C.; Alù, A., Enhanced nonlinearities using plasmonic nanoantennas. Nanophotonics 2012, 1 (3-4), 221-233.

Chong, Y.; Ge, L.; Cao, H.; Stone, A. D., Coherent perfect absorbers: time-reversed lasers. Physical Review Letters 2010, 105 (5), 053901.

Chong, Y.; Ge, L.; Stone, A. D., P T-Symmetry Breaking and Laser-Absorber Modes in Optical Scattering Systems. Physical Review Letters 2011, 106 (9), 093902.

Chu, L. J., Physical Limitations of Omni Directional Antennas. Journal of applied physics 1948, 19 (12), 1163-1175.

Davis, L., Electostatic edge modes of a dielectric wedge. Physical Review B 1976, 14 (12), 5523.

Desurvire, E.; Bayart, D.; Desthieux, B.; Bigo, S., Erbium-doped fiber amplifiers: Device and System Developments. J. Wiley: 2002.

Ding, F.; Kinsey, N.; Liu, J.; Wang, Z.; Shalaev, V. M.; Kildishev, A. In Unidirectional surface plasmon polariton coupler in the visible using metasurfaces, 2014 Conference on Lasers and Electro-Optics (CLEO)-Laser Science to Photonic Applications, 2014.

Engheta, N., An idea for thin subwavelength cavity resonators using metamaterials with negative permittivity and permeability. Antennas and Wireless Propagation Letters, IEEE 2002, 1 (1), 10-13.

Engheta, N., Circuits with light at nanoscales: optical nanocircuits inspired by metamaterials. Science 2007, 317 (5845), 1698-1702.

Engheta, N.; Ziolkowski, R. W., Metamaterials: physics and engineering explorations. John Wiley & Sons: 2006.

Epstein, A.; Eleftheriades, G. V., Floquet-Bloch analysis of refracting Huygens metasurfaces. Physical Review B 2014, 90 (23), 235127.

Epstein, A.; Eleftheriades, G., Passive lossless Huygens metasurfaces for conversion of arbitrary source field to directive radiation. Antennas and Propagation, IEEE Transactions on 2014, 62 (11), 5680-5695.

Esfandyarpour, M.; Garnett, E. C.; Cui, Y.; McGehee, M. D.; Brongersma, M. L., Metamaterial mirrors in optoelectronic devices. Nature nanotechnology 2014, 9 (7), 542-547.

Eustis, S.; El-Sayed, M. A., Why gold nanoparticles are more precious than pretty gold: noble metal surface plasmon resonance and its enhancement of the radiative and nonradiative properties of nanocrystals of different shapes. Chemical Society Reviews 2006, 35 (3), 209-217.

Fan, P.; Chettiar, U. K.; Cao, L.; Afshinmanesh, F.; Engheta, N.; Brongersma, M. L., An invisible metal-semiconductor photodetector. Nature Photonics 2012, 6 (6), 380-385.

Farhat, M.; Chen, P.; Guenneau, S.; Enoch, S., Transformation Wave Physics: Electromagnetics, Elastodynamics, and Thermodynamics, Pan Stanford, to be published.

Farmahini-Farahani, M.; Mosallaei, H., Birefringent reflectarray metasurface for beam engineering in infrared. Optics letters 2013, 38 (4), 462-464.

Feng, L.; Wong, Z. J.; Ma, R.-M.; Wang, Y.; Zhang, X., Single-mode laser by parity-time symmetry breaking. Science 2014, 346 (6212), 972-975.

Feng, L.; Xu, Y.-L.; Fegadolli, W. S.; Lu, M.-H.; Oliveira, J. E.; Almeida, V. R.; Chen, Y.-F.; Scherer, A., Experimental demonstration of a unidirectional reflectionless parity-time metamaterial at optical frequencies. Nature Materials 2013, 12 (2), 108-113.

Fleury, R.; Soric, J.; Alù, A., Physical bounds on absorption and scattering for cloaked sensors. Physical Review B 2014, 89 (4), 045122.

Fleury, R.; Sounas, D. L.; Alu, A., Negative refraction and planar focusing based on parity-time symmetric metasurfaces. Physical Review Letters 2014, 113 (2), 023903.

Fuchs, R., Theory of the optical properties of ionic crystal cubes. Physical Review B 1975, 11 (4), 1732.

Garcia de Abajo, F. J., Graphene plasmonics: challenges and opportunities. Acs Photonics 2014, 1 (3), 135-152.

Gates, B. D.; Xu, Q.; Stewart, M.; Ryan, D.; Willson, C. G.; Whitesides, G. M., New approaches to nanofabrication: molding, printing, and other techniques. Chemical reviews 2005, 105 (4), 1171-1196.

Ge, L.; Stone, A. D., Parity-time symmetry breaking beyond one dimension: The role of degeneracy. Physical Review X 2014, 4 (3), 031011.

Genevet, P.; Yu, N.; Aieta, F.; Lin, J.; Kats, M. A.; Blanchard, R.; Scully, M. O.; Gaburro, Z.; Capasso, F., Ultra-thin plasmonic optical vortex plate based on phase discontinuities. Applied Physics Letters 2012, 100 (1), 013101.

Gomez-Diaz, J. S.; Tymchenko, M.; Alù, A., Hyperbolic plasmons and topological transitions over uniaxial metasurfaces. Physical Review Letters 2015, 114 (23), 233901.

Grady, N. K.; Heyes, J. E.; Chowdhury, D. R.; Zeng, Y.; Reiten, M. T.; Azad, A. K.; Taylor, A. J.; Dalvit, D. A.; Chen, H.-T., Terahertz metamaterials for linear polarization conversion and anomalous refraction. Science 2013, 340 (6138), 1304-1307.

Green, R. B., Scattering from conjugate-matched antennas. Antennas and Propagation, IEEE Transactions on 1966, 14 (1), 17-21.

Greenleaf, A.; Kurylev, Y.; Lassas, M.; Uhlmann, G., Cloaking a sensor via transformation optics. Physical Review E 2011, 83 (1), 016603.

Gustafsson, M.; Sohl, C.; Kristensson, G. In Physical limitations on antennas of arbitrary shape, Proceedings of the Royal Society of London A: Mathematical, Physical and Engineering Sciences, The Royal Society: 2007; pp 2589-2607.

Harrington, R., Time-Harmonic Electromagnetic Fields. John Wiley & Sons: 2001.

Hecht, B.; Sick, B.; Wild, U. P.; Deckert, V.; Zenobi, R.; Martin, O. J.; Pohl, D. W., Scanning near-field optical microscopy with aperture probes: Fundamentals and applications. The Journal of Chemical Physics 2000, 112 (18), 7761-7774.

Helsing, J.; McPhedran, R. C.; Milton, G. W., Spectral super-resolution in metamaterial composites. New Journal of Physics 2011, 13 (11), 115005.

Holloway, C. L.; Dienstfrey, A.; Kuester, E. F.; O'Hara, J. F.; Azad, A. K.; Taylor, A. J., A discussion on the interpretation and characterization of metafilms/metasurfaces: The two-dimensional equivalent of metamaterials. Metamaterials 2009, 3 (2), 100-112.

Holloway, C. L.; Kuester, E. F.; Gordon, J. A.; Hara, J. O.; Booth, J.; Smith, D. R., An overview of the theory and applications of metasurfaces: The two-dimensional equivalents of metamaterials. Antennas and Propagation Magazine, IEEE 2012, 54 (2), 10-35.

Holloway, C. L.; Mohamed, M. A.; Kuester, E. F.; Dienstfrey, A., Reflection and transmission properties of a metafilm: With an application to a controllable surface composed of resonant particles. Electromagnetic Compatibility, IEEE Transactions on 2005, 47 (4), 853-865.

Houck, A. A.; Brock, J. B.; Chuang, I. L., Experimental observations of a left-handed material that obeys Snell's law. Physical Review Letters 2003, 90 (13), 137401.

Husu, H.; Siikanen, R.; Mäkitalo, J.; Lehtolahti, J.; Laukkanen, J.; Kuittinen, M.; Kauranen, M., Metamaterials with tailored nonlinear optical response. Nano Letters 2012, 12 (2), 673-677.

Ishimaru, A., Wave propagation and scattering in random media. Academic press New York: 1978.

Jacob, Z.; Alekseyev, L. V.; Narimanov, E., Optical hyperlens: far-field imaging beyond the diffraction limit. Optics Express 2006, 14 (18), 8247-8256.

Jelinek, L.; Machac, J., A Polarizability Measurement Method for Electrically Small Particles. Antennas and Wireless Propagation Letters, IEEE 2014, 13, 1051-1053.

Joannopoulos, J. D.; Johnson, S. G.; Winn, J. N.; Meade, R. D., Photonic crystals: molding the flow of light. Princeton university press: 2011.

Kahn, W. K.; Kurss, H., Minimum-scattering antennas. Antennas and Propagation, IEEE Transactions on 1965, 13 (5), 671-675.

Karilainen, A. O.; Tretyakov, S. A., Circularly polarized receiving antenna incorporating two helices to achieve low backscattering. Antennas and Propagation, IEEE Transactions on 2012, 60 (7), 3471-3475.

Kelly, K. L.; Coronado, E.; Zhao, L. L.; Schatz, G. C., The optical properties of metal nanoparticles: the influence of size, shape, and dielectric environment. The Journal of Physical Chemistry B 2003, 107 (3), 668-677.

Kettunen, H.; Wallén, H.; Sihvola, A., Electrostatic response of a half-disk. Journal of Electrostatics 2009, 67 (6), 890-897.

Kildishev, A. V.; Boltasseva, A.; Shalaev, V. M., Planar photonics with metasurfaces. Science 2013, 339 (6125), 1232009.

Kim, M.; Wong, A. M.; Eleftheriades, G. V., Optical Huygens' metasurfaces with independent control of the magnitude and phase of the local reflection coefficients. Physical Review X 2014, 4 (4), 041042.

Klar, T.; Perner, M.; Grosse, S.; Von Plessen, G.; Spirkl, W.; Feldmann, J., Surface-plasmon resonances in single metallic nanoparticles. Physical Review Letters 1998, 80 (19), 4249.

Kuester, E. F.; Mohamed, M. A.; Piket-May, M.; Holloway, C. L., Averaged transition conditions for electromagnetic fields at a metafilm. Antennas and Propagation, IEEE Transactions on 2003, 51 (10), 2641-2651.

Kuiper, S.; Hendriks, B., Variable-focus liquid lens for miniature cameras. Appl. Phys. Lett. 2004, 85 (7), 1128-1130.

Kurs, A.; Karalis, A.; Moffatt, R.; Joannopoulos, J. D.; Fisher, P.; Soljačić, M., Wireless power transfer via strongly coupled magnetic resonances. Science 2007, 317 (5834), 83-86.

Kwon, D.-H.; Pozar, D. M., Optimal characteristics of an arbitrary receive antenna. Antennas and Propagation, IEEE Transactions on 2009, 57 (12), 3720-3727.

Lai, Y.; Ng, J.; Chen, H.; Han, D.; Xiao, J.; Zhang, Z.-Q.; Chan, C. T., Illusion optics: the optical transformation of an object into another object. Physical Review Letters 2009, 102 (25), 253902.

Landy, N.; Sajuyigbe, S.; Mock, J.; Smith, D.; Padilla, W., Perfect metamaterial absorber. Physical Review Letters 2008, 100 (20), 207402.

Landy, N.; Smith, D. R., A full-parameter unidirectional metamaterial cloak for microwaves. Nature Materials 2013, 12 (1), 25-28.

Lee, J.; Nam, S., Fundamental aspects of near-field coupling small antennas for wireless power transfer. Antennas and Propagation, IEEE Transactions on 2010, 58 (11), 3442-3449.

Leonhardt, U., Optical conformal mapping. Science 2006, 312 (5781), 1777-1780.

Li, G.; Kang, M.; Chen, S.; Zhang, S.; Pun, E. Y.-B.; Cheah, K. W.; Li, J., Spin-enabled plasmonic metasurfaces for manipulating orbital angular momentum of light. Nano letters 2013, 13 (9), 4148-4151.

Li, J.; Pendry, J., Hiding under the carpet: a new strategy for cloaking. Physical Review Letters 2008, 101 (20), 203901.

Li, X.; Xiao, S.; Cai, B.; He, Q.; Cui, T. J.; Zhou, L., Flat metasurfaces to focus electromagnetic waves in reflection geometry. Optics letters 2012, 37 (23), 4940-4942.

Lin, D.; Fan, P.; Hasman, E.; Brongersma, M. L., Dielectric gradient metasurface optical elements. science 2014, 345 (6194), 298-302.

Lin, Z.; Ramezani, H.; Eichelkraut, T.; Kottos, T.; Cao, H.; Christodoulides, D. N., Unidirectional invisibility induced by P T-symmetric periodic structures. Physical Review Letters 2011, 106 (21), 213901.

Litchinitser, N. M.; Maimistov, A. I.; Gabitov, I. R.; Sagdeev, R. Z.; Shalaev, V. M., Metamaterials: electromagnetic enhancement at zero-index transition. Optics Letters 2008, 33 (20), 2350-2352.

Liu, L.; Zhang, X.; Kenney, M.; Su, X.; Xu, N.; Ouyang, C.; Shi, Y.; Han, J.; Zhang, W.; Zhang, S., Broadband metasurfaces with simultaneous control of phase and amplitude. Advanced Materials 2014, 26 (29), 5031-5036.

Liu, N.; Mesch, M.; Weiss, T.; Hentschel, M.; Giessen, H., Infrared perfect absorber and its application as plasmonic sensor. Nano letters 2010, 10 (7), 2342-2348.

Lu, Y.-J.; Kim, J.; Chen, H.-Y.; Wu, C.; Dabidian, N.; Sanders, C. E.; Wang, C.-Y.; Lu, M.-Y.; Li, B.-H.; Qiu, X., Plasmonic nanolaser using epitaxially grown silver film. science 2012, 337 (6093), 450-453.

Luk'yanchuk, B.; Zheludev, N. I.; Maier, S. A.; Halas, N. J.; Nordlander, P.; Giessen, H.; Chong, C. T., The Fano resonance in plasmonic nanostructures and metamaterials. Nature materials 2010, 9 (9), 707-715.

Luo, Y.; Lei, D. Y.; Maier, S. A.; Pendry, J., Broadband light harvesting nanostructures robust to edge bluntness. Physical review letters 2012, 108 (2), 023901.

Ma, Y. G.; Sahebdivan, S.; Ong, C.; Tyc, T.; Leonhardt, U., Evidence for subwavelength imaging with positive refraction. New Journal of Physics 2011, 13 (3), 033016.

Maci, S.; Minatti, G.; Casaletti, M.; Bosiljevac, M., Metasurfing: Addressing waves on impenetrable metasurfaces. Antennas and Wireless Propagation Letters, IEEE 2011, 10, 1499-1502.

Maier, S. A., Plasmonics: fundamentals and applications. Springer Science & Business Media: 2007.

Makris, K. G.; El-Ganainy, R.; Christodoulides, D. N.; Musslimani, Z. H., Beam dynamics in P T symmetric optical lattices. Physical Review Letters 2008, 100 (10), 103904.

Malitson, I., Interspecimen Comparison of the Refractive Index of Fused Silica*,†. JOSA 1965, 55 (10), 1205-1209.

Mann, S. A.; Garnett, E. C., Extreme light absorption in thin semiconductor films wrapped around metal nanowires. Nano letters 2013, 13 (7), 3173-3178.

McCall, S.; Platzman, P.; Dalichaouch, R.; Smith, D.; Schultz, S., Microwave propagation in two-dimensional dielectric lattices. Physical Review Letters 1991, 67 (15), 2017.

McPhedran, R.; Perrins, W., Electrostatic and optical resonances of cylinder pairs. Applied physics 1981, 24 (4), 311-318.

Milton, G. W., The theory of composites. Cambridge monographs on applied and computational mathematics: 2002.

Mohammadi Estakhri, N.; Alù, A., Manipulating optical reflections using engineered nanoscale metasurfaces. Physical Review B 2014, 89 (23), 235419.

Mohammadi Estakhri, N.; Alù, A., Minimum-scattering superabsorbers. Physical Review B, Rapid Communications 2014, 89 (12), 121416.

Mohammadi Estakhri, N.; Alù, A., Parity-time symmetry breaking and amplifier-absorber transitions in plasmonic nanoparticles. 2015 Conference on Lasers and Electro-Optics (CLEO)-Laser Science to Photonic Applications, 2015.

Mohammadi Estakhri, N.; Alù, A., Physics of unbounded, broadband absorption/gain efficiency in plasmonic nanoparticles. Physical Review B 2013, 87 (20), 205418.

Mohammadi Estakhri, N.; Alu, A., Ultra-thin unidirectional carpet cloak and wavefront reconstruction with graded metasurfaces. Antennas and Wireless Propagation Letters, IEEE 2014, 13, 1775-1778.

Mohammadi Estakhri, N.; Alu, A., Wavefront Transformation with Gradient Metasurfaces, under review.

Mohammadi Estakhri, N.; Argyropoulos, C.; Alù, A., Graded metascreens to enable a new degree of nanoscale light management. Phil. Trans. R. Soc. A 2015, 373 (2049), 20140351.

Mohammadi Estakhri, N.; Neder, V.; Knight, M.; Polman, A.; Alu, A., Wide-Angle, Broadband Graded Metasurface for Back Reflection, under review.

Monticone, F.; Mohammadi Estakhri, N.; Alù, A., Full control of nanoscale optical transmission with a composite metascreen. Physical Review Letters 2013, 110 (20), 203903.

Munson, R. E.; Haddad, H. A.; Hanlen, J. W., Microstrip reflectarray for satellite communication and radar cross-section enhancement or reduction. Google Patents: 1987.

Ni, X.; Emani, N. K.; Kildishev, A. V.; Boltasseva, A.; Shalaev, V. M., Broadband light bending with plasmonic nanoantennas. Science 2012, 335 (6067), 427-427.

Ni, X.; Kildishev, A. V.; Shalaev, V. M., Metasurface holograms for visible light. Nature communications 2013, 4.

Ni, X.; Wong, Z. J.; Mrejen, M.; Wang, Y.; Zhang, X., An ultrathin invisibility skin cloak for visible light. Science 2015, 349 (6254), 1310-1314.

Noginov, M.; Zhu, G.; Bahoura, M.; Adegoke, J.; Small, C.; Ritzo, B.; Drachev, V.; Shalaev, V., Enhancement of surface plasmons in an Ag aggregate by optical gain in a dielectric medium. Optics letters 2006, 31 (20), 3022-3024.

Noginov, M.; Zhu, G.; Belgrave, A.; Bakker, R.; Shalaev, V.; Narimanov, E.; Stout, S.; Herz, E.; Suteewong, T.; Wiesner, U., Demonstration of a spaser-based nanolaser. Nature 2009, 460 (7259), 1110-1112.

Novotny, L., Effective wavelength scaling for optical antennas. Physical Review Letters 2007, 98 (26), 266802.

Orazbayev, B.; Estakhri, N. M.; Beruete, M.; Alù, A., Terahertz carpet cloak based on a ring resonator metasurface. Physical Review B 2015, 91 (19), 195444.

Ordal, M. A.; Bell, R. J.; Alexander, R.; Long, L.; Querry, M., Optical properties of fourteen metals in the infrared and far infrared: Al, Co, Cu, Au, Fe, Pb, Mo, Ni, Pd, Pt, Ag, Ti, V, and W. Applied optics 1985, 24 (24), 4493-4499.

Ordal, M.; Long, L.; Bell, R.; Bell, S.; Bell, R.; Alexander, R.; Ward, C., Optical properties of the metals al, co, cu, au, fe, pb, ni, pd, pt, ag, ti, and w in the infrared and far infrared. Appl. Opt. 1983, 22 (7), 1099-1119.

Pala, R. A.; White, J.; Barnard, E.; Liu, J.; Brongersma, M. L., Design of plasmonic thin film solar cells with broadband absorption enhancements. Advanced Materials 2009, 21 (34), 3504-3509.

Papakostas, A.; Potts, A.; Bagnall, D.; Prosvirnin, S.; Coles, H.; Zheludev, N., Optical manifestations of planar chirality. Physical Review Letters 2003, 90 (10), 107404.

Pendry, J. B., Negative refraction makes a perfect lens. Physical Review Letters 2000, 85 (18), 3966.

Pendry, J. B.; Schurig, D.; Smith, D. R., Controlling electromagnetic fields. Science 2006, 312 (5781), 1780-1782.

Pfeiffer, C.; Grbic, A., Bianisotropic metasurfaces for optimal polarization control: analysis and synthesis. Physical Review Applied 2014, 2 (4), 044011.

Pfeiffer, C.; Grbic, A., Metamaterial Huygens' surfaces: tailoring wave fronts with reflectionless sheets. Physical review letters 2013, 110 (19), 197401.

Pitkonen, M., A closed-form solution for the polarizability of a dielectric double half-cylinder. Journal of Electromagnetic Waves and Applications 2010, 24 (8-9), 1267-1277.

Pohl, D. W.; Denk, W.; Lanz, M., Optical stethoscopy: Image recording with resolution λ/20. Applied physics letters 1984, 44 (7), 651-653.

Polman, A., Plasmonics applied. Science 2008, 322 (5903), 868-869.

Pors, A.; Nielsen, M. G.; Bernardin, T.; Weeber, J.-C.; Bozhevolnyi, S. I., Efficient unidirectional polarization-controlled excitation of surface plasmon polaritons. Light: Science & Applications 2014, 3 (8), e197.

Pors, A.; Nielsen, M. G.; Eriksen, R. L.; Bozhevolnyi, S. I., Broadband focusing flat mirrors based on plasmonic gradient metasurfaces. Nano letters 2013, 13 (2), 829-834.

Pozar, D. M., Microwave engineering. John Wiley & Sons: 1997.

Pozar, D. M.; Targonski, S. D.; Syrigos, H., Design of millimeter wave microstrip reflectarrays. Antennas and Propagation, IEEE Transactions on 1997, 45 (2), 287-296.

Pozar, D., Flat lens antenna concept using aperture coupled microstrip patches. Electronics Letters 1996, 32 (23), 2109-2111.

Prodan, E.; Radloff, C.; Halas, N. J.; Nordlander, P., A hybridization model for the plasmon response of complex nanostructures. Science 2003, 302 (5644), 419-422.

Rainwater, D.; Kerkhoff, A.; Melin, K.; Soric, J.; Moreno, G.; Alù, A., Experimental verification of three-dimensional plasmonic cloaking in free-space. New Journal of Physics 2012, 14 (1), 013054.

Rakić, A. D.; Djurišić, A. B.; Elazar, J. M.; Majewski, M. L., Optical properties of metallic films for vertical-cavity optoelectronic devices. Applied optics 1998, 37 (22), 5271-5283.

Ramakrishna, S. A.; Pendry, J. B., Removal of absorption and increase in resolution in a near-field lens via optical gain. Physical Review B 2003, 67 (20), 201101.

Ruan, Z.; Fan, S., Superscattering of light from subwavelength nanostructures. Physical review letters 2010, 105 (1), 013901.

Rumsey, V., Reaction concept in electromagnetic theory. Physical Review 1954, 94 (6), 1483.

Ruschhaupt, A.; Delgado, F.; Muga, J., Physical realization of-symmetric potential scattering in a planar slab waveguide. Journal of Physics A: Mathematical and General 2005, 38 (9), L171.

Russell, P., Photonic crystal fibers. science 2003, 299 (5605), 358-362.

Rüter, C. E.; Makris, K. G.; El-Ganainy, R.; Christodoulides, D. N.; Segev, M.; Kip, D., Observation of parity–time symmetry in optics. Nature Physics 2010, 6 (3), 192-195.

Sadiku, M. N. O., Numerical techniques in electromagnetics. CRC, Boca Raton, FL: 2001.

Salandrino, A.; Alù, A.; Engheta, N., Parallel, series, and intermediate interconnections of optical nanocircuit elements. 1. Analytical solution. JOSA B 2007, 24 (12), 3007-3013.

Sautter, J. r.; Staude, I.; Decker, M.; Rusak, E.; Neshev, D. N.; Brener, I.; Kivshar, Y. S., Active tuning of all-dielectric metasurfaces. ACS nano 2015, 9 (4), 4308-4315.

Savoia, S.; Castaldi, G.; Galdi, V.; Alù, A.; Engheta, N., PT-symmetry-induced wave confinement and guiding in ε-near-zero metamaterials. Physical Review B 2015, 91 (11), 115114.

Schurig, D.; Mock, J.; Justice, B.; Cummer, S. A.; Pendry, J. B.; Starr, A.; Smith, D., Metamaterial electromagnetic cloak at microwave frequencies. Science 2006, 314 (5801), 977-980.

Selvanayagam, M.; Eleftheriades, G. V., An active electromagnetic cloak using the equivalence principle. Antennas and Wireless Propagation Letters, IEEE 2012, 11, 1226-1229.

Selvanayagam, M.; Eleftheriades, G. V., Discontinuous electromagnetic fields using orthogonal electric and magnetic currents for wavefront manipulation. Optics Express 2013, 21 (12), 14409-14429.

Selvanayagam, M.; Eleftheriades, G., Polarization control using tensor Huygens surfaces. Antennas and Propagation, IEEE Transactions on 2014, 62 (12), 6155-6168.

Shalaev, V. M., Optical negative-index metamaterials. Nature photonics 2007, 1 (1), 41-48.

Shalaev, V. M.; Cai, W.; Chettiar, U. K.; Yuan, H.-K.; Sarychev, A. K.; Drachev, V. P.; Kildishev, A. V., Negative index of refraction in optical metamaterials. Optics letters 2005, 30 (24), 3356-3358.

Silveirinha, M. G.; Engheta, N., Theory of supercoupling, squeezing wave energy, and field confinement in narrow channels and tight bends using ε near-zero metamaterials. Physical Review B 2007, 76 (24), 245109.

Sipe, J.; Van Kranendonk, J., Macroscopic electromagnetic theory of resonant dielectrics. Physical Review A 1974, 9 (5), 1806.

Smith, D. R.; Padilla, W. J.; Vier, D.; Nemat-Nasser, S. C.; Schultz, S., Composite medium with simultaneously negative permeability and permittivity. Physical Review Letters 2000, 84 (18), 4184.

Soukoulis, C. M.; Wegener, M., Past achievements and future challenges in the development of three-dimensional photonic metamaterials. Nature Photonics 2011, 5 (9), 523-530.

Sounas, D. L.; Alù, A., Extinction symmetry for reciprocal objects and its implications on cloaking and scattering manipulation. Optics letters 2014, 39 (13), 4053-4056.

Sounas, D. L.; Fleury, R.; Alù, A., Unidirectional cloaking based on metasurfaces with balanced loss and gain. Physical Review Applied 2015, 4 (1), 014005.

Stockman, M. I., Spaser action, loss compensation, and stability in plasmonic systems with gain. Physical review letters 2011, 106 (15), 156802.

Suchowski, H.; O'Brien, K.; Wong, Z. J.; Salandrino, A.; Yin, X.; Zhang, X., Phase mismatch–free nonlinear propagation in optical zero-index materials. Science 2013, 342 (6163), 1223-1226.

Sun, S.; He, Q.; Xiao, S.; Xu, Q.; Li, X.; Zhou, L., Gradient-index meta-surfaces as a bridge linking propagating waves and surface waves. Nature Materials 2012, 11 (5), 426-431.

Sun, S.; Yang, K.-Y.; Wang, C.-M.; Juan, T.-K.; Chen, W. T.; Liao, C. Y.; He, Q.; Xiao, S.; Kung, W.-T.; Guo, G.-Y., High-efficiency broadband anomalous reflection by gradient meta-surfaces. Nano Letters 2012, 12 (12), 6223-6229.

Sun, Y.; Xia, Y., Shape-controlled synthesis of gold and silver nanoparticles. Science 2002, 298 (5601), 2176-2179.

Taillaert, D.; Bienstman, P.; Baets, R., Compact efficient broadband grating coupler for silicon-on-insulator waveguides. Optics letters 2004, 29 (23), 2749-2751.

Taillaert, D.; Van Laere, F.; Ayre, M.; Bogaerts, W.; Van Thourhout, D.; Bienstman, P.; Baets, R., Grating couplers for coupling between optical fibers and nanophotonic waveguides. Japanese Journal of Applied Physics 2006, 45 (8R), 6071.

Tretyakov, S., Analytical modeling in applied electromagnetics. Artech House: 2003.

Tsai, M.-W.; Chuang, T.-H.; Meng, C.-Y.; Chang, Y.-T.; Lee, S.-C., High performance midinfrared narrow-band plasmonic thermal emitter. Applied physics letters 2006, 89 (17), 173116.

Wang, J.; Qu, S.; Ma, H.; Xu, Z.; Zhang, A.; Zhou, H.; Chen, H.; Li, Y., High-efficiency spoof plasmon polariton coupler mediated by gradient metasurfaces. Applied Physics Letters 2012, 101 (20), 201104.

Whitman, G. M.; Schwering, F., Reciprocity identity for periodic surface scattering. IEEE Transactions on Antennas and Propagation 1979, 27, 252-254.

Wu, Q.; Hewitt, T.; Zhang, X. C., Two□dimensional electro□optic imaging of THz beams. Appl. Phys. Lett. 1996, 69 (8), 1026-1028.

Wu, Q.; Litz, M.; Zhang, X. C., Broadband detection capability of ZnTe electro□optic field detectors. Applied Physics Letters 1996, 68 (21), 2924-2926.

Wu, Y.; Zhang, C.; Estakhri, N. M.; Zhao, Y.; Kim, J.; Zhang, M.; Liu, X. X.; Pribil, G. K.; Alù, A.; Shih, C. K., Intrinsic optical properties and enhanced plasmonic response of epitaxial silver. Advanced Materials 2014, 26 (35), 6106-6110.

Xiao, S.; Drachev, V. P.; Kildishev, A. V.; Ni, X.; Chettiar, U. K.; Yuan, H.-K.; Shalaev, V. M., Loss-free and active optical negative-index metamaterials. Nature 2010, 466 (7307), 735-738.

Yu, N.; Capasso, F., Flat optics with designer metasurfaces. Nature materials 2014, 13 (2), 139-150.

Yu, N.; Genevet, P.; Kats, M. A.; Aieta, F.; Tetienne, J.-P.; Capasso, F.; Gaburro, Z., Light propagation with phase discontinuities: generalized laws of reflection and refraction. science 2011, 334 (6054), 333-337.

Yu, Z.; Raman, A.; Fan, S., Fundamental limit of nanophotonic light trapping in solar cells. Proceedings of the National Academy of Sciences 2010, 107 (41), 17491-17496.

Zhang, B.; Chan, T.; Wu, B.-I., Lateral shift makes a ground-plane cloak detectable. Physical review letters 2010, 104 (23), 233903.

Zhao, Y.; Alù, A., Manipulating light polarization with ultrathin plasmonic metasurfaces. Physical Review B 2011, 84 (20), 205428.

Zhao, Y.; Belkin, M.; Alù, A., Twisted optical metamaterials for planarized ultrathin broadband circular polarizers. Nature communications 2012, 3, 870.

Zhao, Y.; Engheta, N.; Alù, A., Homogenization of plasmonic metasurfaces modeled as transmission-line loads. Metamaterials 2011, 5 (2), 90-96.

Zheludev, N. I.; Prosvirnin, S.; Papasimakis, N.; Fedotov, V., Lasing spaser. Nature Photonics 2008, 2 (6), 351-354.

Zhu, X.; Feng, L.; Zhang, P.; Yin, X.; Zhang, X., One-way invisible cloak using parity-time symmetric transformation optics. Optics letters 2013, 38 (15), 2821-2824.

Zou, L.; Withayachumnankul, W.; Shah, C. M.; Mitchell, A.; Bhaskaran, M.; Sriram, S.; Fumeaux, C., Dielectric resonator nanoantennas at visible frequencies. Optics express 2013, 21 (1), 1344-1352.